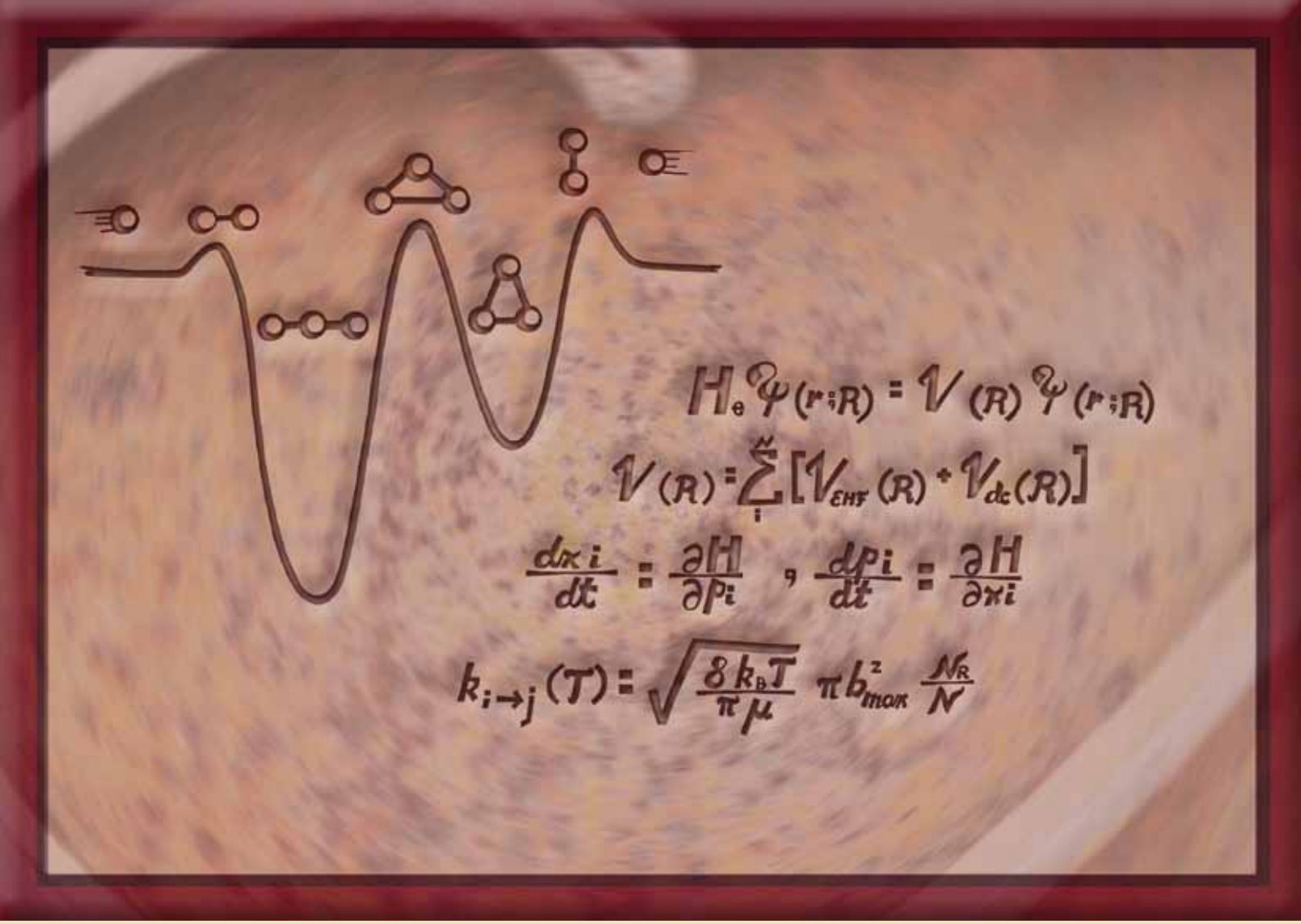

Breno Rodrigues Lamaghere Galvão

POTENTIAL ENERGY SURFACES AND DYNAMICS OF ATMOSPHERIC REACTIONS

Ph.D. thesis in Chemistry, Theoretical Chemistry, under the supervision of Professor A. J. C. Varandas and presented to the Departamento de Química of Universidade de Coimbra

June 2012

· U C ·

Universidade de Coimbra

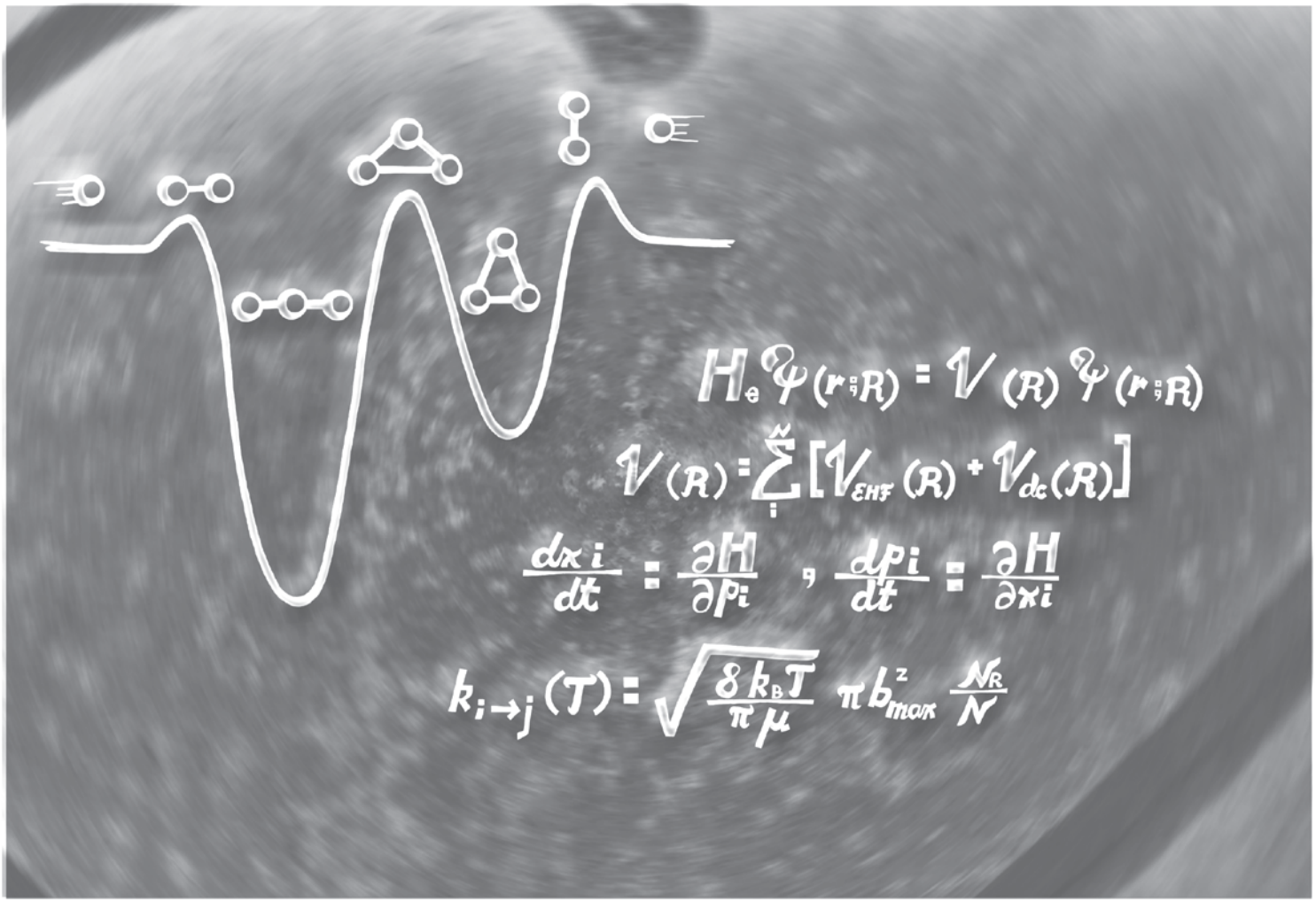

Breno Rodrigues Lamaghere Galvão

POTENTIAL ENERGY SURFACES AND DYNAMICS OF ATMOSPHERIC REACTIONS

Ph.D. thesis in Chemistry, Theoretical Chemistry, under the supervision of Professor A. J. C. Varandas and presented to the Departamento de Química of Universidade de Coimbra

June 2012

· U C ·

Universidade de Coimbra

à minha família

Agradecimentos

Não seria possível me expressar aqui com a devida intensidade o quanto sou grato a diversas pessoas, por cada ajuda e ensinamento que recebi. Primeiramente gostaria de agradecer ao meu orientador, Professor António Joaquim de Campos Varandas, por todas as oportunidades concedidas que me possibilitaram realizar o doutoramento, e por tudo que foi aprendido sob sua supervisão. Não tenho dúvidas de que deverei a ele qualquer êxito científico que por ventura obtiver. Agradeço também em especial ao meu orientador na graduação, Professor João Pedro Braga, por tudo que aprendi sob sua supervisão e pela fundamental ajuda em me encaminhar para este doutoramento.

A meus pais devo não só este doutoramento, mas por abrirem cada oportunidade que tive durante a vida toda. Por me moldarem como pessoa, pela educação e pelos valores que me passaram. Pelo amor incondicional, carinho e pelo privilégio de pertencer a essa família. A lista não caberia nessa página, simplesmente os amo muito. Agradeço também pelo carinho da minha família: à minha irmã, meus primos, tios e avós.

Aos amigos do grupo QT&C que me acompanharam durante todo esse período de trabalho, especialmente Vinícius, Caridade e Viegas por tudo em que me ajudaram e pela companhia por todos esses anos. Aos bons amigos que fiz nessa cidade e aos bons amigos de longa data: David, Pedro, Daniel, Helbert, Bebeto, Leo, Monoh, Luís, ao Goku e a outros que me falta espaço para mencionar. Agradeço também à Mari-Anna pelo trabalho artístico na capa da tese.

Para finalizar agradeço a Fundação Para a Ciência e a Tecnologia, pelo apoio financeiro concedido através da bolsa SFRH/BD/61229/2009.

Abstract

In this Ph.D. thesis three chemical systems of atmospheric relevance (H_2O, N_3 and NO_2) were studied by theoretical means and exclusively from first principles. High level methods of electronic structure calculations were employed for the modeling of potential energy surfaces (PES) using the double many-body expansion, while the reaction dynamics problem was solved by quasiclassical methods. The first part gives the theoretical background that concerns the methodology used during the research: starting from the concept of a PES and its limitations, the survey continues to the calculation and modeling, followed by the description of reaction dynamics and quasiclassical trajectories.

The second part presents the results obtained on the research itself. Firstly, a highly accurate PES for the water molecule capable of describing its dissociation limits is obtained, and subsequent calculations of the vibrational levels have shown that this PES mimics the experimental values within $1\,\mathrm{cm}^{-1}$. The focus is then changed to collisions between atomic and molecular nitrogen, where a PES of chemical accuracy was obtained for the study of the system in the ground state. Using this surface, a quasiclassical study of such collisions was performed and theoretical predictions were obtained for the rate constants. The increasing interest in this system led us to also study the excited state of atomic nitrogen, which involved multi-valued PESs and nonadiabatic dynamics. For the third system, a study of collisions between nitric oxide and oxygen was pursued, allowing a better understanding of the reaction that gives rise to NO($v = 1$) in the atmosphere and the implications in modeling it.

Resumo

Nesta dissertação foram abordados três sistemas químicos de interesse para o estudo da atmosfera (H_2O, N_3 e NO_2) através de uma perspectiva teórica e exclusivamente a partir de primeiros princípios. Foram realizados cálculos avançados de estrutura electrónica necessários para a modelação de superfícies de energia potencial (SEP) através da dupla expansão multicorpos, sendo a dinâmica das colisões realizada através do método quasiclássico. A primeira parte apresenta o embasamento teórico necessário para a investigação feita. Começando pela definição do conceito de SEP e suas limitações, passa-se para os métodos de cálculos e sua representação analítica, terminando com a aplicação das mesmas para o estudo de dinâmica.

Na segunda parte apresentam-se resultados obtidos durante a investigação. Primeiramente obtêm-se uma SEP global e de alta precisão para a molécula H_2O capaz de descrever os limites dissociativos da mesma, onde o cálculo dos níveis vibracionais mostra que esta SEP apresenta concordância com os valores experimentais em torno de $1\,cm^{-1}$. O foco é então passado para as colisões entre nitrogénio atómico e molecular, onde uma SEP de precisão química é obtida para o estudo de tal sistema no estado fundamental. Utilizando essa superfície foi realizado um estudo quasiclássico das colisões, onde foram obtidas previsões teóricas para as constantes de velocidade. O crescente interesse neste sistema levou ao estudo dessas colisões para o estado excitado do nitrogénio atómico, envolvendo neste caso SEPs multi-valoradas e dinâmica não adiabática. Para o terceiro sistema químico foi realizado um estudo das colisões entre óxido nítrico e oxigénio, que permitiu um maior entendimento da reação que dá origem ao NO($v = 1$) na atmosfera e as implicações na modelação da mesma.

Contents

Acronyms

ACVXZ	Augmented correlation-consistent polarized core-valence basis sets
AVXZ	Augmented correlation consistent basis sets
BO	Born-Oppenheimer
CAS	Complete Active Space
CASPT2	Complete Active Space with Second-order Perturbation Theory
CASSCF	Complete Active Space Self Consistent Field
CBS	Complete Basis Set
CCSD	Coupled-Cluster with Single and Double excitations
CCSD(T)	Coupled-Cluster with Single and Double and Perturbative Triple excitations
CI	Configuration Interaction or Conical Intersection
CIRRIS-1A	Cryogenic Infrared Instrumentation for Shuttle
CS	Correlation Scaling
CSF	Configuration State Function
CVRQD	Core-Valence Relativistic Quantum electrodynamics
D2	Two-Electron Contribution to the Darwin term
DBOC	Diagonal Born-Oppenheimer Correction
DC	Dynamical Correlation
DIM	Diatomics-in-Molecules

DMBE	Double Many-Body Expansion
DVR3D	Discrete Variable Representation for three Dimensions
EHF	Extended Hartree Fock
EHFACE2U	EHF Approximate Correlation Energy including the United-atom limit
ES	Energy Switching
FCI	Full Configuration Interaction
GDA	Global Diabatization Angle
GP	Geometric Phase
GTO	Gaussian Type Orbital
HF	Hartree Fock
KM	Karton and Martin extrapolation protocol
L4	LAGROBO-4 potential energy surface
L4w	LAGROBO-4 potential energy surface with ad-hoc long-range term
LAGROBO	Largest Angle Generalized Rotating Bond Order
LEPS	London-Eyring-Polanyi-Sato
MBE	Many-Body Expansion
MCSCF	Multi Configuration Self Consistent Field
MGB	Momentum Gaussian Binning
MRCI	Multi-Reference Configuration Interaction
MRCISD	MRCI with with singles and doubles excitations
MRCI(Q)	Multi-Reference Configuration Interaction with Davidson correction
MSX	Minima on the Seam of Crossing
MVD1	One-electron Mass Velocity and Darwin term
PES	Potential Energy Surface
QCT	Quasiclassical Trajectory
QCT-IEQMT	QCT-Internal Energy Quantum Mechanical Threshold

QCT-IVEQMT	QCT-Intermediate Vibrational Energy Quantum Mechanical Threshold
QCT-NVEQMT	QCT-Rotational and Vibrational Energy Quantum Mechanical Threshold
QCT-QMT	QCT-Quantum Mechanical Threshold
QCT-VEQMT	QCT-Vibrational Energy Quantum Mechanical Threshold
RMSD	root mean square deviation
RRKM	Rice–Ramsperger–Kassel–Marcus
SCF	Self Consistent Field
STO	Slater Type Orbital
TDQD	Time-Dependent Quantum Dynamics
TIDQ	Time-Independent Quantum Dynamics
TS	Transition State
TSH	Trajectory Surface Hopping
USTE	Uniform Singlet- and Triplet-pair Extrapolation
WSHDSP	Wang-Stallcop-Huo-Dateo-Schwenke-Partridge
ZPE	Zero-Point Energy

Preface

The chemistry of the atmosphere is a very interesting scientific topic that has allowed mankind to unveil important details of nature, such as the greenhouse effect, the oxygen/nitrogen/carbon cycles, weather phenomena and so on. Currently, there is an enormous interdisciplinary research effort aimed at understanding every detail concerning the atmosphere and, even so, there are problems yet to be clarified such as the ozone deficit[1].

From the theoretical point of view, it is a very unique part of chemistry, since the most important constituents of the atmosphere are small atoms and clusters and its elementary reactions happen in gas phase. This allows for a much more rigorous treatment than for solids, liquids or biological reactions. One can study each collision individually by resolving the reactants and products state-by-state and predicting macroscopic data capable of achieving experimental accuracy, or even predict new relevant data where no experiments can be performed.

Within the Born-Oppenheimer framework[2], the most standard theoretical pathway to study reaction dynamics and/or spectroscopy goes as follows: calculate the electronic energy for a representative set of molecular geometries, model them to a suitable functional form to obtain the potential energy surface (PES) and solve the nuclear motion problem. All of the above steps are surveyed in the first part of this doctoral thesis, while the second part shows the results of our work on three specific systems: the water molecule, the collisions between atomic and molecular nitrogen and collisions between atomic oxygen and nitrogen oxide. The following paragraphs summarize the relevance of these systems in the atmosphere and the major results obtained in this work.

Although water vapor is a trace constituent of the atmosphere, it plays a very important environmental role, being one the most potent greenhouse gas and the principal cause of all weather phenomena[3]. We have improved[4–6] a global potential energy surface (obtained exclusively from first principles), giving it spectroscopic accuracy up to 20.000 cm^{-1}. This has only been achieved before for a few systems with small number of electrons, where highly accurate electronic structure calculations can be performed and corrected for all sorts of physical effects, such as relativistic and quantum electrodynamics. The final PES obtained[6] using the energy-switching scheme[7–9] also describes the dissociative limits, allowing first principle predictions of the ro-vibrational levels up to the continuum limit, or even study reactive dynamics, (such as $O(^1D) + H_2 \rightarrow OH + H$ and its inverse) on a spectroscopic accurate potential energy surface.

The major component of Earth's atmosphere is molecular nitrogen (achieving 78% of the total volume), which is also the principal molecule in other atmospheres such as in Titan and Triton (Saturn and Neptune largest moons). Although it is mostly an inert species, nitrogen reactions play an important role when extreme thermal environmental conditions occur. For example, in the reentry of a spacecraft into Earth's atmosphere, or comet/meteor entry into Titan[10], temperatures around 20000 K can be achieved, and under this regime the available nitrogen can be excited, dissociated or ionized. The design of spacecraft heat shields needs the heat load and reactivity data for nitrogen reactions. Since experimental measurements for these high temperature processes are difficult and extrapolations from lower temperature data are also unreliable, the theoretical approach provides the most suitable way of obtaining such data[10].

As part of a research collaboration with the European Space Agency (ESA Contract 21790/08/NL/HE)[11], we performed a thorough study of $N(^4S)$+N_2 collisions which consisted of two parts. First, high level *ab initio* energies for the $N_3(^4A'')$ system were calculated along with modeling of an accurate PES[12] using double many-body expansion theory[13], where new features have been discovered and an improved level of accuracy obtained. Second, rate constants were calculated[14] by integrating quasiclassical trajectories[15] with the addition of an importance sampling method that we have developed to accelerate convergence in reactions with large barriers. This study have shown that

quantum mechanical effects are negligible for the averaged rate constants due to the heavy atomic masses involved. Recently, detailed electronic structure calculations of the transition state for the $N(^4S)$+N_2 reaction[16] have confirmed that the barrier height of our potential energy surface is at most $\sim 0.4 \text{kcal}\,\text{mol}^{-1}$ apart from the best estimate available thus far, making our predictions of the reaction rate constant the most reliable ones reported in the literature.[17–23]

After completing the study of $N(^4S)$+N_2 dynamics, we have decided to also investigate the collisions for the excited state of the nitrogen atom $N(^2D)$, because there were no theoretical or experimental work available, despite the fact that this species is largely found in the extreme conditions mentioned above and even in the ionosphere under ordinary conditions. The $N(^2D)$+N_2 interaction potential is attractive and leads to the formation of the stable azide radical, which has a linear structure. An increasing interest in this system has been observed in the scientific literature since experimental evidence of a new cyclic form was found in 2003[24], which is not yet isolated. This isomer is believed to be a good candidate for high energy and density materials, since its decomposition to N+N_2 would release a large amount of energy without leaving pollutant products. Another motivation is that the linear form of the azide radical is formed on solid molecular nitrogen under intense radiation fields that can break the nitrogen triple bond, and such conditions are known to be present in various low-temperature interstellar and solar system environments such as Triton and Pluto. In fact, Hudson and Moore[25] have proposed the use of linear N_3 as a tracer to follow the abundance of molecular nitrogen in space.

Given the importance of this doublet state, we have obtained the first set of global potential energy surfaces for the system[26,27], which constitute a double-sheeted function for the $1,2^2A''$ states and another for the $1,2^2A'$ states, describing both linear and cyclic wells, the dissociation limits, and all transition states for the $N(^2D)$+N_2 reaction. This allowed for the first time the prediction of rate constants for such collisions, where nonadiabatic effects have been incorporated using the trajectory surface hopping method[28–30] and important conclusions on its dynamics were obtained. We hope that our theoretical results may help experimentalists on a better understanding of the azide chemistry.

The third system studied under this doctoral program was nitric oxide (NO), which

in spite of being present only in minor concentration on Earth's atmosphere, it is responsible for the mid infrared emission of it, since the major components do not radiate in this spectral range. For this reason, NO plays a fundamental role in the cooling down mechanism of the lower thermosphere[31,32], by converting kinetic energy into radiation, which happens in two steps: first from vibrational excitation by collision with atomic oxygen

$$NO(v = 0) + O \rightarrow NO(v = 1) + O$$

followed by emission of an infrared photon

$$NO(v = 1) \rightarrow NO(v = 0) + 5.3\mu m$$

The experimental measurements[33–36] of the rate constant for the above vibrational excitation are normally obtained from the inverse process (relaxation) through the use of detailed balance. From the theoretical side there has been a controversy[37,38] on whether the product NO($v = 1$) shows a thermalized rotational distribution. This is a relevant detail since the knowledge of the correspondence between local temperature and rotational envelopes of the $1 \rightarrow 0$ transition, together with available experimental data[39], can be used to model the temperature as a function of altitude on the thermosphere, where the available techniques are few[40].

We have revisited this issue[41] using accurate PESs developed in our group, and have shed some new insights on such collisions. Our work corroborates older models[37] in that the product rotational distributions are thermalized at local temperature.

Bibliography

[1] B. J. Finlayson-Pitts and J. N. Pitts Jr., *Chemistry of the Upper and Lower Atmosphere: Theory Experiments and Applications* (Academic Press, New York, 2000).

[2] M. Born and J. R. Oppenheimer, Ann. Phys. **84**, 457 (1927).

[3] J. M. Wallace and P. V. Hobbs, *Atmospheric Science: An Introductory Survey* (Elsevier, Amsterdam, 2006).

[4] O. L. Polyansky, A. G. Császár, S. V. Shirin, N. F. Zobov, P. Barletta, J. Tennyson, D. W. Schwenke, and P. J. Knowles, Science **299**, 539 (2003).

[5] P. Barletta, S. V. Shirin, N. F. Zobov, O. L. Polyansky, J. Tennyson, E. F. Valeev, and A. G. Császár, J. Chem. Phys. **125**, 204307 (2006).

[6] B. R. L. Galvão, S. P. J. Rodrigues, and A. J. C. Varandas, J. Chem. Phys. **129**, 044302 (2008).

[7] A. J. C. Varandas, J. Chem. Phys. **105**, 3524 (1996).

[8] A. J. C. Varandas, J. Chem. Phys. **107**, 867 (1997).

[9] A. J. C. Varandas, A. I. Voronin, and P. J. S. B. Caridade, J. Chem. Phys. **108**, 7623 (1998).

[10] D. Wang, J. R. Stallcop, W. M. Huo, C. E. Dateo, D. W. Schwenke, and H. Partridge, J. Chem. Phys. **118**, 2186 (2003).

[11] B. R. L. Galvão, V. C. Mota, P. J. S. B. Caridade, and A. J. C. Varandas, *Accurate electronic manifolds and their use in dynamics*, Tech. rep., European Space Agency (2012), chap. 5, p. 121.

[12] B. R. L. Galvão and A. J. C. Varandas, J. Phys. Chem. A **113**, 14424 (2009).

[13] A. J. C. Varandas, Adv. Chem. Phys. **74**, 255 (1988).

[14] P. J. S. B. Caridade, B. R. L. Galvão, and A. J. C. Varandas, J. Phys. Chem. A **114**, 6063 (2010).

[15] G. H. Peslherbe, H. Wang, and W. L. Hase, Adv. Chem. Phys. **105**, 171 (1999).

[16] A. J. C. Varandas, J. Chem. Phys. **133**, 064104 (2010).

[17] R. A. Back and J. Y. P. Mui, J. Phys. Chem. **66**, 1362 (1962).

[18] A. Bar-Nun and A. Lifshitz, J. Chem. Phys. **47**, 2878 (1967).

[19] R. K. Lyon, Can. J. Chem. **50**, 1437 (1972).

[20] A. Laganà, E. Garcia, and L. Ciccarelli, J. Phys. Chem. **91**, 312 (1987).

[21] E. Garcia and A. Laganà, J. Phys. Chem. A **101**, 4734 (1997).

[22] E. Garcia, A. Saracibar, A. Laganà, and D. Skouteris, J. Phys. Chem. A **111**, 10362 (2007).

[23] D. Wang, W. M. Huo, C. E. Dateo, D. W. Schwenke, and J. R. Stallcop, J. Chem. Phys. **120**, 6041 (2004).

[24] N. Hansen and A. M. Wodtke, J. Phys. Chem. A **107**, 10608 (2003).

[25] R. L. Hudson and M. H. Moore, Astrophys. J. **568**, 1095 (2002).

[26] B. R. L. Galvão and A. J. C. Varandas, J. Phys. Chem. A **115**, 12390 (2011).

[27] B. R. L. Galvão, P. J. S. B. Caridade, and A. J. C. Varandas, Submitted to the J. Chem. Phys. (2012).

[28] J. C. Tully and R. K. Preston, J. Chem. Phys. **55**, 562 (1971).

[29] R. K. Preston and J. C. Tully, J. Chem. Phys. **54**, 4297 (1971).

[30] J. C. Tully, in *Modern Theoretical Chemistry, Dynamics of Molecular Collisions, Part B*, edited by W. Miller (Plenum Press, New York, 1977), p. 217.

[31] G. Kockarts, Geophys. Res. Lett. **7**, 137 (1980).

[32] A. S. Zachor, R. D. Sharma, R. M. Nadile, and A. T. Stair, J. Geophys. Res. **90**, 9776 (1985).

[33] J. A. Dodd, R. B. Lockwood, E. S. Hwang, and S. M. Miller, J. Chem. Phys. **111**, 3498 (1999).

[34] E. S. Hwang, K. J. Castle, and J. A. Dodd, J. Geophys. Res. **108**, 1109 (2003).

[35] H. V. Lilenfeld, Phillips Laboratory Final Report PL-TR-94-2180, Phillips Lab., Hanscom Air Force Base (1994).

[36] R. P. Fernando and I. W. Smith, Chem. Phys. Lett. **66**, 218 (1979).

[37] M. Quack and J. Troe, Ber. Bunsen-Ges. Phys. Chem. **79**, 170 (1975).

[38] R. D. Sharma and J. W. Duff, Geophys. Res. Lett. **24**, 2407 (1997).

[39] R. D. Sharma, H. Dothe, and F. von Esse, J. Geophys. Res. **101**, 17129 (1996).

[40] J. Kurihara and K.-I. Oyama, Rev. Sci. Instrum. **76**, 083101 (2005).

[41] B. R. L. Galvão, J. A. Corzo-Espinoza, P. J. S. B. Caridade, and A. J. C. Varandas, Int. J. Chem. Kinet. **43**, 345 (2011).

Part I

Theoretical Background

Chapter 1

Potential energy surfaces: concept and theory

1.1 The Born-Oppenheimer approximation

From non-relativistic quantum-mechanics, a molecular system in a stationary state is completely described by the Schrödinger equation $H\Psi = E\Psi$, where H is the Hamiltonian operator containing the potential and kinetic energy for all electrons and nuclei involved. Unfortunately, the exact and analytical solution for the Schrödinger equation is restricted to very simple systems[1] and, when dealing with molecules with more than two electrons, one must use approximations.

The first step for tackling the molecular Hamiltonian problem is the Born-Oppenheimer[2] (BO) approximation which, besides reducing the complexity of the mathematical equations to be solved, can also provide insights about chemical concepts. The base of this approximation lies on the fact that the mass of the nuclei is much higher than the mass of the electrons, being the kinetic energy of the nuclei considered as a perturbation to the electronic Hamiltonian and the electronic motion problem can be solved independently for fixed nuclear arrangements. It is only after this approximation that it is theoretically reasonable to think of chemical structures or nuclear trajectories, which are common chemical concepts but do not make sense under a pure quantum mechanical perspective.

The concept of the potential energy surface (PES) arises as a function that returns the electronic energy for a given molecular geometry.

In mathematical terms, the non-relativistic Hamiltonian for a molecule with N electrons and M nuclei, in atomic units, is written as:

$$H = -\sum_{\mathrm{A}}^{M} \frac{1}{2M_{\mathrm{A}}} \nabla_{\mathrm{A}}^2 - \sum_{i=1}^{N} \frac{1}{2} \nabla_i^2 - \sum_{i=1}^{N} \sum_{\mathrm{A}=1}^{M} \frac{Z_{\mathrm{A}}}{r_{i\mathrm{A}}} + \sum_{i=1}^{N} \sum_{j>i}^{N} \frac{1}{r_{ij}} + \sum_{\mathrm{A}}^{M} \sum_{\mathrm{B}>\mathrm{A}}^{M} \frac{Z_{\mathrm{A}} Z_{\mathrm{B}}}{R_{\mathrm{AB}}} \tag{1.1}$$

where R_{AB} and r_{ij} refer to the distances between pairs of nuclei and electrons (respectively), $r_{i\mathrm{A}}$ is the distance between electron i and nucleus A, M_{A} the mass of the nucleus A and Z_{A} its atomic number.

Now, following the Born-Oppenheimer approximation, the nuclear kinetic energy operator is omitted (due to the magnitude of the factor $1/2M_{\mathrm{A}}$, which expresses the ratio between the electronic and nuclear masses) and the electronic Hamiltonian for a fixed nuclear configuration is written as:

$$H_e = -\sum_{i=1}^{N} \frac{1}{2} \nabla_i^2 - \sum_{i=1}^{N} \sum_{\mathrm{A}}^{M} \frac{Z_{\mathrm{A}}}{r_{i\mathrm{A}}} + \sum_{i=1}^{N} \sum_{j>i}^{N} \frac{1}{r_{ij}} + \sum_{\mathrm{A}}^{M} \sum_{\mathrm{B}>\mathrm{A}}^{M} \frac{Z_{\mathrm{A}} Z_{\mathrm{B}}}{R_{\mathrm{AB}}} \tag{1.2}$$

This is also an Hermitian operator and its eigenvectors form a orthogonal basis which spans the subspace of electronic solutions. Since the nuclear repulsion is a constant for a given geometry, it has no effect on the electronic eigenvectors (being only added to the eigenvalues). Considering $\mathbf{r}$ and $\mathbf{R}$ as collective coordinates of the electrons and nuclei (respectively), the electronic Schrödinger equation is then given by:

$$H_e \left|\Phi_j(\mathbf{r};\mathbf{R})\right\rangle = V_j(\mathbf{R}) \left|\Phi_j(\mathbf{r};\mathbf{R})\right\rangle \tag{1.3}$$

The electronic wave function Φ_j depends explicitly on the electronic coordinates and parametrically on the nuclear ones, as indicated by the semicolons, and the index j denotes the electronic state. This equation cannot generally be solved exactly, and the search for its numerical solution is the subject of electronic structure calculations (Chapter 2).

The separation of the electronic Hamiltonian allows for the calculation of the potential energy for any fixed geometry of the molecule and provides a chemical picture of the

nuclei moving under the influence of a potential energy surface $V(\mathbf{R})$ caused by the motion of the electrons. It can be thought that the electronic wave function adapts itself instantaneously to any change in the nuclear configuration, or that the electrons follow "adiabatically" the motion of the nuclei[3–5].

The potential energy surface is a cornerstone on theoretical studies, since it is necessary for predicting any chemical property such as molecular spectra, reaction cross sections and even thermodynamic properties, and the accuracy of the results will largely depend on the accuracy of the PES. As recent studies have shown, the errors on theoretical calculations of the spectra of light molecular systems[6,7] lie largely on the numerical methods employed to solve Eq. (1.3), while the error due to the separation of the nuclear and electronic motion (BO approximation) can be safely considered as negligible, causing less deviation from the experimental values then the neglect of relativistic and quantum-electrodynamics effects.

After obtaining the PES in an analytical form, one can go back to the total Schrödinger equation to find the eigenvalues of the nuclear motion which will correspond to the vibrational and rotational levels of the molecule. If the Hamiltonian was rigorously separable between nuclear and electronic motion, the total wave function would simply be the product of an electronic and a nuclear parts $|\Psi\rangle = \chi(\mathbf{R})|\Phi(\mathbf{r};\mathbf{R})\rangle$ and each electronic state could be studied independently. By applying this wavefunction in the total time-independent Schrödinger equation and applying $\langle\Phi|$ to the left, the nuclear motion is obtained as:

$$\left[-\sum_{\mathrm{A}}^{M}\frac{1}{2M_{\mathrm{A}}}\left(\nabla_{\mathrm{A}}^{2}-\Lambda\right)+V(\mathbf{R})\right]\chi(\mathbf{R})=\varepsilon\chi(\mathbf{R}) \tag{1.4}$$

where the integration is performed over electronic coordinates and Λ is the term (derived next section) that results from operating the gradient of nuclear coordinates on the electronic wave function. This is known as *"Born-Oppenheimer approximation"* and it is normally further simplified by neglecting Λ, giving

$$\left[-\sum_{\mathrm{A}}^{M}\frac{1}{2M_{\mathrm{A}}}\nabla_{\mathrm{A}}^{2}+V(\mathbf{R})\right]\chi(\mathbf{R})=\varepsilon\chi(\mathbf{R}) \tag{1.5}$$

which is known as the *"Born-Oppenheimer adiabatic approximation"*, or briefly *"adi-*

abatic approximation"[8]. The larger the energetic difference between neighboring electronic states, the weaker the dependence of $|\Phi_j(\mathbf{r};\mathbf{R})\rangle$ on the nuclear coordinates will be, making the neglect of Λ a good approximation.

Since the nuclei are relatively heavy particles, a classical treatment of the time-dependent problem on $V(\mathbf{R})$ is often the best way to obtain reaction rate constants, where one is looking for the time evolution of the system instead of bound states. Using classical trajectories (Chapter 4), the nuclei are treated as classical particles under the influence of the potential $V(\mathbf{R})$ calculated by quantum mechanical means, which turns out to be a very successful approach, given the complexity of the quantum dynamics formalism. Nevertheless, the time-dependent Schrödinger equation may also be applied within the adiabatic context[9], also by expressing the total molecular wave function as a product of the electronic eigenfunction and allowing the nuclear part to vary over time as $|\Psi\rangle = \chi(\mathbf{R},t)|\Phi(\mathbf{r};\mathbf{R})\rangle$. By proceeding as in Eq. (1.4) it is obtained

$$\left(-\sum_{\mathrm{A}}^{M}\frac{1}{2M_{\mathrm{A}}}\nabla_{\mathrm{A}}^2 + V(\mathbf{R})\right)\chi(\mathbf{R},t) = i\hbar\frac{\partial\chi(\mathbf{R},t)}{\partial t} \tag{1.6}$$

and from this equation the propagation of a wave-packet can be calculated[10] in order to study a collisional process or the kinetics of a chemical reaction.

1.2 Beyond the adiabatic approach

The adiabatic wave function, $|\Psi_j\rangle = \chi_j|\Phi_j\rangle$, is a very good approximation for the molecular problem if the electronic states are widely separated, but it is not capable of describing it when two or more electronic surfaces become degenerate or near-degenerate for some nuclear arrangement[11]. Since the solutions of the electronic Schrödinger equation [Eq. (1.3)] form a complete orthonormal set, the total molecular wave function may be expanded as:

$$|\Psi(\mathbf{r},\mathbf{R})\rangle = \sum_j \chi_j(\mathbf{R})\,|\Phi_j(\mathbf{r};\mathbf{R})\rangle \tag{1.7}$$

which is called the Born-Huang expansion[8,12]. Although the completeness of such expansion (in principle including a summation over the continuum), Eq. (1.7) is often used

truncated on few terms and can provide insights on nonadiabatic phenomena.

The coupling between different electronic states within the Born-Huang expansion can be obtained by taking the inner product of the electronic basis functions $\langle\Phi_i|$ with the the total molecular Schrödinger equation:

$$-\sum_{\mathrm{A}}^{M}\frac{1}{2M_{\mathrm{A}}}\langle\Phi_i|\nabla_{\mathrm{A}}^2|\Psi(\mathbf{r},\mathbf{R})\rangle+\langle\Phi_i|H_e|\Psi(\mathbf{r},\mathbf{R})\rangle=E_i\langle\Phi_i|\Psi(\mathbf{r},\mathbf{R})\rangle \tag{1.8}$$

After expanding $|\Psi(\mathbf{r},\mathbf{R})\rangle$ as Eq. (1.7) and applying the chain rule to the first term, one gets the following set of equations for the motion of the nuclei (in matrix form)

$$\left[-\sum_{\mathrm{A}}^{M}\frac{1}{2M_{\mathrm{A}}}\left(\mathbf{I}\nabla_{\mathrm{A}}^2+2\mathbf{F}^{(\mathrm{A})}(\mathbf{R})\cdot\nabla_{\mathrm{A}}+\mathbf{G}^{(\mathrm{A})}(\mathbf{R})\right)+\mathbf{V}(\mathbf{R})-E\mathbf{I}\right]\boldsymbol{\chi}(\mathbf{R})=0 \tag{1.9}$$

where $\boldsymbol{\chi}(\mathbf{R})$ is a column vector whose components are the nuclear wave functions, $\mathbf{I}$ is an appropriate identity matrix and $\mathbf{V}$ is a diagonal matrix with the elements given by the eigenvalues of the electronic Schrödinger equation ($V_j=\langle\Phi_j|H_e|\Phi_j\rangle$). The elements of the coupling matrices $\mathbf{F}$ and $\mathbf{G}$ are given by:

$$\begin{aligned}\mathbf{F}_{ij}^{(\mathrm{A})}&=\langle\Phi_i|\boldsymbol{\nabla}_{\mathrm{A}}\Phi_j\rangle\\ G_{ij}^{(\mathrm{A})}&=\langle\Phi_i|\nabla_{\mathrm{A}}^2\Phi_j\rangle\end{aligned} \tag{1.10}$$

where the dependence on the nuclear coordinates is omitted for simplicity. $\mathbf{F}_{ij}$ and G_{ij} are the first and second order nonadiabatic coupling elements, respectively. Note that the *"Born-Oppenheimer approximation"* and the *"adiabatic approximation"* described in the previous section are obtained from Eq. (1.9) by neglecting the non-diagonal coupling terms or the complete matrices (respectively)[8]. It is worth noting that for real valued electronic wavefunctions, the diagonal elements of $\mathbf{F}$ vanish and only the matrix G_{ii} play a role in the *Born-Oppenheimer approximation*. It also follows from the *antihermitian* nature of the derivative coupling matrix that its off-diagonal elements are related by $\mathbf{F}_{ij}=-\mathbf{F}_{ji}$

The divergent behavior of the adiabatic approach for nuclear arrangements where two electronic surfaces become near-degenerate is easily observed from the $\mathbf{F}_{ij}$ nonadiabatic coupling element. Following a process analogous to the Hellman-Feynman theorem

($\langle\Phi_j|\nabla$ is applied to $H_e|\Phi_i\rangle$) one obtains

$$\mathbf{F}_{ji}^{(\mathrm{A})} = \frac{\langle\Phi_j|\nabla_{\mathrm{A}} H_e|\Phi_i\rangle}{V_i - V_j} \tag{1.11}$$

and thus the closer two electronic states get to each other, the larger $\mathbf{F}_{ji}$ will be, making the adiabatic approach collapse for electronic degeneracies.

To overcome the numerical problems associated with the adiabatic representation, the concept of a "diabatic" state may be invoked. In this new representation, instead of using Eq. (1.7) the total molecular wave function is expanded on an electronic basis with a fixed reference $\mathbf{R}^0$, such that

$$|\Psi(\mathbf{r},\mathbf{R})\rangle = \sum_j \chi_j(\mathbf{R})\,|\Phi_j(\mathbf{r};\mathbf{R}^0)\rangle \tag{1.12}$$

Although this approximation is simpler, since it only takes the calculation of the electronic wave function in a single point, its convergence is much slower[13]. When applying such expansion to the total molecular Schrödinger equation, a set of equations similar to 1.9 is found, which clearly is not coupled by the nuclear kinetic energy operator and therefore do not show the above mentioned singularities. On the other hand, the electronic potential matrix is non-diagonal in the new basis. The differences can be thought as follows: In the adiabatic representation the nonadiabatic coupling is caused by the nuclear kinetic energy operator, and thus it is valid for slow moving nuclei (compared to the energy gap between electronic states). In the diabatic representation the coupling of states is caused by electron-nuclear interaction (of the electronic Hamiltonian) and thus is valid when this interaction is small compared to the fast moving nuclei[10].

If both sets were complete they would be exact and therefore equivalent, being related by an unitary transformation[10]. Generally however, a small subset of the adiabatic wavefunctions is used to obtain the diabatic ones, and the transformation is constructed to fulfill some requirement, such as making the nonadiabatic coupling vanish[13], or in some cases for making the diabatic states represent different electronic configurations or even chemical bond patterns[14]. In the two-states case the adiabatic-to-diabatic (ATD)

transformation reads[13,15]

$$\begin{pmatrix} \Phi_1^d \\ \Phi_2^d \end{pmatrix} = \begin{pmatrix} \cos\alpha & \sin\alpha \\ -\sin\alpha & \cos\alpha \end{pmatrix} \begin{pmatrix} \Phi_X^a \\ \Phi_B^a \end{pmatrix} \tag{1.13}$$

where the dependence on the nuclear coordinate is omitted for simplicity, and the superscripts a and d are used to differentiate between adiabatic/diabatic representations. The ATD mixing angle α "rotates" one representation into the other. If such two state diabatic wavefunction is applied to the total molecular Schrödinger equation, the set of equations obtained [as in Eq. (1.9)] is of course not decoupled and can be written in terms of the original adiabatic ones. Since the diabatic wavefunctions are not eigenfunctions of the electronic Hamiltonian, the potential matrix is not diagonal, and its elements $V_{ij}^d = \langle \Phi_i^d | H_e | \Phi_j^d \rangle$ are given by:

$$\begin{pmatrix} V_{11}^d & V_{12}^d \\ V_{12}^d & V_{22}^d \end{pmatrix} = \begin{pmatrix} \cos\alpha & \sin\alpha \\ -\sin\alpha & \cos\alpha \end{pmatrix} \begin{pmatrix} V_X^a & 0 \\ 0 & V_B^a \end{pmatrix} \begin{pmatrix} \cos\alpha & -\sin\alpha \\ \sin\alpha & \cos\alpha \end{pmatrix} \tag{1.14}$$

Another major difference of this new set of equations is the derivative coupling. Recalling that its off-diagonal are null, the transformed off-diagonal elements are found to be

$$\mathbf{F}_{12}^d = \boldsymbol{\nabla}\alpha + \mathbf{F}_{12}^a \tag{1.15}$$

In most cases one is interested in a representation where the derivative coupling vanishes, and setting $\mathbf{F}_{ij}^d = 0$ leads to a first-order differential equation for the mixing angle

$$\boldsymbol{\nabla}\alpha = -\mathbf{F}_{12}^a \tag{1.16}$$

Therefore by calculating the derivative coupling in the adiabatic representation, one can in principle define the ATD mixing angle that will provide a diabatic representation with no nuclear derivative coupling. As it will be seen, though, there are other less computationally demanding methods (and consequently less rigorous) to obtain an appropriate diabatic representation, and Eq. (1.14) is an important starting point for the modeling of multi-valued PESs even without the knowledge of the mixing angle[16].

Bibliography

[1] W. Kolos and L. Wolniewicz, Rev. Mod. Phys. **35**, 473 (1963).

[2] M. Born and J. R. Oppenheimer, Ann. Phys. **84**, 457 (1927).

[3] I. R. Levine, *Quantum Chemistry* (Prentice hall, Englewood, 1991).

[4] A. Szabo and N. E. Ostlund, *Modern Quantum Chemistry* (McMillan, 1982).

[5] C. Cohen-Tannoudji, B. Diu, and F. Laloe, *Quantum Mechanics* (Wiley, New York, 1977).

[6] O. L. Polyansky, A. G. Császár, S. V. Shirin, N. F. Zobov, P. Barletta, J. Tennyson, D. W. Schwenke, and P. J. Knowles, Science **299**, 539 (2003).

[7] P. Barletta, S. V. Shirin, N. F. Zobov, O. L. Polyansky, J. Tennyson, E. F. Valeev, and A. G. Császár, J. Chem. Phys. **125**, 204307 (2006).

[8] L. S. Cederbaum, in *Conical Intersections: Electronic Structure, Dynamics & Spectroscopy*, edited by W. Domcke, D. R. Yarkony, and H. Köppel (World Scientific Publishing, 2004), vol. 15 of *Advanced Series in Physical Chemistry*, chap. 1, p. 3.

[9] N. E. Henrisken and F. Y. Hansen, *Theories of Molecular Reaction Dynamics* (Oxford University Press, Oxford, 2008).

[10] J. Z. H. Zhang, *Theory and Applications of Quantum Molecular Dynamics* (World Scientific, Singapore, 1999).

[11] A. J. C. Varandas, in *Conical Intersections: Electronic Structure, Dynamics & Spectroscopy*, edited by W. Domcke, D. R. Yarkony, and H. Köppel (World Scientific Publishing, 2004), vol. 15 of *Advanced Series in Physical Chemistry*, chap. 5, p. 205.

[12] M. Born and K. Huang, *Dynamical Theory of Crystal Lattices* (Clarendon Press, Oxford, 1954).

[13] H. Köppel, in *Conical Intersections: Electronic Structure, Dynamics & Spectroscopy*, edited by W. Domcke, D. R. Yarkony, and H. Köppel (World Scientific Publishing, 2004), vol. 15 of *Advanced Series in Physical Chemistry*, chap. 4, p. 175.

[14] L. Piela, *Ideas of Quantum Chemistry* (Elsevier, Amsterdam, 2007).

[15] M. Boggio-Pasqua, A. I. Voronin, P. Halvick, J. C. Rayez, and A. J. C. Varandas, Mol. Phys. **98**, 1925 (2000).

[16] J. N. Murrell, S. Carter, I. M. Mills, and M. F. Guest, Mol. Phys. **42**, 605 (1981).

Chapter 2

Calculation of potential energy surfaces

2.1 Introduction

The initial step for building a potential energy surface from first principles (*ab initio*) consists in the choice of an accurate numerical solution for the electronic Schrödinger Equation [Eq. (1.3)]. For systems with sufficiently small number of electrons, it is feasible to use accurate quantum chemical methods to obtain high quality potential energy surfaces, which in turn can provide reliable predictions on the molecular system. On the other hand, with increasing number of electrons, the possibility of high accuracy is reduced due to the large amount of time required by the most advanced approaches, and when heavy atoms are present, even the non-relativistic treatment has its reliability questioned. Thus one is left with the problem of choosing the most suitable method for the specific system under study.

For the most common methods, the numerical solution involves a large amount of integrations over basis sets and iterative procedures that are used to determine the best energies possible, a task that demands heavy computational resources and time, increasing with accuracy level and molecular complexity.

With the astonishing progress in molecular physics and computational capacity, it is

becoming now feasible to obtain higher accuracy in less time, which allows for small systems (such as the water molecule[1,2]) the possibility of using theoretical predictions to achieve experimental accuracy and even predicting values where experimental measures are not available.

In the present chapter, a survey of the *ab initio* tools contained in this thesis is performed. It starts with the description of the electronic wave function and the powerful variational approach, while the methods are presented from Section 2.4 to 2.7. A description of the most used one-electron basis functions and their extrapolation to the complete basis set limit are given from Section 2.8 to 2.11.

2.2 Many-electron wave functions

Since the electronic Schrödinger equation [Eq. (1.3)] involves only electronic spatial coordinates, it would be possible to use approximate wave functions that depends just on such coordinates. However, from the Pauli exclusion principle, it is known that a realistic many-electron wave function must be antisymmetric with respect to the interchange of the spatial and spin coordinates of any two electrons. To satisfy this principle, the wave function is written as composed by orbitals (single-electron wave functions) containing both spatial and spin parts (represented by the orthonormalized functions α and β), as a Slater determinant:

$$\Psi(\mathbf{x}_1, \mathbf{x}_2, ..., \mathbf{x}_N) = (N!)^{-1/2} \begin{vmatrix} \chi_i(\mathbf{x}_1) & \chi_j(\mathbf{x}_1) & ... & \chi_k(\mathbf{x}_1) \\ \chi_i(\mathbf{x}_2) & \chi_j(\mathbf{x}_2) & ... & \chi_k(\mathbf{x}_2) \\ \vdots & \vdots & \ddots & \vdots \\ \chi_i(\mathbf{x}_N) & \chi_j(\mathbf{x}_N) & ... & \chi_k(\mathbf{x}_N) \end{vmatrix} = |\chi_i \chi_j \cdots \chi_k\rangle \tag{2.1}$$

where $\mathbf{x}_i$ is the collective coordinate (including spin) of electron i, and χ_j represents the jth spin-orbital, such that the Slater determinant has N electrons occupying N spin-orbitals without determining a specific orbital for each electron. The lines in this determinant are labeled by electrons while columns are labeled by spin-orbitals. Note that a Slater determinant is completely described by its spin-orbitals, making possible the use of the short notation on the right hand side of Eq. (2.1).

The particular importance of Slater determinants, is that the calculated probability of two electrons with the same spin to occupy the same position (*i.e.* $\mathbf{x}_1 = \mathbf{x}_2$) is null (the matrix would have two equal lines, and the resulting determinant zero). It is said that an exchange correlation is introduced (the motion of two electrons with same spin is correlated). However it is common to refer to a single Slater determinant as an uncorrelated wave function since the motion of the electrons with opposite spin still remains totally uncorrelated.

2.3 Variational method

When finding approximate solutions for an eigenvalue problem such as the electronic Schrödinger equation ($H|\Phi_i\rangle = \varepsilon_i|\Phi_i\rangle$ with $i = 0, 1, ...$), the variational principle provides a useful tool to optimize coefficients in a trial function. Since the eigenfunctions $|\Phi_i\rangle$ of an Hermitian operator form a complete basis set, any function $|\Omega\rangle$ (with the same boundary conditions) can be expanded as:

$$|\Omega\rangle = \sum_i |\Phi_i\rangle c_i = \sum_i |\Phi_i\rangle\langle\Phi_i|\Omega\rangle \tag{2.2}$$

For the expectation value of the Hamiltonian with the trial function, the closure relation is used to obtain[3]

$$\langle\Omega|H|\Omega\rangle = \sum_{ij}\langle\Omega|\Phi_i\rangle\langle\Phi_i|H|\Phi_j\rangle\langle\Phi_j|\Omega\rangle = \sum_i \varepsilon_i|\langle\Phi_i|\Omega\rangle|^2 \tag{2.3}$$

Since all ε_i are always equal or greater than the first eigenvalue ε_0, and assuming a normalized trial function ($\sum_i |\langle\Phi_i|\Omega\rangle|^2 = 1$), one obtain the following inequality for the trial expectation value:

$$\langle\Omega|H|\Omega\rangle \geq \sum_i \varepsilon_0|\langle\Phi_i|\Omega\rangle|^2 = \varepsilon_0 \tag{2.4}$$

The inequality above states that the expectation value of the Hamiltonian in the trial wave function is always greater or equal than the exact ground state energy, and the equality holds if the trial function is the exact solution. Thus, a good trial wave function

is expected to provide an energy as low as possible, allowing the optimization of its coefficients for this purpose.

If the trial wave function is chosen to be a linear function (a combination of n linearly independent basis functions, $|\Omega\rangle = \sum_i^n c_i|f_i\rangle$), it can be shown[3] that the problem of finding n minimum energies (corresponding to n bound states) is reduced to the solution of the matrix equation **HC** = **SCE**, where **H** is the representation of the Hamiltonian operator in the finite basis functions, **C** is a matrix formed by the optimized coefficients of the bound-state wave functions, **S** is the overlap matrix whose elements are $S_{ij} = \langle f_i|f_j\rangle$ and **E** is a diagonal matrix formed by the n minimum energies.

2.4 The Hartree-Fock approximation

The Hartree-Fock (HF) approximation plays a major role in electronic structure calculations, since it provides a method to achieve the best variational energy within the single-determinant approach, *i.e.* the best wave function formed by a single electronic configuration. As a matter of fact, this description of each electron occupying one spin-orbital is the normal picture that chemists use when thinking about a molecular system. Also, even when performing other higher level methods of electronic structure calculation, the first step is normally the Hartree-Fock solution.

The basic idea of the method is to replace the many-electrons problem by separated one-electron parts where the instantaneous interactions between electrons are replaced by "fields" seen by each one. Making an initial guess for the spin-orbitals and using them to calculate such averaged field for each electron, one can obtain improved spin-orbitals. Repeating the procedure with the new orbitals until self-consistency (the procedure is called self-consistent field, SCF) one obtains the Hartree-Fock optimized wave function.

To describe the equations involved in such method[3], the separation of the Hamiltonian of an N-electron system into one- and two-electrons contributions is performed (with

nuclear repulsion omitted) yielding $H = O_1 + O_2$, where

$$\begin{aligned} O_1 &= \sum_i^N h(i) = \sum_i^N \left(-\frac{1}{2}\nabla_i^2 - \sum_A \frac{Z_A}{r_{iA}} \right) \\ O_2 &= \sum_i^N \sum_{j>i}^N r_{ij}^{-1} \end{aligned} \tag{2.5}$$

To obtain the energy with the approximated wave function [$|\Psi_0\rangle = |\chi_a\chi_b\cdots\chi_N\rangle$, as in Eq. (2.1)] the determinant is solved and, after integrating out terms due to the orthonormality of the spin-orbitals, the energy is given by

$$E_0 = \langle\Psi_0|H|\Psi_0\rangle = \sum_a^N \langle a|h|a\rangle + \frac{1}{2}\sum_{ab}^N \langle ab|ab\rangle - \langle ab|ba\rangle \tag{2.6}$$

where it is introduced the notation of one- and two-electron integrals

$$\begin{aligned} \langle i|h|j\rangle &= \int \chi_i^*(\mathbf{x}_1) h(1) \chi_j(\mathbf{x}_1) d\mathbf{x}_1 \\ \langle ij|kl\rangle &= \int \chi_i^*(\mathbf{x}_1)\chi_j^*(\mathbf{x}_2) r_{12}^{-1} \chi_k(\mathbf{x}_1)\chi_l(\mathbf{x}_2) d\mathbf{x}_1 d\mathbf{x}_2 \end{aligned} \tag{2.7}$$

The integration coordinates are dummy variables (chosen as the coordinates of electron one and two), and the notation of the integrals does not need an electron specific index.

Once a trial function is given, its coefficients can be optimized with the variational method such as to minimize E_0. For this the Lagrange's method of undetermined multipliers is used, constrained to the orthonormality of the spin-orbitals. After deriving the equations, followed by an appropriate unitary transformation of the orbitals, the Hartree-Fock equations are obtained

$$f|\chi_a\rangle = \varepsilon_a|\chi_a\rangle \tag{2.8}$$

where f is the Fock operator, defined as

$$f(1) = h(1) + \sum_b^N \left[\mathscr{J}_b(1) - \mathscr{K}_b(1) \right] \tag{2.9}$$

and the dummy index 1 is used, while $\mathscr{J}$ and $\mathscr{K}$ are respectively the coulomb and exchange operators:

$$\begin{aligned} \mathscr{J}_b(1)\chi_a(1) &= \left[\int d\mathbf{x}_2 \, \chi_b^*(2) \, r_{12}^{-1} \, \chi_b(2) \right] \chi_a(1) \\ \mathscr{K}_b(1)\chi_a(1) &= \left[\int d\mathbf{x}_2 \, \chi_b^*(2) \, r_{12}^{-1} \, \chi_a(2) \right] \chi_b(1) \end{aligned} \tag{2.10}$$

The Fock operator substitutes the instantaneous interaction between pairs of electrons by the average of each interaction over all space and spin coordinates through the Coulomb operator. It also includes the exchange contribution that arises from the anti-symmetric nature of the wave function.

Note that the Hartree-Fock equation [Eq. (2.8)] is not a linear eigenvalue one, since it shows a functional dependence on its solutions, and must be solved with iterative procedures. The common approach to solve these equations was first proposed by Roothaan[4], based on linear expansion of the orbitals in a finite basis function ($|\chi_a\rangle = \sum_i^K c_i|\phi_i\rangle$). Using the variational method, the integro-differential equations for the Hartree-Fock orbitals can be reduced to the calculation of the expansion coefficients via the matrix eigenvalue equation **FC** = **SCE**, where **F** is the Fock matrix (the representation of the Fock operator in the finite basis functions) and **S** is a matrix with elements given by the overlap of the basis functions.

The iterative process is started by making an initial guess of the coefficients matrix (**C**), and then solving the Roothaan equation with it. This process involves the evaluation of a huge number of one- and two-electron integrals and diagonalization of the Fock matrix, from where an improved coefficient matrix is obtained. The procedure is repeated until self consistency, *i.e.* until the difference between two steps is negligible.

The solution of this problem yields a set of K orthonormal and optimized orbitals, being the N of lowest energies called occupied spin-orbitals ($\chi_a, \chi_b, \cdots$), and the remaining $K - N$ *unoccupied* or *virtual* ones ($\chi_r, \chi_s, \cdots$). The determinant formed from the occupied set of orbitals is the Hartree-Fock wave function. If an infinite basis set were to be used, the result achieved would be the so-called *Hartree-Fock limit*, although in practice one must use a finite basis, with its size limited by the computational resources available (the use of K basis functions, leads to a number of two electron integrals of the order of $K^4/8$).

2.5 Multiconfiguration SCF

Since the Hartree-Fock approach is based on a single determinant wave function, it

cannot describe molecular geometries where different electronic configurations play an important role. The multiconfiguration self-consistent field (MCSCF) approach consists of writing the wave function as a linear combination of different configuration state functions (CSF)

$$|\Psi_{\mathrm{MCSCF}}\rangle = \sum_i a_i |\Psi_i\rangle \tag{2.11}$$

and performing an optimization of the expansion coefficients (a_i) and the orbitals of all determinants $|\Psi_i\rangle$ together, making the equations more complicated than Roothaan's. This approach is highly desirable when describing bond breaking processes, since the electron configuration of the fragments may not be suitably described by the HF configuration of the covalent molecule.

This simultaneous optimization demands considerably more computational effort, making the choice of the set of CSF to be used an important issue. Partitioning the molecular orbitals space into inactive, active and virtual orbitals (typically core, valence and unoccupied), one can construct a set of CSF distributing the active electrons among the active orbitals in all possible combinations. A MCSCF calculation with this set of CSFs is called complete active space self-consistent field[5–8] (CASSCF).

The CASSCF approach introduces a correlation between electrons that arises from the presence of nearly degenerate electronic configurations (called static correlation), but since its orbital space is small (not much more than 10 electrons and ten orbitals), it is incapable of providing the correlation that arises from the instantaneous Coulomb repulsion between electrons.

2.6 The CI and MRCI approaches

After performing a HF calculation using a basis composed by K functions, a set of K optimized spin-orbitals are obtained where the N lowest in energy compose the HF determinant, the best single-determinant approximation to the ground state within that basis. Of course the energy obtained in such approach does not account for the correlation between electrons with opposite spin, and must be improved for accurate results.

This can be achieved with the use of more determinants.

The combinations of N orbitals from a set of K elements gives a large number of other possible determinants (given by a binomial coefficient), and the Hartree Fock is one of those. To describe all other possible determinants it is convenient to use the HF one ($|\Psi_0\rangle$) as a reference, and label the others according to how they differ from it. For example, promoting one electron from the spin-orbital χ_a to χ_r gives the excited configuration $|\Psi_a^r\rangle$. A similar notation can be used for doubly and further excited determinants.

Using this notation, the configuration interaction (CI) wave function is then given as

$$|\mathrm{CI}\rangle = c_0|\Psi_0\rangle + \sum_{ra} c_a^r|\Psi_a^r\rangle + \sum_{ab\,rs} c_{ab}^{rs}|\Psi_{ab}^{rs}\rangle + \cdots \tag{2.12}$$

Note that the spin-orbitals are determined in the previous step for $|\Psi_0\rangle$, the reference, and are fixed for all the excitations in the above expansion. In this method only the expansion coefficients are optimized with the variational method such as to give the lowest energy. If a complete basis set was used to construct the HF determinant, the CI wave function would be exact within the non-relativistic and Born-Oppenheimer framework. The optimization of the CI coefficients, however, involves the diagonalization of very large matrices and is a very expensive calculation if compared to the HF and MC-SCF methods. In real calculations, not only the basis set must be finite but also the full CI expansion (FCI) must be truncated. In the most common approach only the singles and double excitations (CISD) are kept, as they make the most important contribution. Furthermore the number of possible determinants for higher excitations is much larger, making it extremely more computationally consuming.

Since the "exact" energy of the system is given by a full CI calculation, it is possible to exactly define the total electron correlation energy as:

$$E_{\mathrm{cor}} = E_{\mathrm{FCI}} - E_{\mathrm{HF}} \tag{2.13}$$

Of course such equation corresponds to an ideal limit, since one is always restricted to the basis set size, but this definition can be extended to the correlation energy within a particular basis set (E_{cor}^X).

For regions of the potential energy surface where the system cannot be described properly with the HF configuration (*e.g.* far from the equilibrium geometry) the single reference FCI method has slower convergence and the truncated CI expansion recovers a smaller part of the total correlation. To overcome such problems, the CI calculations can be done using a larger reference space, containing more configurations, such as the MCSCF wave function. This is the idea behind the multireference CI (MRCI) approach, which consists of starting the CI procedure with the MCSCF wave function as the reference space and introducing excitations from each reference CSF.

Frequently, the MRCI calculation is also truncated to include just single and double excitations (MRCISD), and this approach is widely accepted as one of the most accurate ways of obtaining the molecular energy over the whole configurational space, although it is often not feasible for large systems due to its computational demand.

Another important term that must be defined in this context is the dynamical correlation energy:

$$E_{\mathrm{dc}} = E_{\mathrm{MRCI}} - E_{\mathrm{CASSCF}} \tag{2.14}$$

Given that the CASSCF energy contains "static correlation", this part of the total correlation energy accounts for the instantaneous Coulomb repulsion between electrons.

2.7 Coupled-Cluster theory

If compared to other *ab initio* methods, the coupled-cluster theory uses a rather distinct approach to the electronic problem, since its wave function is not expressed as a linear combination of determinants and it does not make use of the variational method. Although this leads to a result that is not necessarily an upper bound to the exact value, the unsystematic convergence turns out to be irrelevant due to the accuracy obtained.

In order to introduce the coupled-cluster wave function, it is useful to describe any excitation (μ) from the Hartree-Fock determinant in terms of the operator $\hat{\tau}_\mu$[9], which acts on the reference wave-function by promoting the excitation, such as $\hat{\tau}^{rs}_{ab}|\Psi_0\rangle = |\Psi^{rs}_{ab}\rangle$ (in terms of the second quantization formalism, this operator is written such as $\hat{\tau}^{rs}_{ab} = a^\dagger_s a_b a^\dagger_r a_a$, where a and $a^\dagger$ are the annihilation and creation operators). A linear combination of

excited determinants, such as the CI wave function, could thus be written as:

$$|\mathrm{CI}\rangle = \left(1 + \sum_{\mu} C_{\mu}\hat{\tau}_{\mu}\right)|\Psi_0\rangle \tag{2.15}$$

The electronic correlation arises majorly as a result of instantaneous interactions among two electrons (a pair cluster) and thus the pair interactions, represented by double excitations, play the most important role. However, for an accurate description of the correlation energy, the contribution from clusters of all sizes must be considered, such as triple excitations and even "single" clusters that can account for relaxation of the spin-orbitals after a many-electron process[9]. In the coupled-cluster model, the effect of a given excitation μ on any state, is to change it as applying $(1 + t_{\mu}\hat{\tau}_{\mu})$, where t_{μ} is the corresponding amplitude. The coupled-cluster wave function is written as the result of the application of these correlating operators into the Hartree-Fock determinant:

$$|\mathrm{CC}\rangle = \left(\prod_{\mu}\left(1 + t_{\mu}\hat{\tau}_{\mu}\right)\right)|\Psi_0\rangle \tag{2.16}$$

where the coefficients are not linearly independent due to the product form. For example, the amplitude of the single excitation $a \rightarrow r$ appears in the single excited determinant $t_a^r\hat{\tau}_a^r|\Psi_0\rangle$, as well as in higher excited ones, such as $t_a^r t_b^s\hat{\tau}_a^r\hat{\tau}_b^s|\Psi_0\rangle$.

Therefore, the truncation of the expansion by considering only double excitations contains all even-excited determinants, due to the successive application of the pair operators. In the same way, the truncation of the expansion to consider only singles and doubles excitations (CCSD) leads to a wave function containing all determinants of the full CI[9], with a reduced number of coefficients.

It is obvious that the same excitation μ cannot be applied more than once in a determinant, because that would require the annihilation of an empty spin orbital ($\hat{\tau}_{\mu}^2 = 0$), and thus the correlating operators are the taylor expansion of an exponential function ($1 + t_{\mu}\hat{\tau}_{\mu} = \exp\left(t_{\mu}\hat{\tau}_{\mu}\right)$) and Eq. (2.16) can be written as:

$$|\mathrm{CC}\rangle = \exp\left(\hat{T}\right)|\Psi_0\rangle \tag{2.17}$$

which is the exponential ansatz of the coupled-cluster theory, where the cluster operator $\hat{T}$ represents a summation over all excitations, *i. e.* $\sum_{\mu} t_{\mu}\hat{\tau}_{\mu}$.

The product form of the coupled-cluster wave function gives to the method a very useful energy separability[10]. Consider for example two non interacting species, such as two hydrogen molecules (A and B). Since the molecular orbitals chosen in any electronic structure calculation will be localized at each fragment, the excitation operators can be separated as

$$\hat{T} = \hat{T}_A + \hat{T}_B \tag{2.18}$$

since the mixed excitations will have null amplitudes. The wave function becomes then

$$|\mathrm{CC}\rangle = \exp\left(\hat{T}\right)|_0\rangle = \exp\left(\hat{T}_A\right)\exp\left(\hat{T}_B\right)|\Psi_0\rangle \tag{2.19}$$

and using the fact that, at infinite separation, the reference wave-function can be factorized (the determinant of a block diagonal matrix is the product of the determinants of the individual blocks), the total wave function may be written as a product of fragment wave functions. As a result of this separability, the energy calculated on the supermolecule equals the sum of the energies of the fragments, which is an important characteristic of the coupled cluster method, called size consistency. It is easy to see that the truncated CI wave function cannot be written as a product between fragments

$$|\mathrm{CI}\rangle = (1 + C_A\hat{\tau}_A C_B\hat{\tau}_B)|\Psi_0\rangle \tag{2.20}$$

and therefore is not size consistent. This is not the case if one considers the full CI wave function, since the linear operator in this case may be written as an expanded exponential.

2.8 One-electron basis functions

For the *ab initio* methods described in the previous sections, the use of a basis set to expand the one-electron orbitals is always necessary, so one is left with a problem of choosing the most convenient form that is capable of successfully achieve three criteria: 1) allow systematic extension for completeness, 2) rapid convergence and 3) fast integration. Since the eigenfunctions of a Hermitian operator constitute a complete orthonormal set, it is possible to take the solutions of the one-electron system in a central-field (hydrogenic

wave functions) as a possible choice. These wave functions are well described in quantum mechanics literature and have the following form in spherical coordinates:

$$\psi(r,\theta,\phi) = R(r)Y(\theta,\phi) \tag{2.21}$$

where $Y(\theta,\phi)$ are the usual spherical harmonics, and the radial part, $R(r)$, contains an associate Laguerre polynomial multiplied by an exponential in r, which ensures that the wave function decays exponentially for large distances. Particularly, although the hydrogenic wave functions have the correct exponential behavior, they are not an useful basis set because its completeness depends also on the continuum states. Furthermore, they become very diffuse due to the polynomial part.

Retaining the exponential form of the hydrogenic wave functions, but without the complicated part of the Laguerre polynomials, one can form a basis set with variable exponents called Slater-type orbitals (STO). Although the orthonormality property is now lost, it can be proven that STOs form a complete basis set.

Regarding the three criteria of a good basis set, the STOs are known to fulfill the first and second of them, however the integration over many-center two-electron STOs is a complicated and time-consuming task. This problem has been so difficult to overcome that STO basis have been almost discarded and most part of the modern electronic structure calculations uses radial distributions that do not decay exponentially: the Gaussian-type orbitals (GTOs). Although it can be shown that at large distances the molecular orbitals should decay as $\exp(-\zeta r)$, the use of GTOs is largely compensated by the fact that the complicated four center integrals are reduced to two-center ones (since the products of two Gaussians of different centers is another Gaussian in a third center). The complex spherical-harmonics GTOs are given by[11]:

$$\psi^{\mathrm{GTO}}_{\alpha,l,m}(r,\theta,\phi) = N_{\alpha,l}\, r^l \exp(-\alpha r^2) Y_{lm}(\theta,\phi) \tag{2.22}$$

where $N_{\alpha,l}$ is a normalization constant and l is the angular momentum quantum number.

Since the GTO basis cannot describe the characteristic cusp at $r = 0$ present in the STOs (GTO functions actually have a maximum at this point) and also have a different decay for large separations, contractions procedures are often employed to circumvent

these problems. The contraction process consists of writing each basis function as a combination of more than one Gaussian with the coefficients fitted to reproduce the behavior of an STO of a given exponential ζ (zeta). Since a non-linear optimization of such parameter is not a practical procedure, standard exponents obtained from optimization for a small set of molecules are normally used. In this case, the contraction coefficients would be determined previously for the basis, and remain fixed during the SCF calculation. As one example, a simple basis that uses this contraction scheme is the STO-3G, where the notation stands for a combination of three Gaussian functions such as to reproduce a Slater-type orbital. Despite of increasing the number of integrations that must be solved for each orbital, the use of contraction schemes are still very time saving if compared to a calculation using the actual STO basis.

Considering an *ab initio* calculation in a polyatomic molecule, a basis set such as the STO-3G must, at least, have the minimum number of functions per atom necessary to describe the occupied orbitals on it with the proper symmetry (*s*,*p*,*d*...). Obviously, accurate results cannot be expected from such minimal approach since it does not have sufficient variational flexibility and therefore more basis functions must be added to approach the ideal complete limit.

One possible way of increasing the basis set size is to use more than one function per orbital in the minimal basis set. A basis that uses two functions of different exponential constant (ζ, zeta) for each orbital is called a double-zeta basis set, and adds variational flexibility, since it may allow separately a diffuse and a denser part of the orbital, depending on the molecular environment. This description is readily extended to more than two functions per orbital (triple-zeta, quadruple-zeta and so on). It is relevant to mention that the common approach is to increase the number of functions only of the valence orbitals, leaving the core orbitals with a single function, since they have smaller contribution to the bond formation. Such procedure is often called split valence shell basis set.

One difficulty that the above basis can experience is that atomic orbitals may not be suitable to describe the molecular "environment", for example the spherical *s* orbitals of the hydrogen atom are different in space orientation from that of the H_2 molecule and

hence will show slow convergence on this molecule. To improve the basis set for this type of problem, it is necessary the inclusion of "polarization functions". A polarized basis set is one that contains functions with angular orbital numbers (l) higher than the occupied atomic ones, *e.g.* p orbitals in the hydrogen case, or d-type functions in first row atoms.

2.9 Correlation-consistent basis

The normal approach to obtain basis sets suitable for Hartree-Fock calculations, as previously described, is to find contractions of primitive Gaussians that reproduce an optimized Slater function of a given exponent (ζ). However for correlated calculations such as MRCI, the properties required for the basis are more complicated since the virtual space, necessary to describe the excitations, should be capable of recovering a large part of the correlation energy and the virtual orbitals optimized for Hartree-Fock calculations are not suitable for this purpose. Therefore it is important to use basis calibrated to provide an appropriate set of virtual orbitals for correlated calculations.

Studying the variation of the correlation energy of the oxygen atom with the addition of polarized orbitals, Dunning[12] proposed an efficient basis that separates the orbitals in occupied and correlated sets. For each atom, the basis is constructed by optimizing the first set of orbitals (occupied) for an accurate representation of the atomic Hartree-Fock ground-state while the second set (correlating) are added such as to maximize the contribution to the correlation energy. It was shown that a hierarchy of correlation-consistent basis set could be set up, adding groups of orbitals with similar contribution to the correlation energy simultaneously. It was also found that primitive Gaussian functions are efficient for describing the correlating orbitals, and with compact sets of GTOs the accuracy is preserved while avoiding excessive integrations.

The basis functions obtained with such procedure were called correlation-consistent polarized valence basis set, denoted by cc-pVXZ, where the basis hierarchy is represented by the cardinal number X. Such hierarchy is obtained from the occupied orbitals by successively adding one function of each angular momentum up to $l_{max} = X$, as displayed

Table 2.1: Structure of Dunning basis set[a].

	H-He	B-Ne	Al-Ar
occupied [b]	[1*s*]	[2*s*1*p*]	[3*s*2*p*]
cc-pV*DZ*	[2*s*1*p*]	[3*s*2*p*1*d*]	[4*s*3*p*1*d*]
cc-pV*TZ*	[3*s*2*p*1*d*]	[4*s*3*p*2*d*1*f*]	[5*s*4*p*2*d*1*f*]
cc-pV*QZ*	[4*s*3*p*2*d*1*f*]	[5*s*4*p*3*d*2*f*1*g*]	[6*s*5*p*3*d*2*f*1g]
cc-pV5Z	[5*s*4*p*3*d*2*f*1*g*]	[6*s*5*p*4*d*3*f*2*g*1*h*]	[7*s*6*p*4*d*3*f*2*g*1*h*]

[a] The numbers correspond to the amount of orbitals with same l and different exponent.

[b] The occupied set is optimized separately for a HF calculation.

in Table 2.1 (note that H and He are exceptions of l_{max} rule, since there is no core set). The term "valence" in the basis name explicits the fact that its quality is of *X*'tuple-zeta but in a split-valence way. In fact, the core-correlation energy can be neglected in many molecular calculations since it is nearly constant over all the potential energy surface and its effect on properties such as stationary geometries and well depths are very low.

Extensions of the correlation-consistent basis set are also available for a better description of core correlation effects or anionic systems and excited states. In the correlation-consistent polarized core-valence sets (cc-pCV*X*Z)[13] the normal cc-pV*X*Z basis are augmented with functions with exponents optimized to maximize the core-correlation energy (with higher exponents), while in the augmented correlation-consistent polarized valence basis set (aug-cc-pV*X*Z)[14] it is added one more function to each angular momentum, optimized to improve the description of atomic anions, where more diffuse orbitals are necessary.

Another important aspect of the correlation-consistent basis set is that its use for uncorrelated calculations is also a great advantage if compared to other basis set, such as those constructed by Gaussian contractions and including split valence and polarization functions (*e.g.* 6-31G,6-31G*,6-31G**[15–17]). Besides of providing better agreement with properties calculated in the Hartree-Fock limit, it offers a systematic convergence to the

complete basis set limit while increasing the cardinal number X.

2.10 Extrapolation to the complete basis set limit

Since the Hartree-Fock method treats the electron-electron interaction in an average way, the wave function amplitude for one electron does not depend on the instantaneous position of another one. However in the exact wave function, the probability amplitude for one electron is shifted away from the position of the others, creating a coulomb hole around them. As can be seen in Eq. (1.2), the electronic Hamiltonian has singularities whenever two electrons or one electron and one nuclei have the same coordinates, which imposes a nuclear and an electronic Coulomb cusp conditions[9].

One can thus expect that the convergence of the Hartree-Fock wave function is achieved much faster, since no effort is put into describing the electronic Coulomb cusp, being this complicated task left to the correlated calculation. Due to this different behavior towards convergence, the normal approach is to separately treat the Hartree-Fock and correlated parts[18].

Although the convergence of the correlation energy is slow and involves larger computational efforts, it is systematic if done with the correlation-consistent basis set, which allows the extrapolation to the complete basis set (CBS) limit. One simple rule (although with physical motivations) consists of approximating the error of a calculation with the cc-pVXZ basis set as AX^{-3}, where the exact energy would be related to the calculated one by:

$$E_{\infty}^{\mathrm{cor}} \approx E_{X}^{\mathrm{cor}} + AX^{-3} \tag{2.23}$$

Note that the energies subscripts represent the cardinal number of the basis and the CBS limit corresponds to $X = \infty$. The value of E_{∞}^{cor} can be estimated by calculating the correlation energy in two different basis of ranks X and Y (since Eq. (2.23) has just two unknown parameters)

$$\begin{aligned} E_{\infty}^{\mathrm{cor}} &\approx E_{X}^{\mathrm{cor}} + AX^{-3} \\ E_{\infty}^{\mathrm{cor}} &\approx E_{Y}^{\mathrm{cor}} + AY^{-3} \end{aligned} \tag{2.24}$$

and solving the system to obtain the extrapolated energy E_∞^{cor}, one gets

$$E_\infty^{\text{cor}} \approx \frac{X^3 E_X^{\text{cor}} - Y^3 E_Y^{\text{cor}}}{X^3 - Y^3} \tag{2.25}$$

For a more rigorous treatment of the error, it was showed by Schwartz[19], with perturbation theory applied for two electron systems, that the convergence of the one-electron basis with respect to its angular momentum number l goes as:

$$E_l^{\text{cor}} = -\frac{45}{256}\left(l+\frac{1}{2}\right)^{-4}\left[1-\frac{5}{4}\left(l+\frac{1}{2}\right)^{-2}+O\left[\left(l+\frac{1}{2}\right)^{-6}\right]\right] \tag{2.26}$$

The same result was demonstrated and generalized for atoms with an arbitrary number of electrons by Kutzelnigg and Morgan[20]. The error due to the omission of all basis function with $l > L$ can be estimated integrating* the Schwartz expansion[21]:

$$E_{L+1}^{\text{cor}} = E_\infty^{\text{cor}} - \sum_{m=4} A_{m-1}(L+1)^{-m+1} \tag{2.27}$$

where A_{m-1} are numerical coefficients. Note that, if one relates the cardinal number X of the basis set with $L+1$ and only consider the first term in the above expansion, Eq. (2.23) is recovered, suggesting some physical motivation for it. Although $X = L + 1$ applies to H and He in the Dunning's basis set (see table 2.1), for atoms from B to Ar it is changed to $L = X$.

Helgaker[22] analyzed extrapolation laws of the general form:

$$E_X^{\text{cor}} = a + b(X+c)^{-3+d} \tag{2.28}$$

But found that no significant improvement was obtained with the inclusion of the parameters c and d, and since the fit of more than two parameter would require more calculations, they kept the $c = d = 0$ form. Nevertheless, variations of this formula have been extensively used, for example Truhlar[18] proposed the use of such formula with $c = 0$ and fixing d such as to minimize the root-mean-square error for three systems. The use of this formula with $d = 0$ and c fixed from some other condition is also well recognized[23].

*Note that $\int_{L+\frac{1}{2}}^{\infty}(l+\frac{1}{2})^{-m}dl = \frac{1}{m-1}(L+1)^{-m+1}$

With the aim of improving the accuracy by considering more terms of the Schwartz expansion, Varandas[24] proposed an extrapolation scheme written as:

$$E_X^{\mathrm{cor}} = E_\infty^{\mathrm{cor}} + A_3 X^{-3} + A_4 X^{-4} \tag{2.29}$$

where the two-points fit could be kept by noticing that A_4 can be related to A_3. This offered a method capable of predicting the CBS correlation energy with a root mean squared deviation (rmsd) of only a few milliHartrees for a set of 33 systems. The method is also more consistent in the sense that the predicted energies vary little with the pair of cardinal numbers chosen for the extrapolation.

Highly accurate calculations performed with wave-functions that depend explicitly on interelectronic coordinates, performed by Klopper[25], gave a new insight on basis set extrapolations. In addition to providing benchmark results for the systems CH_2, H_2O, HF, N_2, CO, Ne and F_2 from which any extrapolation can be compared, the results established that the singlet and triplet pair energies (within coupled-cluster theory) have different convergence, as X^{-3} and X^{-5} respectively.

With this result in mind, Varandas proposed a new extrapolation[21] that accounts explicitly for the singlet and triplet pair contributions, with a scheme similar to Eq. (2.29). Such an approach, called uniform singlet- and triplet-pair extrapolation (USTE), has the form

$$E_X^{\mathrm{cor}} = E_\infty^{\mathrm{cor}} + \frac{A_3}{(X+\alpha)^{-3}} + \frac{A_5}{(X+\alpha)^{-5}} \tag{2.30}$$

where A_5 and A_3 are related by $A_5 = A_5(0) + cA_3^n$. In this way, E_∞^{cor} and A_3 are determined from a fit to two calculations with different basis set, while the other parameters are fixed from optimization to 23 atomic and molecular systems. Such extrapolation scheme yields very good accordance with the highly accurate results of Klopper[25]. One important feature of the USTE method is that it retains the accuracy when extrapolating from smaller pairs of cardinal numbers, while the traditional approaches work best only when extrapolating from large pairs of basis set. This makes the USTE method highly desirable for systems with a large number of electrons, where calculations with higher basis sets are prohibitive[26–33].

As for the Hartree-Fock or CASSCF energies, several extrapolation laws have also been proposed, and since it is a necessary step to obtain the extrapolated total energy, one must also be concerned with the choice of a suitable method. One extrapolation formula that has been extensively used[23], is the exponential form:

$$E_X^{\mathrm{HF}} = E_\infty^{\mathrm{HF}} + A\exp(-bX) \tag{2.31}$$

where the E_∞^{HF} must be obtained from at least three energies calculated with different values of X. Since the uncorrelated calculation is relatively inexpensive, and affordable for large cardinal numbers (*e.g.* $X = 6$), the extrapolated energies within this formula are considered to represent the Hartree-Fock limit. More recently Karton and Martin[34] proposed an exponential law to be determined from two *ab initio* energies:

$$E_X^{\mathrm{HF}} = E_\infty^{\mathrm{HF}} + A(X+1)\exp(-9\sqrt{X}) \tag{2.32}$$

which shows errors around $10\mu E_h$ if extrapolated from AV5Z and AV6Z basis set. However, in situations where such large basis sets are prohibitive, and only AV(T, Q)Z basis are affordable it is recommended[34] the use of the inverse power form:

$$E_X^{\mathrm{HF}} = E_\infty^{\mathrm{HF}} + B/X^{5.34} \tag{2.33}$$

This formula is known to perform very well with a root mean squared error of $206\mu E_h$, with just two inexpensive calculations.

2.11 Scaling of the correlation energy

The number of *ab initio* energies involved in the description of a whole potential energy surface is normally huge. Typically, one uses 10 geometries to represent each one-dimensional cut what gives rise to a set of 10^τ points, where τ is the total number of dimensions of the configurational space. Recall that for a N-atom molecule $\tau = 3N - 6$.

It is clear that an accurate description of the complete PES is a very time-consuming task, and therefore schemes to reduce the computational effort are desirable. For this purpose, the correlation scaling (CS) method was proposed by Varandas and Piecuch[35],

which consists of a simple, yet robust, way to reduce the labor required to generate an accurate global PES corresponding to a larger basis set. This scheme consists on calculating the whole PES with basis of rank $X-2$ and $X-1$ and predicting the correlation energy at rank X with a single point calculation at this level.

The formula used to perform such scaling is given by:

$$E_X^{\mathrm{cor}}(\mathbf{R}) = \chi_{X,X-1}(\mathbf{R}) E_X^{\mathrm{cor}}(\mathbf{R}) \tag{2.34}$$

where the scaling function χ assumes the form:

$$\chi_{X,X-1}(\mathbf{R}) = 1 + \frac{S_{X-1,X-2}(\mathbf{R}) - 1}{S_{X-1,X-2}(\mathbf{R}_e) - 1} \left[S_{X,X-1}(\mathbf{R}_e) - 1 \right] \tag{2.35}$$

where the reference geometry ($\mathbf{R}_e$) can be any point of the potential energy surface, and

$$S_{m,n}(\mathbf{R}) = \frac{E_m^{\mathrm{cor}}(\mathbf{R})}{E_n^{\mathrm{cor}}(\mathbf{R})} \tag{2.36}$$

Such approach was tested and proved to be efficient to predict the total correlation (from coupled cluster methods) and also its dynamical part (from MRCI) for different basis families[36–38]. Also available are generalizations of the correlation scaling method to account for more than one pivotal geometry and for extrapolating, not just for $m+1$, but merging the scaling with the USTE method (CS/USTE)[26], providing accurate energies with costs as low as possible. The accuracy of the method has been checked for diatomic molecules through vibrational calculations, which provide a severe test of the approach, with very good results being generally observed[26].

Bibliography

[1] O. L. Polyansky, A. G. Császár, S. V. Shirin, N. F. Zobov, P. Barletta, J. Tennyson, D. W. Schwenke, and P. J. Knowles, Science **299**, 539 (2003).

[2] P. Barletta, S. V. Shirin, N. F. Zobov, O. L. Polyansky, J. Tennyson, E. F. Valeev, and A. G. Császár, J. Chem. Phys. **125**, 204307 (2006).

[3] A. Szabo and N. E. Ostlund, *Modern Quantum Chemistry* (McMillan, 1982).

[4] C. C. J. Roothaan, Rev. Mod. Phys. **23**, 69 (1951).

[5] B. O. Roos, P. R. Taylor, and P. E. M. Siegbahn, Chem. Phys. **48**, 157 (1980).

[6] P. Siegbahn, A. Heiberg, B. Roos, and B. Levy, Phys. Scr. **21**, 323 (1980).

[7] P. Siegbahn, J. Almlöfand, A. Heiberg, and B. Roos, J. Chem. Phys. **74**, 2384 (1981).

[8] K. Ruedenberg, M. W. Schmidt, M. M. Gilbert, and S. T. Elbert, Chem. Phys. **71**, 41 (1982).

[9] T. Helgaker, P. Jorgensen, and J. Olsen, *Molecular Electronic-Structure Theory* (Wiley, New York, 2000).

[10] T. D. Crawford and H. F. Schaefer, in *Reviews in Computational Chemistry*, edited by K. B. Lipkowitz and D. B. Boyd (John Wiley & Sons, New York, 2000), p. 33.

[11] T. Helgaker, W. Klopper, and D. P. Tew, Mol. Phys. **106**, 2107 (2008).

[12] T. H. Dunning, J. Chem. Phys. **90**, 1007 (1989).

[13] D. E. Woon and T. H. Dunning Jr., J. Chem. Phys. **103**, 4572 (1995).

[14] R. A. Kendall, T. H. Dunning Jr., and R. J. Harrison, J. Chem. Phys. **96**, 6796 (1992).

[15] W. J. Hehre, R. Ditchfield, and J. A. Pople, J. Chem. Phys. **56**, 2257 (1972).

[16] P. C. Harihara and J. A. Pople, Theoret. Chim. Acta **28**, 213 (1973).

[17] J. S. Binkley, J. A. Pople, , and W. J. Hehre, J. Am. Chem. Soc. **102**, 939 (1980).

[18] D. G. Truhlar, Chem. Phys. Lett. **294**, 45 (1998).

[19] C. Schwartz, Phys. Rev. **126**, 1015 (1962).

[20] W. Kutzelnigg and J. D. Morgan III, J. Chem. Phys. **96**, 4484 (1992).

[21] A. J. C. Varandas, J. Chem. Phys. **126**, 244105 (2007).

[22] T. Helgaker, W. Klopper, H. Koch, and J. Noga, J. Chem. Phys. **106**, 9639 (1997).

[23] D. Feller, K. A. Peterson, and T. D. Crawford, J. Chem. Phys. **124**, 054107 (2006).

[24] A. J. C. Varandas, J. Chem. Phys. **113**, 8880 (2000).

[25] W. Klopper, Mol. Phys. **99**, 481 (2001).

[26] A. J. C. Varandas, Chem. Phys. Lett. **443**, 398 (2007).

[27] A. J. C. Varandas, J. Chem. Phys. **129**, 234103 (2008).

[28] Y. Z. Song and A. J. C. Varandas, J. Chem. Phys. **130**, 134317 (2009).

[29] A. J. C. Varandas, Chem. Phys. Lett. **463**, 225 (2008).

[30] A. J. C. Varandas, J. Comp. Chem. **30**, 379 (2009).

[31] A. J. C. Varandas, J. Phys. Chem. A **112**, 1841 (2008).

[32] A. J. C. Varandas, Chem. Phys. Lett. **471**, 315 (2009).

[33] G. M. A. Junqueira and A. J. C. Varandas, J. Phys. Chem. A **112**, 10413 (2008).

[34] A. Karton and J. M. L. Martin, Theoret. Chim. Acta **115**, 330 (2006).

[35] A. J. C. Varandas and P. Piecuch, Chem. Phys. Lett. **430**, 448 (2006).

[36] B. R. L. Galvão, S. P. J. Rodrigues, and A. J. C. Varandas, J. Chem. Phys. **129**, 044302 (2008).

[37] B. R. L. Galvão and A. J. C. Varandas, J. Phys. Chem. A **113**, 14424 (2009).

[38] J. J. Lutz and P. Piecuch, J. Chem. Phys. **128**, 154116 (2008).

Chapter 3

Analytical modeling of *ab initio* energies

As presented so far, highly accurate *ab initio* energies can be calculated for fixed molecular geometries within the Born-Oppenheimer approximation. However, for each arrangement of the atoms one separated time-consuming task is necessary, and any theoretical model that requires quick evaluation over various points, has the bottleneck of the pointwise calculation. This barrier is overcome by performing calculations over a representative set of geometries and fitting them (see appendix A) using an analytic function, which can provide a fast, continuous and differentiable representation of the surface.

An example of the importance of such functions is the study of chemical kinetics for a given reaction. Whether the study is performed quantum mechanically or classically the potential energy surface (PES) plays a fundamental role, being incorporated through the Hamiltonian and dictating the interactions between the involved species, and after integrating the equations of motion accurate reaction rate constants and cross sections can be obtained and may be compared to experimental data. Although direct dynamics methods[1–4] have been proposed to couple dynamics and electronic structure calculations (avoiding a global analytical form), the computational time required in an *ab initio* calculation severely restricts the usefulness of such approach.

Another example of great importance is the prediction of vibrational levels of a

molecule as the eigenvalues of the nuclear Schrödinger equation [Eq. (1.5)]. For diatomic molecules, where only one vibrational degree of freedom exists, it is possible to perform the task directly from calculated *ab initio* energies. For a triatomic or larger molecule however, the need of a large number of points makes such approach prohibitive, and again the fitted potential energy surface is the best choice.

There are several criteria that a PES must fulfill in order to provide accurate results. For example, it must respect the symmetry of the molecule and give the exact same value if two equivalent atoms are permuted. For scattering problems, it also must smoothly connect the dissociative limits to the interaction region of the configuration space. Generally, it should represent accurately the available experimental or theoretical data, and have a reasonable behavior where no such data is available. Another criteria and qualities that a PES should present are summarized in the literature[5–7].

Few functional forms have the capacity of describing correctly the dissociative limits of a molecule. Perhaps the most simple one is the semi-empirical London-Eyring-Polanyi-Sato (LEPS[8–10]) derived from molecular orbital theory for the H_3 system. Although it does not show enough flexibility to describe complex features of potential energy surfaces, it has been widely used due to its simplicity. Another popular method, based on semi-empirical valence bond theory, is the diatomics in molecules (DIM)[11–13]. In the next sections, focus will be given to two general strategies that can be used for fitting polyatomics including dissociation limits.

3.1 Many-body expansion

The many-body expansion (MBE)[14–18] was first proposed by Murrell *et al.* and consists of writing the PES as a summation over the contribution of each fragment:

$$V_{\mathrm{ABC}\cdots\mathrm{N}} = \sum_{\mathrm{A}} V_{\mathrm{A}}^{(1)} + \sum_{\mathrm{AB}} V_{\mathrm{AB}}^{(2)}(R_{\mathrm{AB}}) + \sum_{\mathrm{ABC}} V_{\mathrm{ABC}}^{(3)}(R_{\mathrm{AB}}, R_{\mathrm{BC}}, R_{\mathrm{CA}}) + \ldots + V_{\mathrm{ABC}\ldots\mathrm{N}}^{(n)} \tag{3.1}$$

where R_i are the interatomic distances. The summation of one-body terms ($\sum_{\mathrm{A}} V_{\mathrm{A}}^{(1)}$) corresponds to the energy of the isolated atoms and is normally set to zero. The two-body energy contributions $V_{\mathrm{AB}}^{(2)}(R_{\mathrm{AB}})$ are representations of the isolated diatomics potential

curve, normally chosen as an extended Rydberg function and tends asymptotically to zero as R_{AB} approaches infinity.

The three-body term ($V^{(3)}_{ABC}$) depends on the shape of the triangle formed by the triatom ABC, and its value on a particular geometry is determined by subtracting the two- and one-body contributions from the total energy (generally calculated from *ab initio* methods) at that configuration. The $V^{(3)}_{ABC}$ function is then fitted (appendix A) to reproduce the values obtained above. A similar reasoning applies for higher order terms.

A necessary condition for each $n-$body term is that it goes to zero whenever one of the atoms involved in the fragment is removed to infinity. A functional form that satisfies this condition, and is widely used to fit the calculated three-body energies, is composed by a polynomial in the collective set of coordinates ($\mathbf{R}$) multiplied by a range decaying factor:

$$V^{(3)}_{ABC}(\mathbf{R}) = P(\mathbf{R}) \prod_{i=1}^{3} \left[1 - \tanh \gamma_i (R_i - R_i^0)\right] \tag{3.2}$$

Although exemplified for the three-body term, the extension of this equation for higher order n-body terms is straightforward: the contribution of its fragments are removed from the total energy, and fitted to a functional form similar to Eq. (3.2), *i.e.* composed by a polynomial dependent on all internal coordinates and multiplied by a suitable range decaying factor.

Although it is in principle possible to build a potential energy surface for molecules of any size using this strategy, the complexity of the fit increases considerably with the number of atoms. To describe a N-body system, there are $3N - 6$ coordinates involved, and the multidimensional fit is a limiting factor for many practical reasons. For example, to deal with a pentatomic molecule, one have to perform a fit in nine dimensions.

3.2 Double many-body expansion

If the distance between two interacting molecules is large enough to make orbital overlap negligible, the system can be well described by perturbation theory, where the unperturbed Hamiltonian is considered to be the Hamiltonian of the individual fragments. The

leading terms in the perturbation expansion are the first-order electrostatic and second-order contributions to the induction and dispersion energies[19,20], which for large separations can be expanded as an inverse power series on the distance between them (multipolar expansion). Although for long-range parts of the potential the multipolar expansion shows the correct physical behavior, it is not suitable to describe the short range interaction, making distinct functional forms more adequate on different parts of the PES.

Within the double many-body expansion (DMBE) theory[21–24], the description of each n-body term is divided into an Extended Hartree-Fock (EHF), that describes short range interactions, and a dynamical correlation (dc) part that accounts for electrostatic, induction and dispersion energies in a physically correct form, allowing an accurate description of the whole potential energy surface. Starting from the many-body expansion from Eq. (3.1) the separation is done as:

$$V^{(n)} = V^{(n)}_{\mathrm{EHF}} + V^{(n)}_{\mathrm{dc}} \tag{3.3}$$

For the two-body terms, the approach generally used is the extended Hartree-Fock approximate correlation energy method for diatomic molecules, including the united-atom limit (EHFACE2U)[25]. In this case, the EHF and dc terms assume the forms:

$$\begin{aligned} V^{(2)}_{\mathrm{EHF}}(R) &= -\frac{D}{R}\left(1+\sum_{i=1}^{n} a_i r^i\right)\exp\left\{-\gamma_0\left[1+\gamma_1\tanh(\gamma_2 r)\right]r\right\} \\ V^{(2)}_{\mathrm{dc}}(R) &= -\sum_{n=6,8,10,\ldots} C_n\left[1-\exp\left(-A_n\frac{R}{\rho}-B_n\frac{R^2}{\rho^2}\right)\right]^n R^{-n} \end{aligned} \tag{3.4}$$

where $r=R-R_e$ is the displacement from the equilibrium diatomic geometry and D and a_i ($i = 1, ..., n$) are adjustable parameters of the EHF part, fitted to reproduce the *ab initio* interaction energies. The parameters of the $V^{(2)}_{\mathrm{dc}}$ term, however, are obtained from previous knowledge on the long-range forces such as the dispersion coefficients of the atom-atom interaction (C_n). The bracketed term in $V^{(2)}_{\mathrm{dc}}$ is a charge damping function for the long-range dispersion energy, with the auxiliary functions being $A_n=\alpha_0 n^{-\alpha_1}$ and $B_n=\beta_0\exp(-\beta_1 n)$[21,22], while the parameters $\alpha_0, \alpha_1, \beta_0$ and β_1 are of universal-type (the same

for any diatomic). The scaling parameter ρ is defined as $\rho=5.5+1.25R_0$ and $R_0=2(\langle r_A^2\rangle^{1/2}+\langle r_B^2\rangle^{1/2})$ is the Le Roy[26] parameter, while $\langle r_X^2\rangle$ is the expectation value of the squared radius for the outermost electrons of atom X. These functions show the appropriate physical behavior for long range regions and also for extremely short bond distances (collapsed diatomic), giving the DMBE approach a great advantage when modeling PESs for triatomics or larger molecules, since the Coulombic behavior is ensured whenever any two atoms approach each other, by the $1/R$ factor of $V_{\mathrm{EHF}}^{(2)}$.

For three-body fragments, the EHF part is still written as a polynomial times a decaying range function as in the MBE method [Eq. (3.2)], while the dynamical correlation energy term will depend on the reactants type and what are the most prominent terms in a multipole expansion. For an ordinary atom-diatom interaction, without a large quadrupole moment, the dynamical correlation usually assumes the form[27]

$$V_{\mathrm{dc}}^{(3)} = -\sum_{i}^{3}\sum_{n} f_i(\mathbf{R})C_n^{(i)}(R_i,\theta_i)\chi_n(r_i)r_i^{-n} \tag{3.5}$$

where R_i, r_i, and θ_i are the Jacobi coordinates (R_i is the bond distance, say AB, r_i the corresponding C $-$ AB separation, and θ_i the included angle), and $f_i=\frac{1}{2}\{1-\tanh\left[(3R_i-R_j-R_k)\right]\}$ is a switching function. The damping function $\chi_n(r_i)$ is similar to that of Eq. (3.4) and the atom-diatom dispersion coefficients in Eq. (3.5) have the form:

$$C_n^{(i)}(R_i,\theta_i) = \sum_{L} C_n^L(R)P_L(\cos\theta_i) \tag{3.6}$$

where $P_L(\cos\theta_i)$ denotes the L-th Legendre polynomial. The dispersion coefficients are estimated with the procedure described in Ref. 28 and using dipolar polarizabilities calculated from *ab initio* methods. The atom-diatom dispersion coefficients calculated for a set of internuclear distances are then fitted to the functional form:

$$C_n^{L,\mathrm{A-BC}}(R) = C_n^{L,\mathrm{AB}} + C_n^{L,\mathrm{AC}} + D_M\left[1+\sum_{i=1}^{3} a_i(R-R_M^{(L)})^i\right]\exp\left[-\sum_{i=1}^{3} b_i(R-R_M^{(L)})^i\right] \tag{3.7}$$

where $C_n^{L,\mathrm{AB}}$ is the atom-atom dispersion coefficient for $L=0$ and zero for other values of L, and the other parameters are determined from the fit.

If higher order fragments are necessary, the continuation of the series is performed in a similar manner. Although molecules with more than three atoms were not studied

during the work presented in this thesis, examples of the DMBE method applied to such cases can be found in Refs. 29–32.

3.3 Multi-sheeted potentials

The modeling of adiabatic PESs is often complicated by the presence of conical intersections, where the adiabatic energies change in a discontinuous way and simple polynomials cannot mimic the corresponding cusp. The concept of a diabatic state from Section 1.2 is invoked to circumvent such problem and the diabatic representation of the electronic Hamiltonian [Eq. (1.14)] is modeled using smooth functions.

In the two-states case, if the adiabatic energies V_X^a and V_B^a are obtained pointwise as the solution of the electronic Schrödinger equation, the diabatic potential elements are obtained for each point using Eq. (1.14), giving:

$$\begin{aligned} V_{11}^d(\mathbf{R}) &= V_X^a(\mathbf{R})\cos^2\alpha(\mathbf{R}) + V_B^a(\mathbf{R})\sin^2\alpha(\mathbf{R}) \\ V_{22}^d(\mathbf{R}) &= V_X^a(\mathbf{R})\sin^2\alpha(\mathbf{R}) + V_B^a(\mathbf{R})\cos^2\alpha(\mathbf{R}) \\ V_{12}^d(\mathbf{R}) &= [V_B^a(\mathbf{R}) - V_X^a(\mathbf{R})]\cos\alpha(\mathbf{R})\sin\alpha(\mathbf{R}) \end{aligned} \tag{3.8}$$

Note that the transformation is not unique, and depends on the mixing angle $\alpha(\mathbf{R})$. As mentioned in Section 1.2, there are several approaches for obtaining this parameter[14,33–42].

The diabatic points obtained for V_{11}^d and V_{22}^d after this transformation can then be fitted to polynomial forms of the MBE or DMBE families as if they represented the PES of a hypothetical molecule. The non-diagonal element (V_{12}^d) on the other hand has different properties, such as the asymptotic limit and the fact that it must be zero for parts of the PES in which the intersection happens. Following the work of Murrell *et al.*[35], this term is written as a polynomial times a range factor [as in Eq. (3.2)], but also multiplied by a function that makes it vanish for some symmetrical configurations.

After the three diabatic elements are fitted to analytic functions, the adiabatic sheets are recovered as the eigenvalues of the diabatic matrix [Eq. (1.14)], giving

$$V_{B/X}^a(\mathbf{R}) = \frac{1}{2}[V_{11}^d(\mathbf{R}) + V_{22}^d(\mathbf{R})] \pm \frac{1}{2}\sqrt{[V_{22}^d(\mathbf{R}) - V_{11}^d(\mathbf{R})]^2 + 4V_{12}^d(\mathbf{R})^2} \tag{3.9}$$

where the cusp and degeneracy of the sheets due to the conical intersection is given by construction.

3.4 Energy-switching

For reactive dynamics, one is normally interested in chemical accuracy, with errors less than $1\,\mathrm{kcal\,mol^{-1}}$, and thus the deviations of the fitted PESs are normally of this order. When studying the ro-vibrational spectra, however, the errors in experimental measurements can be as low as $1\,\mathrm{cm^{-1}}$, which is extremely hard to obtain when fitting a global PES with an ordinary number of parameters and *ab initio* points.

In order to achieve spectroscopic accuracy for a global PES, the energy-switching method was proposed[27], where a local polynomial that accurately predicts the spectra is merged with a global form. Labeling the spectroscopically accurate potential as V_2, and the global one as V_1, they are merged into a combined potential V_{ES} as

$$V_{\mathrm{ES}} = f(\Delta E)V_1(\mathbf{R}) + [1 - f(\Delta E)]V_2(\mathbf{R}) \tag{3.10}$$

where $\Delta E = E - E_0$ is the displacement from some reference energy, and $f(\Delta E)$ is a switching function that approaches 0 for large negative energy displacements and +1 for large positive ones

$$f = \frac{1}{2}\left\{1 + \tanh[(\gamma_0 + \gamma_1 \Delta E^m)\Delta E]\right\} \tag{3.11}$$

When applying the ES scheme, one needs to define the variable E to measure the displacement from the reference energy E_0 in Eq. (3.10) as a function that grows uniformly from the bottom of the potential well[27]. This function could in principle be chosen as V_2, the PES that describes the well, but such local PESs are often not well-behaved for large displacements from equilibrium, and hence cannot be used directly. To circumvent this problem, the displacement from the reference energy may be written as

$$\Delta E = V_2 + \phi(\mathbf{R}) - E_0 \tag{3.12}$$

where $\phi(\mathbf{R})$ is a correction term suitably chosen to compensate the non-uniform growing of the local function in case.

This approach has been successfully applied to the potential energy surfaces of triatomic and tetratomic molecules[43,44], including multi-sheeted ones[45–47], and have originated some of the most accurate global forms reported thus far for those systems.

Bibliography

[1] A. Warshel and M. Karplus, J. Am. Chem. Soc. **94**, 5612 (1972).

[2] K. Bolton, W. L. Hase, and G. H. Peslherbe, *Direct dynamics simulations of reactive systems* (World Scientific Publishing, 1998), p. 143.

[3] A. J. C. Varandas and P. E. Abreu, Chem. Phys. Lett. **293**, 261 (1998).

[4] R. Pascual, G. C. Schatz, G. Lendvay, and D. Troya, J. Phys. Chem. A **106**, 4125 (2002).

[5] J. S. Wright and S. K. Gray, J. Chem. Phys. **69**, 67 (1978).

[6] J. N. L. Connor, Comp. Phys. Comm. **17**, 117 (1979).

[7] G. C. Schatz, Rev. Mod. Phys. **61**, 669 (1989).

[8] F. London, Z. Electrochem. **35**, 552 (1929).

[9] H. Eyring and M. Polanyi, Z. Phys. Chem. B **12**, 279 (1931).

[10] S. Sato, J. Chem. Phys. **23**, 2465 (1955).

[11] F. O. Ellison, J. Am. Chem. Soc. **85**, 3540 (1963).

[12] J. C. Tully, Adv. Chem. Phys. **42**, 63 (1980).

[13] P. J. Kuntz, in *Atom-Molecule Collision Theory*, edited by R. Bernstein (Plenum, New York, 1979), p. 79.

[14] J. N. Murrell, S. Carter, S. C. Farantos, P. Huxley, and A. J. C. Varandas, *Molecular Potential Energy Functions* (Wiley, Chichester, 1984).

[15] K. S. Sorbie and J. N. Murrell, Mol. Phys. **29**, 1387 (1975).

[16] J. N. Murrell, K. S. Sorbie, and A. J. C. Varandas, Mol. Phys. **32**, 1359 (1976).

[17] S. C. Farantos, E. C. Leisegang, J. N. Murrell, J. J. C. Teixeira-Dias, and A. J. C. Varandas, Mol. Phys. **34**, 947 (1977).

[18] J. N. Murrell, S. Carter, and A. J. C. Varandas, Mol. Phys. **35**, 1325 (1978).

[19] I. G. Kaplan, *Intermolecular Interactions: Physical Picture, Computational Methods and Model Potentials* (John Wiley & Sons, 2006).

[20] A. J. Stone, *The theory of intermolecular forces* (Oxford University Press, 1996).

[21] A. J. C. Varandas, J. Mol. Struct. Theochem. **21**, 401 (1985).

[22] A. J. C. Varandas, Adv. Chem. Phys. **74**, 255 (1988).

[23] A. J. C. Varandas, in *Lecture Notes in Chemistry*, edited by A. Laganà and A. Riganelli (Springer, Berlin, 2000), vol. 75, p. 33.

[24] A. J. C. Varandas, in *Conical Intersections: Electronic Structure, Dynamics & Spectroscopy*, edited by W. Domcke, D. R. Yarkony, and H. Köppel (World Scientific Publishing, 2004), vol. 15 of *Advanced Series in Physical Chemistry*, chap. 5, p. 205.

[25] A. J. C. Varandas and J. D. Silva, J. Chem. Soc. Faraday Trans. **88**, 941 (1992).

[26] R. J. Le Roy, Spec. Period. Rep. Chem. Soc. Mol. Spectrosc. **1**, 113 (1973).

[27] A. J. C. Varandas, J. Chem. Phys. **105**, 3524 (1996).

[28] M. A. Matías and A. J. C. Varandas, Mol. Phys. **70**, 623 (1990).

[29] A. J. C. Varandas and H. G. Yu, Mol. Phys. **91**, 301 (1997).

[30] M. Y. Ballester and A. J. C. Varandas, Phys. Chem. Chem. Phys. **7**, 2305 (2005).

[31] L. A. Poveda and A. J. C. Varandas, J. Chem. Phys. **131**, 044309 (2009).

[32] Y. Q. Li and A. J. C. Varandas, J. Phys. Chem. A **114**, 6669 (2010).

[33] M. Baer, Chem. Phys. Lett. **35**, 112 (1975).

[34] H. Werner and W. Meyer, J. Chem. Phys. **74**, 5802 (1981).

[35] J. N. Murrell, S. Carter, I. M. Mills, and M. F. Guest, Mol. Phys. **42**, 605 (1981).

[36] T. Pacher, L. S. Cederbaum, and H. Köppel, Adv. Chem. Phys. **84**, 293 (1993).

[37] W. Domcke, C. Woywod, and M. Stengle, Chem. Phys. Lett. **226**, 257 (1994).

[38] G. J. Atchity and K. Ruedenberg, Theor. Chem. Acc. **97**, 47 (1997).

[39] A. J. Doblyn and P. J. Knowles, Mol. Phys. **91**, 1107 (1997).

[40] V. C. Mota and A. J. C. Varandas, J. Phys. Chem. A **112**, 3768 (2008).

[41] A. J. C. Varandas, J. Chem. Phys. **129**, 234103 (2008).

[42] A. J. C. Varandas, Chem. Phys. Lett. **471**, 315 (2009).

[43] A. J. C. Varandas, S. P. J. Rodrigues, and P. A. J. Gomes, Chem. Phys. Lett. **297**, 458 (1998).

[44] W. Ansari and A. J. C. Varandas, J. Phys. Chem. A **106**, 9338 (2002).

[45] A. J. C. Varandas, J. Chem. Phys. **107**, 867 (1997).

[46] A. J. C. Varandas, A. I. Voronin, and P. J. S. B. Caridade, J. Chem. Phys. **108**, 7623 (1998).

[47] A. J. C. Varandas, J. Chem. Phys. **119**, 2596 (2003).

Chapter 4

Gas phase dynamics

4.1 Introduction

For an elementary reaction of the type A + B $\rightarrow$ C + D, the theory of chemical kinetics states that the rate of products formation is proportional to the concentration of reactants as

$$\frac{d[\mathrm{C}]}{dt} = k(T)[\mathrm{A}][\mathrm{B}] \tag{4.1}$$

and it depends on the temperature of the system through the thermal reaction rate constant $k(T)$[1]. From a theoretical point of view, if the reaction is taking place in gas phase, this rate constant can be obtained from the analysis of collisions between the two reactants, where the interaction energy between all atoms involved is provided by the electronic potential energy surface (PES) within the Born Oppenheimer framework (see Section 1.1). Although the PES is obtained from pure quantum mechanical calculations, the motion of the nuclei in such collisions is here treated with classical mechanics, which is a very successful approach specially for large temperatures and heavier atoms where quantum effects are less significant.

One aspect of quantum mechanics worth keeping under consideration is the quantization of the internal energies of reactants and products, such as to allow the study of state-to-state phenomena. Therefore, in the following derivations classical mechanics will be used to follow the motion of the nuclei in a quantum mechanical based PES, where

the energy of the reactants and products (at the initial and final time) are restricted to the corresponding energy levels, in what is called the quasiclassical approach.

4.2 Rate constants and cross sections

The macroscopic system in which the reaction takes place is decomposed as an ensemble of colliding particles with different quantum states and speeds, such as in

$$\mathrm{A}_{(i,\boldsymbol{v}_\mathrm{A})} + \mathrm{B}_{(j,\boldsymbol{v}_\mathrm{B})} \rightarrow \mathrm{C}_{(l,\boldsymbol{v}_\mathrm{C})} + \mathrm{D}_{(m,\boldsymbol{v}_\mathrm{D})} \tag{4.2}$$

Note that this equation may also describe non-reactive collisions if C and D are identical to A and B, in which case it is considered "inelastic" if the quantum numbers of the products (l and m) are different from those of the reactants (i and j) and "elastic" if they are kept the same.

The rate of formation of a product molecule is proportional to the number of collisions occurring between A and B per unit of time[2], and to express this "collisional frequency" two variables must be introduced. The first is the number density of a species (η) which corresponds to the number of molecules per unit of volume, while the second is the relative velocity between the reactants, defined as $v = |\boldsymbol{v}_\mathrm{A} - \boldsymbol{v}_\mathrm{B}|$. The "collisional frequency" between $\mathrm{A}_{(i,\boldsymbol{v}_\mathrm{A})}$ and $\mathrm{B}_{(j,\boldsymbol{v}_\mathrm{B})}$ will then be proportional to their number densities and relative velocity, and mathematically expressing this proportionality the rate in which $\mathrm{C}(l, \boldsymbol{v}_\mathrm{C})$ will be formed is written as:

$$\left.\frac{d\eta_\mathrm{C}(l, \boldsymbol{v}_\mathrm{C})}{dt}\right|_{\boldsymbol{v}_\mathrm{A},\boldsymbol{v}_\mathrm{B}} = \sigma(ij, v|l, \boldsymbol{v}_\mathrm{C})\, v\, \eta_\mathrm{A}(i, \boldsymbol{v}_\mathrm{A})\eta_\mathrm{B}(j, \boldsymbol{v}_\mathrm{B}) \tag{4.3}$$

where the proportionality constant $\sigma(ij, v|l, \boldsymbol{v}_\mathrm{C})$ is the so-called reactive cross-section. Physically, this new variable represents an effective area in which a collision between reactants takes place and gives a product molecule in a specific final state, and as it will be shown later, it is closely related the probability that the collision leads to reaction.

Eq. (4.3) describes a very specific event, restricted to a single translational energy between reactants and each one having its specific quantum state. Under real conditions, such as in the atmosphere or a gas sample, such variables are not controlled and

show a distribution over all possible values. To study these cases, it becomes necessary to integrate the *differential* cross sections to obtain *thermalized* rate constants, or in other words, allow for any possible quantum number and kinetic energy while properly considering their probability.

Therefore one is interested in replacing the number density defined within a specific velocity $\eta_{\mathrm{A}}(i, \boldsymbol{v}_{\mathrm{A}})$ by the general number density of a particle $n_{\mathrm{A}(i)}$ in the gas. This requires previous knowledge of the velocity distribution of the reactants $f_{\mathrm{A}(i)}(\boldsymbol{v}_{\mathrm{A}})$, which gives the probability of finding the particle A(i) with velocity $\boldsymbol{v}_{\mathrm{A}}$, and is expressed as

$$\eta_{\mathrm{A}}(i, \boldsymbol{v}_{\mathrm{A}}) = n_{\mathrm{A}(i)} f_{\mathrm{A}(i)}(\boldsymbol{v}_{\mathrm{A}}) \tag{4.4}$$

The same is applied for B(j) molecules, and substituting these expressions on Eq. (4.3) and integrating over the velocity of the reactants, one obtains

$$\frac{d\eta_{\mathrm{C}}(l, \boldsymbol{v}_{\mathrm{C}})}{dt} = \int_{\boldsymbol{v}_{\mathrm{A}}\boldsymbol{v}_{\mathrm{B}}} \sigma(ij, v|l, \boldsymbol{v}_{\mathrm{C}})\, v f_{\mathrm{A}(i)}(\boldsymbol{v}_{\mathrm{A}}) f_{\mathrm{B}(j)}(\boldsymbol{v}_{\mathrm{B}}) d\boldsymbol{v}_{\mathrm{A}} d\boldsymbol{v}_{\mathrm{B}}\ n_{\mathrm{A}(i)} n_{\mathrm{B}(j)} \tag{4.5}$$

If one is not concerned with the velocity of the products, the integration can be also performed in respect to $\boldsymbol{v}_{\mathrm{C}}$, giving

$$\frac{dn_{\mathrm{C}(l)}}{dt} = \left[\int_{\boldsymbol{v}_{\mathrm{A}}\boldsymbol{v}_{\mathrm{B}}} \sigma(ij, v|l)\, v f_{\mathrm{A}(i)}(\boldsymbol{v}_{\mathrm{A}}) f_{\mathrm{B}(j)}(\boldsymbol{v}_{\mathrm{B}}) d\boldsymbol{v}_{\mathrm{A}} d\boldsymbol{v}_{\mathrm{B}} \right] n_{\mathrm{A}(i)} n_{\mathrm{B}(j)} \tag{4.6}$$

where a notation for the integrated cross sections as $\sigma(ij, v|l) = \int_{\boldsymbol{v}_{\mathrm{C}}} \sigma(ij, v|l, \boldsymbol{v}_{\mathrm{C}}) d\boldsymbol{v}_{\mathrm{C}}$ is introduced. Comparing this equation with (4.1), and identifying the number densities as concentrations, it is seen that it gives the rate of $\mathrm{C}_{(l)}$ formation from the reaction:

$$\mathrm{A}_{(i)} + \mathrm{B}_{(j)} \rightarrow \mathrm{C}_{(l)} + \mathrm{D} \tag{4.7}$$

where the quantum states of the reactants and products are fixed, and the corresponding rate constant can be extracted, giving

$$k_{(ij|l)} = \int_{\boldsymbol{v}_{\mathrm{A}}\boldsymbol{v}_{\mathrm{B}}} \sigma(ij, v|l)\, v f_{\mathrm{A}(i)}(\boldsymbol{v}_{\mathrm{A}}) f_{\mathrm{B}(j)}(\boldsymbol{v}_{\mathrm{B}}) d\boldsymbol{v}_{\mathrm{A}} d\boldsymbol{v}_{\mathrm{B}} \tag{4.8}$$

The next step towards describing a gas phase reaction, in which all quantum states are populated with different probabilities, is to perform an averaged sum over all such states:

$$\frac{dn_{\mathrm{C}}}{dt} = \sum_{ijl} \int_{\boldsymbol{v}_{\mathrm{A}}\boldsymbol{v}_{\mathrm{B}}} \sigma(ij, v|l)\, v f_{\mathrm{A}(i)}(\boldsymbol{v}_{\mathrm{A}}) f_{\mathrm{B}(j)}(\boldsymbol{v}_{\mathrm{B}}) d\boldsymbol{v}_{\mathrm{A}} d\boldsymbol{v}_{\mathrm{B}}\, n_{\mathrm{A}(i)} n_{\mathrm{B}(j)} \tag{4.9}$$

In order to recover the general expression of Eq. (4.1) the state specific number density must be replaced by the total one. This is easily performed noting that they are related by $n_{\mathrm{A}(i)} = n_{\mathrm{A}} p_{\mathrm{A}(i)}$, where $p_{\mathrm{A}(i)}$ is the probability that reactant A is found in state i. Replacing this on the above equation gives

$$\frac{dn_{\mathrm{C}}}{dt} = \left[\sum_{ijl} p_{\mathrm{A}(i)} p_{\mathrm{B}(j)} \int_{\boldsymbol{v}_{\mathrm{A}}\boldsymbol{v}_{\mathrm{B}}} \sigma(ij, v|l)\, v f_{\mathrm{A}(i)}(\boldsymbol{v}_{\mathrm{A}}) f_{\mathrm{B}(j)}(\boldsymbol{v}_{\mathrm{B}}) d\boldsymbol{v}_{\mathrm{A}} d\boldsymbol{v}_{\mathrm{B}} \right] n_{\mathrm{A}} n_{\mathrm{B}} \tag{4.10}$$

and once again, by comparison with Eq. (4.1), the rate constant can be theoretically written as the bracketed term above

$$\begin{aligned} k(T) &= \sum_{ijl} p_{\mathrm{A}(i)} p_{\mathrm{B}(j)} \int_{\boldsymbol{v}_{\mathrm{A}}\boldsymbol{v}_{\mathrm{B}}} \sigma(ij, v|l)\, v f_{\mathrm{A}(i)}(\boldsymbol{v}_{\mathrm{A}}) f_{\mathrm{B}(j)}(\boldsymbol{v}_{\mathrm{B}}) d\boldsymbol{v}_{\mathrm{A}} d\boldsymbol{v}_{\mathrm{B}} \\ &= \sum_{ijl} p_{\mathrm{A}(i)} p_{\mathrm{B}(j)} k_{(ij|l)} \end{aligned} \tag{4.11}$$

Finally, if the state specific cross-sections or rate constants are not relevant, as in many experimental cases, we can define the total cross section as $\sigma(v) = \sum_{ijl} p_{\mathrm{A}(i)} p_{\mathrm{B}(j)} \sigma(ij, v|l)$. Noting that at thermal equilibrium the velocity distribution for the translational motion of the reactants is independent of the internal quantum state, the above equation is written in the global form:

$$k(T) = \int_{\boldsymbol{v}_{\mathrm{A}},\boldsymbol{v}_{\mathrm{B}}} \sigma(v)\, v f_{\mathrm{A}}(\boldsymbol{v}_{\mathrm{A}}) f_{\mathrm{B}}(\boldsymbol{v}_{\mathrm{B}}) d\boldsymbol{v}_{\mathrm{A}} d\boldsymbol{v}_{\mathrm{B}} \tag{4.12}$$

To solve this integral, it is necessary to determine expressions for the cross-section $\sigma(v)$ and the probability distribution of the velocities $f(\boldsymbol{v})$. These two variables are discussed in the next sections.

4.3 The Maxwell-Boltzmann distribution

The kinetic energy probability distribution for a molecule in gas phase can be obtained through statistical mechanics from the general expression

$$p(E_i) = w(E_i) \exp\left(-\frac{E_i}{k_{\mathrm{B}} T}\right) Q(T)^{-1} \tag{4.13}$$

where k_B is the Boltzmann constant, T is the temperature of the system and $Q(T)$ is the partition function, which imposes that the summation over all the probabilities will be unitary

$$Q(T) = \sum_i w(E_i) \exp\left(-\frac{E_i}{k_B T}\right) \tag{4.14}$$

while the variable $w(E_i)$ is the degeneracy of each energy level. For an ideal gas, such energy levels are obtained from basic quantum mechanics to be the solutions of the Schrödinger equation for a free particle of mass m moving in a three dimensional container (*e.g.* a cube with side L)

$$E = \frac{h^2}{8mL^2}\left(n_x^2 + n_y^2 + n_z^2\right) \tag{4.15}$$

where h is the Plank's constant and n_i are a set of positive integer quantum numbers. In the case of a particle in a box, the evaluation of the infinite sum for the partition function cannot be written in a simple analytic form. However, the presence of the L^{-2} term makes the difference between subsequent levels so small, that the summation can be approximated by an integral over the states, avoiding the use of $w(E_i)$.

$$\begin{aligned} Q(T) &= \left[\int_0^\infty \exp\left(-\frac{h^2 n^2}{8mL^2 k_B T}\right) dn\right]^3 \\ &= (2\pi m k_B T)^{3/2} \frac{L^3}{h^3} \end{aligned} \tag{4.16}$$

The last step to solve Eq. (4.13) is to find the degeneracy of each energy E_i, which is not a well behaved function. To contour such problem one may define a function $\phi(\epsilon)$ as the number of states with energy lower than a fixed ϵ, being its use only justified for large energy values where the it becomes smooth. It is possible to obtain an approximate analytical form for such function noting that the coordinates n_x, n_y and n_z form a three dimensional space, and Eq. (4.15) defines a sphere inside it[3]. Considering $\phi(\epsilon)$ as continuous, the summation over the states (with energy lower than ϵ) can be approximated by an integral where the result is the volume of such sphere.

$$\phi(\epsilon) = \frac{\pi}{6}\left(\frac{8mL^2\epsilon}{h^2}\right)^{3/2} \tag{4.17}$$

With this result, the degeneracy $w(E)$ can be written as the number of states with energy between E and $E + \Delta E$, extracted from Eq. (4.17) as the difference $\phi(E + \Delta E) - \phi(\epsilon)$:

$$w(\epsilon) = \frac{\pi}{4} (8m)^{3/2} \frac{L^3}{h^3} E^{1/2} \Delta E + O(\Delta E^2) \tag{4.18}$$

and the energy probability distribution is:

$$p(E)dE = 2\pi \left(\frac{1}{\pi k_B T} \right)^{3/2} E^{1/2} \exp\left(-\frac{E}{k_B T} \right) dE \tag{4.19}$$

To obtain the velocity distribution from the above equation, a simple substitution from $E = mv^2/2$ and $dE = mvdv$ is necessary, giving

$$f(\boldsymbol{v})d\boldsymbol{v} = 4\pi \left(\frac{m}{2\pi k_B T} \right)^{3/2} v^2 \exp\left(-\frac{mv^2}{2k_B T} \right) d\boldsymbol{v} \tag{4.20}$$

which is called the Maxwell-Boltzmann distribution of speeds and, using this expression, one can proceed to the solution of Eq. (4.12).

4.4 Rate constant at thermal equilibrium

Using the Maxwell-Boltzmann distribution at a fixed temperature T for the reactants translational motion irrespective of their quantum state is the same as assuming thermal equilibrium. In order to integrate Eq. (4.12) with the use of such velocities distributions, it is convenient to change the coordinates from $\boldsymbol{v}_A$ and $\boldsymbol{v}_B$ to the center-of-mass and relative velocities ($\boldsymbol{v}_{cm}$ and $\boldsymbol{v}$), since the integrand in Eq. (4.12) only involves the relative velocity. This is performed using the relations

$$\begin{aligned} \boldsymbol{v} &= \boldsymbol{v}_A - \boldsymbol{v}_B \\ \boldsymbol{v}_{cm} &= (m_A \boldsymbol{v}_A + m_B \boldsymbol{v}_B)/M \\ m_A \boldsymbol{v}_A^2 + m_B \boldsymbol{v}_B^2 &= M \boldsymbol{v}_{cm}^2 + \mu \boldsymbol{v}^2 \end{aligned} \tag{4.21}$$

where M is the sum of the reactants masses ($m_A + m_B$) and μ their reduced mass ($m_A m_B/M$). Since the Jacobian determinant for this change of variables is one, the relation between the velocity elements is $d\boldsymbol{v}_A d\boldsymbol{v}_B = d\boldsymbol{v}_{cm} d\boldsymbol{v}$. Applying now Eq. (4.20) to

Eq. (4.12) and changing the coordinates, it is obtained that

$$k(T) = \int_{\boldsymbol{v}_{cm}} \int_{\boldsymbol{v}} \sigma(v)\, v \left(\frac{m_A m_B}{(2\pi k_B T)^2}\right) \exp\left[-\frac{1}{k_B T}\left(M\boldsymbol{v}_{cm}^2 + \mu\boldsymbol{v}^2\right)\right] d\boldsymbol{v}_{cm} d\boldsymbol{v} \tag{4.22}$$

Since the only unknown in this equation is the reaction-cross section, which depends only on the radial part of the relative velocity vector, it is desirable to integrate over the three coordinates of the center of mass velocity and over the orientation of the relative speed (expressing it in polar coordinates). This leaves the integral in terms of only one dimension: the radial part of the relative velocity vector ($v = |\boldsymbol{v}|$), where it is obtained

$$k(T) = 4\pi \left(\frac{\mu}{2\pi k_B T}\right)^{3/2} \int_0^\infty \sigma(v)\, v^3 \exp\left(-\frac{\mu v^2}{2k_B T}\right) dv \tag{4.23}$$

or, expressing it in terms of the relative translational energy (E_{tr})

$$k(T) = \frac{1}{k_B T}\left(\frac{8}{\pi\mu k_B T}\right)^{1/2} \int_0^\infty \sigma(E_{tr})\, E_{tr} \exp\left(-\frac{E_{tr}}{k_B T}\right) dE_{tr} \tag{4.24}$$

The only unknown for the evaluation of the rate constant is then the reaction cross section, which will be analyzed in the following section.

4.5 Expression for the cross-section

Among all initial specifications that are necessary to describe a single collision between the reactants, only two belong exclusively to the collision itself, while the others refer to one of the reactants alone. The first is the relative velocity or kinetic energy (subject of the previous sections) and the other is the impact parameter of the collision, which is a very useful concept in scattering studies.

In order to facilitate its definition, the origin of the coordinate system is fixed on the center of mass of reactant B, which is at rest in the proposed frame and considered the scattering center. As schematically shown in Figure 4.1, the impact parameter is extracted from the initial time, when the two species are very far apart and the interaction energy can be considered null. It is defined as the distance between the reactant A and a line passing through reactant B, parallel to the velocity vector[4]. When this parameter is small

the collision is considered to be frontal, while for a large enough value, the distance between the two fragments will be always too large for the interaction to take place, and the outcome will be a non-reactive process.

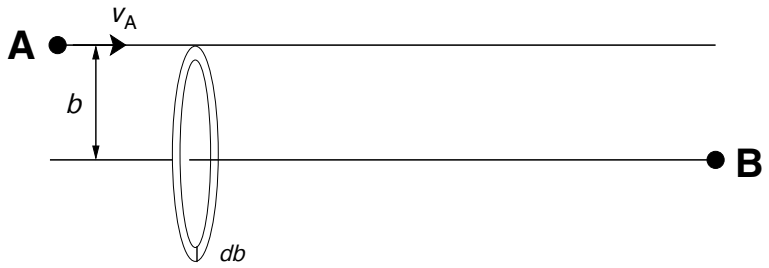

Figure 4.1: Schematic definition of the impact parameter b, and an element of area given the cylindrical collision zone.

Suppose that a large number of collisions are occuring between the two species in gas phase. The outcome of a particular trajectory starting with a well defined impact parameter b, relative velocity v and reactants at quantum states i and j, cannot be determined in a direct way. This is because it also depends on the internal attributes of the reactants, such as their angular orientation (which give rise to steric effects) and the "phase" of the vibrational modes. Therefore the concept of a reaction probability must come into play, being expressed as:

$$P(ij, v, b|l) = \frac{N_{C(l,\boldsymbol{v}_C)}|_b}{N_{traj}|_b} \tag{4.25}$$

where $N_{traj}|_b$ is the number of collisions starting with impact parameter b and $N_{C(l,\boldsymbol{v}_C)}|_b$ is the number of reactive ones, while the probability $P(ij, v, b|l)$ is defined as this ratio.

In a real situation however, the impact parameter is not controlled and it is necessary to integrate over all its possible values. For this, the value of $N_{traj}|_b$ is given as the number of A molecules entering the reaction zone through an element of area equal to $dA = 2\pi bdb$ as

$$N_{traj}|_b = \eta_{A(i,\boldsymbol{v}_A)} v\, t\, 2\pi bdb \tag{4.26}$$

Substituting this equation on the definition of the probability [Eq. (4.25)], and integrating

over b it is obtained that

$$N_{\mathrm{C}(l,\boldsymbol{v}_\mathrm{C})} = \eta_{\mathrm{A}(i,\boldsymbol{v}_\mathrm{A})} v\, t \int_0^\infty P(ij, v, b|l, \boldsymbol{v}_\mathrm{C}) 2\pi b db \tag{4.27}$$

and after that, taking the derivative of this expression with respect to time and diving by the volume one gets

$$\frac{d\eta_{\mathrm{C}(l,\boldsymbol{v}_\mathrm{C})}}{dt} = (V)^{-1} \eta_{\mathrm{A}(i,\boldsymbol{v}_\mathrm{A})} v \int_0^\infty P(ij, v, b|l, \boldsymbol{v}_\mathrm{C}) 2\pi b db \tag{4.28}$$

Since B is here considered the scattering center, the value of $\eta_{\mathrm{B}(i,\boldsymbol{v}_\mathrm{B})}$ is unitary and it is possible to compare the above equation with Eq. (4.3), from where is obtained that the cross section is related to the probability as

$$\sigma(ij, v|l, \boldsymbol{v}_\mathrm{C}) = 2\pi \int_0^\infty P(ij, v, b|l, \boldsymbol{v}_\mathrm{C}) b db \tag{4.29}$$

If the velocity of the product molecules are not relevant, they may be integrated out to obtain

$$\sigma(ij, v|l) = 2\pi \int_0^\infty P(ij, v, b|l) b db \tag{4.30}$$

Which is the quasiclassical mechanical expression for the cross section, regardless of the form of the reactants or their specific properties. If the cross section is known, it can be related to the reaction rate constants using Eq. (4.8) and (4.11)

4.6 Monte Carlo sampling

Up to this point the derivation of the rate constant equations could be done analytically in the framework of classical mechanics. However, as seen above, the determination of the cross section involves the integration of a non-analytic function that depends on the concept of a reactive event as the outcome of a collision. If the reactants are in a particular internal configuration, $P(ij, v, b|l)$ is obtained from a simulation process, being one if the reaction occurred or zero otherwise.

In the quasiclassical trajectories (QCT) simulation, the Monte Carlo method[5] is employed to perform the integration of the reaction probability over all possible internal

configuration of the reactants, weighted by an appropriate distribution function. This method represents a very powerful numerical technique to solve multidimensional integrals, and to exemplify its application for the QCT approach a reaction between an atom and a diatomic is described here, which encompasses the cases studied in this thesis.

Although the atom does not have any internal degree of freedom, the diatomic may start the collision in any orientation with respect to the collision plane (given by the angles θ and ϕ). The direction of its angular momentum vector η is also random while its module J is obtained from the rotational quantum number. It further has a "vibrational phase", *i.e.* the value of the bond distance r may be found in any value within the turning points r_- and r_+ (where the kinetic energy is null and the potential holds all the vibrational energy). The average over all possible values is then given by the integral

$$\langle P(b)\rangle = \int_{\theta=0}^{\pi}\int_{\phi=0}^{2\pi}\int_{\eta=0}^{2\pi}\int_{r=r_-}^{r_+} P(b;\theta,\phi,\eta,r) \left(\frac{1}{\pi}\sin\theta d\theta\right)\left(\frac{1}{2\pi}d\phi\right)\left(\frac{1}{2\pi}d\eta\right)\left[G(r)dr\right] \tag{4.31}$$

where the infinitesimal elements of each variable are grouped with the respective probability normalization factor, and $G(r)$ is the probability distribution of the bond distance. Note that the evaluation of the integrand P at an specific point comes as the result of the integration of the classical equations of motion, where the initial conditions are given by the coordinates of that point, and it can only assume two values: 1 if the reaction occurred and 0 otherwise.

This multiple integral cannot be solved analytically since the integrand is not an ordinary function, and the Monte Carlo method is then used to solve it taking advantage of the probability distribution functions to evaluate the integrand more frequently where it is more relevant. For a brief review on this method, suppose that an integral is transformed through a change of variables in such a way that the new variables range from 0 to 1 and where the modified integrand F_n contain the probability distributions, such as

$$I = \int_{\xi_1=0}^{1}\int_{\xi_2=0}^{1}\cdots\int_{\xi_n=0}^{1} F_1(\xi_1)F_2(\xi_2)\ldots F_n(\xi_n)d\xi_1 d\xi_2\ldots d\xi_n \tag{4.32}$$

The integrand is then evaluated on a large set of the new variables chosen randomly and

the integral is approximated as

$$I \sim \frac{1}{L}\sum_{i}^{L} F(\xi_1(i), \xi_2(i) \ldots, \xi_n(i)) \tag{4.33}$$

where L is the number of points. From a computational point of view, the generation of a series of random numbers for each integration point is an extensive subject of its own, given the large amount required. Supposing that a good algorithm to generate pseudorandom numbers between 0 and 1 is available, one must then change the variables in Eq. (4.31) (θ, ϕ, η, r) such that the new variables contain a probability distribution according to the Monte Carlo method. The integral in the new set of primed variables is written as

$$\langle P(b)\rangle = \int_{\theta'=0}^{1}\int_{\phi'=0}^{1}\int_{\eta'=0}^{1}\int_{r'=0}^{1} P(b;\theta',\phi',\eta')d\theta' d\phi' d\eta' dr' \tag{4.34}$$

and since all values of the three angles are equally probable, it is easy to derive that

$$\begin{aligned}\theta' &= -\frac{1}{2}\cos\theta + \frac{1}{2}\\ \phi' &= \frac{1}{2\pi}\phi\\ \eta' &= \frac{1}{2\pi}\eta\end{aligned} \tag{4.35}$$

The function r', on the other hand, requires further work since the probability distribution function of r cannot be given in analytic form. It is known, however, that the probability that r is found between r and $r+dr$ is proportional to the amount of time the system is found there, *i.e.* it is proportional to $(dr/dt)^{-1}$ or to p^{-1}, and its selection must be performed with more than one random number using the von Neumann rejection technique[6,7]

A large set of these primed variables is then generated randomly, providing a collection of the initial conditions, which will correspond to an integration point. The value of the integrand is then calculated by solving the equations of motion, and analyzing whether the products are formed or not at the final state. The result of the integral is given by:

$$\langle P(b)\rangle = \frac{1}{N(b)}\sum_{i}^{N} P(b;\theta_i',\phi_i',\eta_i')) = \frac{N_R(b)}{N(b)} \tag{4.36}$$

where N_R is simply the number of trajectories that led to reaction.

4.6.1 Impact parameter and translational energy

After integrating over the internal degrees of freedom of the reactants to obtain the probability, it is possible to integrate over the impact parameter [Eq. (4.30)] to obtain the cross-section, and further integrate the cross section over the translational energy to obtain the rate constants [Eq. (4.24)]. Such integrations are also performed with the Monte Carlo method.

For the first part, a maximum value for the impact parameter b_{max} must be defined since this variable does not have a finite upper limit, and it must be sufficiently large to ensure that the reaction probability is zero for $b \geq b_{max}$. If b' is defined as b^2/b_{max}^2, which then varies from 0 to 1, the integral may be transformed as

$$\sigma(ij, v|l) = 2\pi \int_0^1 \langle P(b) \rangle \left(\frac{b_{max}^2}{2} \right) db' \tag{4.37}$$

where $db' = 2b/b_{max}^2$. From the Monte Carlo solution of this integral, it is found that

$$\begin{aligned} \sigma(ij, v|l) &= \pi b_{max}^2 \langle P \rangle \\ &= \pi b_{max}^2 \frac{N_R}{N} \end{aligned} \tag{4.38}$$

This is the general result for quasiclassical trajectories calculations of the cross section, and is also obtained in diatom/diatom collisions or even for polyatomics, because although the integral on the reactants internal degrees of freedom will be much larger, the result will still be N_R/N.

Finally, for a thermal rate constant to be obtained, the relative translational energy between the two species must be sampled for the desired temperature as in Eq. (4.24). This is performed by generating a random number between 0 and 1 that will correspond to the cumulative probability [$G(E_{tr})$] that the energy will be found between 0 and the sampled value[8]. In one of the publications included in this thesis, we have developed[9] a new method for sampling the translational energy, aimed at increasing the efficiency for reactions with large potential barriers and based on importance sampling techniques[10].

After integrating the equations of motion for a large number of initial conditions sampled randomly with the distributions described above, the Monte Carlo result for the

final equation for $k(T)$ is given by

$$k_{(ij|l)}(T) = \left(\frac{8k_{\mathrm{B}}T}{\pi\mu}\right)^{1/2} \pi b_{max}^2 \frac{N_R}{N} \tag{4.39}$$

where N_R and N now include trajectories starting with all possible attributes, and the term multiplying the cross section is the average thermal velocity, obtained from the velocity probability distribution [Eq. (4.20)] as $\int vf(v)dv$.

The total reaction cross section can be obtained from the state-specific ones as stated by Eq. (4.11), where the probability of each state ($p_{\mathrm{A}(i)}$) is given by its Boltzmann distribution [see Eq. (4.13)]. Since the reactant B is an atom considered to react always in the same electronic state, the index j is ignored and it is obtained

$$k(T) = \sum_{il} \frac{w(E_i)\exp\left(-E_i/k_{\mathrm{B}}T\right)}{Q_{\mathrm{A}}} k_{(i|l)} \tag{4.40}$$

where $w(E_i)$ is the degeneracy of the ith state of the diatomic.

4.7 Integrating the equations of motion

By studying the time evolution of a sufficiently large number of trajectories, Eq. (4.39) can be evaluated and the final rate constants obtained. Within the quasiclassical method the time evolution of the system is given by classical mechanics (with the initial quantized conditions being relaxed) and the integration of the equations of motion is often performed with Hamilton's formalism[11] since it involves only first-order differential equations.

Assuming a Cartesian coordinate system, the Hamiltonian is given by

$$H(\mathbf{x}, \mathbf{p}_x) = \sum_{i=1}^{N} \left[\frac{1}{2m_A}p_{x_i}^2 + \frac{1}{2m_B}p_{x_{i+3}}^2 + \frac{1}{2m_C}p_{x_{i+6}}^2\right] + V(\mathbf{R}) \tag{4.41}$$

where N is the number of atoms. Focusing once again in the triatomic case ($N = 3$), the position of atom A is given by (x_1, x_2, x_3), while atoms B and C are located at (x_4, x_5, x_6) and (x_7, x_8, x_9) respectively, and these elements together constitute the nine dimensional vector $\mathbf{x}$ (a similar definition holds to the vector $\mathbf{p}_x$). The potential energy surface $V(\mathbf{R})$

is a function of the three internuclear distances $\mathbf{R} = \left(R_{\mathrm{AB}}(\mathbf{x}), R_{\mathrm{BC}}(\mathbf{x}), R_{\mathrm{AC}}(\mathbf{x})\right)$, and the Hamilton's equations of motion are then written as

$$\begin{aligned} \frac{dx_i}{dt} &= \frac{\partial H}{\partial p_{x_i}} = \frac{\partial T}{\partial p_{x_i}} && (i = 1, \ldots, 9) \\ \frac{dp_{x_i}}{dt} &= -\frac{\partial H}{\partial x_i} = -\frac{\partial V}{\partial x_i} = \sum_{k=1}^{3} -\frac{\partial V}{\partial R_k}\frac{\partial R_k}{\partial x_i} && (i = 1, \ldots, 9) \end{aligned} \tag{4.42}$$

which gives a total of 18 coupled differential equations.

Most part of the available software for dynamics solve the equations of motion in Cartesian coordinates, since it does not restrict the number of atoms. However it is often interesting to change to a coordinate system that separates the position of the center of mass from the intramolecular distances, since this is a constant of motion and its elimination reduces the number of coupled equations. For a triatomic system, the Jacobi coordinates show several interesting properties, not only separating the center of mass, but also the coordinates of the reactant diatomic and the relative motion of the incoming atom. This is useful in several occasions, from integrating Hamilton's equation to analyzing the properties of the products after collision. The transformation from Cartesian to Jacobi coordinates may be performed as[12,13]:

$$\begin{aligned} q_i &= x_{i+6} - x_{i+3} && (i = 1, 2, 3) \\ Q_i &= x_i - \frac{1}{(m_B + m_C)}\left[m_B x_{i+3} + m_C x_{i+6}\right] && (i = 1, 2, 3) \\ S_i &= \frac{1}{(m_{\mathrm{A}} + m_{\mathrm{B}} + m_{\mathrm{C}})}\left[m_A q_i + m_B q_{i+3} + m_C q_{i+6}\right] && (i = 1, 2, 3) \end{aligned} \tag{4.43}$$

where the vector $\mathbf{q}$ represents the diatomic, $\mathbf{Q}$ the relative motion between the atom A and the center of mass of BC and $\mathbf{S}$ the position of the center of mass. The generalized momenta ($\mathbf{p}, \mathbf{P}, \mathbf{P}_S$), the transformation matrices and the Hamilton's equation in Jacobi coordinates are given on Appendix B.

There are several methods for numerical integration of coupled differential equations[14], where for the case of classical trajectories, the energy conservation is often used as a criteria to assess the accuracy of the algorithm used. The most conventional methods, such as Runge-Kutta, show poor energy accuracy in long time runs and the energy

error often increases linearly with time[15]. A generally accepted approach for the classical equations of motion are the combined fourth-order Runge-Kutta-Gill and sixth-order Adams-Moulton algorithms using fixed-size time step[16].

4.8 Incorporating quantum effects

As mentioned above, in the QCT approach the time evolution of the system is given only by classical mechanics (initial quantized conditions relaxed). This approach has shown to be very successful in several cases, specially when the masses of the atoms are large and the electronic states are well separated. If the QCT results need to be improved, or if processes involving excited electronic states must be studied, it is often preferable to incorporate quantum effects on the classical trajectories, than to perform full quantum mechanical studies, given the large computational demand that may render them infeasible.

The cases for which classical mechanics fails may be divided into two distinct situations. For small nuclear masses and velocities, the atomic wavelength will be significant and effects like tunneling and level quantization are more likely to be important. On the other hand, electronic transitions are controlled primarily by the separation between electronic energy levels, a property that is independent of the atomic masses. The prominence of the two kinds of quantum effects are controlled by independent "small parameters"[17].

During the research carried out in this thesis, it was found interesting to estimate the importance of the zero-point energy (ZPE) leakage and also that of electronic transitions, and the methods used to incorporate such effects in the quasiclassical approach are given in the next section.

4.8.1 Zero-point energy leakage

The quantum mechanical constraint that the system cannot lie under the zero-point energy is obviously not obeyed by the classical equations of motion and, as an example of the errors that this may bring to dynamical properties, one can imagine that the cross

sections for endoergic reactions will be overestimated. For correcting this problem within the quasiclassical method the approaches are divided between active and non-active.

In the so-called active schemes[18–21] a normal mode analysis is performed at each integration step to check whether all normal modes have energy superior to the ZPE. In case the condition is violated for a given mode, the trajectory is corrected by changing its point in phase space according to a given scheme. These methods often find problems for an exact conservation of energy and angular momentum, or in some cases make the trajectory not time-reversible.

In the non-active approaches, the integration of the equations of motions is performed as usual, but a criterion is imposed in the final (or initial) energy of the system. For example, in the quantum mechanical energy threshold[22] (QCT-QMT), only trajectories that show enough total energy to reach the zero-point energy of the products are integrated, being all others considered as non-reactive. More restrictive methods have been proposed, such as those by Nyman *et al.*[23] in which the vibrational energy of the product molecule is used as criterion. A hierarchy of approaches has been proposed by Varandas *et al.*[8,24] in which different components of the product molecule energy are analysed. In the QCT-internal energy quantum mechanical threshold (QCT-IEQMT) method, the internal energy must be above the ZPE, whereas in the QCT-VEQMT (QCT-vibrational energy quantum mechanical threshold) only the vibrational energy is considered. A mix between the two is achieved in the QCT-IVEQMT (QCT-intermediate vibrational energy quantum mechanical threshold) accepting trajectories that have an internal energy above the ZPE, but slightly lower vibrational energy within a given tolerance. In case the product molecule shows some physical requirement for the rotational energy, the QCT-NVEQMT (QCT-rotational and vibrational energy quantum mechanical threshold) is applied.

As a final remark, one should notice that simply discarding such trajectories for one of the above methods may introduce a statistical error in the analysis, a problem that was addressed by Varandas in Ref. 25 where a simple model denoted unified statistical (US) model was proposed.

4.8.2 Electronic transitions

The first attempt to incorporate electronic transitions into quasiclassical trajectories was performed by Tully and Preston[26–28] where it was developed what is called the trajectory surface hopping (TSH) approach. In their work, it was found that the Landau-Zenner probability[29,30] works well for electronic transitions in the H_3^+ case, but the model required that a function describing the locus of the crossing seam was provided, and hops could only occur when the trajectory passed through a surface crossing. Given the success of the TSH approach in allowing quasiclassical trajectories to predict rate constants for new processes such as charge transfer and quenching of excited species, it has received considerable theoretical attention and several new methods have been proposed[17,31–33].

A particular method, which is used later in this thesis, is the Voronin *et al.*[33] implementation of Tully's original method. In this approach, after the initial conditions are selected the trajectory starts on the ground adiabatic potential energy surface (V_X) and the integration of the equations of motion proceed as usual. Instead of requiring a function to describe the locus of the crossing seam and checking for hops only there, the trajectory is monitored at every integration step and if the energy gap between the two adiabatic sheets ($\Delta V = V_B - V_X$) reaches a minimum, the probability for a nonadiabatic transition is calculated using the Landau-Zener formula:

$$P_{\mathrm{LZ}} = \exp\left(-2\pi A^2/\hbar B u\right) \tag{4.44}$$

where u is the velocity, and A and B are the parameters that define the splitting between V_X and V_B at the instant t, given by

$$\Delta V = [B^2 u^2 (t-\tau)^2 + 4A^2]^{1/2} \tag{4.45}$$

where τ is the time corresponding to the minimum of ΔV. The three unknown parameters are determined using the three previous integration steps. After calculating the Landau-Zener probability a random number ξ is generated and, if $P_{\mathrm{LZ}} < \xi$, the trajectory continues on the same PES, or if $P_{\mathrm{LZ}} > \xi$ the trajectory hops to the other potential energy surface and the integration continues from there.

The hopping occur without a change in the molecular geometry, according to the Frank-Condon principle[34], and in general there will be a small energy gap between the two sheets at that point. Since the trajectory will gain/lose potential energy, the kinetic part must be corrected such as to conserve the total energy. There is no consensus regarding a correct direction to which the change in momentum must be applied: some authors choose to give it in the direction of the gradient $\nabla(V_B - V_X)$ while others choose the nonadiabatic coupling vector direction[35] (both are perpendicular to the crossing seam). As an example, the case of a triatomic system in which the correction is applied to the momentum of the smallest diatomic[26] will be detailed in the next paragraphs.

If the integration is performed in Cartesian coordinates (as in most programs) the momentum vector ($\mathbf{P}_c$) must be transformed to the Jacobi one ($\mathbf{P}_J$) for an A-BC triatom in which BC is the smallest interatomic distance, such that the correction can be applied in this direction. The transformation is given by

$$\mathbf{P}_J = \mathbf{A}\,\mathbf{P}_c \tag{4.46}$$

where the matrix $\mathbf{A}$ is defined in Appendix B. In this way, the Cartesian momentum of each atom ($\mathbf{p}_A, \mathbf{p}_B, \mathbf{p}_C$) is changed to the generalized momenta corresponding to the diatom ($\mathbf{p}_{BC}$), the relative A-BC, and the center of mass motions. Since the geometry is not changed, the transformation of the coordinates is only performed to obtain the position of C relative to B ($\mathbf{q}_{BC}$). A correction $\mathbf{c}$ is then added to the momentum, such that

$$\mathbf{P}'_J = \mathbf{P}_J + \mathbf{c} \tag{4.47}$$

where the primed variables will indicate the final (adjusted) ones. After the procedure, the corrected Cartesian momentum can be obtained back as:

$$\begin{aligned} \mathbf{P}'_c =& \mathbf{A}^{-1}\mathbf{P}'_J \\ =& \mathbf{P}_c + \mathbf{A}^{-1}\mathbf{c} \end{aligned} \tag{4.48}$$

and the only problem left is to obtain the vector $\mathbf{c}$. Since the correction is applied to the diatomic, only the three elements corresponding to its motion will be non-zero (the other six must be null), and its direction must lie on the diatomic axis such as not to change the

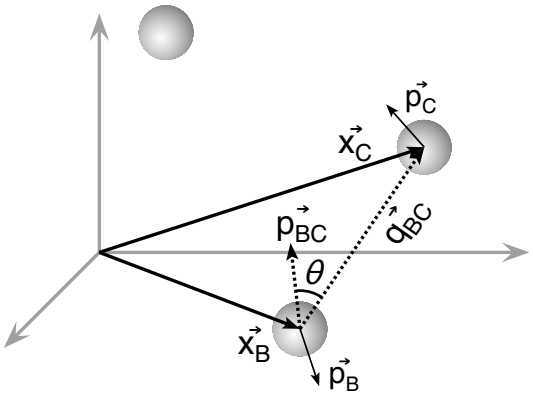

Figure 4.2: Coordinates and momenta of the smallest diatomic in Cartesian (solid) and Jacobi (dashed) systems used in correcting the trajectory after a hopping.

angular momentum of the system (note that $\mathbf{p}_{BC}$ also includes rotation and may point to any direction, see Figure 4.2). If we define the unit vector $\hat{\mathbf{u}} = \mathbf{q}_{BC}/\|\mathbf{q}_{BC}\|$, the direction of the correction must be either $+\hat{\mathbf{u}}$ or $-\hat{\mathbf{u}}$ (stretching or shortening the bond length) and the vector can thus be written as

$$\mathbf{c} = \Delta_p[\sigma\hat{\mathbf{u}}] \tag{4.49}$$

where the six null elements of $\mathbf{c}$ are omitted for simplicity. The variable $\sigma = \pm 1$ can be found by projecting the total diatomic momentum onto the bond axis, from where it is defined the radial component of the diatomic momentum (p_r):

$$\begin{aligned} (\mathbf{p}_{BC} \cdot \mathbf{q}_{BC}) &= \|\mathbf{p}_{BC}\|\|\mathbf{q}_{BC}\| \cos\theta \\ p_r = \|\mathbf{p}_{BC}\| \cos\theta &= \frac{(\mathbf{p}_{BC} \cdot \mathbf{q}_{BC})}{\|\mathbf{q}_{BC}\|} \end{aligned} \tag{4.50}$$

And from the sign of of p_r one gets the value of σ. Note that by doing so we choose $\sigma\hat{\mathbf{u}}$ to have the same direction as the vector $\mathbf{p}_r$, but the correction $\mathbf{c}$ may still remove or add momentum to the system depending only on the value of Δ_p. It is straightforward to prove that a correction in this direction will not change the angular momentum of the diatomic (and hence the total angular momentum):

$$\begin{aligned} \mathbf{L}'_{BC} =& \mathbf{q}_{BC} \times \mathbf{p}'_{BC} = \mathbf{q}_{BC} \times (\mathbf{p}_{BC} + \Delta_p\sigma\hat{\mathbf{u}}) \\ =& \mathbf{q}_{BC} \times \mathbf{p}_{BC} = \mathbf{L}_{BC} \end{aligned} \tag{4.51}$$

The magnitude of the correction (Δp) is uniquely determined by the requirement that the total energy must not be changed after the hop. Let us define the radial kinetic energy as total minus rotational energy, such that

$$K_r = \frac{\|\mathbf{p}_{BC}\|^2}{2\mu} - \frac{\|\mathbf{q}_{BC} \times \mathbf{p}_{BC}\|^2}{2\mu\|\mathbf{q}_{BC}\|^2} = \frac{p_r^2}{2\mu} \tag{4.52}$$

where μ is the reduced mass of the diatom, and to obtain the right hand side the definition of cross product $\|\mathbf{q}_{BC} \times \mathbf{p}_{BC}\| = \|\mathbf{q}_{BC}\|\|\mathbf{p}_{BC}\| \sin\theta$ is used. After the hopping, such radial kinetic energy must be changed such as to accommodate the difference in potential energy ΔV at the time of the hopping, and so it reads

$$K_r' = K_r \pm \Delta V \tag{4.53}$$

and the $\pm$ sign reflects the fact that the energy gap must be added if the trajectory is hopping to the lower sheet or subtracted if it is hopping to the upper one. In the latter case it may happen that a negative final energy is obtained, and the hopping is considered to be classically forbidden and therefore canceled. Finally, the magnitude of the correction is obtained as

$$\Delta_p = \|\mathbf{p}_r'\| - \|\mathbf{p}_r\| = \sqrt{2\mu K_r'} - \sqrt{2\mu K_r} \tag{4.54}$$

which, after being applied as described above, guarantees that the trajectory will conserve energy and momentum.

4.9 Final ro-vibrational states

After integrating the classical equations of motion for a given initial condition, the rotational and vibrational energies of the product molecule can assume any value, having a continuous distribution. However it is often interesting to study a reaction as a state-to-state phenomena, and for that purpose one needs to attribute energy quantum numbers for the products. In this section the atom-diatom collision is again the focus of attention.

4.9.1 Semiclassical binning

The semiclassical binning is the traditional way of extracting a quantum number from the products. The rotational quantum number of the final diatomic molecule is obtained from its angular momentum as[12]

$$\hbar j(j+1) = \mathbf{L}_{BC} \cdot \mathbf{L}_{BC} \tag{4.55}$$

where the transformation to Jacobi coordinates is used for the products, and the quantum number is obtained by solving this equation for j and rounding the positive root to an integer. In turn the vibrational energy is given by the semiclassical (Bohr-Sommerfeld) quantization rule for a non-rotating molecule:

$$\left(v + \frac{1}{2}\right) h = 2 \int_{r_-}^{r_+} p_r \, dr = 2 \int_{r_-}^{r_+} \sqrt{2\mu K_r} \, dr \tag{4.56}$$

where again the equation is solved for ν and rounded to an integer. The variables r_- and r_+ are the turning points of the diatomic vibration which may be obtained with the Newton-Raphson method, and the integral must be solved numerically.

4.9.2 Momentum Gaussian binning

A more elaborated scheme for binning the QCT output is the recently proposed Momentum Gaussian Binning (MGB[36,37]). Within this approach, instead of assigning a quantum number for each trajectory, a probability distribution over all quantum numbers is given, which is summed over all the calculated trajectories and normalized. The state-specific cross section and rate constant can be calculated afterwards by using the probability of an specific state as given by such distribution.

The physical motivation for this approach is found by considering the i-th trajectory as a wave package ψ^i and expanding it in terms of the products orthonormal ro-vibrational eigen-states $\phi_{\alpha\beta}$

$$\psi^i = \sum_{\alpha\beta} c^i_{\alpha\beta} |\phi_{\alpha\beta}\rangle \tag{4.57}$$

where the coefficients $c^i_{\alpha\beta}$ contain information about how much of the trajectory i is localized at the diatomic eigenvalue $E_{\alpha\beta} = \langle \phi_{\alpha\beta} | H | \phi_{\alpha\beta} \rangle$. The internal energy obtained

from the integration of the classical trajectory can be expressed as:

$$\begin{aligned}\varepsilon^i = \langle\psi^i|H|\psi^i\rangle &= \sum_{\alpha\beta}\left(c^{i}_{\alpha\beta}{}^{\star}c^{i}_{\alpha\beta}\right)\langle\phi_{\alpha\beta}|H|\phi_{\alpha\beta}\rangle \\ &= \sum_{\alpha\beta} W^i_{\alpha\beta}E_{\alpha\beta}\end{aligned} \tag{4.58}$$

where W^i is a two dimensional probability matrix, whose elements are understood as weights. The final desired probability that a product molecule is found in the state v, j is expressed a sum of W_{vj} over all trajectories.

$$P_{vj} = \sum_{i=1}^{N_{traj}} W^i_{vj} \tag{4.59}$$

The main problem now is to obtain an approximated way to determine the matrix W^i for each trajectory, since its exact determination would imply a knowledge of the coefficients $c^i_{\alpha\beta}$, which are not achievable. Assuming separability of the vibrational and rotational degrees of freedom, one gets $W^i_{\alpha\beta} = W^i_\alpha W^i_\beta$, and the MGB approach consists of writing these weights as:

$$W^i_\alpha = \frac{1}{\rho_\alpha\sqrt{\pi}}\exp\left[-\left(\frac{\sqrt{E_\alpha}-\sqrt{\varepsilon^i}}{\rho_\alpha\sqrt{\overline{E}_\alpha}}\right)^2\right] \tag{4.60}$$

where ρ is a unitless Gaussian decay parameter and $\overline{E}_\alpha$ is an average separation of two neighboring levels from the basis $[(E_{\alpha+1} - E_{\alpha-1})/2]$. Note that this Gaussian is centered at the trajectory energy, making the most weighted states as those with eigenvalues near it. A similar expression holds for the rotational levels (W^i_β).

The parameters ρ_α and ρ_β are considered fine-tuning constant to give the method even more realism. The value of ρ_α is fixed at $\rho_\alpha = 0.1$ while ρ_β is determined as ρ_α times the ratio of the average spacing between vibrational levels and the average spacing between rotational levels.

The use of the MGB scheme provides a smoother distribution over the quantum states of the product[9,37–40], if compared to the semiclassical approach, since every trajectory contributes for different quantum states with a given probability, instead of assigning just one number. Besides that, the MGB is a non-active scheme that accounts for the leakage of zero-point energy in QCT. The reason is that if a trajectory have a final energy inferior

to the ZPE of the product diatomic ($\varepsilon < E_0$), its probability contribution to the ground state population will be smaller, if compared to a trajectory ending up with $\varepsilon = E_0$.

Bibliography

[1] G. W. Castellan, *Physical Chemistry* (Addison-Wesley, Reading, MA, 1983).

[2] N. E. Henrisken and F. Y. Hansen, *Theories of Molecular Reaction Dynamics* (Oxford University Press, Oxford, 2008).

[3] D. A. McQuarrie, *Statistical Mechanics* (University Science Books, Sausalito, 2000).

[4] R. D. Levine, *Molecular Reaction Dynamics* (Cambridge University Press, Cambridge, 2005).

[5] N. Metropolis, A. W. Rosembluth, M. N. Rosembluth, A. H. Teller, and E. Teller, J. Chem. Phys. **21**, 1087 (1953).

[6] J. H. Hammersley and D. C. Handscomb, *Monte Carlo Methods* (Chapman and Hall, London, 1964).

[7] R. N. Porter, L. M. Raff, and W. H. Miller, J. Chem. Phys. **63**, 2214 (1975).

[8] A. J. C. Varandas, J. Brandão, and M. R. Pastrana, J. Chem. Phys. **96**, 5137 (1992).

[9] P. J. S. B. Caridade, B. R. L. Galvão, and A. J. C. Varandas, J. Phys. Chem. A **114**, 6063 (2010).

[10] J. T. Muckerman and M. B. Faist, J. Phys. Chem. **83**, 79 (1979).

[11] H. Goldstein, *Classical Mechanics* (Addison-Wesley, Reading, 1980).

[12] D. G. Truhlar and J. T. Muckerman, in *Atom-Molecule Collision Theory*, edited by R. Bernstein (Plenum, New York, 1981), p. 505.

[13] M. Karplus, R. N. Porter, and R. D. Sharma, J. Chem. Phys. **43**, 3259 (1965).

[14] W. H. Press, S. A. Teukolsky, W. T. Vetterling, and B. P. Flannery, *Numerical Recipes in Fortran: the Art of Scientific Computing* (Cambridge University Press, New York, 1992).

[15] F. Zhang, Comp. Phys. Comm. **99**, 53 (1996).

[16] W. L. Hase, R. J. Duchovic, X. Hu, A. Komornicki, K. F. Lim, D. Lu, G. H. Peslherbe, K. N. Swamy, S. R. V. Linde, A. J. C. Varandas, H. Wang, and R. J. Wolf, QCPE Bull. **16**, 43 (1996).

[17] J. C. Tully, J. Chem. Phys. **93**, 1061 (1990).

[18] J. M. Bowman, B. Gadzy, and Q. Sun, J. Chem. Phys. **91**, 2859 (1989).

[19] W. H. Miller, W. L. Hase, and C. L. Darling, J. Chem. Phys. **91**, 2863 (1989).

[20] A. J. C. Varandas and J. M. C. Marques, J. Chem. Phys. **100**, 1908 (1994).

[21] K. F. Lim and G. C. McCormack, J. Chem. Phys. **102**, 1705 (1995).

[22] D. G. Truhlar, J. Phys. Chem. **83**, 188 (1979).

[23] G. Nyman and J. Davidsson, J. Chem. Phys. **92**, 2415 (1990).

[24] A. J. C. Varandas, J. Chem. Phys. **99**, 1076 (1993).

[25] A. J. C. Varandas, Chem. Phys. Lett. **225**, 18 (1994).

[26] J. C. Tully and R. K. Preston, J. Chem. Phys. **55**, 562 (1971).

[27] R. K. Preston and J. C. Tully, J. Chem. Phys. **54**, 4297 (1971).

[28] J. C. Tully, in *Modern Theoretical Chemistry, Dynamics of Molecular Collisions, Part B*, edited by W. Miller (Plenum Press, New York, 1977), p. 217.

[29] L. Landau, Physik. Z. Sowjetunion **2**, 46 (1932).

[30] C. Zener, Proc. Roy. Soc. (London) **A137**, 696 (1932).

[31] N. C. Blais and D. G. Truhlar, J. Chem. Phys. **79**, 1334 (1983).

[32] M. S. Topaler, T. C. Allison, D. W. Schwenke, and D. G. Truhlar, J. Chem. Phys. **109**, 3321 (1998).

[33] A. I. Voronin, J. M. C. Marques, and A. J. C. Varandas, J. Phys. Chem. A **102**, 6057 (1998).

[34] P. W. Atkins, *Molecular Quantum Mechanics* (Oxford University Press, Oxford, 1983).

[35] G. C. Schatz, L. A. Pederson, and P. J. Kuntz, Faraday Discuss. **108**, 357 (1997).

[36] L. Bonnet and J. C. Rayez, Chem. Phys. Lett. **277**, 183 (1997).

[37] A. J. C. Varandas, Chem. Phys. Lett. **439**, 386 (2007).

[38] Y. Z. Song, P. J. S. B. Caridade, and A. J. C. Varandas, J. Phys. Chem. A **113**, 9213 (2009).

[39] J. Zhao, Y. Xu, D. Yue, and Q. Meng, Chem. Phys. Lett. **471**, 160 (2009).

[40] B. R. L. Galvão, J. A. Corzo-Espinoza, P. J. S. B. Caridade, and A. J. C. Varandas, Int. J. Chem. Kinet. **43**, 345 (2011).

Appendix A

Fitting to a linear model

The problem of fitting N data points to a given function often appears on modeling, and a special application here is the fit of a potential energy surface to *ab initio* energies. The general linear least squares method can be employed when the data is to be fitted to a function with M linear coefficients a_k such as

$$y(x) = \sum_{k=1}^{M} a_k X_k(x) \tag{A.1}$$

where $X_k(x)$ are generally called basis functions. Note that these functions may not have a linear dependence on x, but only the parameters a_k must. Considering each data point to have a "weighting" factor σ_i, the merit function is defined as[1]

$$\chi^2 = \sum_{i=1}^{N} \left[\frac{y_i - \sum_{k=1}^{M} a_k X_k(x_i)}{\sigma_i} \right]^2 \tag{A.2}$$

The minimization of such function in respect with all the parameters, *i.e.* $\partial\chi^2/\partial a_j = 0$, will provide the optimal coefficients

$$\frac{\partial \chi^2}{a_j} = \sum_{i=1}^{N} \frac{2}{\sigma_i^2} \left[y_i - \sum_{k=1}^{M} a_k X_k(x_i) \right] X_j(x_i) = 0 \tag{A.3}$$

rearranging the terms above leads to

$$\sum_{j=1}^{M} \sum_{i=1}^{N} \frac{X_j(x_i) X_k(x_i)}{\sigma_i^2} a_j = \sum_{i=1}^{N} \frac{y_i X_k(x_i)}{\sigma_i^2} \tag{A.4}$$

which is called *normal equations* of the least squares problem. they can be rewritten in matrix form as

$$\boldsymbol{\alpha} \,.\, \boldsymbol{a} = \boldsymbol{\beta} \tag{A.5}$$

where $\boldsymbol{\alpha}$ is a $M \times M$ square matrix, while $\boldsymbol{\beta}$ and $\boldsymbol{a}$ are column vectors running the M coefficients, with elements defined as

$$\begin{aligned} \alpha_{kj} &= \sum_{i=1}^{N} \frac{X_j(x_i) X_k(x_i)}{\sigma_i^2} \\ \beta_k &= \sum_{i=1}^{N} \frac{y_i X_k(x_i)}{\sigma_i^2} \end{aligned} \tag{A.6}$$

The problem of determining the optimal coefficients is then reduced to a matrix multiplication, as

$$\begin{aligned} \boldsymbol{a} &= \boldsymbol{\alpha}^{-1} \boldsymbol{\beta} \\ a_j &= [\alpha]_{jk}^{-1} \left[\sum_{i=1}^{N} \frac{y_i X_k(x_i)}{\sigma_i^2} \right] \end{aligned} \tag{A.7}$$

where the inversion of the matrix $\boldsymbol{\alpha}$ is generally performed by a Gauss-Jordan method.

All of the above derivation did not depend on the form of the x coordinates, just that the function is given at several points, which makes it easy to generalize to a multi-dimensional fit. Simply by replacing the x coordinate on Eq. (A.1) by a vector $\mathbf{x}$ of any dimensionality, the formulation above can be used and the algorithm easily adapted.

Appendix B

Jacobi coordinates for atom-diatom collisions

As noted in section 4.7, the use of Jacobi coordinates is useful for many aspects of atom-diatom collisions, given that they separate well between the properties of the reactants and the properties of the collision itself. This appendix gives all the necessary transformations (from Cartesian coordinates) for position and momentum, together with the Hamilton's equations of motion in these generalized coordinates.

Assuming a Cartesian coordinate system where the position of atom A is given by (x_1, x_2, x_3) and the atoms B and C that compose the diatomic are (x_4, x_5, x_6) and (x_7, x_8, x_9), the transformation to Jacobi coordinates [Eq. (4.43)] can be written in matrix form, facilitating inversion and manipulation. Setting the 9 Cartesian coordinates in a column vector

and the 9 Jacobi coordinates in another, it is obtained:

$$\begin{pmatrix} q_1 \\ q_2 \\ q_3 \\ Q_1 \\ Q_2 \\ Q_3 \\ S_1 \\ S_2 \\ S_3 \end{pmatrix} = \begin{pmatrix} 0 & 0 & 0 & -1 & 0 & 0 & 1 & 0 & 0 \\ 0 & 0 & 0 & 0 & -1 & 0 & 0 & 1 & 0 \\ 0 & 0 & 0 & 0 & 0 & -1 & 0 & 0 & 1 \\ 1 & 0 & 0 & -\frac{m_B}{m_{BC}} & 0 & 0 & -\frac{m_C}{m_{BC}} & 0 & 0 \\ 0 & 1 & 0 & 0 & -\frac{m_B}{m_{BC}} & 0 & 0 & -\frac{m_C}{m_{BC}} & 0 \\ 0 & 0 & 1 & 0 & 0 & -\frac{m_B}{m_{BC}} & 0 & 0 & -\frac{m_C}{m_{BC}} \\ \frac{m_A}{m_{ABC}} & 0 & 0 & \frac{m_B}{m_{ABC}} & 0 & 0 & \frac{m_C}{m_{ABC}} & 0 & 0 \\ 0 & \frac{m_A}{m_{ABC}} & 0 & 0 & \frac{m_B}{m_{ABC}} & 0 & 0 & \frac{m_C}{m_{ABC}} & 0 \\ 0 & 0 & \frac{m_A}{m_{ABC}} & 0 & 0 & \frac{m_B}{m_{ABC}} & 0 & 0 & \frac{m_C}{m_{ABC}} \end{pmatrix} \begin{pmatrix} x_1 \\ x_2 \\ x_3 \\ x_4 \\ x_5 \\ x_6 \\ x_7 \\ x_8 \\ x_9 \end{pmatrix} \tag{B.1}$$

where m_{BC} and m_{ABC} denote the mass of the diatom ($m_B + m_C$) and the mass of the whole system, respectively. Using the Gauss-Jordan elimination method, the inverse transformation is obtained as:

$$\begin{pmatrix} x_1 \\ x_2 \\ x_3 \\ x_4 \\ x_5 \\ x_6 \\ x_7 \\ x_8 \\ x_9 \end{pmatrix} = \begin{pmatrix} 0 & 0 & 0 & \frac{m_{BC}}{m_{ABC}} & 0 & 0 & 1 & 0 & 0 \\ 0 & 0 & 0 & 0 & \frac{m_{BC}}{m_{ABC}} & 0 & 0 & 1 & 0 \\ 0 & 0 & 0 & 0 & 0 & \frac{m_{BC}}{m_{ABC}} & 0 & 0 & 1 \\ -\frac{m_C}{m_{BC}} & 0 & 0 & -\frac{m_A}{m_{ABC}} & 0 & 0 & 1 & 0 & 0 \\ 0 & -\frac{m_C}{m_{BC}} & 0 & 0 & -\frac{m_A}{m_{ABC}} & 0 & 0 & 1 & 0 \\ 0 & 0 & -\frac{m_C}{m_{BC}} & 0 & 0 & -\frac{m_A}{m_{ABC}} & 0 & 0 & 1 \\ \frac{m_B}{m_{BC}} & 0 & 0 & -\frac{m_A}{m_{ABC}} & 0 & 0 & 1 & 0 & 0 \\ 0 & \frac{m_B}{m_{BC}} & 0 & 0 & -\frac{m_A}{m_{ABC}} & 0 & 0 & 1 & 0 \\ 0 & 0 & \frac{m_B}{m_{BC}} & 0 & 0 & -\frac{m_A}{m_{ABC}} & 0 & 0 & 1 \end{pmatrix} \begin{pmatrix} q_1 \\ q_2 \\ q_3 \\ Q_1 \\ Q_2 \\ Q_3 \\ S_1 \\ S_2 \\ S_3 \end{pmatrix} \tag{B.2}$$

The generalized momentum of: the diatom BC (**p**), the A+BC relative motion (**P**) and that of the center of mass ($\mathbf{P}_S$); can be obtained by a canonical transformation. Employing the F_2-type generator function[2–4]:

$$F_2(\mathbf{p}, \mathbf{P}, \mathbf{P}_s, \mathbf{q}, \mathbf{Q}, \mathbf{S}) = \sum_{j=1}^{3} \left[p_j q_j(\mathbf{x}) + P_j Q_j(\mathbf{x}) + P_{S_j} S_j(\mathbf{x}) \right] \tag{B.3}$$

the equations that relate the momenta in Cartesian coordinates with the generalized

Jacobi momenta are given by

$$\begin{aligned} p_{x_i} &= \partial F_2/\partial x_i \qquad\qquad (i = 1, \ldots, 9) \\ p_{x_i} &= \sum_{j=1}^{3} \left[p_j \frac{\partial q_j(\mathbf{x})}{\partial x_i} + P_j \frac{\partial Q_j(\mathbf{x})}{\partial x_i} + P_{S_j} \frac{\partial S_j(\mathbf{x})}{\partial x_i} \right] \end{aligned} \tag{B.4}$$

and the problem of obtaining the relation between these two sets is reduced to the solution of the above 9 equations. The result in matrix form is given by:

$$\begin{pmatrix} p_{x_1} \\ p_{x_2} \\ p_{x_3} \\ p_{x_4} \\ p_{x_5} \\ p_{x_6} \\ p_{x_7} \\ p_{x_8} \\ p_{x_9} \end{pmatrix} = \begin{pmatrix} 0 & 0 & 0 & 1 & 0 & 0 & \frac{m_{\mathrm{A}}}{m_{\mathrm{ABC}}} & 0 & 0 \\ 0 & 0 & 0 & 0 & 1 & 0 & 0 & \frac{m_{\mathrm{A}}}{m_{\mathrm{ABC}}} & 0 \\ 0 & 0 & 0 & 0 & 0 & 1 & 0 & 0 & \frac{m_{\mathrm{A}}}{m_{\mathrm{ABC}}} \\ -1 & 0 & 0 & -\frac{m_{\mathrm{B}}}{m_{\mathrm{BC}}} & 0 & 0 & \frac{m_{\mathrm{B}}}{m_{\mathrm{ABC}}} & 0 & 0 \\ 0 & -1 & 0 & 0 & -\frac{m_{\mathrm{B}}}{m_{\mathrm{BC}}} & 0 & 0 & \frac{m_{\mathrm{B}}}{m_{\mathrm{ABC}}} & 0 \\ 0 & 0 & -1 & 0 & 0 & -\frac{m_{\mathrm{B}}}{m_{\mathrm{BC}}} & 0 & 0 & \frac{m_{\mathrm{B}}}{m_{\mathrm{ABC}}} \\ 1 & 0 & 0 & -\frac{m_{\mathrm{C}}}{m_{\mathrm{BC}}} & 0 & 0 & \frac{m_{\mathrm{C}}}{m_{\mathrm{ABC}}} & 0 & 0 \\ 0 & 1 & 0 & 0 & -\frac{m_{\mathrm{C}}}{m_{\mathrm{BC}}} & 0 & 0 & \frac{m_{\mathrm{C}}}{m_{\mathrm{ABC}}} & 0 \\ 0 & 0 & 1 & 0 & 0 & -\frac{m_{\mathrm{C}}}{m_{\mathrm{BC}}} & 0 & 0 & \frac{m_{\mathrm{C}}}{m_{\mathrm{ABC}}} \end{pmatrix} \begin{pmatrix} p_1 \\ p_2 \\ p_3 \\ P_1 \\ P_2 \\ P_3 \\ P_{S_1} \\ P_{S_2} \\ P_{S_3} \end{pmatrix} \tag{B.5}$$

The Hamiltonian in the generalized coordinates is obtained by substituting the above expressions on Eq. (4.41), giving:

$$H(\mathbf{q}, \mathbf{Q}, \mathbf{p}, \mathbf{P}, \mathbf{P}_S) = \sum_{i=1}^{3} \left[\frac{p_i^2}{2\mu_{BC}} + \frac{P_i^2}{2\mu_{A,BC}} + \frac{P_{S_i}^2}{2M_{ABC}} \right] + V\left(\mathbf{q}, \mathbf{Q}\right) \tag{B.6}$$

where the reduced masses corresponding to the relative motion are $\mu_{BC} = m_B m_C / m_{BC}$ and $\mu_{A,BC} = m_A m_{BC} / m_{ABC}$. As can be seen, this Hamiltonian does not depend on the three coordinates of the center of mass, thus reducing the number of Hamilton's equations. While it is true that it still depends on the momenta of the center of mass (by its kinetic energy), one can define the coordinate system to move with the uniform motion of the center of mass without loss of generality, and therefore forget about the three Hamilton's

equations concerning P_{S_1}, P_{S_1} and P_{S_3}. The resulting equations of motion are:

$$\begin{aligned}
\frac{dq_i}{dt} &= \frac{\partial H}{\partial p_i} = \frac{\partial T}{\partial p_i} && (i = 1,2,3)\\
\frac{dQ_i}{dt} &= \frac{\partial H}{\partial P_i} = \frac{\partial T}{\partial P_i} && (i = 1,2,3)\\
\frac{dp_i}{dt} &= -\frac{\partial H}{\partial q_i} = -\frac{\partial V}{\partial q_i} = \sum_{k=1}^{3} -\frac{\partial V}{\partial R_k}\frac{\partial R_k}{\partial q_i} && (i = 1,2,3)\\
\frac{dP_i}{dt} &= -\frac{\partial H}{\partial Q_i} = -\frac{\partial V}{\partial Q_i} = \sum_{k=1}^{3} -\frac{\partial V}{\partial R_k}\frac{\partial R_k}{\partial Q_i} && (i = 1,2,3)
\end{aligned} \tag{B.7}$$

For completeness, the transformation of the momenta back to Cartesian coordinates is obtained using the Gauss-Jordan elimination method, giving

$$\begin{pmatrix} p_1 \\ p_2 \\ p_3 \\ P_1 \\ P_2 \\ P_3 \\ P_{S_1} \\ P_{S_2} \\ P_{S_3} \end{pmatrix} = \begin{pmatrix} 0 & 0 & 0 & -\frac{m_C}{m_{BC}} & 0 & 0 & \frac{m_B}{m_{BC}} & 0 & 0 \\ 0 & 0 & 0 & 0 & -\frac{m_C}{m_{BC}} & 0 & 0 & \frac{m_B}{m_{BC}} & 0 \\ 0 & 0 & 0 & 0 & 0 & -\frac{m_C}{m_{BC}} & 0 & 0 & \frac{m_B}{m_{BC}} \\ \frac{m_{BC}}{m_{ABC}} & 0 & 0 & -\frac{m_A}{m_{ABC}} & 0 & 0 & -\frac{m_A}{m_{ABC}} & 0 & 0 \\ 0 & \frac{m_{BC}}{m_{ABC}} & 0 & 0 & -\frac{m_A}{m_{ABC}} & 0 & 0 & -\frac{m_A}{m_{ABC}} & 0 \\ 0 & 0 & \frac{m_{BC}}{m_{ABC}} & 0 & 0 & -\frac{m_A}{m_{ABC}} & 0 & 0 & -\frac{m_A}{m_{ABC}} \\ 1 & 0 & 0 & 1 & 0 & 0 & 1 & 0 & 0 \\ 0 & 1 & 0 & 0 & 1 & 0 & 0 & 1 & 0 \\ 0 & 0 & 1 & 0 & 0 & 1 & 0 & 0 & 1 \end{pmatrix} \begin{pmatrix} p_{x_1} \\ p_{x_2} \\ p_{x_3} \\ p_{x_4} \\ p_{x_5} \\ p_{x_6} \\ p_{x_7} \\ p_{x_8} \\ p_{x_9} \end{pmatrix} \tag{B.8}$$

Bibliography

[1] W. H. Press, S. A. Teukolsky, W. T. Vetterling, and B. P. Flannery, *Numerical Recipes in Fortran: the Art of Scientific Computing* (Cambridge University Press, New York, 1992).

[2] H. Goldstein, *Classical Mechanics* (Addison-Wesley, Reading, 1980).

[3] D. G. Truhlar and J. T. Muckerman, in *Atom-Molecule Collision Theory*, edited by R. Bernstein (Plenum, New York, 1981), p. 505.

[4] M. Karplus, R. N. Porter, and R. D. Sharma, J. Chem. Phys. **43**, 3259 (1965).

Part II

Publications

Energy-switching potential energy surface for the water molecule revisited: A highly accurate singled-sheeted form

B. R. L. Galvão, S. P. J. Rodrigues, and A. J. C. Varandas[a)]
Departamento de Química, Universidade de Coimbra, 3004-535 Coimbra, Portugal

(Received 24 April 2008; accepted 11 June 2008; published online 22 July 2008)

A global *ab initio* potential energy surface is proposed for the water molecule by energy-switching/merging a highly accurate isotope-dependent local potential function reported by Polyansky *et al.* [Science **299**, 539 (2003)] with a global form of the many-body expansion type suitably adapted to account explicitly for the dynamical correlation and parametrized from extensive accurate multireference configuration interaction energies extrapolated to the complete basis set limit. The new function mimics also the complicated Σ/Π crossing that arises at linear geometries of the water molecule. © *2008 American Institute of Physics*. [DOI: 10.1063/1.2953580]

I. INTRODUCTION

The energy-switching[1] (ES) approach aims at providing the accuracy of a local spectroscopically determined polynomial to a global form fitted to *ab initio* energies and/or other information, by switching from one to the other along the energy coordinate. The method has been successfully applied to the potential energy surfaces (PESs) of triatomic and tetratomic molecules including multisheeted ones, having originated some of the most accurate global forms reported thus far for those systems.[1–6]

Recently, extensive *ab initio* calculations capable of achieving near-spectroscopic accuracy have been reported for the ground state ($\bar{X}\,^1A'$) of the water molecule[7,8] (see also Ref. 9 for one of the first PESs that achieved accuracy in the few cm^{-1} range in the immediate neighborhood of the equilibrium geometry). In that work,[7,8] the calculated *ab initio* energies were extrapolated to the complete basis set limit with standard schemes[10,11] and corrections added to account for small energy contributions. These include core correlation,[12] first-order perturbation theory one-electron mass velocity and Darwin term, first-order perturbation theory two-electron contribution to the Darwin term, Breit interaction, one-electron Lamb shift, and the diagonal Born–Oppenheimer correction. The calculated energies, which cover regions up to 25 000 cm^{-1} above the minimum of the potential well, have further been fitted to different and independent functional forms. The isotope-dependent local PES so obtained by summing all such contributions has been named[7,8] as CVRQD, a notation that we keep hereinafter.

As noted above, the CVRQD form is valid for energies up to 25 000 cm^{-1}, and hence cannot be generally used for dynamics studies, particularly those for the reaction $O(^1D)+H_2(X\,^1\Sigma_g^+)\rightarrow OH(X\,^2\Pi)+H(^2S)$. In the present work, we propose to extend its domain of validity by making it reproduce the correct behavior over the whole configuration space of the molecule. This will be achieved by merging the local CVRQD form with a global PES of the many-body expansion[13] (MBE) type [suitably upgraded to explicitly include the dynamical correlation (DC) as in double MBE (Refs. 14 and 15) theory, and hence termed MBE/DC] via the ES (Ref. 1) scheme.

In the new PES, dubbed ES-1v-II to recognize its single-sheeted (1v) nature and the fact that it upgrades a previous form[1] of the same family (here denoted as ES-1v-I), the CVRQD potential will contribute with an accurate *ab initio* behavior for regions of the potential well up to about 25 000 cm^{-1} and will be continued at higher energies by the MBE/DC global PES. This differs from previous work[1] in that it has been suitably modified to show the proper behavior at the locus of the Σ/Π conical intersection arising for collinear geometries and remove small unphysical features (e.g., for the H atom attack to OH at small valence angles). For this purpose, we have utilized local Gaussian-type three-body terms calibrated such as to reproduce the differences between the original MBE/DC PES and an extensive set of *ab initio* energies calculated anew in the present work using the internally contracted multireference configuration interaction method with the popular quasidegenerate Davidson correction for quadruple excitations [MRCI(Q)]. Such energies have been further extrapolated to the complete one electron basis set (CBS) limit by using the hybrid correlation scaling (CS) uniform singlet- and triplet-pair extrapolation[16] (USTE) method with a single pivotal geometry for the CS [denoted $CS^1/USTE(T,Q)$].

The paper is organized as follows. Section II provides a description of the CS/extrapolation of the *ab initio* energies, while Sec. III gives the details of the corrections made in the original global MBE/DC potential function. In turn, Sec. IV summarizes the ES procedure, and Sec. V the main results and features of the new PES. Some conclusions are in Sec. VI.

II. *AB INITIO* CALCULATIONS AND EXTRAPOLATION SCHEME

In this work, we have used an extrapolation scheme[16] that allows the prediction of *ab initio* energies at the CBS

[a)]Author to whom correspondence should be addressed. Electronic mail: varandas@qtvs1.qui.uc.pt.

TABLE I. Fitted coefficients of Gaussian part of Eq. (6).

i	b_{i1}/a_0^{-2}	R_{i1}^0/a_0	b_{i2}/a_0^{-2}	R_{i2}^0/a_0	b_{i3}/a_0^{-2}	R_{i3}^0/a_0
1	0.264 191 17	2.159 076 70	0.264 191 17	2.159 076 70	1.425 853 30	0.908 987 45
2	1.090 382 80	2.100 329 80	0.973 006 41	1.033 660 30	1.811 609 70	1.224 764 00
4	0.816 481 21	1.649 841 40	0.816 481 21	1.649 841 40	1.618 454 60	0.912 500 77
5	0.148 955 79	−0.028 404 82	0.148 955 79	−0.028 404 82	1.787 999 10	1.098 454 40
6	0.009 842 28	−5.620 763 80	0.498 718 98	2.482 977 10	3.351 300 30	2.163 604 50
8	0.136 237 09	−0.097 815 45	0.278 564 27	0.568 552 81	1.823 974 80	1.121 564 30
10	0.389 745 73	1.761 554 70	2.622 919 70	1.609 231 00	0.635 580 70	1.054 538 20
12	0.534 009 97	1.442 590 60	1.380 052 90	1.722 220 10	1.566 585 80	0.957 656 23
14	0.742 299 94	2.876 212 60	0.010 239 77	9.306 752 50	0.825 963 35	4.570 817 20
16	0.737 052 86	2.580 001 60	0.103 676 89	2.079 570 20	0.813 123 50	3.526 564 30
18	0.944 074 13	0.071 254 70	2.369 776 80	2.137 895 60	0.395 001 15	8.706 489 20
20	0.167 354 19	0.080 049 53	0.529 168 06	1.200 917 30	0.714 090 80	5.662 203 00
22	0.643 422 26	2.001 109 90	0.827 094 16	1.365 643 50	0.730 760 10	5.278 494 30
24	1.145 802 40	1.620 316 10	0.764 130 56	1.689 270 80	0.839 685 53	5.067 419 90
26	0.730 698 71	2.851 697 90	0.084 891 12	4.614 987 00	0.526 748 74	4.472 527 20
28	0.213 175 74	1.846 039 20	0.711 557 58	1.221 829 90	0.784 410 99	5.682 441 60
30	0.891 998 02	2.836 271 20	0.107 613 26	0.173 192 89	0.759 870 71	5.191 141 50
32	0.703 119 70	2.139 430 00	0.357 407 07	1.282 616 20	0.240 451 27	5.600 313 90
34	8.440 049 90	1.466 400 00	33.057 822 00	3.188 377 90	15.246 358 00	4.666 400 00
36	3.565 438 30	2.379 094 70	20.105 490 00	3.623 022 50	0.469 805 00	6.594 463 00

limit by using small basis sets of the aug-cc-pCVXZ (Ref. 17) (abbreviated ACVXZ) family. The raw energies have been computed by using the MRCI(Q) (Refs. 18 and 19) method as implemented in the MOLPRO (Ref. 20) suite of programs for electronic structure calculations.

The CS^1/USTE(T,Q) method involves six basic steps:[16] (a) calculation of the PES as a grid of MRCI(Q) energies with both the $X-2$ and $X-1$ basis sets, followed by similar calculations for some prechosen geometries (pivots) with the target basis set of cardinal number X (here chosen as $X=Q:4$); (b) calculation for all considered geometries of the PES at the reference complete-active-space (CAS) level with the target basis set; (c) extrapolation to the CBS limit (i.e., $X=\infty$) of the CAS PES; (d) prediction by extrapolation to $X=\infty$ of the DC energy at the pivots by using the USTE (Ref. 21) method; (e) prediction of the CBS DC energies of the remaining points by CS (Ref. 22) using the $X=D,T$ and CBS DC energies at the pivots; (f) calculation of the full CBS PES by adding the CAS/CBS and extrapolated DC energies from step (c) and (d) and (e).

The extrapolation in step (c) of the raw CAS energies has been performed with the two-point extrapolation protocol proposed by Karton and Martin,[23]

$$E_X^{\mathrm{CAS}}(\mathbf{R}) = E_\infty^{\mathrm{CAS}}(\mathbf{R}) + B/X^{5.34}, \tag{1}$$

where $\mathbf{R}$ specifies the three-dimensional vector of space coordinates. Recall that these extrapolations (as well as those reported in the following paragraph) are carried pointwise, with E_∞^{CAS} and B being parameters determined from a fit to the raw CAS energies calculated with the TZ and QZ basis sets.

Similarly, the USTE extrapolation needed in step (d) assumes the form[21]

$$E_X = E_\infty + A_3/(X+\alpha)^3 + [A_5(0) + cA_3^{5/4}]/(X+\alpha)^5, \tag{2}$$

where $A_5(0)=0.003\,768\,545\,9E_h$ and $c=-1.178\,477\,13E_h^{-1/4}$, with $\alpha=-3.0/8.0$. Note that the CBS extrapolated DC energies are obtained using a twofold scheme. First, the correlation energies at the pivotal geometries are CBS extrapolated by using Eq. (2) with the (T,Q) pair of calculated raw values. Then, the correlation energies at the remaining geometries are obtained by using the CS method which, for a single pivotal geometry, assumes the form[22]

$$\Delta E_\infty^{\mathrm{dc}}(\mathbf{R}) = \chi_{\infty,3}(\mathbf{R})\Delta E_3^{\mathrm{dc}}(\mathbf{R}), \tag{3}$$

where $\Delta E^{\mathrm{dc}}=E-E^{\mathrm{CAS}}$ stands for the DC energy, and the basis sets are indicated by the cardinal numbers in subscript (note that the CBS limit corresponds to $X=\infty$); E stands for the total MRCI(Q) energy. In turn, the scaling function χ assumes the form

$$\chi_{\infty,3}(\mathbf{R}) = 1 + \frac{S_{3,2}(\mathbf{R})-1}{S_{3,2}(\mathbf{R}_e)-1}[S_{\infty,3}(\mathbf{R}_e)-1], \tag{4}$$

where $\mathbf{R}_e$ indicates the pivotal geometry, and

$$S_{m,n}(\mathbf{R}) = \frac{\Delta E_m^{\mathrm{dc}}(\mathbf{R})}{\Delta E_n^{\mathrm{dc}}(\mathbf{R})}. \tag{5}$$

Thus, CBS extrapolation via Eq. (3) utilizes the correlation energies calculated with the $X=D:2$ and $X=T:3$ basis sets using a single pivotal geometry at which the correlation energy has also been calculated with the $X=Q:4$ basis set; for further details, we address the reader to the original paper.[16] Suffice it to say here that the reference geometry ($\mathbf{R}_e$) can be any point of the PES. For the present work, we have chosen a configuration with an intermediate energy which, in Jacobi coordinates, is defined by $R_{\mathrm{HH}}=1.25R_m$, $r=1.0$ Å (this is the distance from the oxygen atom to the center of mass of the hydrogen molecule), and $\alpha=90°$; R_m is the distance of H_2 at

TABLE II. Fitted coefficients in polynomials of Eq. (8) (in atomic units).

i	c_{i0}	c_{i1}	c_{i2}	c_{i3}	c_{i4}	c_{i5}	c_{i6}	c_{i7}
1	$0.321\,323\,02\times10^{+1}$	$-0.563\,516\,21\times10^{+0}$	$0.148\,042\,72\times10^{+1}$	⋯	$-0.954\,564\,42\times10^{+0}$	$0.804\,429\,06\times10^{-1}$	⋯	⋯
2, 3	$0.119\,140\,16\times10^{+1}$	$-0.123\,836\,04\times10^{+1}$	$-0.289\,292\,00\times10^{+1}$	⋯	⋯	⋯	$0.517\,308\,59\times10^{-1}$	$-0.525\,811\,65\times10^{+1}$
4	$0.773\,371\,39\times10^{+1}$	$0.492\,603\,84\times10^{+1}$	⋯	⋯	$-0.278\,996\,08\times10^{+1}$	$0.359\,321\,04\times10^{+0}$	⋯	⋯
5	$-0.184\,580\,13\times10^{+1}$	$0.152\,629\,12\times10^{+2}$	$-0.483\,212\,28\times10^{+2}$	⋯	⋯	⋯	$0.198\,371\,72\times10^{+1}$	⋯
6, 7	$0.129\,412\,53\times10^{-1}$	$-0.281\,087\,44\times10^{-1}$	$0.144\,561\,02\times10^{-2}$	⋯	⋯	⋯	$0.195\,935\,53\times10^{-1}$	⋯
8, 9	$-0.199\,767\,76\times10^{+0}$	$-0.593\,087\,80\times10^{+1}$	$0.214\,904\,96\times10^{+2}$	$0.560\,624\,52\times10^{+0}$	⋯	⋯	⋯	⋯
10, 11	$0.206\,658\,04\times10^{-1}$	$0.231\,953\,77\times10^{+0}$	$-0.943\,679\,68\times10^{-1}$	⋯	⋯	⋯	$-0.133\,519\,26\times10^{-1}$	$0.110\,550\,59\times10^{+0}$
12, 13	$-0.202\,659\,83\times10^{+1}$	$-0.277\,197\,58\times10^{+1}$	$-0.237\,054\,35\times10^{-1}$	⋯	⋯	⋯	$-0.738\,506\,73\times10^{+0}$	$0.500\,806\,88\times10^{-2}$
14, 15	$0.390\,876\,62\times10^{+1}$	$0.725\,150\,66\times10^{-3}$	$0.275\,549\,18\times10^{-3}$	$0.505\,124\,25\times10^{-5}$	$-0.791\,568\,58\times10^{+0}$	$0.417\,745\,85\times10^{-1}$	⋯	⋯
16, 17	$0.208\,587\,72\times10^{+1}$	$0.398\,890\,77\times10^{-1}$	$0.884\,058\,11\times10^{-3}$	$0.211\,650\,38\times10^{-3}$	$-0.693\,356\,49\times10^{+0}$	$0.705\,124\,90\times10^{-1}$	⋯	⋯
18, 19	$0.398\,948\,21\times10^{+5}$	$-0.403\,471\,69\times10^{+3}$	$-0.555\,340\,39\times10^{+3}$	$0.501\,934\,52\times10^{+2}$	⋯	⋯	$-0.207\,408\,64\times10^{+5}$	⋯
20, 21	$-0.123\,452\,65\times10^{+3}$	$0.119\,989\,75\times10^{+1}$	$-0.482\,849\,92\times10^{+0}$	⋯	$0.344\,628\,14\times10^{+2}$	$-0.193\,896\,94\times10^{+1}$	⋯	⋯
22, 23	$0.563\,186\,65\times10^{+2}$	$0.603\,062\,76\times10^{+0}$	$-0.356\,493\,17\times10^{+0}$	⋯	$-0.937\,159\,63\times10^{+1}$	$0.247\,131\,06\times10^{+0}$	⋯	⋯
24, 25	$-0.258\,805\,03\times10^{+2}$	$-0.523\,963\,75\times10^{+1}$	$-0.500\,303\,50\times10^{+0}$	⋯	$0.623\,658\,83\times10^{+1}$	$-0.613\,389\,51\times10^{+0}$	⋯	⋯
26, 27	$-0.403\,871\,65\times10^{+1}$	$-0.312\,129\,36\times10^{-1}$	$0.105\,849\,14\times10^{-2}$	⋯	$0.767\,655\,51\times10^{+0}$	$-0.362\,832\,17\times10^{-1}$	⋯	⋯
28, 29	$0.133\,040\,18\times10^{+2}$	$0.388\,677\,91\times10^{+0}$	$0.237\,721\,55\times10^{-1}$	⋯	$-0.420\,240\,58\times10^{+1}$	$0.235\,056\,18\times10^{+0}$	⋯	⋯
30, 31	$-0.754\,331\,58\times10^{+0}$	$0.122\,891\,73\times10^{+0}$	$0.468\,010\,26\times10^{-1}$	⋯	⋯	⋯	$0.107\,878\,66\times10^{+1}$	$-0.458\,176\,18\times10^{+0}$
32, 33	$-0.169\,864\,89\times10^{+1}$	$-0.367\,596\,56\times10^{+0}$	$-0.402\,319\,22\times10^{-1}$	⋯	$-0.699\,905\,87\times10^{-1}$	$0.205\,659\,93\times10^{-1}$	⋯	⋯
34, 35	$0.407\,811\,28\times10^{+0}$	$-0.661\,261\,08\times10^{-1}$	$0.261\,912\,96\times10^{-1}$	⋯	⋯	⋯	$-0.397\,734\,71\times10^{+0}$	$0.104\,630\,61\times10^{+0}$
36, 37	$-0.467\,947\,99\times10^{-1}$	$0.464\,850\,39\times10^{-2}$	$-0.387\,827\,22\times10^{-2}$	⋯	⋯	⋯	$0.509\,202\,46\times10^{-1}$	$-0.133\,278\,79\times10^{-1}$

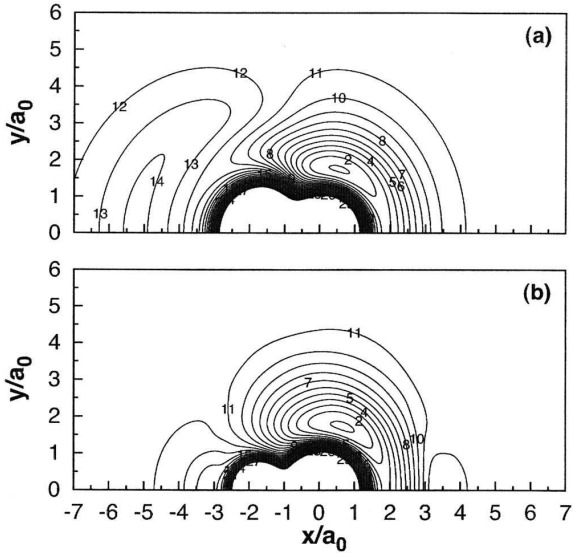

FIG. 1. Contours for a H atom moving around an equilibrium OH diatomic (R_e=1.8344a_0) which lies along the x axis with the center of mass fixed at the origin and the H atom located in the negative x-axis side: (a) MBE/DC I; (b) MBE/DC II. Contours start at $-0.3675E_h$ at intervals of $0.018\,375E_h$. In this and all subsequent plots, the zero of energy corresponds to the three separated atoms, with the equilibrium well depth being $D_e=-0.370\,065E_h$.

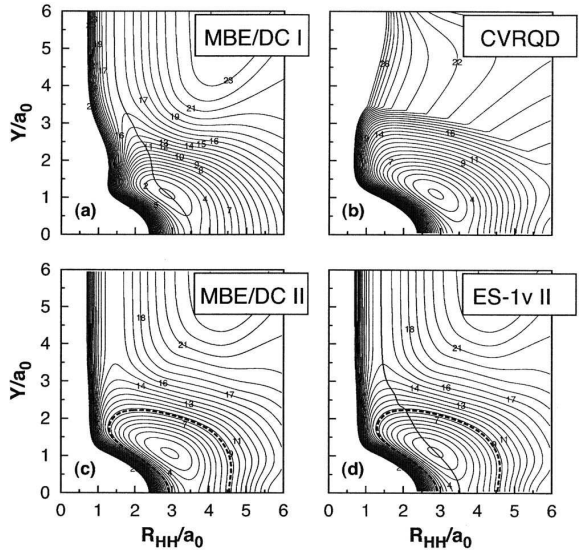

FIG. 2. Contours for a C_{2v} insertion of O into H_2. Contours start at $-0.3675E_h$ at intervals of $0.018\,375E_h$. The dashed line corresponds to the E_0 energy and the solid line to the minimum energy path.

its minimum potential energy (R_m=0.741 Å). The above extrapolation scheme can yield accurate potentials at costs as low as virtually possible.[16] Its accuracy has thus far been tested on diatomic molecules through vibrational calculations which provide a severe test of the approach, with very good results being generally observed.[16]

III. IMPROVING THE MBE/DC PES

The MBE/DC PES utilized elsewhere[1] has here been corrected by calculating its difference to the CBS extrapolated *ab initio* energies at the grid of points to be specified later. The energy differences so obtained have then been fitted to the general form

$$G^{(3)}(\mathbf{R}) = \sum_{i=1}^{37} P_i(\mathbf{R}) \exp\left[-\sum_{j=1}^{3} b_{ij}(R_j - R_{ij}^0)^2 \right], \tag{6}$$

where the summation runs over the index i that identifies the various Gaussian forms (each multiplied by a polynomial form in the three interatomic coordinates: $j=1,2,3$). Note

TABLE III. Parameters used for the energy switching.

E_0/cm^{-1}	31 200
γ_0/E_h^{-1}	22
γ_1/E_h^{-3}	2.5×10^5
m	2
A/mE_h	0.01
a_1	2.5
a_3	2.5
δ/a_0	18.0

that these polynomials have been written in terms of D_{3h} symmetry coordinates,

$$\begin{pmatrix} Q_1 \\ Q_2 \\ Q_3 \end{pmatrix} = \begin{pmatrix} \sqrt{1/3} & \sqrt{1/3} & \sqrt{1/3} \\ 0 & \sqrt{1/2} & -\sqrt{1/2} \\ \sqrt{2/3} & -\sqrt{1/6} & -\sqrt{1/6} \end{pmatrix} \begin{pmatrix} R_3 \\ R_2 \\ R_1 \end{pmatrix}, \tag{7}$$

where R_1 and R_2 are OH bond distances and R_3 is the HH one. For the ith polynomial in the first summation of Eq. (6), we have chosen the general form

$$P_i(\mathbf{R}) = c_{i0} + c_{i1}Q_2^2 + c_{i2}Q_2^4 + c_{i3}Q_2^6 + c_{i4}Q_1 + c_{i5}Q_1^2 + c_{i6}Q_3 + c_{i7}Q_3^2. \tag{8}$$

To warrant the proper symmetry in a permutation of R_1 and R_2, no odd powers of the variable Q_2 can be utilized in constructing the polynomials. Regarding the Gaussian decaying terms, the above symmetry requirement can be satisfied either by employing a single Gaussian with $R_{i1}^0=R_{i2}^0$ (and hence $b_{i1}=b_{i2}$) centered at a geometry with C_{2v} symmetry or a Gaussian function centered at an arbitrary geometry of C_s symmetry ($R_{i,1}^0 \neq R_{i,2}^0$) but accompanied by an $(i+1)$th pair located at a geometry with the distances R_1 and R_2 reversed,

$$G_i(\mathbf{R}) = P_i(\mathbf{R})\{\exp[-b_{i1}(R_1 - R_{i1}^0)^2 - b_{i2}(R_2 - R_{i2}^0)^2 - b_{i3}(R_3 - R_{i3}^0)^2]\}, \tag{9}$$

$$G_{i+1}(\mathbf{R}) = P_i(\mathbf{R})\{\exp[-b_{i1}(R_2 - R_{i1}^0)^2 - b_{i2}(R_1 - R_{i2}^0)^2 - b_{i3}(R_3 - R_{i3}^0)^2]\}. \tag{10}$$

Thus, whenever a nonsymmetrical reference geometry is indicated in Table I, a summation over a Gaussian pair is implied. For example, since the ordering index $i=3$ is missing in Table I, a pair of terms for $i=2,3$ must be included as implied by Eqs. (9) and (10).

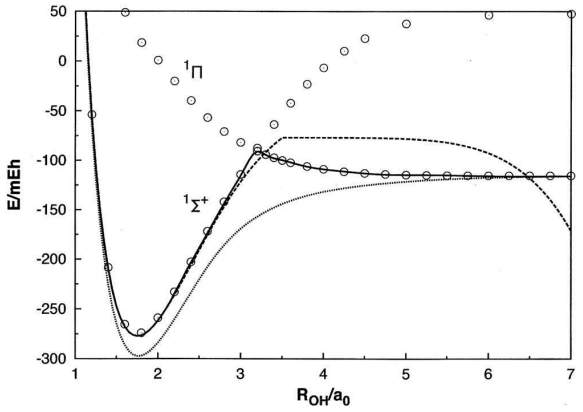

FIG. 3. Cut of the water PES for H attacking OH fixed at $R_{OH}=1.4664a_0$ with a valence angle of 180°. The solid line shows the ES-1v-II PES, while the CVRQD and MBE/DC I results are indicated by the dashed and dotted lines, respectively. The points show the extrapolated *ab initio* energies for the ground and excited states.

The fitting procedure has been carried out using the Levenberg–Marquardt method.[24] The above function, which has 212 adjustable parameters, including the polynomial and Gaussian coefficients (Tables I and II), has been fitted to a total of 2375 *ab initio* points covering the regions defined by (a) $1.4<R_{HO}/a_0<3.0$, $1<r_{HO-H}/a_0<15$, and $0°<\alpha<180°$; (b) $1<R_{H_2}/a_0<2.1$, $1<r_{O-H_2}/a_0<20$, and $0°<\alpha<90°$ (R, r, and α are the atom-diatom Jacobi coordinates). A final global root mean square deviation of $0.482mE_h$ has been obtained. The original[1] and new surfaces will be referred to onward as MBE/DC I and MBE/DC II, respectively.

An example of the correction described above is shown for the H+OH reaction channel in Fig. 1 where a cut corresponding to a H atom moving around an equilibrium OH molecule is depicted for both the MBE/DC I and MBE/ DC II PESs. As seen, the MBE/DC I PES shows an unphysical barrier for the H atom attacking at small valence angles, which grows as the angle approaches zero. This feature is now corrected in MBE/DC II which mimics accurately the behavior predicted by the CBS extrapolated MRCI(Q) energies. Also shown in this plot is a cusp in the new PES that arises as the valence angle approaches 180° due to the crossing of the Σ and Π states for linear HOH geometries. This feature also mimics accurately the one observed at CBS extrapolated MRCI(Q) level.

IV. APPLICATION OF ES METHODOLOGY

Following the ES (Ref. 1) method, we will label the spectroscopically accurate CVRQD form as V_2, and call V_1 to the global MBE/DC II function. They are energy switched/merged in the global PES V_{ES} by writing

$$V_{ES}=f(\Delta E)V_1(\mathbf{R})+[1-f(\Delta E)]V_2(\mathbf{R}), \tag{11}$$

where $\Delta E=E-E_0$ is the displacement from some reference energy and $f(\Delta E)$ is a switching function that approaches 0 for large negative energy displacements and +1 for large positive ones, chosen as[1]

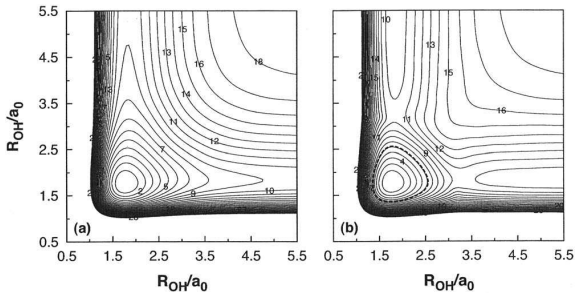

FIG. 4. Contours for bond stretching of linear HOH. Contours start at $-0.32E_h$ with intervals of $0.018E_h$. (a) MBE/DC I; (b) ES-1v-II. Indicated by the dashed line is the contour corresponding to the reference switching energy E_0.

$$f=\tfrac{1}{2}\{1+\tanh[(\gamma_0+\gamma_1\Delta E^m)\Delta E]\}. \tag{12}$$

Not surprisingly the switching occurs smoothly without leaving any scars of the merging, which reflects the excellent compatibility of the two merged potentials. As the CVRQD form is isotope dependent and the MBE/DC II is not, the approach can be applied in the same manner for the different isotopologue potentials provided in the CVRQD work.[7,8] Although the global PES (V_1) is mass independent, we believe that this will have no effect on the spectroscopic studies that will be carried out on V_{ES} in the following section. In fact, mass effects are expected to be very small and only significant for regions of the PES with relevance for spectroscopic calculations, where MBE/DC II has clearly a very small contribution to the ES PES (ES-1v-II).

When applying the ES scheme, one needs do define the variable E to measure the displacement from the reference energy E_0 in Eq. (11) as a function that grows uniformly from the bottom of the potential well.[1] This function could in principle be chosen as V_2, the PES that describes the well. However, since this function is not well behaved for large displacements from equilibrium, it cannot be used directly. This is the case for the CVRQD potential, which shows spurious minima for largely stretched structures, and hence the use of $\Delta E=V_2-E_0$ would enhance the development of artifacts in the ES PES. To circumvent this problem, the displacement from the reference energy will be written as

$$\Delta E=V_2+\phi(\mathbf{R})-E_0, \tag{13}$$

where $\phi(\mathbf{R})$ is a correction term that prevents the nonuniform growing of the CVRQD function. It assumes the form

$$\phi(\mathbf{R})=A\exp[a_1(R_1+R_2)+a_3R_3-\delta], \tag{14}$$

where the parameters have been chosen by trial and error such as to ensure that the spurious deep minima arising in the CVRQD potential do not perturb the final ES PES. Moreover, $\phi(\mathbf{R})$ has been chosen from the requirement that it assumes a value smaller than 1 cm^{-1} for regions with an energy smaller then E_0. The other constants have been taken from Ref. 1 except for small changes suggested by the vibrational calculations reported in the following section. The whole set of parameters used in the ES scheme is gathered in Table III. A global view of the ES scheme is given in Fig. 2, which shows the potentials participating in the ES process

TABLE IV. Accuracy of CVRQD and ES-1v-II PESs in reproducing observed vibrational band origins of $H_2^{16}O$. The differences are expressed as observed-calculated in cm^{-1}.

(n_1,n_2,n_3)	Obs.	CVRQD	ES	(n_1,n_2,n_3)	Obs.	CVRQD	ES
010	1 594.746	−0.329	−0.329	001	3 755.929	0.201	0.202
020	3 151.630	−0.566	−0.565	011	5 331.267	−0.245	−0.241
100	3 657.053	0.004	0.005	021	6 871.520	−0.628	−0.622
030	4 666.791	−0.783	−0.781	101	7 249.819	0.598	0.616
110	5 234.975	−0.519	−0.518	031	8 373.852	−0.918	−0.909
040	6 134.015	−1.066	−1.065	111	8 807.000	−0.029	−0.011
120	6 775.093	−0.872	−0.870	041	9 833.587	−1.178	−1.171
200	7 201.540	0.347	0.348	121	10 328.730	−0.436	−0.410
002	7 445.045	0.161	0.143	201	10 613.353	1.227	1.285
050	7 542.437	−1.420	−1.420	003	11 032.405	0.460	0.324
130	8 273.977	−1.105	−1.101	131	11 813.205	−0.668	−0.627
210	8 761.579	−0.341	−0.342	211	12 151.253	0.433	0.477
060	8 869.954	−2.217	−2.222	013	12 565.006	0.135	0.027
012	9 000.140	−0.255	−0.265	221	13 652.658	0.144	0.202
070	10 086.045	−2.738	−2.753	301	13 830.937	2.051	2.205
220	10 284.369	−0.720	−0.717	071	13 835.373	−2.576	−2.696
022	10 521.762	−0.713	−0.714	023	14 066.196	−0.365	−0.453
300	10 599.687	1.089	1.113	103	14 318.813	1.239	1.210
102	10 868.876	0.466	0.455	151	14 647.977	−1.231	−1.194
080	11 253.997	−2.413	−2.432	231	15 119.031	−0.056	0.035
230	11 767.388	−0.948	−0.938	311	15 347.958	1.182	1.280
032	12 007.776	−1.068	−1.066	033	15 534.707	−0.758	−0.847
310	12 139.316	0.280	0.297	113	15 832.780	0.641	0.621
112	12 407.662	−0.217	−0.225	241	16 546.319	−0.308	−0.184
090	12 533.724	−2.512	−2.529	321	16 821.634	1.542	1.702
400	13 828.278	2.032	2.139	401	16 898.842	2.744	2.995
122	13 910.881	−0.698	−0.699	123	17 312.551	0.161	0.164
202	14 221.159	1.006	0.876	203	17 495.528	2.178	2.056
004	14 537.504	0.888	0.318	331	18 265.821	1.073	1.256
330	15 108.239	−0.060	−0.007	411	18 393.315	2.064	2.075
410	15 344.504	1.072	1.138	133	18 758.633	−0.144	−0.136
212	15 742.803	0.095	−0.060	213	18 989.960	1.317	1.042
420	16 823.319	0.874	0.951	341	19 679.192	0.645	0.875
222	17 227.380	−0.306	−0.505	501	19 781.103	4.644	5.020
302	17 458.214	1.954	1.560	421	19 865.285	2.090	1.787
104	17 748.107	1.745	1.385	223	20 442.777	1.295	0.995
600	19 781.323	−1.053	−2.228	303	20 543.129	3.028	2.284
610	21 221.569	3.556	3.370	511	21 221.827	3.486	3.352
700	22 529.288	5.959	4.941	431	21 314.448	2.446	1.444
				601	22 529.440	5.940	4.949
				701	25 120.277	6.459	−1.838
$\sigma(80)$						1.860	1.632

for C_{2v} geometries. As seen, the poor behavior of the CVRQD form for large displacements away from equilibrium has disappeared in the ES-1v-II PES.

V. RESULTS AND DISCUSSION

As noted above, the ES PES from the present work (ES-1v-II) shows negligible differences from the CVQRD potential for geometries with energies below 25 000 cm^{-1}, where this potential was constructed to work. Thus, the properties calculated for every isotopologue in Ref. 8 should remain valid here, namely, equilibrium structure, barrier to linearity, anharmonic force field, harmonic frequency, vibrational fundamentals, zero-point energy, vibrational band origins, and rotational term values. Clearly, the local nature of CVQRD prevents any use of it for reaction dynamics calculations, namely, cross sections and rate constants for the $O(^1D)+H_2$ reaction. Because the ES-1v II PES shows the correct asymptotic limits, such a handicap has now been removed.

Another important aspect of the new PES refers to the locus of Σ/Π crossing seam for linear HOH configurations (the minimum of the crossing seam arises at $R_1=1.8250a_0$, $R_2=3.2713a_0$, with an energy of $-0.152\,074E_h$ with respect to the three dissociated atoms). This feature too is also mimicked correctly by the ES-1v-II PES as illustrated in the one-dimensional cut of the PES in Fig. 3. Moreover, as Fig. 4 shows, it describes accurately the conical intersection discussed above, which is a feature hard to reproduce when fitting global PESs.

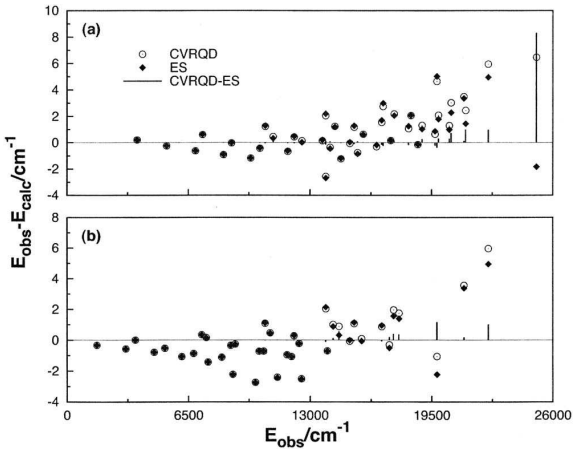

FIG. 5. Differences of the vibrational band origins from the experimental values for the CVRQD and ES-1v-II PESs. The vertical bars represent the differences between the two potentials. Panel (a) shows the odd levels and (b) the even ones.

Table IV compares the calculated vibrational frequencies ($J=0$) of the present ES-1v II PES with those reported[8] for the CVRQD form. Also included for comparison are the experimental values for $H_2^{16}O$ (taken as reported in Ref. 8). The variational vibrational calculations were performed using the DVR3D code[25] for separate even and odd states, using the same basis set parameters as in Ref. 8. The attribution of the vibrational quantum numbers to the vibrational energies has been made, following previous work,[26,27] by a combination of automatic attribution and graphical inspection of wave functions. As can be seen from Table IV, the root mean square deviations from the observed values are nearly the same for both potentials.

Figure 5 compares the errors on the calculated vibrational frequencies for the ES-1v-II and CVRQD PESs relative to the experimental values and shows the differences between the former two. As can be seen, the vibrational spectra from the ES-1v-II PES are almost identical to the one from CVRQD for the range of energies where experimental frequencies are available, with the former showing even a small improvement for the higher energy levels. Thus, we expect that the ES-1v II PES here reported can be valuable in predicting realistic vibrational-rotational frequencies above 25 000 cm^{-1} and virtually up to the dissociation limit.

VI. CONCLUSIONS

We have obtained a single-sheeted PES for the ground state of the water molecule by ES a highly accurate isotope-dependent *ab initio* local potential function and a global form calibrated from MRCI(Q) energies that has been CBS extrapolated. The resulting global ES form describes accurately all regions of configuration space including the locus of Σ/Π conical intersection at linear geometries. It should therefore be highly reliable for dynamics calculations (classical or quantum), in particular, of the reaction $O(^1D)+H_2 \rightarrow OH+H$.

ACKNOWLEDGMENTS

This work has the support of Fundação para a Ciência e Tecnologia, Portugal (Contract Nos. POCI/QUI/60501/2004 and POCI/AMB/60261/2004), under the auspices of POCI 2010 of Quadro Comunitário de Apoio III co-financed by FEDER.

[1] A. J. C. Varandas, J. Chem. Phys. **105**, 3524 (1996); **107**, 5987E (1997).
[2] A. J. C. Varandas, J. Chem. Phys. **107**, 867 (1997).
[3] A. J. C. Varandas, A. I. Voronin, and P. J. S. B. Caridade, J. Chem. Phys. **108**, 7623 (1998).
[4] A. J. C. Varandas, S. P. J. Rodrigues, and P. A. J. Gomes, Chem. Phys. Lett. **297**, 458 (1998).
[5] W. Ansari and A. J. C. Varandas, J. Phys. Chem. A **106**, 9338 (2002).
[6] A. J. C. Varandas, J. Chem. Phys. **119**, 2596 (2003).
[7] O. L. Polyansky, A. G. Császár, S. V. Shirin, N. F. Zobov, P. Barletta, J. Tennyson, D. W. Schwenke, and P. J. Knowles, Science **299**, 539 (2003).
[8] P. Barletta, S. V. Shirin, N. F. Zobov, O. L. Polyansky, J. Tennyson, E. F. Valeev, and A. G. Császár, J. Chem. Phys. **125**, 204307 (2006).
[9] J. M. L. Martin, J. P. François, and R. Gijbels, J. Chem. Phys. **96**, 7633 (1992).
[10] A. Halkier, T. Helgaker, P. Jörgensen, W. Klopper, and J. Olsen, Chem. Phys. Lett. **302**, 437 (1999).
[11] T. Helgaker, W. Klopper, H. Koch, and J. Noga, J. Chem. Phys. **106**, 9639 (1997).
[12] H. Partridge and D. W. Schwenke, J. Chem. Phys. **106**, 4618 (1997).
[13] J. N. Murrell, S. Carter, S. C. Farantos, P. Huxley, and A. J. C. Varandas, *Molecular Potential Energy Functions* (Wiley, Chichester, 1984).
[14] A. J. C. Varandas, *Modeling and Interpolation of Global Multi-Sheeted Potential Energy Surfaces*, Advanced Series in Physical Chemistry (World Scientific, Singapore, 2004), Chap. 5, p. 91.
[15] A. J. C. Varandas, Adv. Chem. Phys. **74**, 255 (1988).
[16] A. J. C. Varandas, Chem. Phys. Lett. **443**, 398 (2007).
[17] D. E. Woon and T. H. Dunning, Jr., J. Chem. Phys. **103**, 4572 (1995).
[18] H.-J. Werner and P. J. Knowles, J. Chem. Phys. **89**, 5803 (1988).
[19] H. J. Werner and P. J. Knowles, Chem. Phys. Lett. **145**, 514 (1988).
[20] H.-J. Werner, P. J. Knowles, J. Almlöf *et al.*, MOLPRO is a package of *ab initio* programs (1998).
[21] A. J. C. Varandas, J. Chem. Phys. **126**, 244105 (2007).
[22] A. J. C. Varandas and P. Piecuch, Chem. Phys. Lett. **430**, 448 (2006).
[23] A. Karton and J. M. L. Martin, Theor. Chim. Acta **115**, 330 (2006).
[24] W. H. Press, S. A. Teukolski, W. T. Vetterling, and B. P. Flannery, *Numerical Recipes in Fortran: The Art of Scientific Computing* (Cambridge University Press, New York, 1992).
[25] J. Tennyson, M. A. Kostin, P. Barletta, G. J. Harris, O. L. Polyansky, J. Ramanlal, and N. F. Zobov, Comput. Phys. Commun. **163**, 85 (2004).
[26] A. J. C. Varandas and S. P. J. Rodrigues, Spectrochim. Acta, Part A **58**, 629 (2002).
[27] A. J. C. Varandas and S. P. J. Rodrigues, J. Phys. Chem. A **110**, 485 (2006).

Accurate Double Many-Body Expansion Potential Energy Surface for $N_3(^4A'')$ from Correlation Scaled ab Initio Energies with Extrapolation to the Complete Basis Set Limit†

B. R. L. Galvão and A. J. C. Varandas*

Departamento de Química, Universidade de Coimbra, 3004-535 Coimbra, Portugal

Received: April 22, 2009; Revised Manuscript Received: July 15, 2009

A new global potential energy surface is reported for the $^4A''$ ground electronic state of the N_3 system from double many-body expansion theory and an extensive set of accurate ab initio energies extrapolated to the complete basis set limit. It shows three equivalent metastable potential wells for C_{2v} geometries that are separated from the three $N(^4S) + N_2$ asymptotes by energy barriers as predicted from previous ab initio work. The potential well and barrier height now predicted lie 42.9 and 45.9 kcal mol^{-1} above the atom−diatom dissociation limit, respectively, being about 1 kcal mol^{-1} lower than previous theoretical estimates. The ab initio calculations here reported predict also a $^4B_1/^4A_2$ conical intersection and reveal a new minimum with D_{3h} symmetry that lies 147 kcal mol^{-1} above the atom−diatom asymptote. All major topographical features of the potential energy surface are accurately described by the DMBE function, including the weakly bound van der Waals minima at large atom−diatom separations.

1. Introduction

The nitrogen exchange reaction has recently been the subject of considerable theoretical work since its rate constant is part of the necessary database for the design of spacecraft heat shields.[1] As experimental measurements are available only for two temperatures ($T = 1273$ and 3400 K) and have large error bars,[2–4] theoretical approaches are the only way to accurately obtain the necessary results at the temperatures achieved in the high-speed re-entry of spacecrafts into the Earth's atmosphere.

The first scattering calculations on the title system were performed on a London−Eyring−Polanyi−Sato (LEPS) potential energy surface[5] (PES), which has been for many years the only available one. Only recently, due to the inadequacy of this LEPS form of Laganà et al.[5] to describe the main features of the nitrogen atom−diatom interaction, new PESs by the same group[6,7] (denoted by the authors as L0 to L4) were proposed, with the more recent one (L4)[7] being fitted to 56 ab initio energies that were obtained using CCSD(T) (coupled-cluster singles and doubles with perturbative correction of triples) theory with the aug-cc-pVTZ basis set of Dunning[8,9] (such basis sets are generally denoted as AVXZ, where X = D, T, Q,... is the cardinal number).

The first ab initio based PES for the $N + N_2$ reaction system is due to Wang et al.,[1,10,11] who have utilized it for a quantum dynamics study of the title reaction. This PES (named WSHDSP after their authors) has employed the many-body expansion[12,13] formalism, and has been calibrated through a fit to a set of merged ab initio energies obtained using different quantum chemical treatments and basis sets.

As noted in ref 6, the thermal rate coefficients computed on the WSHDSP PES do not compare with the available experimental data as favorably as those computed on the LEPS form, which may partly be due to incompleteness of the basis set and other corrections such as incompleteness of the n-electron wave function, relativistic, and nonadiabatic corrections. Our major goal in this work will be to obtain a PES extrapolated to the complete basis set (CBS) limit, and model the energies analytically using double many-body expansion (DMBE) theory. The paper is organized as follows. Section 2 provides a description of the ab initio calculations and CBS extrapolation scheme. The modeling of the data using DMBE theory is reported in section 3, and the topological features of the PES discussed in section 4. Section 5 gathers the conclusions.

2. Ab Initio Calculations and Extrapolation Procedure

All ab initio calculations have been done with the Molpro package[14] for electronic structure calculations, and different methods tested using basis sets of the AVXZ[8,9] family (denoted for further brevity as XZ). In spite of achieving good results for regions of configuration space where one N−N bond is close to the equilibrium geometry of the N_2 molecule, the CCSD(T)[15] results do not behave correctly for $N-N_2$ cuts involving stretched diatomics, as one might expect for a single-reference based method. Conversely, the multireference configuration interaction (MRCI) approach, including the popular Davidson correction for quadruples excitations [MRCI(Q)[16,17] shows the proper behavior for the stretched structures. The CASSCF (complete active space self-consistent field) reference space for the MRCI(Q) method involves 15 correlated electrons in 12 active orbitals ($9a' + 3a''$). Unfortunately, the MRCI(Q) method is rather expensive, even using smaller basis sets, which led us to adopt a cost-effective, yet efficient, strategy whereby relatively inexpensive MRCI(Q) calculations are merged with cheap, yet accurate, CCSD(T) ones. To put them at a common level of accuracy, we have extrapolated the calculated energies to the complete basis set limit. For this, we have utilized the uniform singlet- and triplet-pair extrapolation (USTE) method proposed by one of us,[18] which shows advantages over earlier popular methodologies[19–21] and has been shown to yield accurate results even with CBS extrapolation from small basis sets. In fact, such a technique appears to provide a highly desirable route for accurately treating systems with up to a large number of electrons, as recent studies have demonstrated.[22–25] It should be further remarked that CBS extrapolation has shown[24,26] to correct largely for basis set superposition error,[27] supporting the idea

† Part of the "Vincenzo Aquilanti Festschrift".

* Corresponding author. E-mail address: varandas@qtvs1.qui.uc.pt.

10.1021/jp903719h
Published on Web 08/14/2009

that no further corrections are necessary to overcome in a simple and reasonably accurate way such an ubiquitous problem.

Aiming at a consistent description of the PES with different ab initio theories, each one chosen to be used (due to the physics of the problem or a priori design of the overall approach) at a specific region of configuration space, we suggest next a scheme to make them compatible while extrapolating to the CBS limit. As usual, at every geometry, the CBS extrapolated dynamical correlation energy is added to the CBS extrapolated CASSCF energy, yielding the total energy. First, following previous work,[18] the raw CASSCF (or simply CAS) energies are CBS extrapolated with the two-point extrapolation protocol of Karton and Martin (KM)[29] that has been originally proposed for Hartree−Fock energies:

$$E_X^{CAS}(\mathbf{R}) = E_\infty^{CAS}(\mathbf{R}) + B/X^{5.34} \tag{1}$$

where the cardinal number of the basis set is indicated in subscript (note that the CBS limit corresponds to $X = \infty$), and $\mathbf{R}$ is the collective variable of the space coordinates. For Hartree−Fock energies, this formula is known to benchmark perform with a root mean squared error of 206 μE_h or so. Such an accuracy is smaller than achieved by CBS energies obtained by extrapolating X = Q, 5, 6 energies with the exponential CBS extrapolation, and even more so when our improved CBS exponential scheme[18] is used, whereby the exponentially extrapolated energy is averaged with the raw CAS energy for X = 6. Indeed, for N_3 at the geometry corresponding to the C_{2v} minimum, the exponential-CBS and modified exponential-CBS[18] protocols predict the values of −163.434 786 and −163.434 769 E_h, which are less negative by 416 and 432 μE_h than the prediction obtained by the KM formula when applied to CAS energies. Because the error is expected to be smaller for relative energies, such an expected compensation led us to keep the method at its minimum computational complexity by avoiding the burden of having to do further calculations using two extra basis sets (X = 5, 6).

The CCSD(T) dynamical correlation energy is extrapolated with the correlation scaling/unified singlet- and triplet-pair extrapolation method based on a single pivotal geometry[30] [CS[1]/USTE(T,Q)] as follows. First, an energy is calculated with the QZ basis set at a reference geometry (any point of the set of geometries designed for the fit). Then, at this point (referred to as the pivotal geometry), the (T,Q) pair of dynamical correlation energies calculated as the difference between the CCSD(T) and CAS energies are CBS extrapolated using the USTE(T,Q)[18] protocol:

$$E_X^{dc} = E_\infty^{dc} + \frac{A_3}{(X+\alpha)^3} + \frac{A_5(0) + cA_3^{5/4}}{(X+\alpha)^5} \tag{2}$$

where $A_5(0) = 0.003\,768\,545\,9\ E_h$, $c = -1.178\,477\,13\ E_h^{-1/4}$, and $\alpha = -3/8$. The CBS extrapolated dynamical correlation energy is then added to the CBS extrapolated CAS energy to obtain the total energy at the chosen pivotal geometry. Such a strategy has indeed been shown to generate accurate functions as recently reported[25] for the ground electronic state of H_2S. It should be mentioned that the parameters employed in eq 2 are not the ones recommended[18] for CC-type methods but for the MRCI one, since the dynamical correlation (relative to the CASSCF energy, rather than the full correlation with respect to the HF energy) is being extrapolated. This may also ensure further consistency on merging the MRCI(Q) and CCSD(T) energies.

The CBS extrapolated dynamical correlation energies in the remaining CCSD(T) geometries are now obtained by correlation scaling:[28,30]

$$E_\infty^{dc}(\mathbf{R}) = \chi_{\infty,3}(\mathbf{R})\, E_3^{dc}(\mathbf{R}) \tag{3}$$

where the scaling function χ assumes the form

$$\chi_{\infty,3}(\mathbf{R}) = 1 + \frac{S_{3,2}(\mathbf{R}) - 1}{S_{3,2}(\mathbf{R}_e) - 1}[S_{\infty,3}(\mathbf{R}_e) - 1] \tag{4}$$

$\mathbf{R}_e$ is the pivotal geometry, and

$$S_{m,n}(\mathbf{R}) = \frac{E_m^{dc}(\mathbf{R})}{E_n^{dc}(\mathbf{R})} \tag{5}$$

For further details, the reader is addressed to the original papers. Suffice it to say that the reference geometry ($\mathbf{R}_e$) in the single-pivotal scheme[28] utilized here can be any point of the PES, having been taken as the geometry of the C_{2v} minimum of N_3 at the CCSD(T)/AV*T*Z level: $R_1 = R_2 = 2.39a_0$, and $\theta = 119°$.

The above extrapolation scheme can yield accurate potentials at costs as low as one may possibly ambition, its accuracy having been tested for diatomic systems through vibrational calculations. Despite the severe test of the approach, very good results have been obtained,[30] as well as for triatomic[25] and even larger systems[23,24] (these treated with a variant[33] of USTE); see also ref 34 for an application of CS to large systems.

For the CBS extrapolation of the MRCI(Q) dynamical correlation energies, we have first chosen some representative cuts, where the CCSD(T) method begins to breakdown. MR-CI(Q) calculations have then been performed with DZ and TZ basis sets. To obtain a smooth merging of the CBS energies calculated from these two methods, the MRCI(Q) energies are first calibrated using the CCSD(T) ones. For this, we have utilized the CS scheme with $E_\infty^{dc}(\mathbf{R}_e)$ in eq 4 taken as the extrapolated CCSD(T) value obtained above. Such a procedure requires explicit MRCI(Q) calculations only for DZ and TZ basis sets while ensuring that both methods yield identical CBS energies at the pivotal geometry: $E_\infty^{dc}(\text{MRCI(Q)},\mathbf{R}_e) = E_\infty^{dc}(\text{CCSD(T)},\mathbf{R}_e)$. An illustrative cut is presented in Figure 1, where the pivotal geometry has been chosen so as to warrant that CCSD(T) theory provides good results. Note that the scaling function in eq 4 imposes that the extrapolated MRCI(Q) and CCSD(T) energies coincide at $R_e = 3.3a_0$. Thus, no discontinuity arises in the energy along the chosen cut.

3. DMBE Potential Energy Surface

Within the DMBE[31,32,35,36] framework, the potential energy surface is first written as a sum of one-, two-, and three-body terms:

$$V(R_1,R_2,R_3) = V^{(1)} + \sum_{i=1}^{3} V^{(2)}(R_i) + V^{(3)}(R_1,R_2,R_3) \tag{6}$$

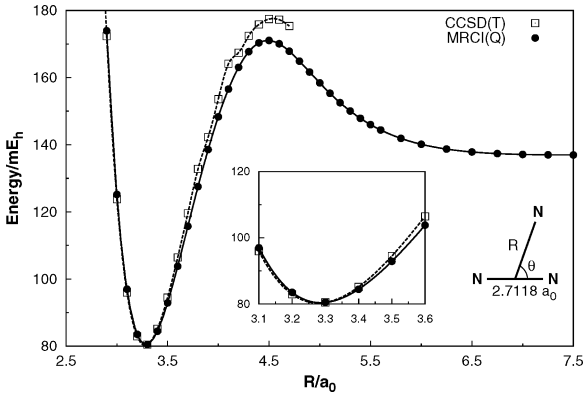

Figure 1. Extrapolated CCSD(T) and MRCI(Q) energies used to calibrate the DMBE PES for a cut corresponding to a N atom approaching N_2 with $R_{NN} = 2.7118a_0$ and the Jacobi angle fixed at 30°. In this and all subsequent plots, the zero of energy corresponds to the N_2 + N reaction channel (with the diatomic in its equilibrium geometry), as described by extrapolated CCSD(T) energies.

To fix the zero of the energy of the PES at a N_2 molecule at equilibrium and one N(^{4}S) atom infinitely separated, we impose that the one-body term equals to $V^{(1)} = -2D_e$, where D_e is the well depth of the N_2 molecule. Clearly, the PES ensures the proper asymptotic limits, i.e., $V(R_e,\infty,\infty) = 0$, and $V(\infty,\infty,\infty) = D_e$. Each n-body term is now split into extended Hartree−Fock [$V^{(n)}_{EHF}$] and dynamical correlation [$V^{(n)}_{dc}$] contributions, whose analytical forms are described in detail in the following sections. Although all such forms have a semiempirical motivation from past work, it should be stressed that they are here utilized to fit the CBS extrapolated data, and hence the resulting PES contains no information at all that is alien to the ab initio methods that have been utilized.

3.1. Two-Body Energy Terms. The diatomic potential curve for the ground state of molecular nitrogen has been modeled using the extended Hartree−Fock approximate correlation energy method for diatomic molecules, including the united-atom limit (EHFACE2U),[37] and fitted to CBS extrapolated energies described in the previous section for the asymptotic atom−diatom cuts. The EHF term assumes the form

$$V^{(2)}_{EHF}(R) = -\frac{D}{R}(1 + \sum_{i=1}^{n} a_i r^i)\exp[-\gamma(r)r] \qquad (7)$$

where $r = R - R_e$ is the displacement from the equilibrium diatomic geometry, D and a_i ($i = 1,..., n$) are adjustable parameters, and the range decaying term in the exponential is given by form $\gamma(r) = \gamma_0[1 + \gamma_1 \tanh(\gamma_2 r)]$.

In turn, the dynamical correlation part assumes the form

$$V^{(2)}_{dc}(R) = -\sum_{n=6,8,10,...} C_n \chi_n(R) R^{-n} \qquad (8)$$

where

$$\chi_n(R) = \left[1 - \exp\left(-A_n\frac{R}{\rho} - B_n\frac{R^2}{\rho^2}\right)\right]^n \qquad (9)$$

is a charge-overlap damping function for the long-range dispersion energy, and the summation in eq 8 is truncated at $n = 10$. In turn, $A_n = \alpha_0 n^{-\alpha_1}$ and $B_n = \beta_0 \exp(-\beta_1 n)$ are auxiliary functions,[31,35] with $\alpha_0 = 16.366\,06$, $\alpha_1 = 0.701\,72$, $\beta_0 = 17.193\,38$, and $\beta_1 = 0.095\,74$ being universal-type parameters. Moreover, $\rho = 5.5 + 1.25R_0$ is a scaling parameter, $R_0 = 2(\langle r_A^2\rangle^{1/2} + \langle r_B^2\rangle^{1/2})$ is the Le Roy[38] parameter for the onset of the undamped R^{-n} expansion, and $\langle r_X^2\rangle$ is the expectation value of the squared radius for the outermost electrons of atom X. All coefficients used in the $N_2(X^1\Sigma_g^+)$ potential curve, and other parameters necessary to construct the DMBE function are given as Supporting Information.

3.2. Three-Body Energy Terms. ***3.2.1. Three-Body Dynamical Correlation Energy.*** The three-body dynamical correlation energy term assumes the form[39]

$$V^{(3)}_{dc} = -\sum_i \sum_n f_i(\mathbf{R})\, C_n^{(i)}(R_i,\theta_i)\, \chi_n(r_i) r_i^{-n} \qquad (10)$$

where R_i, r_i, and θ_i are the Jacobi coordinates (R_i is a NN distance, r_i the N−NN corresponding separation, and θ_i the included angle), and $f_i = {}^1/_2\{1 - \tanh[\xi(\eta R_i - R_j - R_k)]\}$ is a switching function with parameters fixed at $\eta = 6$ and $\xi = 1a_0^{-1}$; corresponding expressions hold for R_j, R_k, f_j, and f_k. Regarding the damping function $\chi_n(r_i)$, we still adopt eq 9 but with R_i replaced by r_i, and R_0 estimated as for the Si−N diatomic (Si corresponds to the united atom of the coalesced N_2 diatom; see ref 39).

The atom−diatom dispersion coefficients in eq 10 also assume their usual form

$$C_n^{(i)}(R_i,\theta_i) = \sum_L C_n^L(R) P_L(\cos\theta_i) \qquad (11)$$

where $P_L(\cos\theta_i)$ denotes the Lth Legendre polynomial. The expansion in eq 11 has been truncated by considering only the coefficients C_6^0, C_6^2, C_8^0, C_8^2, C_8^4, C_{10}^0; all other coefficients have been assumed to make negligible contributions. To estimate the dispersion coefficients, we have utilized the generalized Slater−Kirkwood approximation,[40] with the dipolar polarizabilities calculated at the MRCI/AVQZ level. The atom−diatom dispersion coefficients so calculated for a set of internuclear distances have then been fitted to the functional form

$$C_n^{L,N_1-N_2N_3}(R) = C_n^{L,N_1N_2} + C_n^{L,N_1N_3} + D_M(1 + \sum_{i=1}^{3} a_i r^i)\exp(-\sum_{i=1}^{3} b_i r^i) \qquad (12)$$

where $b_1 = a_1$, and $C_n^{L,NN}$ is the atom−atom dispersion coefficient for $L = 0$ and zero for other values of L. The internuclear dependence of such coefficients are displayed in Figure 2. As noted elsewhere,[39] eq 10 causes an overestimation of the dynamical correlation energy at the atom−diatom dissociation channels. This can be corrected by multiplying the two-body dynamical correlation energy for the ith pair by $\Pi_{j\neq i}(1 - f_j)$, where f_i is the switching function used in $V^{(3)}_{dc}$ term, with corresponding expressions for channels j and k.

3.2.2. Three-Body Extended Hartree−Fock Energy. With the one- and two-body terms and also the three-body dynamical correlation energy at hand, the three-body EHF term can now be determined for every geometry by subtracting the other contributions:

$$V_{\mathrm{EHF}}^{(3)}(\mathbf{R}) = E(\mathbf{R}) - V_{\mathrm{dc}}^{(3)}(\mathbf{R}) - \sum_{i=1}^{3} V^{(2)}(R_i) + 2D_{\mathrm{e}} \tag{13}$$

Of course, the representation of the PES must be symmetric with respect to permutation of the coordinates. Such a requirement is satisfied by using the integrity basis:

$$\Gamma_1 = Q_1 \tag{14}$$

$$\Gamma_2 = Q_2^2 + Q_3^2 \tag{15}$$

$$\Gamma_3 = Q_3(Q_3^2 - 3Q_2^2) \tag{16}$$

where Q_i are symmetry coordinates.[12,13,41] The functions Γ_i are all totally symmetric in the three-particle permutation group S_3. Thus, any polynomial built from Γ_i also transforms as the totally symmetric representation of S_3. The EHF three-body energy is then fitted to a function in these coordinates using a three-body distributed polynomial[42] approach:

$$V_{\mathrm{EHF}}^{(3)}(\mathbf{R}) = \sum_{m=1}^{4} P^{(m)} T^{(m)}(\mathbf{R}) \tag{17}$$

where the polynomials are defined as

$$P^{(m)} = \sum_{i,j,k} c_{ijk}^{(m)} \Gamma_1^i \Gamma_2^j \Gamma_3^k \tag{18}$$

and $T(\mathbf{R})$ is a range-determining factor that ensures that the three-body term vanishes at large interatomic distances,

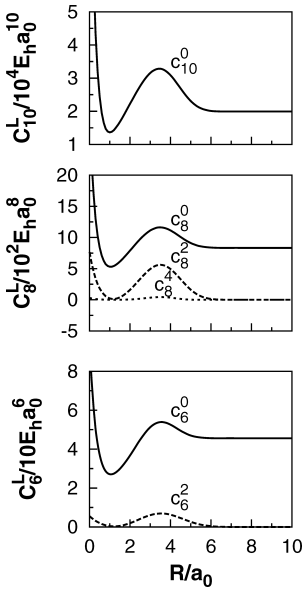

Figure 2. Dispersion coefficients for the atom−diatom asymptotic channel as a function of the diatomic internuclear distance.

$$T^{(m)}(\mathbf{R}) = \prod_{j=1}^{3} \{1 - \tanh[\gamma^{(m)}(R_j - R_0^{(m)})]\} \tag{19}$$

To describe the van der Waals region, a polynomial with the range function above is not suitable since it vanishes with a similar decay rate for all bond distances. To overcome such a difficulty, we have chosen one bond length to have a different reference value and decaying parameter (thus having C_{2v} symmetry). Since this cannot impose the correct permutational symmetry, a summation of three such functions has been utilized. The $V_{\mathrm{EHF}}^{(3)}$ function defined above contains a total of 276 linear parameters (c_{ijk}^m, as given in the Supporting Information) that have been calibrated using a total of 1592 ab initio points. A summary of the errors in the fitting procedure is displayed in stratified form in Table 1. It should be pointed out that larger weights were attributed to the most important regions of the PES, namely stationary points (in particular for the subtle van der Waals minima).

4. Features of DMBE Potential Energy Surface

Table 2 compares the attributes of the two main stationary points of the DMBE form with the corresponding attributes from other potential energy surfaces.[1,7] Also included are the values calculated at CCSD(T)/AVTZ and CCSD(T)/CBS level. As can be seen, the extrapolation of the ab initio energies to the CBS limit leads to a significant decrease in the height of the well and transition state relative to the atom−diatom limit, being predicted respectively as 42.9 and 45.9 kcal mol^{-1}. The energy difference between them is also increased by ~0.6 kcal mol^{-1}, while their geometries are essentially indistinguishable from the raw CCSD(T) ones at the TZ level.

The calculated MRCI(Q) energies (performed just for the ground state) here reported show also a shallow D_{3h} minimum surrounded by two C_{2v} stationary structures, a feature that appears to arise due to a conical intersection between the ground and first excited state of $^4A''$ symmetry, or between the $^4B_1$ and $^4A_2$ states in C_{2v} symmetry, as shown in Figure 3, where single state CASSCF calculations performed for each symmetry are shown. Indeed, as demonstrated in the insert of Figure 3, the wave function changes sign when transported adiabatically along a closed path encircling the point of crossing (with a small radius of $0.6a_0$ to avoid encircling more than one crossing), as it should by the Longuet−Higgins' [43] sign change theorems for a conical intersection. Note that the sign change has been illustrated by plotting the dominant component of the CAS vector along the chosen path, following pioneering work for the LiNaK system.[44]

A full view of the DMBE PES for C_{2v} insertion of a nitrogen atom in the nitrogen diatomic is shown at Figure 4 where the two saddle points and minimum described above are apparent. To improve the representation of this region of the PES, a relatively dense grid of MRCI(Q) points has been calculated and used in the fit. As shown, the DMBE function predicts a D_{3h} minimum with a characteristic bond length of $2.95a_0$, which lies 146.6 kcal mol^{-1} above the N + N_2 reaction asymptote (but still below the energy for the three separated-atoms limit). Such a minimum is connected to the absolute ones by saddle points in the C_s ground state), being the full numerical characterization (geometries, energies, and harmonic vibrational frequencies) of these stationary points reported in Table 3.

TABLE 1: Stratified Global Root-Mean-Square Deviations (in kcal mol^{-1}) of $N_3(^4A'')$ DMBE Potential Energy Surface

energy[a]	N^b	rmsd
0	85	0.001
10	279	0.212
20	335	0.281
30	369	0.358
40	408	0.402
50	704	0.380
60	819	0.451
70	899	0.543
80	971	0.615
90	1017	0.625
100	1073	0.673
250	1443	0.908
500	1528	0.952
1000	1564	0.963
3000	1585	0.979

[a] In kcal mol^{-1} and relative to the N(^{4}S) + N_2 asymptote. [b] Number of calculated ab initio points up to the indicated energy range.

TABLE 2: Stationary Points of $N_3(^4A'')$ Potential Energy Surface, for Different Fitted Forms and CCSD(T) ab Initio Values (at AVTZ and CBS Levels)[a]

feature	property	WSHDSP[b]	L4[c]	AVTZ[d]	CBS	DMBE
Min (C_{2v})	R_1/a_0	2.40	2.40	2.39	2.38	2.38
	R_2/a_0	2.40	2.40	2.39	2.38	2.38
	θ/deg	120	119	119	119	119
	ΔE^e	43.7	44.5	44.7	42.9	42.9
	ω_1/cm^{-1}		860			702
	ω_2/cm^{-1}		1279			1323
	ω_3/cm^{-1}		665			566
sp (C_s)	R_1/a_0	2.23	2.24	2.22	2.20	2.20
	R_2/a_0	2.80	2.77	2.84	2.85	2.83
	θ/deg	119	117	117	117	116
	ΔE^e	47.2	47.4	47.1	45.9	45.9
	ω_1/cm^{-1}		599			511
	ω_2/cm^{-1}		760i			652i
	ω_3/cm^{-1}		1585			1740

[a] The geometries are in valence coordinates. [b] From ref 1. [c] The geometry optimizations with the L4 potential energy surface[7] are from the present work. [d] Ab initio geometry optimization at the CCSD(T)/AVTZ level. [e] In kcal mol^{-1}, relative to the N(^{4}S) + N_2 asymptote.

All major features of the PES are probably better viewed in the relaxed triangular plot[45] of Figure 5 utilizing scaled hyperspherical coordinates ($\beta^\star = \beta/Q$ and $\gamma^\star = \gamma/Q$):

$$\begin{pmatrix} Q \\ \beta \\ \gamma \end{pmatrix} = \begin{pmatrix} 1 & 1 & 1 \\ 0 & \sqrt{3} & -\sqrt{3} \\ 2 & -1 & -1 \end{pmatrix} \begin{pmatrix} R_1^2 \\ R_2^2 \\ R_3^2 \end{pmatrix} \tag{20}$$

Note that the perimeter of the molecule is relaxed such that the energy of the triangle formed by the three atoms is lowest at any point. Clearly visible are the equivalent stationary structures for the N + N_2 exchange reaction (wells and transition states), as well as those in the vicinity of the D_{3h} geometry ($\gamma^\star = \beta^\star = 0$) already commented.

The equivalent N−N_2 van der Waals minima are described with a root mean squared deviation of ∼0.001 kcal mol^{-1} for the 144 ab initio energies shown in Figure 6. Note that there are two types of such minima, one for geometries with C_{2v} symmetry, and the other for geometries with $C_{\infty v}$ symmetry, the deepest being T-shaped like.

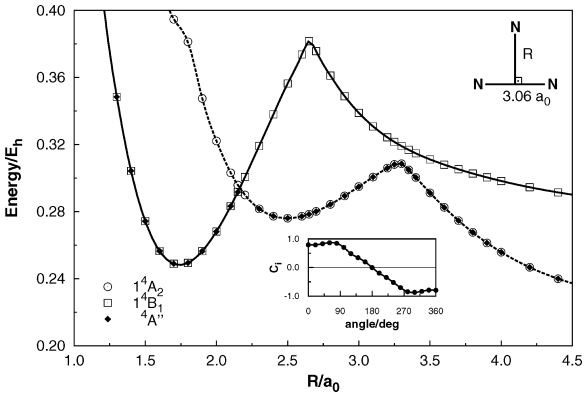

Figure 3. CASSCF description of the conical intersection with the AVTZ basis set. The open symbols connected by smooth splines correspond to points calculated in the $^4A_2$ and $^4B_1$ states of C_{2v} symmetry, while the solid diamonds correspond to calculations with $^4A''$ symmetry (the zero of energy is the CASSCF value for the N(^{4}S) + N_2 channel). Shown in the inset is an illustration of the sign change theorem for a closed path (circle) around the conical intersection (the point of crossing shown in the main plot): c_i is the coefficient of the dominant configuration in the CASSCF wave function of the first $^4A''$ state.

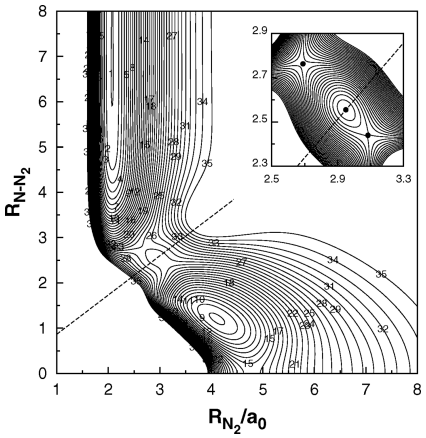

Figure 4. Contours plot for the C_{2v} insertion of the N atom into N_2. Contours are equally spaced by 10 mE_h, starting at zero. The dashed line shows the location of D_{3h} geometries while the inset displays a zoom around the D_{3h} minima (contours spaced by 0.5 mE_h), with the stationary points indicated by filled circles.

The isotropic and leading anisotropic terms in a Legendre expansion of the N−N_2 interaction potential are important quantities for the study of scattering processes, with the sign of V_2 indicating whether or not the molecule prefers to orient its axis along the direction of the incoming atom: a negative value favors the collinear approach while a positive value favors the approach through C_{2v} geometries. Such potentials are shown in Figure 7. Note that the well and barrier in the short-range region of the leading anisotropic component, V_2, correspond to the C_{2v} well and C_s transition state, while the negative values attained by both the isotropic and anisotropic components at distances larger than 6 a_0 reflect the attractive nature of the van der Walls interaction.

TABLE 3: D_{3h} Minimum and Nearby Stationary Features Arising from Approximating Conical Intersection with Single-Sheeted DMBE Formalism[a]

	Min (D_{3h})	sp_1[b] (C_{2v})	sp_2 (C_{2v})
R_1/a_0	2.95	2.69	3.08
R_2/a_0	2.95	3.07	2.89
R_3/a_0	2.95	3.07	2.89
ΔE^c	146.6	151	147.5
ω_1/cm^{-1}	1278	1258i	1271
ω_2/cm^{-1}	855	1233i	964i
ω_3/cm^{-1}	855	1209	1020

[a] See the text. [b] Saddle point with two imaginary frequencies. [c] In kcal mol^{-1}, relative to the $N(^4S) + N_2$ asymptote.

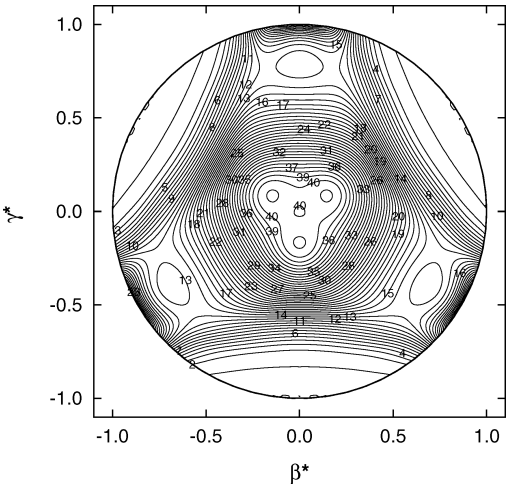

Figure 5. Relaxed triangular plot of the hypersurface. Contours are equally spaced by 6 mE_h, starting at zero.

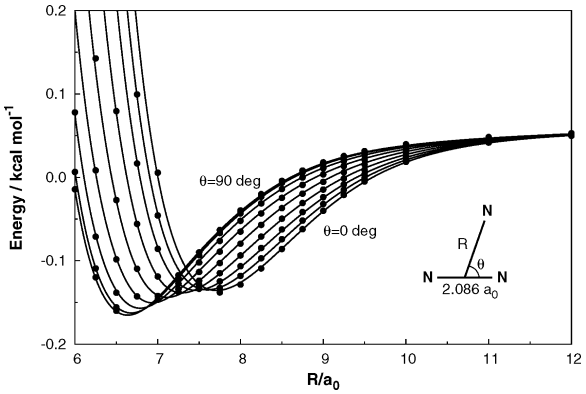

Figure 6. Cuts of DMBE potential energy surface along the atom−diatom radial coordinate for a fixed diatomic bond distance of $2.086a_0$ at the van der Waals region for several angles of insertion. The solid points are the extrapolated CCSD(T) while the lines corresponds to the fitted surface.

Finally, we report the results of a preliminary dynamics study aiming at testing the DMBE potential energy surface here reported. Specifically, we have run trajectories for the exchange reaction $N + N_2 \rightarrow N_2 + N$ using the quasiclassical trajectory method as implemented in the Venus computer code.[46] The rate constants here reported have been calculated directly using Maxwell−Boltzmann distributions for the translational energy and rovibrational quantum states.[47] Due to the high barrier of the exchange reaction ($E_0 = 45.9$ kcal mol^{-1}, including the zero-point energies of the reactants and transition state), all trajectories with internal energy below E_0 were not integrated and simply considered as nonreactive.[48] A total of 6.4×10^5 trajectories has been run for each temperature, with the impact parameter being $b_{max} = 1.8$ Å (determined as usual by a trial and error procedure). Table 4 compares the thermal rate coefficients so calculated at two temperatures with the results obtained from other potential energy surfaces. The results for the DMBE and L4 PESs have been calculated using our own QCT approach for a better comparison, while those of WSHDSP utilized the quantal J−K-shifting method. As expected from the smaller barrier in the DMBE function, a larger reactivity is predicted than with other available forms, pointing to a slightly better agreement with the available experimental data.

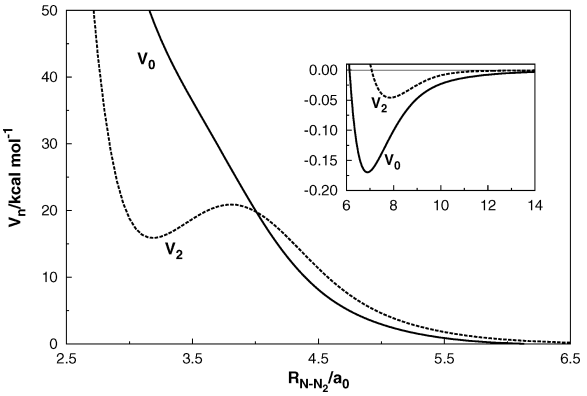

Figure 7. Isotropic (V_0) and leading anisotropic (V_2) components of the $N-N_2$ interaction potential, with the diatomic fixed at the equilibrium geometry.

TABLE 4: Logarithm of the Thermal Rate Coefficient (in cm^3s^{-1}) for the $N + N_2$ Exchange Reaction

temp (K)	DMBE[a]	L4[a]	WSHDSP[b]	exp
1273	−18.4	−18.7	−18.5	≤ -16.9[c]
3400	−12.9	−13.0	−13.0	-12.3 ± 1.0[d]

[a] From QCT calculations carried out in the present work. [b] Reference 6. [c] Reference 3. [d] Reference 4.

5. Conclusions

We have reported a single-sheeted DMBE potential energy surface for the quartet state of N_3 based on a fit to CBS extrapolated CCSD(T) and MRCI(Q) energies. A procedure of the smooth merger of these two correlated methods at the CBS-limit has been developed to calculate the points on the single potential energy surface based on the modified correlation scaling (CS)-scheme which assures that there exist no discontinuities. The MRCI(Q)/CBS energies are calibrated using the CCSD(T)/CBS result at the pivotal geometry (e.g., local minimum). In fact, the procedure is formulated in such a way that at the reference pivotal geometry of N_3 the MRCI(Q)/CBS energy coincides exactly with the CCSD(T)/CBS energy. The DMBE potential energy surface describes accurately all topographical features of the calculated ab initio energies, except for the conical intersections that have been replaced by narrowly avoided ones. As an asset of DMBE theory, the van der Waals regions are also described accurately. Finally, exploratory quasiclassical trajectories on the atom−diatom nitrogen reaction have shown that the PES is suitable for any kind of dynamics studies. A detailed report of such studies is planned for a future publication.

Acknowledgment. This work has the support of European Space Agency under ESTEC Contract No. 21790-/08/NL/HE, and Fundação para a Ciência e Tecnologia, Portugal (contracts POCI-/QUI/60501/2004, POCI/AMB/60261/2004) under the auspices of POCI 2010 of Quadro Comunitário de Apoio III cofinanced by FEDER.

Supporting Information Available: All coefficients necessary to construct the potential energy surface here reported. This material is available free of charge via the Internet at http://pubs.acs.org.

References and Notes

(1) Wang, D.; Stallcop, J. R.; Huo, W. M.; Dateo, C. E.; Schwenke, D. W.; Partridge, H. *J. Chem. Phys.* **2003**, *118*, 2186.
(2) Back, R. A.; Mui, J. Y. P. *J. Phys. Chem.* **1962**, *66*, 1362.
(3) Bar-Nun, A.; Lifshitz, A. *J. Chem. Phys.* **1967**, *47*, 2878.
(4) Lyon, R. K. *Can. J. Chem.* **1972**, *50*, 1437.
(5) Laganà, A.; Garcia, E.; Ciccarelli, L. *J. Phys. Chem.* **1987**, *91*, 312.
(6) Garcia, E.; Saracibar, A.; Laganà, A.; Skouteris, D. *J. Phys. Chem. A* **2007**, *111*, 10362.
(7) Garcia, E.; Saracibar, A.; Gomez-Carrasco, S.; Laganà, A. *Phys. Chem. Chem. Phys.* **2008**, *10*, 2552.
(8) Dunning, T. H., Jr. *J. Chem. Phys.* **1989**, *90*, 1007.
(9) Kendall, R. A.; Dunning, T. H., Jr.; Harrison, R. J. *J. Chem. Phys.* **1992**, *96*, 6769.
(10) Wang, D.; Huo, W. M.; Dateo, C. E.; Schwenke, D. W.; Stallcop, J. R. *Chem. Phys. Lett.* **2003**, *379*, 132.
(11) Wang, D.; Huo, W. M.; Dateo, C. E.; Schwenke, D. W.; Stallcop, J. R. *J. Chem. Phys.* **2004**, *120*, 6041.
(12) Varandas, A. J. C.; Murrell, J. N. *Faraday Discuss. Chem. Soc.* **1977**, *62*, 92.
(13) Murrell, J. N.; Carter, S.; Farantos, S. C.; Huxley, P.; Varandas, A. J. C. *Molecular Potential Energy Functions*; Wiley: Chichester, U.K., 1984.
(14) Werner H. J. Knowles, P. J. *MOLPRO is a package of ab initio programs*; Almlöf, J., Amos, R. D. , Deegan, M. J. O., Elbert, S. T., Hampel, C., Meyer, W., Peterson, K. A., Pitzer, R., Stone, A. J., Taylor, P. R., Lindh. R., contributors; 1998.
(15) Watts, J. D.; Gauss, J.; Bartlett, R. J. *J. Chem. Phys.* **1993**, *98*, 8718.
(16) Werner, H. J.; Knowles, P. J. *J. Chem. Phys.* **1988**, *89*, 5803.
(17) Knowles, P. J.; Werner, H. J. *Chem. Phys. Lett.* **1988**, *145*, 514.
(18) Varandas, A. J. C. *J. Chem. Phys.* **2007**, *126*, 244105.
(19) Helgaker, T.; Klopper, W.; Koch, H.; Noga, J. *J. Chem. Phys.* **1997**, *106*, 9639.
(20) Truhlar, D. G. *Chem. Phys. Lett.* **1998**, *294*, 45.
(21) Varandas, A. J. C. *J. Chem. Phys.* **2000**, *113*, 8880.
(22) Varandas, A. J. C. *J. Chem. Phys.* **2008**, *129*, 234103.
(23) Varandas, A. J. C. *Chem. Phys. Lett.* **2008**, *463*, 225.
(24) Varandas, A. J. C. *J. Comput. Chem.* **2009**, *30*, 379.
(25) Song, Y. Z.; Varandas, A. J. C. *J. Chem. Phys.* **2009**, *130*, 134317.
(26) Varandas, A. J. C. *Theor. Chem. Acc.* **2008**, *119*, 511.
(27) Boys, F.; Bernardi, F. *Mol. Phys.* **1970**, *19*, 553.
(28) Varandas, A. J. C.; Piecuch, P. *Chem. Phys. Lett.* **2006**, *430*, 448.
(29) Karton, A.; Martin, J. M. L. *Theor. Chem. Acc.* **2006**, *115*, 330.
(30) Varandas, A. J. C. *Chem. Phys. Lett.* **2007**, *443*, 398.
(31) Varandas, A. J. C. *Adv. Chem. Phys.* **1988**, *74*, 255.
(32) Varandas, A. J. C. *Advanced Series in Physical Chemistry*; World Scientific Publishing: Singapore, 2004; Chapter *5*, p 91.
(33) Varandas, A. J. C. *J. Phys. Chem. A* **2008**, *112*, 1841.
(34) Lutz, J. J.; Piecuch, P. *J. Chem. Phys.* **2008**, *128*, 154116.
(35) Varandas, A. J. C. *J. Mol. Struct. (THEOCHEM)* **1985**, *21*, 401.
(36) Varandas, A. J. C. *Lecture Notes in Chemistry*; Laganà, A., Riganelli, A., Eds.; Springer: Berlin, 2000; Vol. 75, p 33.
(37) Varandas, A. J. C.; Silva, J. D. *J. Chem. Soc., Faraday Trans.* **1992**, *88*, 941.
(38) Le Roy, R. J. *Spec. Period. Rep. Chem. Soc. Mol. Spectrosc.* **1973**, *1*, 113.
(39) Varandas, A. J. C. *J. Chem. Phys.* **1996**, *105*, 3524.
(40) Matías, M. A.; Varandas, A. J. C. *Mol. Phys.* **1990**, *70*, 623.
(41) Murrell, J. N.; Sorbie, K. S.; Varandas, A. J. C. *Mol. Phys.* **1976**, *32*, 1359.
(42) Martínez-Núñez, E.; Varandas, A. J. C. *J. Phys. Chem. A* **2001**, *105*, 5923.
(43) Longuet-Higgins, H. C. *Proc. R. Soc. Ser. A* **1975**, *344*, 147.
(44) Varandas, A. J. C.; Tennyson, J.; Murrell, J. N. *Chem. Phys. Lett.* **1979**, *61*, 431.
(45) Varandas, A. J. C. *Chem. Phys. Lett.* **1987**, *138*, 455.
(46) Hase, W. L.; Duchovic, R. J.; Hu, X.; Komornicki, A.; Lim, K. F.; Lu, D.; Peslherbe, G. H.; Swamy, K. N.; Linde, S. R. V.; Varandas, A. J. C.; Wang, H.; Wolf, R. J. *QCPE Bull.* **1996**, *16*, 43.
(47) Caridade, P. J. S. B.; Varandas, A. J. C. *J. Phys. Chem. A* **2004**, *108*, 3556.
(48) Varandas, A. J. C.; Caridade, P. J. S. B.; Zhang, J. Z. H.; Cui, Q.; Han, K. L. *J. Chem. Phys.* **2006**, *125*, 064312.

JP903719H

Quasiclassical Trajectory Study of Atom-Exchange and Vibrational Relaxation Processes in Collisions of Atomic and Molecular Nitrogen

P. J. S. B. Caridade, B. R. L. Galvão, and A. J. C. Varandas*

Departamento de Química, Universidade de Coimbra, 3004-535 Coimbra, Portugal

Received: February 24, 2010; Revised Manuscript Received: April 8, 2010

Quasiclassical trajectories have been integrated to study the exchange reaction of molecular nitrogen in collisions with atomic nitrogen for temperatures over the range of $1273 \leq T\,(\mathrm{K}) \leq 10\,000$. A recently proposed potential energy surface for the ground A'' quartet state of the system has been employed. If compared to previous theoretical studies, the results of the present work show a higher reactivity due to a lower barrier, with a study of the effect of this height in the thermal rate constant being also performed. Vibrational energy transfer via chemical reaction and/or inelastic collisions are also studied.

1. Introduction

Extreme thermal environmental conditions occur when objects enter Earth's atmosphere. Under such critical conditions, a set of chemical reactions can be promoted, ranging from simple excitation to dissociation and recombination of atoms and molecules. This has implications of key importance on the designing of heat shields for space vehicles as temperatures may reach up to 20 000 K.[1] Their consideration is also essential when simulating objects entry in different planets. One of the most relevant species found in those kinetic modeling studies is molecular nitrogen, since it is the major constituent of Earth's atmosphere as well as of the atmospheres of other planets and satellites. Under such atmospheric conditions, a great quantity of atomic nitrogen can also be found, enhanced by the interaction of molecules with radiation. Of particular relevance are therefore $N + N_2$ collisions, which have been the subject of experimental studies[2−4] at two temperatures, 1273 and 3400 K, both with large uncertainties. The extrapolation of such data to temperatures of 20 000 K or so is then subject to controversy, since it lacks reliability.

Theoretically, the $N(^4S) + N_2$ exchange reaction has been the focus of several dynamics studies relying most of them on the LEPS-type semiempirical potential energy surface (PES) of Laganà et al.[5] The barrier height for the exchange reaction on this PES has been fixed at ∼151 kJ mol^{-1} based on the experimental lower limit[2] for the activation energy. In turn, Wang et al.[1,6,7] reported a PES (hereinafter denoted by WSHDSP) from accurate coupled-cluster singles and doubles calculations with perturbative triples included, CCSD(T),[8] utilizing primarily the augmented triple-ζ basis set of Dunning's correlation consistent type[9,10] (these are generally denoted as aug-cc- pVXZ or AVXZ, with X = T for triple-ζ, Q for quadruple-ζ, and so forth). The WSHDSP PES differs drastically from the LEPS one reported by Laganà et al.,[5] with two equivalent transition states (six overall, due to the permutation symmetry of the nuclei) being predicted for reaction at a nonlinear geometry with an energy of 197 kJ mol^{-1} above the $N + N_2$ classical asymptote. Connecting both transition states is a shallow well ("Lake Eyring") lying 183 kJ mol^{-1} above the dissociation limit.

* To whom correspondence should be addressed. E-mail: varandas@qtvs1.qui.uc.pt.

Due to the inadequacy of the LEPS PES[5] to describe the main features of the nitrogen atom−diatom interaction, additional PESs have been reported ever since by Laganà and collaborators based on the so-called LAGROBO[11] method (denoted as L0, L1, L2, L3,[12,13] L4,[14] and L4w[15]) with L4 and L4w showing topographical similarities to the WSHDSP PES: two transition states (198 kJ mol^{-1}) and a shallow well (186 kJ mol^{-1}) separating them. The L4 PES has been used to study the exchange reaction by running trajectories,[14] with the results showing good agreement with the quantum ones.[1] This might be anticipated to some extent due to the large masses of the particles in play and the high energy regimes involved. Additional calculations (ref 16 and references therein) using the quasiclassical trajectory (QCT[17]) method have been performed to study energy transfer and dissociation in collisions of atomic and molecular nitrogen.

Motivated by recent progress[18,19] to obtain energies at the complete basis set (CBS) limit by scaling and extrapolation of low cost ab initio ones, a new study of the $^4A''$ state has been performed by two of us[20] for the title trinitrogen system. Using both CCSD(T)[8] and MRCI(Q)[21,22] (multireference configuration interaction including the Davidson correction) methods, extrapolated CBS energies have been calculated using AVTZ and AVQZ basis sets.[9,10] In this work, a barrier height of 192 kJ mol^{-1} has been predicted, with Eyring's potential well located 180 kJ mol^{-1} above dissociation. All CBS energies so calculated have further been utilized to calibrate a global PES using double many-body expansion[23,24] (DMBE) theory. Further predictions of the above attributes (194 and 184 kJ mol^{-1}, in the same order) that escaped our attention[20] have been reported by Zhang et al.[25] from MRCI(Q)/AVTZ calculations, among others.

A major aim of the present work is to report a detailed study of the $N + N_2$ exchange reaction based on the above DMBE PES. Because of the large barrier height, importance sampling techniques have been utilized for the translation energy such as to accelerate convergence. Since chemical deactivation can compete with reaction, a vibrational relaxation study of N_2 in collisions with N atoms has also been undertaken. The paper is planned as follows. A brief survey of the DMBE PES and QCT method is given in Section 2. Sections 3 and 4 gather the dynamics studies for reaction and vibrational relaxation, respectively. Some concluding remarks are in Section 5.

10.1021/jp101681m
Published on Web 04/22/2010

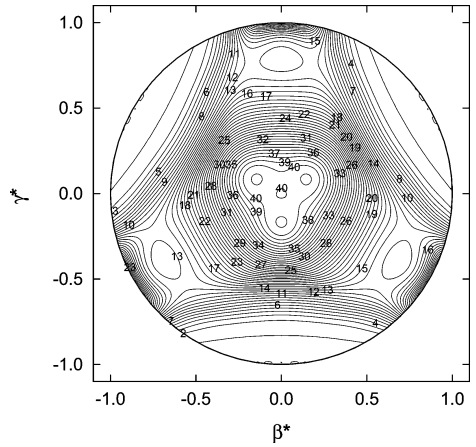

Figure 1. Relaxed triangular plot of the hypersurface. Contours are equally spaced by 16 kJ mol^{-1}, starting at zero.

2. Method

2.1. Potential Energy Surface. As already noted, dynamics calculations have been carried out using the DMBE PES reported elsewhere[20] for the ground $^4A''$ state of N_3. Briefly, this has been obtained from an extensive set of ab initio energies extrapolated to the CBS limit after being split into its CASSCF (complete active space self-consistent field) and dynamical correlation energy components. For the CASSCF energy, the extrapolation has employed an adaptation of the Karton-Martin[19,26] two-point protocol originally utilized for the Hartree−Fock energy, with AVTZ and AVQZ basis sets. In turn, the dynamical correlation energy has been obtained via a single-pivot correlation scaling/uniform singlet- and triplet-pair extrapolation scheme, CS^1/USTE(T, Q).[19] To achieve optimal performance at lowest cost, CCSD(T) calculations were performed over a dense grid of geometries and extrapolated with CS^1/USTE(T, Q). At regions of configuration space where the CCSD(T) approach does not perform well due to its single-reference nature, expensive MRCI(Q)/AV(D, T)Z calculations were performed instead and extrapolated via CS^1/USTE(T, Q) using a CCSD(T) pivotal energy to ensure the smooth merging of both sets of energies; for further details, see ref 20.

An important feature of the CBS energies in comparison with the raw AVTZ ones of WSHDSP is the lowering of the transition-state and well-depth attributes, at geometries essentially indistinguishable from each other. Such CBS energies are reproduced by the DMBE function which employed 1592 ab initio points for its calibration. Moreover, the whole PES is based upon a single, easy to explain, consistent approach. Figure 1 shows a perspective view of the DMBE/CBS PES utilizing optimized hyperspherical coordinates.[27] The overall fit shows chemical accuracy (less than 4 kJ mol^{-1}) up to 12 000 kJ mol^{-1}. Extra care has been given to the fit at stationary points such as the global minimum (i.e., at the N + N_2 van der Walls interaction where the root-mean-squared deviation is less than 4 J mol^{-1}). In comparison with previous reported PESs,[14] the calculated barrier height is smaller by 6.3 kJ mol^{-1}. Also relevant is the shallow D_{3h} minimum ($\beta^* = \gamma^* = 0$ in Figure 1) lying 336 kJ mol^{-1} below the atomization limit. This is surrounded by three equivalent C_{2v} structures arising from the conical intersection between the ground and first excited state of $^4A''$ symmetry, that is, the $^4B_1$ and $^4A_2$ states in C_{2v} symmetry.

2.2. Quasiclassical Trajectory Method. All dynamics calculations here reported have utilized the QCT method, which is widely described in the literature.[17] A time step of 0.2 fs has been chosen warranting a total energy conservation of 0.04 J mol^{-1} or smaller, with the reactants initially separated by 9 Å as the interaction is there negligibly small. The translation energy sampling has been carried out using the expression[17,28]

$$E_{tr} = k_B T \ln(\xi_1 \xi_2) \tag{1}$$

where k_B is the Boltzmann constant, and ξ_i are freshly generated random numbers (for an alternative sampling, see ref 29 and references therein). For a realistic sampling of the internal states of the $N_2(X^1\Sigma_g^+)$ molecule, the method described in ref 30 has been adopted. Briefly, it starts with the cumulative rovibrational Boltzmann distribution

$$P_{vj}(T) = \sum_{(v,j)} g_r(2j + 1) \exp(-E_{vj}/k_B T) Q_{vj}^{-1}(T) \tag{2}$$

where $Q_{vj}(T)$ is the rovibrational partition function involving all N_2 states with appropriate ortho-para symmetry weights (g_r), and the rovibrational energies (E_{vj}) are calculated by solving the nuclear Schrödinger equation for the diatomic fragment.[31] Note that the sum in eq 2 is over rovibrational states, thus avoiding the traditional energy partitioning into vibrational and rotational components. For each temperature, the (v, j) state is sampled via eq 2 when the condition $P_{vj}(T) \geq \xi_3$ is satisfied for a freshly generated random number, ξ_3. For vibrational state-specific calculations, eq 2 is also used by summing only the rotational states for a fixed v; $Q_{j,v}(T)$ will then be the rotational partition function for that specific vibrational state.

3. The N + N_2 Exchange Reaction

The N + N_2 exchange reaction has been studied by several groups using different PESs and dynamics methodologies. Wang et al.[1] used the time-dependent wavepacket method to carry out a 3D calculation on the WSHDSP PES with zero total angular momentum whereas Rampino et al.[15] employed the L4 and L4w functions to perform time-independent quantum studies also for $J = 0$. For a direct comparison of the DMBE with previously reported PESs, QCT trajectories have been run for the N + $N_2(v, j = 0)$ exchange reaction at $J = 0$. To simulate this requirement classically, the condition $\boldsymbol{L} = \boldsymbol{j}$ must be satisfied since $\boldsymbol{J} = \boldsymbol{j} + \boldsymbol{L}$. The impact parameter is therefore sampled from[32]

$$b = \left[\left(L + \frac{1}{2}\right) \pm \frac{1}{2}\right] \frac{h}{2\pi\mu v_r} \tag{3}$$

where $\boldsymbol{L}$ is the orbital angular momentum, h is Planck's constant, μ is the reduced mass of the reactants, and v_r is the relative velocity.

Panel (a) of Figure 2 shows the vibrational state-specific reaction probability as a function of the total energy calculated for three vibrational quantum numbers of N_2: $v = 0$, 1, and 2. As seen, the QCT results for $J = 0$ on the DMBE PES differ substantially from the ones reported by Rampino et al.[15] using time-independent quantum dynamics (TIQD). Such a discrepancy could possibly be attributed to the fact that the barrier for reaction predicted by the DMBE PES is 6.3 kJ mol^{-1} smaller than L4. However, when comparing the dynamical energy threshold, the differences between both PESs are substantially larger, reaching nearly 20 kJ mol^{-1} for $v = 0$. In comparison

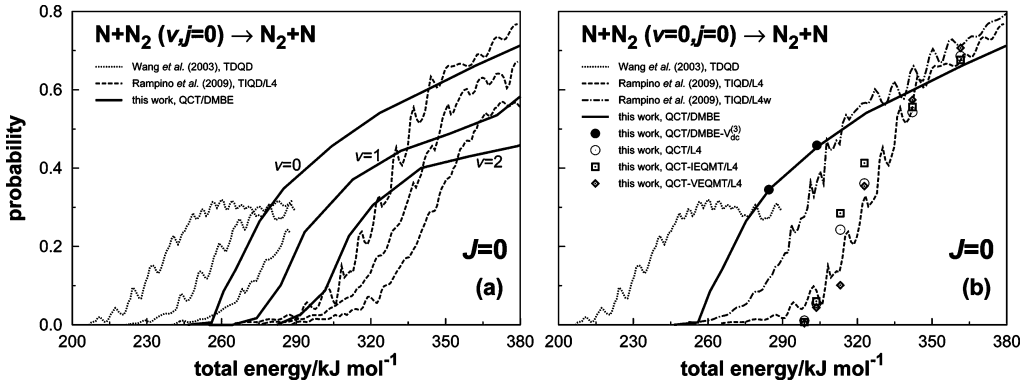

Figure 2. State-specific probabilities for $J = 0$ for different PESs. Panel (a): reactants with vibrational levels $v = 0$, 1, 2 (from left to right). Panel (b) comparison between methodologies for $v = 0$.

with previous results using time-dependent quantum dynamics (TDQD) by Wang et al.,[7] our calculations show a threshold value larger by more than 40 kJ mol^{-1}. A similar discrepancy had been noted by Rampino et al.,[15] which interpreted it as due to long-range forces. Starting from the L4 surface, they have then added an ad-hoc long-range term (the new function denoted by L4w), and the calculations repeated. Somewhat surprisingly, the reaction threshold decreased up to 20 kJ mol^{-1} as shown in panel (b) of Figure 2. In an attempt to rationalize the implications of long-range forces in the title reaction, the long-range term in DMBE has been removed and calculations performed for $v = 0$. Recall that the DMBE PES has built-in the dispersion interaction between N(^4S) and N$_2$($X^1\Sigma_g^+$). As panel (b) of Figure 2 shows, the two sets of results are indistinguishable, suggesting that such reaction cannot be strongly influenced by long-range forces. In fact, this result would somehow ought to be expected from the analysis of the energetics of the reaction, since the dynamics is mostly dictated by the large energy barrier that needs to be overcome for reaction to occur.

One could then attribute such differences to the classical nature of the dynamics approach employed in this work, in particular to the so-called zero-point energy leakage[32−34] (ZPE) problem of classical dynamics that will be analyzed later. To further compare the QCT and quantum results, additional calculations have been carried out on the L4 PES with $v = 0$ and compared with the corresponding TIQD values. The agreement between both sets of results is seen from panel (b) of Figure 2 to be good, although no attempt has been made to describe the region near threshold due to lack of statistics near such a critical point.

As note in the previous paragraph, a well-known problem of the quasiclassical trajectories in calculating reaction probabilities is ZPE leakage. Aiming to approximately account for this problem, nonactive schemes have been proposed,[29,35,36] where trajectories ending with energy lower than the zero-point energy of the diatomic are not considered for the statistical analysis. Two such (extreme) schemes are here analyzed. In QCT-IEQMT (quasiclassical trajectory-internal energy quantum mechanical threshold), the criterion imposes that the total energy of the diatomic must exceed ZPE, whereas in QCT-VEQMT (quasiclassical trajectory-vibrational energy quantum mechanical threshold) the vibrational energy itself must be superior. In addition to the QCT calculations, the above two methods were also tested and compared to the quantal results of Rampino et al.,[15] with the results being displayed on panel (b) of Figure 2. Clearly, the various QCT results compare reasonably well with the TIQD ones.

The lack of statistics and occurrence of rare events are major difficulties for the calculation of the thermal rate coefficient of reactions involving large barriers. For the title reaction, the probability of finding a trajectory above the classical threshold ($E_{tr} \geq 192$ kJ mol^{-1}) at $T = 1273$ K is $\sim 2 \times 10^{-7}$, that is, 2 in 10^7 trajectories have sufficient translational energy to overcome the barrier. A simple scheme to diminish the computational cost is the quantum mechanical threshold scheme[37] where trajectories with total energy bellow 192 kJ mol^{-1} are considered a priori as nonreactive, and hence not run. Importance sampling methods may also be used to speed up convergence, being here utilized for an adequate sampling of the impact parameter. Rather than using eq 1, the Boltzmann distribution has been sectioned, and a different number of trajectories run according to the desired statistics. According to this, the sampling for the open interval $[E' : \infty[$ is obtained as

$$G(E_{tr}) = 1 - \frac{(E_{tr} + k_B T)\exp(-E_{tr}/k_B T)}{(E' + k_B T)\exp(-E'/k_B T)} \quad (4)$$

whereas, for a finite interval $[E' : E'']$, it assumes the form

$$G(E_{tr}) = \frac{(E' + k_B T)\exp(-E'/k_B T) - (E_{tr} + k_B T)\exp(-E_{tr}/k_B T)}{(E' + k_B T)\exp(-E'/k_B T) - (E'' + k_B T)\exp(-E''/k_B T)} \quad (5)$$

In both cases, a fresh random number is generated for each trajectory with the translational energy obtained from the numerical solution of $G(E_{tr}) - \xi = 0$. The rate constant is then calculated using the sector rate constant, $k_i(T)$, multiplied by the appropriate sector weight, w_i:

$$k(T) = g_e \sum_i w_i k_i(T) \quad (6)$$

where $g_e = 1$ is the electronic degeneracy factor appropriate for the title reaction. Note that w_i can be simply evaluated as a ratio of areas under the Boltzmann distribution. The individual rate constants are then obtained by the traditional expression

$$k_i(T) = \left(\frac{8k_B T}{\pi\mu}\right)^{1/2} \pi b_{max}^2 \frac{N_r^i}{N^i} \quad (7)$$

where b_{max} is the maximum impact parameter, and N_r^i and N^i the number of reactive and total trajectories (respectively) all referring to sector i. The associated error is given by $\Delta k_i(T) = [(N^i - N_r^i)/(N^i N_r^i)]^{1/2} k_i(T)$. As usual, the impact parameter is obtained for each temperature and most reactive sector, being kept the same for all other sectors.

Although the partition into sectors is arbitrary, the pivotal energies have been chosen here as

$$E' = \Delta V^{\ddagger} + E_{ZPE}^{\ddagger} - E_{N_2} \quad (v, j = 0) \tag{8}$$

where $E_{ZPE}^{\ddagger} = 13$ kJ mol^{-1} is the ZPE at the transition state, $\Delta V^{\ddagger}$ is the barrier height, and E_{N_2} $(v, j = 0)$ is the internal energy of N_2. Specifically, we have considered the vibrational states $v = 0$ ($E' = 192$ kJ mol^{-1}), $v = 2$ ($E' = 136$ kJ mol^{-1}), and $v = 4$ ($E' = 83$ kJ mol^{-1}). To improve convergence of the calculations, an additional sector has been considered for $T = 1273$ K with the pivotal energy corresponding to the vibrational state $v = 1$ ($E' = 164$ kJ mol^{-1}). The calculations have been carried out first for large pivotal energies, and, if a particular sector has a negligible number of integrated trajectories, no additional sectors are considered. This is a typical situation for low temperatures, where only a small number of vibrational states is populated. For example, for $T = 1273$ K, only two sectors, corresponding to $v = 0$ and $v = 1$, have been considered. Conversely, for $T = 10\,000$ K, all sectors had to be taken into account since higher vibrational states become populated. The results of the calculated rate constants per sector using the present scheme are gathered in Table 1, and the total values are given in Table 2 and are shown in Figure 3. To test the importance sampling method here employed, it has also been applied to the dynamics on the L4 PES. The results are compared with the TIQD ones in Figure 3. The agreement is clearly good, especially for low temperatures. Surprisingly, despite the errors being less than 10% or so, a comparison for high temperatures is not quite as good, with the results from the present work overestimating the TIQD/L4 ones. Since convergence of the QCT calculations is known to be fast at high-T regimes, one tentatively ascribes such differences to the number of states and extrapolation method considered for the TIQD calculations.

A comparison of the QCT results on the DMBE PES with those reported for the L4 and WSHDSP ones using quantum approaches, shows an increase of the rate constant, especially at low temperature regimes. Such a behavior could be anticipated from the smaller barrier height of the DMBE form. For high temperatures, both quantum calculations point to the same limit, although, as noted previously, the QCT method predicts an even larger value. This behavior may have important implications on extrapolating the rate constant for extreme temperature regimes, where the QCT/DMBE results predict a value 2−3 times larger than the quantal ones. For completeness, the temperature dependence can be modeled via the modified Arrhenius form $k(T) = AT^m \exp(-BT^{-1})$, with the fit to our results on DMBE yielding $A = 5.8287 \times 10^{-14}$ K^{-m} cm^3 s^{-1}, $m = 0.9467$, and $B = 23327.67$ K. As Figure 3 shows, the agreement with the experimental results is far from ideal, with the large observed error bars justifying some discussion on the accuracy of the predictions made thus far.

First, we reassess the accuracy of the ab initio calculations by examining the implications on the barrier height (and ultimately on the rate constant) due to inclusion of core correlation effects. In fact, although our ab initio energies have

TABLE 1: Rate Constants Per Sector and Associated Errors ($\times 10^{-10}$ cm^3 s^{-1})[a]

temperature (K)	192.0 − ∞	(4E4)	136.5 − 192.0	(1E5)	82.71 − 136.5	(5E5)	0 − 82.71	(1E6)
1273	$0.9945 \times 10^{-2} \pm 0.6539 \times 10^{-3}$	230	$0.1003 \times 10^{-2} \pm 0.1317 \times 10^{-3}$ [b]	58				
2000	$0.3013 \times 10^{-1} \pm 0.1269 \times 10^{-2}$	556	$0.1431 \times 10^{-2} \pm 0.1761 \times 10^{-3}$	66				
3400	$0.1068 \pm 0.2695 \times 10^{-2}$	1512	$0.1001 \times 10^{-1} \pm 0.5309 \times 10^{-3}$	354	$0.1357 \times 10^{-3} \pm 0.2769 \times 10^{-4}$	24		
4000	$0.1469 \pm 0.3274 \times 10^{-2}$	1917	$0.1637 \times 10^{-1} \pm 0.7066 \times 10^{-3}$	534	$0.2453 \times 10^{-3} \pm 0.3878 \times 10^{-4}$	40		
5000	$0.2382 \pm 0.4358 \times 10^{-2}$	2780	$0.3222 \times 10^{-1} \pm 0.1046 \times 10^{-2}$	940	$0.1337 \times 10^{-2} \pm 0.9571 \times 10^{-4}$	195		
10 000	$0.9261 \pm 0.2007 \times 10^{-1}$	2021	$0.2148 \pm 0.6238 \times 10^{-2}$	1172	$0.4912 \times 10^{-1} \pm 0.1340 \times 10^{-2}$	1340	$0.7936 \times 10^{-2} \pm 0.3813 \times 10^{-3}$	433

[a] The energy intervals for each sector are displayed (in kJ mol^{-1}) with the total number of trajectories given in parentheses. Algo given is the number of reactive trajectories. [b] For this temperature the batch has been shortened to start at 164 ($v = 1$).

TABLE 2: Logarithm of the Thermal Rate Coefficients (in $cm^3\ s^{-1}$) for the N + N_2 Exchange Reaction

temperature (K)	DMBE[a]	L4[a]	WSHDSP[b]	experimental
1273	$-18.27^{0.04}_{-0.05}$	−18.54	−18.5	≤ −16.9[c]
2000	$-15.15^{0.03}_{-0.04}$	−15.38		
3400	$-12.87^{0.02}_{-0.02}$	−12.99	−13.0	−12.3 ± 1.0[d]
4000	$-12.38^{0.01}_{-0.01}$	−12.44		
5000	$-11.77^{0.01}_{-0.01}$	−11.83		
10 000	$-10.45^{0.01}_{-0.01}$	−10.42		

[a] QCT calculations performed in this work. [b] Reference 13. [c] Experiment from ref 3. [d] Experiment from ref 4.

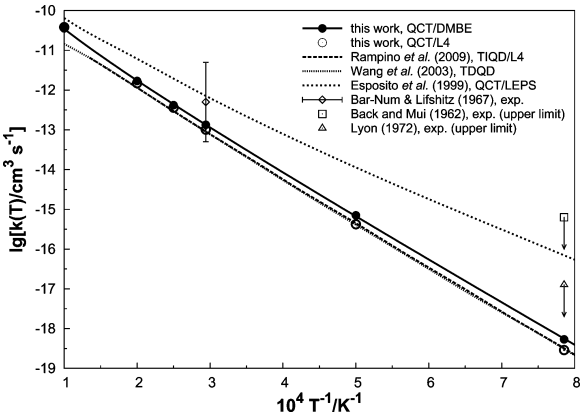

Figure 3. Comparison of the rate constants on the DMBE PES with other data available in literature.

been extrapolated to the CBS limit, the neglect of core-correlation and other effects (relativistic, non-Born−Oppenheimer, etc) can be possible sources of error.

Calculations employing the CCSD(T) method have then be performed with and without core-correlation for fixed molecular geometries with large basis sets such as AVQZ, ACVQZ and pw-CVQZ. Although the results obtained show only a small effect, their predictions are somewhat contradictory possibly due to the fact that the calculations done with the ACVQZ and pw-CVQZ basis have been done at the barrier-geometry predicted from CCSD(T)/AVQZ calculations (this is nearly coincident with the DMBE one) rather than at geometries consistently optimized with such basis. Specifically, a decrease of the barrier height by 1.59 kJ mol^{-1} is predicted with the AVQZ basis (not optimal for studying core correlation effects), whereas increases of 0.70 kJ mol^{-1} and 0.74 kJ mol^{-1} are predicted with the ACVQZ and pw-CVQZ ones (respectively). Of course, relativistic and non Born−Oppenheimer effects are still ignored, although one may expect them to be smaller than the core-correlation[38] ones.

Further trajectories have been run on a modified DMBE PES with a barrier tentatively adjusted to 188 kJ mol^{-1}, thus 4 kJ mol^{-1} lower than the value currently displayed by the DMBE form. The results so obtained show only a slightly enhanced reactivity, and hence are not presented in Figure 3. Instead, we show for comparison similar QCT results by Esposito et al.[39] that have been obtained on a LEPS PES[5] calibrated to fit the rate constant data (this shows a barrier height of ∼151 kJ mol^{-1}). Although, as might be expected, the results show a significantly enhanced reactivity, it should be noted that any drastic reduction of the barrier height to reproduce the experimental value[3] at 3400 K yields a PES that fails (at least) to obey the experimental upper limit[4] of the rate constant at 1273 K (open uptriangle).

We conclude this section with the analysis of the vibrational and rotational distribution of the newly formed N_2 on the DMBE and L4 PESs. For this, we have utilized the momentum Gaussian binning (MGB) method.[40] Briefly, the probability of a rovibrational state (v, j) is given by

$$P_{vj} = \sum_{i=1}^{N} W^i_{vj} \tag{9}$$

where $W^i_{vj} \sim W^i_v W^i_j$, and

$$W^i_k = \frac{1}{\rho_k\sqrt{\pi}} \exp\left[-\left(\frac{\sqrt{E_k} - \sqrt{\varepsilon^i_k}}{\rho_k\sqrt{\bar{E}_k}}\right)^2\right] \tag{10}$$

where E_k is the kth diatomic energy eigenvalue, $\bar{E}_k$ is an average separation between neighboring levels, and ε^i_k is the final energy of the ith trajectory (vibrational or rotational). The Gaussian-decay parameters ρ_v and ρ_j therefore act like fine-tuning constants for further realism. The use of the value $\rho_v = 0.1$ accounts in an approximate way for ZPE leakage, because in this case the contribution to the ground vibrational state population (W^i_0) of a trajectory ending with a vibrational energy $E_v = 0.9E_0$ turns out to be about 48% of the value that would actually be obtained if $E_v = E_0$. In turn, the determination of ρ_j comes from the observation that the spacing of rotational levels is smaller than the vibrational ones; thus, a more accentuated Gaussian decay is expected, that is, $\rho_v/\rho_j < 1$. Its value is then fixed from the ratio of the averaged square-root of vibrational and rotational spacings, with the latter estimated by considering all vibrational states. This yields $\rho_j = 0.234$ for the DMBE PES, and $\rho_j = 0.235$ for L4. For further details, the reader is referred to the original paper.[40]

Figure 4 shows a contour plot for the state-specific probabilities as a function of the product's rovibrational level for $T = 3400$ K. For clarity, the contours have been drawn after fitting the raw results to Boltzmann function such as to provide a smooth behavior. As seen, the DMBE PES shows a vibrationally cooler product's distribution, with the highest probability occurring for $v' = 0$ and $j' = 24$, whereas the L4 PES shows a broader bimodal distribution centered at $v' = 0$ and $v' = 8$.

4. Vibrational Energy Transfer

Vibrational energy transfer via exchange reaction, N + $N_2(v)$ → $N_2(v')$ + N, has been studied using the MBG analysis reported in the previous section, with the rate constants and ratios reported in Table 3 for $T = 3400$ K. One salient feature from these results is the contribution of multiquanta transitions for vibrational relaxation, which clearly dominates over excitation. The most probable transition involves the ground vibrational state as final outcome irrespective of the initial one. For example, for initial vibrational state $v = 5$, the contribution to $v' = 0$ is 36% whereas one-quantum transitions amount to only 13%. The behavior here reported suggests a statistical-type reaction, where all vibrational states have equal probability of occurrence. This may be attributed to the Lake Eyring, which may allow some randomization of the internal energy of N_3. As for excitation, the dominant process corresponds to one-quantum transitions. Note, however, that with the increase of the initial vibrational state the energy difference between the levels becomes smaller, and the dominance of the one-quantum excitation becomes diluted within the statistical error of the QCT

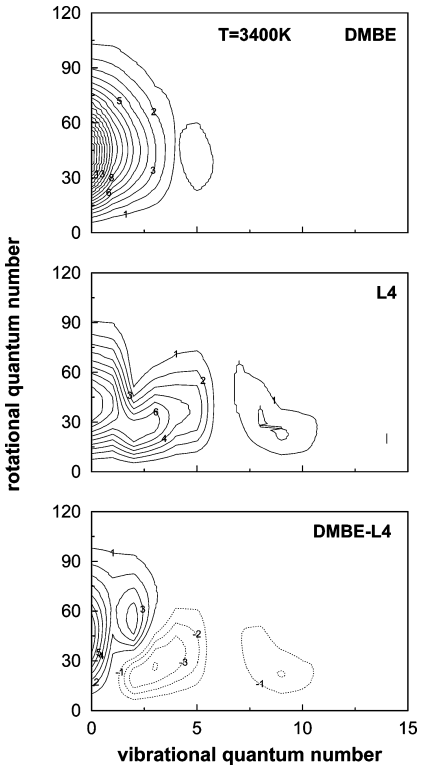

Figure 4. Comparison of the distributions of the products after an exchange reaction between L4 and DMBE PESs. The solid lines are the probability contours starting at 0 and spaced by 0.0001. The dotted lines in the bottom panel (differences) show negative values (where L4 has a higher probability).

method. Analyzing the vibrational-to-all processes we may verify a different behavior. In the case of excitation, the magnitude of the rate constant is nearly independent of the initial vibrational state, except for one-quantum excitations $v = 0 \rightarrow 1$, whereas for deactivation the rate constant for high initial states is almost 5 times larger than the corresponding low-v ones. This may be a consequence of the higher initial internal energy of N_2, which, upon randomization between the various normal modes of the supermolecule, will populate almost equally all vibrational states under $v' = 5$.

The $N + N_2(v)$ energy transfer processes have already been described in detail,[5,16] covering most of the vibrational spectra of the N_2 molecule. In the following, we concentrate on the inelastic state-specific vibrational energy transfer from the rotational-translational thermalized reactants. Thus, we have considered for the analysis only those trajectories that had not sufficient energy to overcome the barrier or, if having done so, returned to the reactants channel. To achieve such a goal, we have used the QCT method of Section 2 for initial vibrational states of $0 \leq v \leq 6$, and temperatures of 3400, 5000, and 10 000 K, being the results analyzed with the MGB method.[40] Although calculations have also been carried out for 1273 K, the reaction is very inefficient for vibrational energy transfer at such a temperature and hence will not be reported.

The final results are presented in Table 4 where one can appreciate the importance of one quantum transition for excitation and deactivation processes, with such behavior being encountered for the three temperatures here studied. Although multiquanta transitions may occur, their contribution is residual, being smaller than 10% for all temperatures and initial vibrational states of the N_2 molecule. Such behavior is closely related with the lack of a deep minimum that would allow energy randomization between the degrees of freedom of the N_3 system. Note that the translational energy and internal excitation (rotational) arises from a Maxwell−Boltzmann distribution and so the total energy content of the system is not enough to overpass the barrier for isomerization and reach the Lake Eyring structure. This contrasts with the case of vibrational energy transfer where bond-breaking is present (see above), being a totally distinct energy transfer process. It is also clear from Table 4 that the probability of the excitation process is, for all temperatures and initial vibrational states, larger than the relaxation one. This is so irrespective of whether one quantum transitions or state-to-all transitions are considered. Such a dominance of excitation over deactivation is illustrated in Figure 5 where the discrepancy is even seen to increase for high temperatures.

For a better understanding of the energy transfer between the different degrees of freedom, and to rationalize the above-mentioned feature of these nonreactive collisions, we now analyze the rotational distribution for a typical process, namely the $v = 4$ quantum transitions at $T = 5000$ K for which rotational temperatures have been obtained by fitting $\ln[P_{vj}/(2j + 1)]$ against the rotational energy.[41] To obtain a smooth representation, we have followed ref 42 by using a smoothing technique whereby each data value is replaced by an average of itself and six nearby neighbors, three to the left and three to the right. As seen from Figure 6, the initial state shows a typical Maxwell−Boltzmann distribution of the rotational levels that peaks at $j = 30$, with the rotational temperature being 4927 K (the oscillations arise from the ortho-para symmetry weights). After the collision process, higher rotational levels become populated for both relaxation and excitation, being the new rotational temperatures 7601 and 13 772 K, respectively. For the relaxation case, a vibrational to rotational energy transfer occurs, with the rotational peak moving to $j' = 48$. However, for the more probable vibrational excitation events, the distribution is found to be bimodal with the distribution peaking at $j' = 55$ and $j' = 98$. If such a distribution is considered to be genuine, one should rather fit the data to a sum of two Boltzmann distributions. This yields two temperatures: 6158 K for the cold distribution (close to the temperature of the initial distribution), and 18 683 K for the other much warmer one.

TABLE 3: Rate Coefficients (in 10^{15} cm^3 s^{-1}) and Branching Ratios for the Chemical Vibrational Relaxation $N + N_2(v) \rightarrow N_2(v') + N$ with $T = 3400$ K

v	$v' = 0$	1	2	3	4	5	$v \rightarrow$ all ($v' < v$)	$v \rightarrow$ all ($v' > v$)
0		31.53 (0.61)	12.64 (0.24)	4.792 (0.09)	2.065 (0.04)	1.016 (0.02)		52.03 (1.00)
1	61.45 (0.68)		17.18 (0.19)	6.754 (0.07)	3.196 (0.04)	2.170 (0.02)	61.45 (0.68)	29.30 (0.32)
2	65.80 (0.49)	45.20 (0.34)		13.03 (0.10)	7.387 (0.06)	1.927 (0.01)	111.0 (0.83)	22.34 (0.17)
3	78.83 (0.41)	50.43 (0.26)	40.42 (0.21)		12.30 (0.06)	9.501 (0.05)	169.7 (0.87)	21.80 (0.11)
4	97.40 (0.35)	68.39 (0.25)	52.92 (0.19)	36.68 (0.13)		20.82 (0.08)	255.4 (0.92)	20.82 (0.08)
5	136.3 (0.36)	69.86 (0.18)	85.63 (0.23)	39.07 (0.10)	49.28 (0.13)		380.2 (1.00)	

TABLE 4: State-to-State and State-to-All Rate Constants and Branching Ratios for the N + N_2 Vibrational Energy Transfer (in cm^3 s^{-1})

v	$v' = 0$	1	2	3	4	5	6	7	8	$v \rightarrow$ all ($v' < v$)	$v \rightarrow$ all ($v' > v$)
$T = 3400$K	10^{13} k										
0		0.621(0.946)	0.035(0.054)								0.656(1.00)
1	0.559(0.213)		1.793(0.683)	0.116(0.044)	0.102(0.039)	0.054(0.021)				0.559(0.21)	2.065(0.79)
2	0.109(0.017)	1.491(0.238)		4.254(0.680)	0.303(0.048)	0.042(0.007)	0.001(0.000)	0.054(0.009)		1.600(0.26)	4.654(0.74)
4	0.163(0.012)	0.219(0.016)	0.653(0.046)	5.829(0.414)		7.056(0.501)	0.105(0.007)		0.054(0.004)	6.864(0.49)	7.215(0.52)
6	0.422(0.010)	1.759(0.041)	0.545(0.013)	0.545(0.013)	1.093(0.026)	14.451(0.339)		23.764(0.557)	0.070(0.002)	18.815(0.44)	23.834(0.56)
$T = 5000$ K	$10^{12}k$										
0		1.275(0.888)	0.102(0.071)	0.025(0.018)	0.015(0.010)	0.006(0.004)		0.004(0.003)			1.427(1.00)
1	0.485(0.147)		2.564(0.776)	0.127(0.038)	0.067(0.020)	0.020(0.006)	0.022(0.007)	0.011(0.003)	0.005(0.001)	0.485(0.15)	2.816(0.85)
2	0.103(0.018)	1.641(0.288)		3.680(0.646)	0.178(0.031)	0.067(0.012)	0.013(0.002)	0.013(0.002)		1.744(0.31)	3.951(0.69)
4	0.019(0.002)	0.230(0.020)	0.492(0.043)	4.392(0.380)		5.905(0.512)	0.380(0.033)	0.073(0.006)	0.036(0.003)	5.133(0.45)	6.394(0.55)
6	0.095(0.005)	0.192(0.010)	0.379(0.019)	0.190(0.010)	0.774(0.039)	6.903(0.347)		10.620(0.534)	0.606(0.030)	8.533(0.43)	11.226(0.57)
$T = 10\,000$ K	$10^{11}k$										
0		3.019(0.782)	0.458(0.119)	0.149(0.039)	0.067(0.017)	0.036(0.009)	0.022(0.006)	0.021(0.005)	0.016(0.004)		3.787(1.00)
1	1.033(0.134)		5.520(0.714)	0.618(0.080)	0.207(0.027)	0.103(0.013)	0.065(0.008)	0.041(0.005)	0.041(0.005)	1.033(0.14)	6.595(0.86)
2	0.307(0.031)	1.965(0.198)		6.316(0.638)	0.736(0.074)	0.183(0.019)	0.129(0.013)	0.067(0.007)	0.036(0.004)	2.272(0.23)	7.467(0.77)
4	0.086(0.006)	0.305(0.023)	0.726(0.054)	3.111(0.230)		7.391(0.547)	1.132(0.084)	0.345(0.026)	0.149(0.011)	4.228(0.32)	9.017(0.68)
6	0.081(0.005)	0.228(0.013)	0.218(0.013)	0.501(0.029)	0.987(0.057)	4.491(0.260)		8.314(0.481)	1.451(0.084)	6.506(0.40)	9.765(0.60)

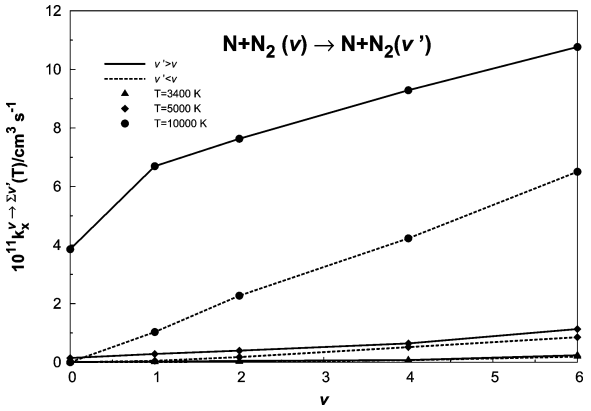

Figure 5. State-specific vibrational excitation (solid lines) and relaxation (dashed lines) rate constants for different temperatures.

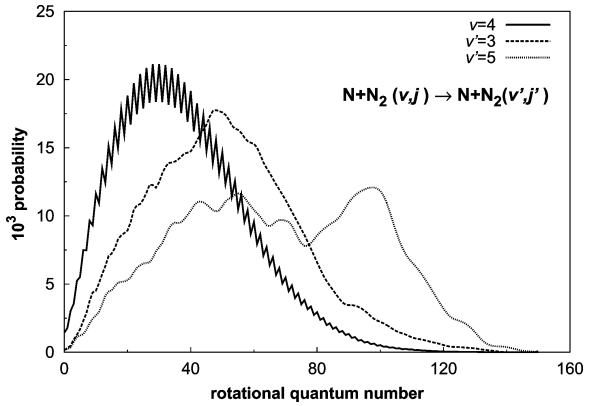

Figure 6. Rotational distribution of the N_2 molecule at $T = 5000$ K for the initial vibrational state $v = 4$ and after collision with one-quantum relaxation ($v' = 3$) and excitation ($v' = 5$). Note that all curves have a normalized probability.

Note that an increase in both the populated rotational and vibrational levels is observed, which seems to indicate that the translational energy may play an important role by being converted into ro-vibrational energy. This may also explain why products can be found in a translational "cold" state.

5. Concluding Remarks

The dynamics of the N + N_2 reaction has been studied by running trajectories on a recently reported ab initio-based DMBE PES for N_3. An importance sampling scheme has been employed for the calculations, thus significantly reducing the computational effort required for desired accuracy. Extensive comparisons with previous theoretical predictions have also been performed, with the results showing a higher reactivity than the most reliable ones reported thus far. An improved agreement with the experimental results has also been obtained, even though the former contain large uncertainties. The state specific reaction probabilities for zero total angular momentum have also been investigated for different energy levels of the N_2 diatomic. A large discrepancy is observed between the previously reported theoretical results of Wang et al.,[7] and our own predictions. An explanation for such differences is yet unclear. Finally, a study has been carried out of vibrational energy transfer in both reactive and nonreactive collisions. For reaction, the results show a tendency to favor products in the ground vibrational state, whereas one-quantum transitions are dominant in the nonreactive process.

Acknowledgment. This work has the support of European Space Agency under ESTEC Contract No. 21790-/08/NL/HE, and Fundaçao para a Ciencia e Tecnologia, Portugal, under contracts PTDC/QUI-QUI/099744/2008 and PTDC/AAC-AMB/099737/2008.

References and Notes

(1) Wang, D.; Stallcop, J. R.; Huo, W. M.; Dateo, C. E.; Schwenke, D. W.; Partridge, H. *J. Chem. Phys.* **2003**, *118*, 2186.
(2) Back, R. A.; Mui, J. Y. P. *J. Phys. Chem.* **1962**, *66*, 1362.
(3) Bar-Nun, A.; Lifshitz, A. *J. Chem. Phys.* **1967**, *47*, 2878.
(4) Lyon, R. K. *Can. J. Chem.* **1972**, *50*, 1437.
(5) Laganà, A.; Garcia, E.; Ciccarelli, L. *J. Phys. Chem.* **1987**, *91*, 312.
(6) Wang, D.; Huo, W. M.; Dateo, C. E.; Schwenke, D. W.; Stallcop, J. R. *Chem. Phys. Lett.* **2003**, *379*, 132.
(7) Wang, D.; Huo, W. M.; Dateo, C. E.; Schwenke, D. W.; Stallcop, J. R. *J. Chem. Phys.* **2004**, *120*, 6041.
(8) Watts, J. D.; Gauss, J.; Bartlett, R. J. *J. Chem. Phys.* **1993**, *98*, 8718.
(9) Dunning, T. H. *J. Chem. Phys.* **1989**, *90*, 1007.
(10) Kendall, R. A.; Dunning, T. H., Jr.; Harrison, R. J. *J. Chem. Phys.* **1992**, *96*, 6796.
(11) Garcia, E.; Laganà, A. *J. Chem. Phys.* **1995**, *103*, 5410.
(12) Garcia, E.; Laganà, A. *J. Phys. Chem. A* **1997**, *101*, 4734.
(13) Garcia, E.; Saracibar, A.; Laganà, A.; Skouteris, D.; Phys, J. **2007**, *111*, 10362.
(14) Garcia, E.; Saracibar, A.; Gomez-Carrasco, S.; Laganà, A. *Phys. Chem. Chem. Phys.* **2008**, *10*, 2552.
(15) Rampino, S.; Skouteris, D.; Laganà, A.; Garcia, E.; Saracibar, A. *Phys. Chem. Chem. Phys.* **2009**, *11*, 1752.
(16) Esposito, F.; Armenise, I.; Capitelli, M. *Chem. Phys.* **2006**, *331*, 1.
(17) Peslherbe, G. H.; Wang, H.; Hase, W. L. *Adv. Chem. Phys.* **1999**, *105*, 171.
(18) Varandas, A. J. C. *J. Chem. Phys.* **2007**, *126*, 244105.
(19) Varandas, A. J. C. *Chem. Phys. Lett.* **2007**, *443*, 398.
(20) Galvão, B. R. L.; Varandas, A. J. C.; Phys, J. **2009**, *113*, 14424.
(21) Werner, H.-J.; Knowles, P. J. *J. Chem. Phys.* **1988**, *89*, 5803.
(22) Werner, H.-J.; Knowles, P. J. *Chem. Phys. Lett.* **1988**, *145*, 514.
(23) Varandas, A. J. C. *Adv. Chem. Phys.* **1988**, *74*, 255.
(24) Varandas, A. J. C., *Modeling and Interpolation of Global Multi-Sheeted Potential Energy Surfaces*; Advanced Series in Physical Chemistry; World Scientific Publishing: 2004; *Ch 5*, pp 91.
(25) Zhang, P.; Morokuma, K.; Wodtke, A. M. *J. Chem. Phys.* **2005**, *122*, 014106.
(26) Karton, A.; Martin, J. M. L. *Theoret. Chim. Acta.* **2006**, *115*, 330.
(27) Varandas, A. J. C. *Chem. Phys. Lett.* **1987**, *138*, 455.
(28) Hase, W. L.; Duchovic, R. J.; Hu, X.; Komornik, A.; Lim, K. F.; Lu, D.-H.; Peslherbe, G. H.; Swamy, K. N.; van de Linde, S. R.; Varandas, A. J. C.; Wang, H.; Wolf, R. J. *VENUS96, QCPE Bull.* **1996**, *16*, 43.
(29) Varandas, A. J. C.; Brandão, J.; Pastrana, M. R. *J. Chem. Phys.* **1992**, *96*, 5137.
(30) Caridade, P. J. S. B.; Varandas, A. J. C. *J. Phys. Chem. A* **2004**, *108*, 3556.
(31) LeRoy, R. J. *LEVEL 7.5: A Computer Program for Solving the Radial Schrödinger Equation for Bound and Quasi-Bound Levels*; University of Waterloo Chemical Physics Research Report CP-(2002).655; University of Waterloo: **2002**.
(32) Varandas, A. J. C. *Chem. Phys. Lett.* **1994**, *225*, 18.
(33) Varandas, A. J. C. *J. Chem. Phys.* **1993**, *99*, 1076.
(34) Varandas, A. J. C. *Chem. Phys. Lett.* **1995**, *235*, 111.
(35) Varandas, A. J. C.; Marques, J. M. C. *J. Chem. Phys.* **1992**, *97*, 4050.
(36) Varandas, A. J. C.; Zhang, L. *Chem. Phys. Lett.* **2004**, *385*, 409.
(37) Truhlar, D. G. *J. Phys. Chem.* **1979**, *83*, 188.
(38) Polyansky, O. L.; Császár, A. G.; Shirin, S. V.; Zobov, N. F.; Barletta, P.; Tennyson, J.; Schwenke, D. W.; Knowles, P. J. *Science* **2003**, *299*, 539.
(39) Esposito, F.; Capitelli, M. *Chem. Phys. Lett.* **1999**, *302*, 49.
(40) Varandas, A. J. C. *Chem. Phys. Lett.* **2007**, *439*, 386.
(41) Varandas, A. J. C.; Llanio-Trujillo, J. L. *J. Theor. Comp. Chem.* **2002**, *1*, 31.
(42) Varandas, A. J. C. *Mol. Phys.* **1995**, *85*, 1159.

JP101681M

Quasiclassical Trajectory Study of the Rotational Distribution for the O + NO($v = 0$) Fundamental Vibrational Excitation

B. R. L. GALVÃO,[1] J. A. CORZO-ESPINOZA,[2] P. J. S. B. CARIDADE,[1] A. J. C. VARANDAS[1]

[1]*Departamento de Química, Universidade de Coimbra, 3004-535 Coimbra, Portugal*
[2]*Universidad Camilo Cienfuegos, Matanzas, Cuba*

Received 30 September 2010; revised 26 November 2011, 16 February 2011; accepted 18 February 2011

DOI 10.1002/kin.20560
Published online 27 April 2011 in Wiley Online Library (wileyonlinelibrary.com).

ABSTRACT: Quasiclassical trajectories have been run to study the fundamental one-quantum vibrational transition formed from collisions of ground-state nitric oxide with atomic oxygen at temperatures of 500, 750, and 1000 K. Two adiabatic potential energy surfaces of different symmetry ($^2A'$ and $^2A''$ of NO_2) have been utilized. The rate constant for the title process is given along with the rotational distributions, and the results shown to corroborate previous atmospheric models that describe the nascent state by a Maxwell–Boltzmann distribution at the local temperature. © 2011 Wiley Periodicals, Inc. Int J Chem Kinet 43: 345–352, 2011

INTRODUCTION

Nitric oxide in its first vibrationally excited state NO($v = 1$) is abundant in the Earth thermosphere, and the infrared emission resulting from de-excitation is known to play an important role on the cooling down mechanism of the atmosphere [1,2]. The P and R branches of the vibrational–rotational emission fall into the 5.3-μm region, and its spectra have been obtained with the Cryogenic Infrared Instrumentation for Shuttle (CIRRIS-1A) aboard the space shuttle Discovery. This experiment has shown [3,4] that such a vibrational level is populated via the superposition of two components, a nonthermal part that is originated from the N(^4S) + O_2 reaction and a thermal one due to NO formed from the collision

$$NO(v = 0) + O \rightarrow NO(v = 1) + O \qquad (1)$$

The CIRRIS-1A nighttime limb radiance has been inverted [5] to obtain the local rotational envelopes of the $1 \rightarrow 0$ vibrational transitions, and from this the rotational temperature as a function of altitude. Since there is no a priori reason to expect that the collisions in Eq. (1) should yield rotationally thermalized NO($v = 1$), the altitude/temperature dependence

Correspondence to: A. J. C. Varandas; e-mail: varandas@qtvs1.qui.uc.pt.
Present address of J. A. Corzo-Espinoza: Departamento de Química, Universidade de Coimbra, 3004-535 Coimbra, Portugal.
Contract grant sponsor: Fundação para a Ciência e Tecnologia, Portugal.
Contract grant numbers: PTDC/QUI-QUI/099744/2008 and PTDC/AAC-AMB/099737/2008.

so obtained might not correspond to the local atmospheric one. However, Quack and Troe [6] have used a statistical adiabatic model to calculate the rotational distribution of the nascent nitric oxide at higher altitudes, having predicted it to peak around the initial rotational levels. This suggests that the rotational envelopes of the 5.3-μm emission could be described by a Maxwell–Boltzmann distribution with the local translational temperature (as has been frequently assumed [2,7]), thus justifying the assumption of thermalized rotation.

There is also the possibility that subsequent collisions of the nascent nitric oxide may cause thermalization, since for low altitudes several collisions may happen during a radiative lifetime. Such a hypothesis has been investigated theoretically by Sharma and Duff [8] by running quasiclassical trajectories (QCT) on two London–Eyring–Polanyi–Sato (LEPS) potential energy surfaces (PESs) [9]. They concluded that the rotational temperature describing the nascent distribution ($T_{\rm rot}$) is about 25% lower than the initial temperature (T) and equalizes it after 3 or 5 collisions. Since for altitudes higher than 130 km ($T \geq 500$ K) no collisions during a radiative lifetime of vibrationally excited NO (around 0.08 s) can be expected, the correspondence $T_{\rm rot} = T$ would not hold. Based on such findings, a suitable relation between $T_{\rm rot}$ and T was proposed and the $T_{\rm rot}$/altitude profile [5] corrected to obtain the local atmospheric temperature. This is an interesting result, since only a few techniques are available to measure the temperature in the lower thermosphere [10].

It is well known, however, that the results of dynamics calculations are strongly influenced by the attributes of the PESs used to integrate the equations of motion, and the functional forms that have been employed in the above study are likely to describe poorly important regions of the molecule configuration space. In fact, they have been fitted to ab initio energies [11,12] covering only the vicinity of the NO_2 minimum.

Since the work of Sharma and Duff [8], higher quality ab initio calculations for both $^2A'$ and $^2A''$ PESs, as well as new analytical fits, have been reported that may be utilized to study the dynamics of NO_2. For example Sayós et al. have reported a series of studies [13,14] for different states of the NO_2 system, focusing mainly on the study of $N + O_2$ collision, whereas Ivanov et al. [15] studied exchange and recombination on the $O(^3P) + NO(^2\Pi)$ reaction with a newly fitted potential function. Although there is a vast literature on the NO_2 system (a complete review is out of the scope of this work), the specificity of the energy transfer of the title transition makes it a subject not so extensively explored. The major goal of this work is therefore to provide a deeper insight on the title energy transfer process. The paper is organized as follows: The section Potential Energy Surfaces provides a survey on the PESs employed, whereas the section QCT Calculations describes the quasiclassical trajectories method. The major results are analyzed in the Section Results and Discussion, and the last section presents the conclusions.

POTENTIAL ENERGY SURFACES

Several adiabatic PESs of different spatial and spin symmetries dissociate to the $O(^3P) + NO(X^2\Pi)$ asymptote, and collisions between these fragments can therefore take place through any of them. However, for a study of the energy transfer process, the contribution of the excited repulsive potentials can be considered as negligible if compared to those that show stable minima. In the case of the title reaction, it is a good approximation to consider only the lowest doublet state of A' and A'' symmetries. In fact, test calculation have shown that the ground quartet state PES can be considered as inefficient for vibrational energy transfer [16].

An accurate analytical representation for studies on the $^2A'$ states of NO_2 is perhaps the multisheeted double many-body expansion [17–20] (DMBE) PES [21], which includes the lowest eight states of the system and reproduces the main topological features of the two lowest states. Indeed, this PES attains near spectroscopy accuracy in regions close to the minimum, which has been obtained by merging the DMBE form with a spectroscopically accurate Taylor series expansion [22] via a multiple energy-switching (ES) [23–26] scheme. Specifically, the multisheeted DMBE PES is based on an 8×8 Hamiltonian matrix constructed via diatomics-in-molecules formalism (see, e.g., [27]), where each matrix element is dressed (corrected) with three-body energy terms that were calibrated using both theoretical and experimental data. In particular, of the manifold of eight $^2A'$ PESs that is obtained upon diagonalization of the potential matrix, the ground-state ($1^2A'$) PES describes accurately all topographical features (the well depth of 3.23 eV matches perfectly the experimental value [28]). It also reproduces the vibrational spectrum of the triatomic, as expected from the ES method mentioned above.

Although the $^2A''$ state is not as much studied as the $^2A'$ one, it also contributes to the reaction dynamics and was included in this work by using the MBE [29] potential energy surface of González et al. [14]. It has been calibrated with ab initio energies calculated at the complete active space self-consistent field (CASSCF)

and second-order perturbation theory using as reference the CASSCF wave function (CASPT2) based on the triple-zeta correlation consistent basis set of Dunning [30,31], generally denoted as cc-pVTZ or simply VTZ. It shows a well depth of 1.02 eV. To correct such a potential to account to long-range interactions, a term [16] that approximately mimics the desired behavior has been added. This accounts for the electrostatic and dispersion energies as obtained from the work of Reignier et al. [32] with the long-range coefficients damped such as to account for charge overlap and exchange effects.

QCT CALCULATIONS

Rate constants for vibrational excitation in O + NO($v = 0$) → O + NO($v = 1$) collisions have been calculated by running independently quasiclassical trajectories [33] for each PES. The initial conditions of the system are simulated as an equilibrium state, where both the initial translational temperature of the reactants and rotational temperature of NO($v = 0$) are thermalized at a fixed value, corresponding to the local atmospheric temperature (T). The nonequilibrium rotational distribution of nascent NO($v = 1$) is subsequently analyzed to obtain a correspondence between its rotational temperature T_{rot} and the initial temperature T (corresponding to the atmospheric one). All trajectories have been run starting with the reactants initially separated by 9 Å (as the interaction is there negligibly small) and using a time step of 0.2 fs such as to warrant a total energy conservation of 0.04 J mol^{-1} or smaller. The translational energy sampling has been done using the expression [33,34]

$$E_{\text{tr}} = k_B T \ln(\xi_1 \xi_2) \tag{2}$$

where k_B is the Boltzmann constant, and ξ_i are freshly generated random numbers (for alternative samplings, see [35,36] and references therein). For a realistic sampling of the rotational states of the NO($v = 0$) diatomic, the method described in [37] has been adopted. Briefly, it starts with the cumulative rotational Boltzmann distribution

$$P_{j;v=0}(T) = \sum_{j''=j_0}^{j} (2j'' + 1) \times \exp(-E_{j'';v=0}/k_B T) Q^{-1}_{j;v=0}(T) \tag{3}$$

where $Q_{j,v=0}(T)$ is the rotational partition function for the vibrational ground state of NO, $j_0 = 1$ is the initial rotational state, and the rotational energies (E_{vj}) are calculated by solving the nuclear Schrödinger equation [38] for the curve describing this diatomic fragment in the PES under study. For each temperature, the ($v = 0$, j) state is sampled via Eq. (3) when the condition $P_{j;v=0}(T) \geq \xi_3$ is satisfied for a freshly generated random number, ξ_3.

The total state-specific rate constant for the process is given as a sum of individual rate constants calculated separately for each symmetry, i.e., $k(j', T) = k_{^2A'}(j', T) + k_{^2A''}(j', T)$, while each term is given (using the Monte Carlo integration) by

$$k_x(j', T) = g_e(T) \left(\frac{8 k_B T}{\pi \mu_{\text{O+NO}}} \right)^{1/2} \pi b^2_{\max} P_{v'=1,j'} \tag{4}$$

where $\mu_{\text{O+NO}}$ is the reduced mass of the reactants, $b_{\max}$ the maximum value of the impact parameter, $P_{v'=1,j'}$ the probability for one quantum vibrational excitation, $g_e(T) = q_{\text{NO}_2}/q_{\text{O}} q_{\text{NO}}$ the electronic degeneracy factor with $q_{\text{NO}_2} = 2$, and

$$q_{\text{O}(^3\text{P})} = 5 + 3\exp(-227.8/T) + \exp(-326.6/T)$$
$$q_{\text{NO}(^2\Pi)} = 2 + 2\exp(-177.1/T) \tag{5}$$

The calculation of $P_{v'=1,j'}$ involves integration of the trajectories and subsequent analysis of the product NO diatomic (whether an oxygen exchange took place or not). To perform a quantization of the continuous vibrational–rotational energy distributions, two distinct approaches are performed and compared. The first is the traditional semiclassical quantization method [34], where the vibrational level is obtained from the Bohr–Sommerfeld quantization rule (upon rounding-off of the real value so obtained to the nearest integer), and the rotational level in a corresponding manner from the diatomic angular momenta. The probability will then be obtained as the ratio between the number of trajectories ending in the desired quantum state and the total number of trajectories.

A more elaborate approach to determine this probability is the momentum gaussian binning (MGB) [39] method, which has been successfully applied for a number of systems [36,39,40]. Instead of assigning a quantum state for each trajectory i, a probability weight distribution (W^i_{vj}) is given to it based on the calculated final energies. The total probability P_{vj} is then obtained by summing over all trajectories:

$$P_{vj} = \sum_{i=1}^{N} W^i_{vj} \tag{6}$$

Assuming as usual the separability of the vibrational and rotational degrees of freedom, i.e., $W^i_{vj} = W^i_v W^i_j$, the weight of the kth level is given by

$$W^i_k = \frac{1}{\rho_k\sqrt{\pi}} \exp\left[-\left(\frac{\sqrt{E_k} - \sqrt{\epsilon^i_k}}{\rho_k\sqrt{\bar{E}_k}} \right)^2 \right] \quad (7)$$

with E_k being the kth diatomic energy eigenvalue, $\bar{E}_k$ an average separation between neighboring levels, and ϵ^i_k is the ending energy of the ith trajectory (vibrational or rotational). The Gaussian-decay parameters ρ_v and ρ_j act fine-tuning constants for further realism. The use of the value $\rho_v = 0.1$ approximately accounts for the lack of zero-point energy (ZPE), because in this way the contribution to the ground vibrational state population (W^i_0) of a trajectory ending with a vibrational energy $E_v = 0.9E_0$ turns out to be about 48% of the value that would actually be obtained if $E_v = E_0$. In turn, the determination of ρ_j comes from the observation that the spacing of rotational levels is smaller than the vibrational ones, and thus, $\rho_v/\rho_j < 1$. Its value is fixed from the ratio of the averaged square root of vibrational and rotational spacings. This leads to $\rho_j = 0.238$ for the $^2A'$ surface and $\rho_j = 0.226$ for the $^2A'$ one. For further details and references to related work, the reader is referred to the original paper [39].

RESULTS AND DISCUSSION

For each temperature and PES, the impact parameter was optimized by trial and error and batches of 150,000 trajectories have been integrated to achieve a fluctuation around 10% for rotational state-specific rate constants, $k_{0\to1}(j', T)$. Figure 1 shows the rotational energy distribution for $T = 750$ K as calculated from different methods. As can be seen, the MGB approach provides a much smoother Maxwell–Boltzmann behavior than the other results (due to the fact that every trajectory contributes for every rotational state) and also an enhanced $v=0 \to 1$ transition probability, as can also be seen in Table I for all temperatures studied. This happens because the semiclassical approach tends to overestimate the $v'=0$ probability, since every trajectory ending with vibrational energy lower than ZPE contributes only for such an inelastic collision.

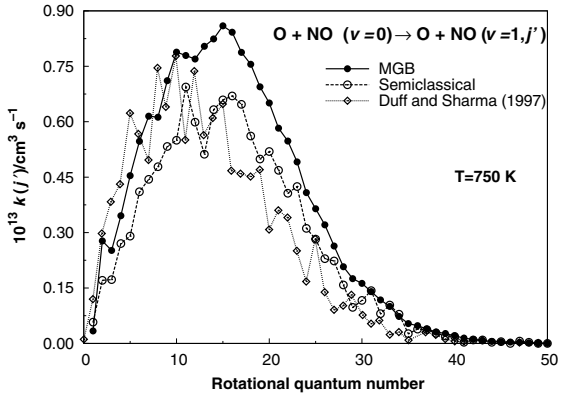

Figure 1 Comparison between different methods for calculating the rate constant for the formation of NO($v = 1$) as a function of the final rotational quantum number for a temperature of $T = 750$ K.

The probability of obtaining higher vibrational states decreases very fast, and collisions between O + NO($v=0$) are known to have negligible contribution [41] to the population of NO($v=2$) in the thermosphere, if compared to the major sources of it, namely $N(^4S, ^2D) + O_2$. For $T = 750$ K, the semiclassical approach does not assign a single trajectory to $v' \geq 3$.

The dependence of the rate constant for vibrational excitation on the temperature is shown in Fig. 2. Also shown are the experimental values from [42–45], which were obtained from measurements of the rate constant for vibrational relaxation of NO($v=1$) by oxygen atoms and subsequently inverted with the detailed balance formula $k_{0\to1}/k_{1\to0} = \exp[-1875/k_BT]$ such as to yield $k_{0\to1}(T)$. As seen, the MGB results deviate somewhat from the experimental ones, although a significant uncertainty and

Table I Rate Constants in $10^{13}k(T)/\text{cm}^3\,\text{s}^{-1}$ for the Fundamental Vibrational Excitation (and Impact Parameters)

	MGB			Semiclassical			$b_{max}/\text{Å}^a$	
T(K)	A'	A''	Total	A'	A''	Total	A'	A''
500	2.8 ± 0.1	2.9 ± 0.1	5.7 ± 0.2	1.9 ± 0.1	1.9 ± 0.1	3.8 ± 0.2	5.0	4.1
750[b]	7.2 ± 0.2	9.4 ± 0.2	16.6 ± 0.4	5.6 ± 0.2	7.1 ± 0.1	12.7 ± 0.3	5.0	4.1
1000	12.9 ± 0.2	18.4 ± 0.3	31.0 ± 0.5	10.1 ± 0.2	14.9 ± 0.3	25.0 ± 0.5	5.0	4.6

[a] Values of impact parameters used for the calculations.
[b] For the A'' surface without long-range term, the values are in the same units 7.0 and 5.3.

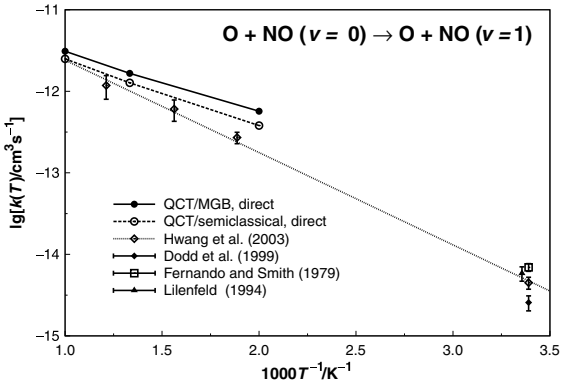

Figure 2 Comparison of the rate constants for the direct $O + NO(v = 0)$ reaction with the values obtained from the experimental rate constants for the backward reaction by using detailed balance.

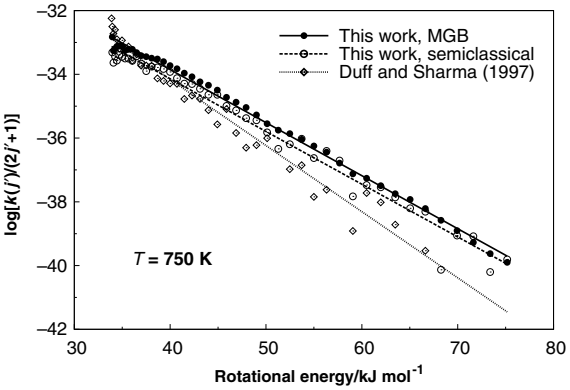

Figure 3 Fit employed to obtain the rotational temperature of $NO(v = 1)$ for $T = 750$ K.

scatter is also observed on the reported experimental values [42–45] at room temperature (these bear a relation and impact on atmospheric modeling [46]). Although we expect the MGB method to yield more reliable and smoother distributions than the traditional semiclassical (histogramatic) approach [39], we keep both for analysis throughout the paper. Note that a condition that must be satisfied for the application of the detailed balance is that the translational motion of both reagents and products shows thermal distributions at the same temperature [47]. It turns out (see later) that this is not the case for the nascent $NO(v=1)$ in the present QCT trajectory study, and hence the detailed balance cannot be expected to hold rigorously for the QCT results of $k_{1\to0}(T)$ so obtained. On the other hand, if translational equilibration occurs under experimental conditions, then it is likely that the detailed balance may apply. Note that such relaxation of the nascent distribution to obtain a Boltzmann one is not taken into account during the trajectory calculations; for the analysis of a related problem concerning $OH + O_2$, see [48].

It has been shown that the dominant contribution for vibrational relaxation processes [39] arises from the A' state, specially from higher initial levels, although both contributions approach each other for relaxation from $v = 1$. Table I shows that for the fundamental excitation, the opposite trend is observed, being $^2A''$ the most important one. Test calculations have been performed for the $^2A''$ state at $T = 750$ K but switching off the added long-range term in the MBE form. This led to a reduction of the rate constant by a factor of 25%, thus becoming basically the same as the $^2A'$ one (footnote of Table I). It then shows how sensitive the dynamics results of a barrierless reaction can be when adding long-range forces. The shape of the rotational distribution is, in turn, not affected by removing the long-range term.

The rotational temperature for the final distributions has been obtained by fitting the logarithm of the rate constant divided by $2j' + 1$ as a function of the rotational energy. Figure 3 compares the fitted lines here obtained with those calculated by Sharma and Duff [8]. As shown, the results from the present work show a higher rotational temperature (smaller slope) and a smoother linear distribution that may be attributed to the better converged results of the corresponding QCT calculations and use of the MGB method. It should be mentioned that the fit of our own QCT results quantized in the semiclassical way shows a very similar slope to the MGB one, demonstrating that the quantization method does not appreciably change the rotational distribution: The difference in slope when compared to the results of Sharma and Duff [8] stems only from the differences in the PESs that have been utilized.

The fitted and calculated rotational distributions of the rate constant are shown in Fig. 4 on a logarithmic scale, where the Maxwell–Boltzmann behavior of the nascent excited nitric oxide, anticipated by several models, can be confirmed to be smooth and single peaked. The rotational temperature obtained through the fitted functions is presented in Fig. 5 as a function of the initial local temperature and compared to the results of Sharma and Duff [8]. As it can be seen, our calculations corroborate previous models that describe the excited nitric oxide rotational distribution by a Maxwell–Boltzmann function with local temperature.

Figure 5 also shows a straight line fitted to both results. The results from this work predict a slope of 0.92 whereas those of Sharma and Duff [8] yield 0.75 (the independent constants are 32.4 and 25.9,

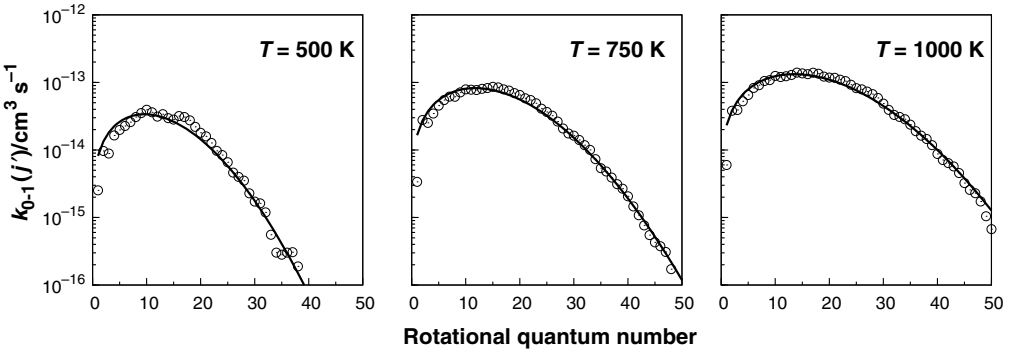

Figure 4 Rotational state-specific rate constants for the formation of NO($v = 1$) for initial reactants thermalized at $T =$ 500, 750, and 1000 K.

respectively). Clearly, for higher temperatures, considerable differences from the $T_{\text{rot}} = T$ line are expected for both cases, but the accuracy of the results may not ensure enough reliability for such extrapolations. To analyze the effect of further collisions of the nascent NO with oxygen atoms, we have also calculated the rate constants for NO($v = 1$) + O energy transfer with the rotational energy sampled with the predicted T_{rot}. As could be anticipated, after one extra collision the products are obtained with a rotational temperature even closer to the local one, but the variation is rather small and further collisions are not investigated. The rotational distribution of such process can be seen at Fig. 6 for the $T = 750$ K case.

Tentatively, one could think of rationalizing the above differences from the results of Sharma and Duff [8] by correlating the final rotational temperature with the NO_2 well depth, since deep minima are expected to enhance randomization of the various degrees of freedom and eventually lead to formation of thermalized products. In fact, the MBE PES of Sayós et al. [13] for the A' state has a potential well slightly deeper than the DMBE one, which could conceivably explain the fact of the associated rotational distribution at $T = 750$ K lying closer to 750 K than the DMBE prediction itself. Thus, one could to some extent attribute the differences between our prediction and the one of Sharma and Duff [8] to the shallower minima of the LEPS forms. More generally though, distinct PESs are known to yield different dynamical results and, indeed, the ones reported above for the $^2A''$ electronic state even show that the inclusion of long-range forces is capable of generating distinct product vibrational–rotational distributions. Since our PESs differ substantially from the LEPS form and describe other features such as conical intersections and long-range attractive forces, it should therefore not come as a surprise that the results generated from them contrast with Sharma's ones. More significant, however, could be to know

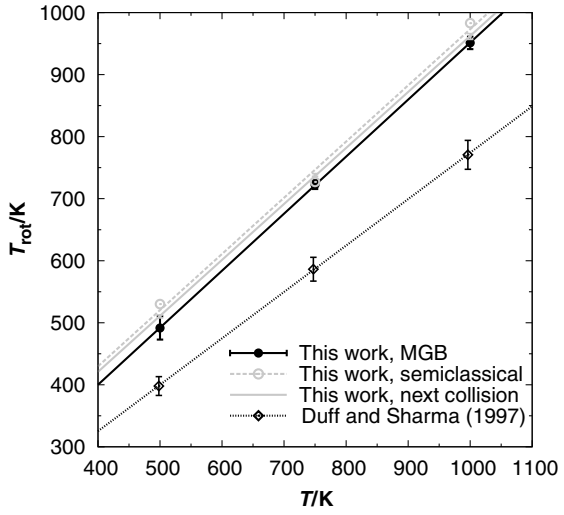

Figure 5 Rotational temperature of the nascent NO($v = 1$) against the initial temperature.

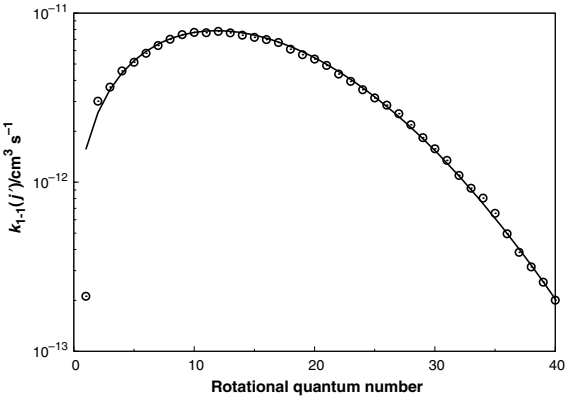

Figure 6 Rotational rate constants for the formation of NO($v = 1$) from a second collision of the nascent NO at $T = 750$ K.

whether the unimolecular dissociation of NO_2 may be characterized as statistical and hence agree with Rice–Ramsperger-Kessel–Marcus (RRKM) theory, since a statistical distribution of energy would then be predicted at the variational transition-state (TS) for NO_2 dissociation. Given that both electronic states of the NO_2 PES here utilized are governed by long-range forces, the position, and properties of the TS are expected to depend on the long-range potential. Unfortunately, although the barrierless PES for the ground $^2A'$ state has been the object of intramolecular dynamics studies [49], no similar work has to our knowledge been reported for the electronic $^2A''$ excited state. Without such a composite study on the two PESs, it will then be impossible to unambiguously ascribe the differences in the final rotational distributions to a single feature of the PESs, in particular the position and height of the centrifugal barriers experienced by the system either when the reactants are approaching each other or when they recede after forming the energyrich NO_2 complex. In any event, since both PESs here utilized describe the long-range attractive forces (absent from LEPS), they should likely mimic such a centrifugal barrier in a more realistic manner, thence yielding improved results.

We have also analyzed the change in translational energy after the collisional process. Since the products have basically the same rotational distribution, the vibrational energy gain from $v = 0$ to $v' = 1$ must occur on the expense of translational energy. This is what is represented in Fig. 7 for the binning at $T = 750$ K. The reactants have a translational energy distribution as obtained from a Maxwell–Boltzmann function for the fixed temperature (resulting from the sampling technique) and the nascent products show a translationally "colder" behavior, being well represented by the fitted curve shown in the figure for a translational temperature of 571 K.

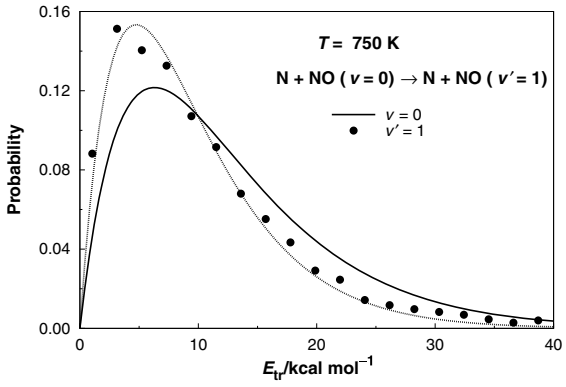

Figure 7 Translational energy distribution for initial and final vibrational states for $T = 750$ K.

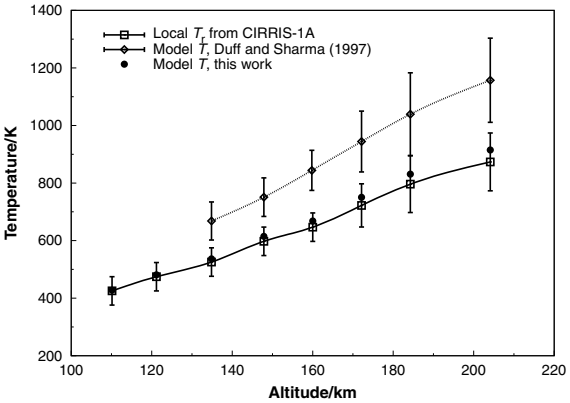

Figure 8 Temperature as a function of altitude as obtained from the CIRRIS-1A database [5], and model corrections for $T/T_{\rm rot}$ correspondence.

In summary, even for high altitudes, where high-temperature regimes are reached, our study corroborates previous work [2,6,7], which suggests that the rotational envelopes of the 5.3-μm emission can be described by a Maxwell–Boltzmann distribution with the local temperature. This contradicts the findings by Sharma and Duff [8] who suggested that it could only be equal for lower temperatures where further collisions of nascent NO with other molecules may cause thermalization. The implications for atmospheric modeling can be seen in Fig 8, where the temperature as a function of altitude inverted from the CIRRIS-1A database [5] is compared with the values corrected by Sharma and Duff [8] and the result from this work.

CONCLUDING REMARKS

Using realistic PESs, we have reported a QCT study that provides an in-depth understanding of the fundamental vibrational excitation of nitric oxide. The results corroborate that the nascent species are formed with a rotational distribution that can be described by a Maxwell–Boltzmann curve for the local temperature, as it has been employed in previous models of the thermosphere.

BIBLIOGRAPHY

1. Kockarts, G. Geophys Res Lett 1980, 7, 137.
2. Zachor, A. S.; Sharma, R. D.; Nadile, R. M.; Stair, A. T. J Geophys Res 1985, 90, 9776.
3. Smith, D. R.; Ahmadijian, M. Geophys Res Lett 1993, 20, 2679.
4. Sharma, R. D.; Dothe, H.; von Esse, F.; Kharchenko, V. A.; Sun, Y.; Dalgarno, A. J Geophys Res 1996, 101, 19707.

5. Sharma, R. D.; Dothe, H.; von Esse, F. J Geophys Res 1996, 101, 17129.
6. Quack, M.; Troe, J. Ber Bunsen-Ges Phys Chem 1975, 79, 170.
7. Ballard, J.; Morris, P. E.; Taylor, F. W. Geophys Res Lett 1993, 20, 1311.
8. Sharma, R. D.; Duff, J. W. Geophys Res Lett 1997, 24, 2407.
9. Duff, J. W.; Sharma, R. D. J Chem Soc Faraday Trans 1997, 93, 2645.
10. Kurihara, J.; Oyama, K.-I. Rev Sci Instrum 2005, 76, 083101.
11. Gillispie, G. D.; Khan, A. U.; Wahl, A. C.; Hosteny, R. P.; Krauss, M. J Chem Phys 1975, 63, 3425.
12. Hirsch, G.; Buenker, R. J. Can J Chem 1985, 63, 1542.
13. Sayós, R.; Oliva, C.; González, M. J Chem Phys 2002, 117, 670.
14. M. González, Miquel, I.; Sayós, R. J. Chem Phys 2001, 115, 8838.
15. Ivanov, M. V.; Zhu, H.; Schinke, R. J Chem Phys 2007, 126, 054304.
16. Caridade, P. J. S. B.; Mota, V. C.; Mohallem, J. R.; Varandas, A. J. C. J Phys Chem A 2008, 112, 960.
17. Varandas, A. J. C. J Mol Struct Theochem 1985, 21, 401.
18. Varandas, A. J. C. Adv Chem Phys 1988, 74, 255.
19. Varandas, A. J. C.; In Lecture Notes in Chemistry, Laganá, A.; Riganelli A. (Eds.); Springer: Berlin, 2000; Vol 75, pp. 33–56.
20. Varandas, A. J. C. Conical Intersections: Electronic Structure, Spectroscopy and Dynamics, World Scientific Publishing: Singapore, 2004; Ch. 5, p. 91. Advanced Series in Physical Chemistry.
21. Varandas, A. J. C. J Chem Phys 2003, 119, 2596.
22. Schryber, J. H.; Polyansky, O. L.; Jensen, P.; Tennyson, J. J Mol Spectrosc 1997, 185, 234.
23. Varandas, A. J. C. J Chem Phys 1996, 105, 3524.
24. Varandas, A. J. C. J Chem Phys 1997, 107, 867.
25. Varandas, A. J. C.; Voronin, A. I.; Caridade, P. J. S. B. J Chem Phys 1998, 108, 7623.
26. Galvão, B. R. L.; Rodrigues, S. P. J.; Varandas, A. J. C. J Chem Phys 2008, 129, 044302.
27. Kuntz, P. J. In Atom-Molecule Collision Theory; Bernstein R. (Ed.); Plenum Press: New York, 1979; p. 79.
28. Jost, R.; Nygard, J.; Pasinski, A.; Delon, A. J Chem Phys 1996, 105, 1287.
29. Murrell, J. N.; Carter, S.; Farantos, S. C.; Huxley, P.; Varandas, A. J. C. Molecular Potential Energy Functions; Wiley: Chichester, UK, 1984.
30. Dunning, T. H., Jr. J Chem Phys. 1989, 90, 1007.
31. Kendall, R. A.; Dunning, T. H., Jr.; Harrison, R. J. J Chem Phys 1992, 96, 6796.
32. Reignier, D.; Stoecklin, T.; Voronin, A.; Rayez, J. C. Phys Chem Chem Phys 2001, 3, 2726.
33. Peslherbe, G. H.; Wang, H.; Hase, W. L. Adv Chem Phys 1999, 105, 171.
34. Hase, W. L.; Duchovic, R. J.; Hu, X.; Komornicki, A.; Lim, K. F.; Lu, D.; Peslherbe, G. H.; Swamy, K. N.; Linde, S. R. V.; Varandas, A. J. C.; Wang, H.; Wolf, R. J.; QCPE Bull 1996, 16, 43.
35. Varandas, A. J. C.; Brandão, J.; Pastrana, M. R. J Chem Phys 1992, 96, 5137.
36. Caridade, P. J. S. B.; Galvão, B. R. L.; Varandas, A. J. C. J Phys Chem A 2010, 114, 6063.
37. Caridade, P. J. S. B.; Varandas, A. J. C. J Phys Chem A 2004, 108, 3556.
38. LeRoy, R. J.; LEVEL 7.5, A computer program for solving the radial Schrödinger equation for bound and quasibound levels; University of Waterloo Chemical Physics Research Report CP-655, 2002.
39. Varandas, A. J. C. Chem Phys Lett 2007, 439, 386.
40. Song, Y. Z.; Caridade, P. J. S. B.; Varandas, A. J. C. J Phys Chem A 2009, 113, 9213.
41. Sharma, R. D.; Wheeler, N. B.; Wise, J. O.; Dothe, H.; Duff, J. W. Geophys Res Lett 2000, 27, 349.
42. Dodd, J. A.; Lockwood, R. B.; Hwang, E. S.; Miller, S. M. J Chem Phys 1999, 111, 3498.
43. Hwang, E. S.; Castle, K. J.; Dodd, J. A. J Geophys Res 2003, 108, 1109.
44. Lilenfeld, H. V. Phillips Laboratory Final Report PL-TR-94-2180; Phillips Laboratory, Hanscom Air Force Base, 1994.
45. Fernando, R. P.; Smith, I. W. Chem Phys Lett 1979, 66, 218.
46. Sharma, R. D.; Roble, R. G. Comp Phys Commun 2002, 3, 841.
47. Levine, R. D.; Bernstein, R. B. Molecular Reaction Dynamics and Chemical Reactivity; Oxford University Press: New York, 1987.
48. Varandas, A. J. C. J Phys Chem A 2003, 107, 3769.
49. Grebenshchikov, S. Yu.; Beck, C.; H. Flöthman, Schinke, R.; Sato, S. J Chem Phys 1999, 111, 619.

THE JOURNAL OF PHYSICAL CHEMISTRY A

ARTICLE

pubs.acs.org/JPCA

Ab Initio Based Double-Sheeted DMBE Potential Energy Surface for $N_3(^2A'')$ and Exploratory Dynamics Calculations

B. R. L. Galvão and A. J. C. Varandas*

Departamento de Quimica, Universidade de Coimbra, 3004-535 Coimbra, Portugal

Supporting Information

ABSTRACT: We report a global accurate double-sheeted potential energy surface for the lowest doublet states with $^2A''$ symmetry of the N_3 radical using the double many-body expansion method. The functional form ensures by construction the degeneracy of the two adiabatic sheets along the D_{3h} line and the corresponding cusp behavior. Calibrated from multireference configuration interaction energies, it reproduces all the predicted stationary structures on both sheets and ensures a correct description of the dissociation limits. A test quasiclassical trajectory study of $N(^2D) + N_2$ collisions is also reported in the lowest adiabatic sheet of the potential energy surface. The results commend it for both classical and quantum dynamics studies, while serving as a building block for the potential energy surfaces of larger nitrogen allotropes and azides.

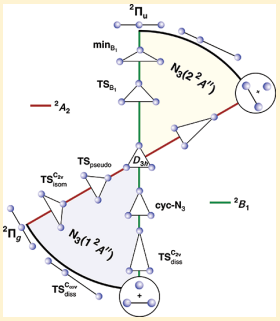

1. INTRODUCTION

New allotropes of nitrogen have been recently much studied,[1,2] because they stand as good candidates for high energy and density materials. For such studies, a deep understanding of its simplest trimeric form (N_3) is of fundamental importance. In fact, it may play a role on intermediate reactions, and has been suggested as a starting material for building larger polynitrogenic structures such as $N_4(T_d)$.[3] The unstable quartet state of N_3 has recently been studied in our group[4,5] due to the importance of $N(^4S) + N_2$ collisions on designing spacecraft heat shields. In this work, we focus on the bound trinitrogen doublet state, which is of key importance for studying the $N(^2D) + N_2$ reaction either in solid matrices or in atmospheric collisions. Although such collisions have been much studied experimentally,[6−13] no theoretical work regarding its dynamics has thus far been performed.

The $N_3(^2A'')$ ground-state potential energy surface (PES) is known experimentally[14−16] to have a linear minimum ($^2\Pi_g$), while a ring isomer[17] of B_1 symmetry has found support on experimental evidence.[18−23] Ab initio calculations[24] confirmed this isomer to be stable with respect to both spin-allowed and spin-forbidden decomposition and separated from the linear minima by a barrier of 33 kcal mol^{-1}. Moreover, its stability in reactions with several atmospheric compounds has been a matter of theoretical investigation.[25,26] The stationary structures of six PESs (two of $^2A''$ symmetry, three $^2A'$, and one $^4A''$) have been much studied by Morokuma and co-workers,[24,27,28] and previously by other groups[3,17,29,30] for geometry optimizations, fundamental frequencies, dipole moments, and minima of crossing seams (MSX).

The linear form of the azide radical (N_3) can be formed on solid molecular nitrogen under intense radiation fields that can break the nitrogen triple bond, with such conditions being known to abund in various low-temperature interstellar and solar system environments such as Triton (Neptune's largest moon) and Pluto.[13] In fact, Hudson and Moore[11] have proposed the use of linear N_3 as a tracer to follow the abundance of molecular nitrogen in space. The reaction of N_3 formation in solid nitrogen has been considered in many experimental studies at low temperature (10−35 K),[6−13] but no evidence of both the cyclic isomer and cyclic/linear reaction pathway has been found, although the cyclic form can be theoretically expected under high energy collisions.[24]

Although the linear isomer is only slightly endoergic relatively to $N(^4S) + N_2$,[31] large barriers caused by the spin-forbidden nature of this process are predicted,[24] and hence, this reaction is unlikely to form the azide radical.[12] On the other hand, the formation of N_3 from $N(^2D) + N_2$ collisions is predicted to be highly exothermic while showing small reaction barriers (3 kcal mol^{-1} for the linear isomer and 7 kcal mol^{-1} for the cyclic one[24]). Such collisions should also be interesting for studies of the atmosphere because this excited state of atomic nitrogen is copiously formed in the ionosphere via dissociative recombination of NO^+ and N_2^+.[32] Moreover, $N(^2D)$ can be generated under experimental conditions via quenching of $N_2(A^3\Sigma_u^+)$ by $N(^4S)$ atoms.[3,33−36]

For accurate studies of reaction dynamics of the above processes, it is mandatory to have a PES, desirably in analytic form, capable of describing the dissociative limits, barriers on the entrance channel and valence regions, and other relevant

Received: August 1, 2011
Revised: September 17, 2011
Published: September 19, 2011

topological attributes. Note that the energy necessary to dissociate the system is similar to the isomerization barrier, and hence, the two processes can compete. As a result, any rigorous study of ring closing dynamics should allow for unimolecular decomposition. Analytical representations of the adiabatic PESs proposed thus far for the quartet state have the correct dissociation behavior because their main interest has been on the $N(^4S)$ + N_2 exchange reaction.[4,5,37,38] Conversely, the PESs for the doublet states have been mostly targeted to understand the vibrational spectra of the ring isomer, and hence, only local forms for the latter have thus far been reported.[39−41] More recently, interest arose on ring-closing dynamics studies,[28] with fits of an extended region of configurational space (including cyclic and linear regions) being proposed for two $^2A''$ and three $^2A'$ electronic states. Yet, none of such fits describes the barriers to dissociation and the correct dissociative behavior.

The aim of the present work is to provide the first global analytical representation of the $^2A''$ states of the azide radical, which describes all topological details of the two lowest sheets using double many-body expansion (DMBE)[42−45] theory for the modeling. In particular, a view close to the one adopted for the triplet state of H_3^+ will be adopted.[46] Such a PES should then be useful both for reaction dynamics and for ro-vibrational calculations of the spectra up to the continuum (possibly requiring some further work for enhanced accuracy). Moreover, it may be utilized as a building block for the PESs of larger nitrogen allotropes. The paper is organized as follows. Section 2 contains a summary of the doublet electronic sheets and the details of the ab initio methods employed in this work. The modeling of the PES is described in section 3, while section 4 gathers the main results. A quasiclassical trajectory study performed for the $N(^2D)$ + N_2 reaction is presented on section 5. The conclusions are in section 6.

2. AB INITIO CALCULATIONS AND STATIONARY STRUCTURES

Although this work is concerned only with states of $^2A''$ symmetry, a brief summary of the intricate behavior of other electronic sheets is shown for C_{2v} configurations. The five electronic states that correlate with the $N(^2D)$ + N_2 dissociation limit are considered, namely, 1^2A_2, 1^2B_1, 1^2B_2, 1^2A_1, and 2^2A_2. Note that three other states (2^2B_2, 2^2A_1, and 2^2B_1) exist that correlate with $N(^2P)$ + N_2, but these are of no concern here. They lie higher in energy and show a large number of crossings between themselves and with the quartet state ones. Because such states are repulsive in character, they are not expected to make an important contribution in atom + diatom reaction dynamics.

Calculations at the CASSCF (complete active space self-consistent field) level of theory have first been performed for a grid of values of the ∠NNN angle, fixing a C_{2v} symmetry and optimizing the bond length. Note that, for an acute ∠NNN angle, the optimization leads to the dissociation limit, as the lowest energy corresponds to very large bond lengths. The results are shown in Figure 1, which allows a simple visualization of almost all the important features for both states that correlate with $^2A''$ in C_s symmetry ($^2B_1$ and $^2A_2$) and also the ones corresponding to $^2A'$ ($^2B_2$ and $^2A_1$), shown in gray. These probing CASSCF calculations show qualitative agreement with previous ones based on higher levels of theory[27] that have been utilized for the location of the stationary structures and crossings (including $^2A'/^2A''$).

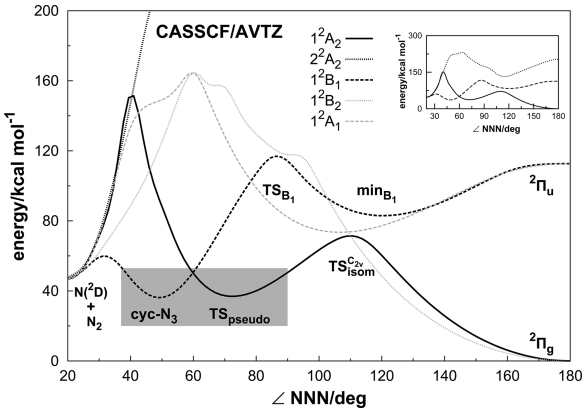

Figure 1. Optimized C_{2v} energy profile, as obtained via CASSCF/AVTZ optimizations at a grid of fixed angles. The electronic states correlating with $^2A''$ are shown in black and the stationary structures assigned, while the ones correlating with $^2A'$ are in gray. Shown by the shaded area are the three important structures associated with cyclic trinitrogen. The insert shows the behavior of the second $^2A_2$ state.

As shown, the azide radical has its deepest minimum at linear geometries, yielding a $^2\Pi_g$ electronic state which is doubly degenerate and correlates with $1^2A'$ and $1^2A''$ in C_s symmetry. In turn, the upper sheet yields a $^2\Pi_u$ structure with two imaginary degenerate bending modes and subject to Renner-Teller deformation via a split into the $2^2A'$ and $2^2A''$ electronic states. The $^2A'$ states will not be fitted in the present work but Figure 1 illustrates an overview of its topology. They are seen to lie high in energy and showing mostly a repulsive behavior for bent geometries. In fact, the most significant detail appears to be the intersection at (or near) a D_{3h} configuration where the $^2A_1$ and $^2B_2$ states become degenerate to form an $^2E'$ state. Distortion of this structure forms a minimum (on the bending coordinate only) of $^2A_1$ symmetry, which is also a result from the Renner−Teller stabilization of the $^2\Pi_u$ structure. While the $^2B_2$ state shows a rather complicated behavior caused by crossings with a third state of $^2A'$ symmetry, it does not form any low lying stable structure, except the $^2\Pi_g$ minimum. Because the present work focuses on the first two $^2A''$ states ($^2B_1$ and $^2A_2$), which hold the cyclic and linear isomers, the following discussion will be restricted to such states.

Starting from a linear symmetrical configuration and reducing the symmetry to C_{2v} by bending, the $^2A_2$ ground state passes through an isomerization barrier (which looks like a transition state in the reduced dimensionality of the plot, and is shortly denoted for later reference as $TS^{C_{2v}}_{isom}$), while the $^2B_1$ upper state shows a local minimum (min_{B_1}) and, subsequently, a transition state (TS_{B_1}); a new transition state connecting min_{B_1} with the $N(^2D)$ + N_2 dissociation channel has also been found and will be described later. At the D_{3h} configuration, that is, ∠NNN = 60°, both states become degenerate at the conical intersection of $^2E''$ symmetry, which then distorts to form two ring structures, the cyclic isomer (cyc-N_3) and the transition state for pseudorotation (TS_{pseudo}). Because the two structures lie close in energy, the pseudorotation motion is almost barrier-free,[39,40] with the vibrational wave function spanning both the cyc-N_3 and TS_{pseudo} regions. Figure 1 also shows that, for a T-shaped path, the dissociation on the ground state has a small barrier, while the upper presents a complicated behavior due to the approach of the second state of $^2A_2$ symmetry. This (2^2A_2) lies much higher in

dx.doi.org/10.1021/jp2073396 |J. Phys. Chem. A 2011, 115, 12390–12398

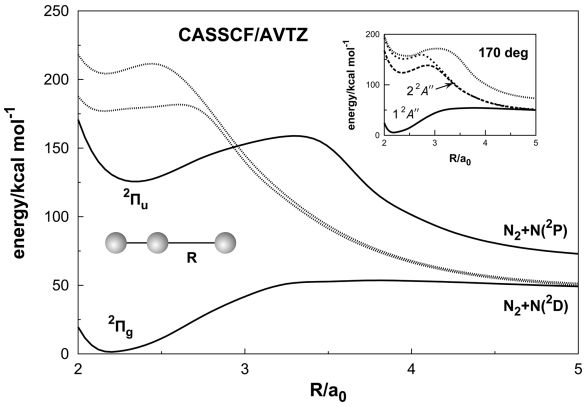

Figure 2. Linear dissociation obtained via CASSCF/AVTZ calculations for $^2A''$ states at a grid of values of one bond length, with the other relaxed. The insert shows the dissociation at a value of ∠NNN fixed at 170°.

energy, showing (see inset) a bent minimum that corresponds to a highly energetic form of N_3.

Because Figure 1 is restricted to C_{2v} geometries, it hides the fact that $TS_{isom}^{C_{2v}}$ is actually a second-order saddle point where the antisymmetric stretching mode leads to the real isomerization transition state ($TS_{isom}^{C_s}$), although both forms lie energetically close to each other (within 1 kcal mol^{-1}). Another feature that could not obviously be shown in such a C_{2v} cut refers to linear dissociation, which is shown in Figure 2 for the A'' states. Note that, although the $^2\Pi_u$ state would dissociate to N(^2P) + N_2, the crossing with a third state makes the $2^2A''$ sheet dissociate instead to N(^2D) + N_2 for all other bond angles, as show in the inset for ∠NNN = 170°.

To model the DMBE function, we have performed multireference configuration interaction calculations, including the Davidson correction, MRCI(Q),[47,48] with the MOLPRO package[49] and AVTZ[50,51] basis set. Unfortunately, the state-averaged calculations for the two lower states of $^2A''$ symmetry have shown severe difficulties to converge for large atom−diatom separations, as both states become degenerate at this asymptote, and hence, they cannot describe the barriers on the entrance channel that are crucial in reactive dynamics. To overcome such a problem, we have also performed single-state calculations on the lower sheet that cover this region. Although such single-state calculations yield results that differ slightly from the state-averaged ones, the differences involved are rather small (with a root-mean-squared error of ∼0.2 kcal mol^{-1} at the critical regions near the conical intersections and at a set of randomly chosen geometries). Because this deviation is expected to be smaller than the errors due to the fitting procedure and even the expected accuracy of the ab initio methodology itself, we have also used such single-state calculations on the fit of the lower sheet.

We have tested the accuracy of the MRCI(Q)/AVTZ energies by performing single point calculations with the AVQZ basis followed by extrapolation to the complete basis set limit (CBS). Although AVQZ geometry optimizations for all the stationary structures would be desirable, we have checked that the energy of cyc-N_3 relative to the linear minimum calculated on optimized AVQZ geometries differs only by 0.003 kcal mol^{-1} when compared with the result calculated at the corresponding AVTZ geometries, and hence, the very demanding AVQZ optimizations can be safely avoided.

Table 1. Stationary Structures on the Lower Sheet of $N_3(1^2A'')$[a]

		MRCI(Q)			Fitted	
structure	property	AVTZ[b]	AVQZ[c]	CBS[c]	ref 28	DMBE
$^2\Pi_g$	R/a_0	2.24			2.24	2.24
	θ/deg	180			180	180
	ΔV	0.0	0.0	0.0	−0.7	0.0
cyc-N_3	R/a_0	2.77			2.86	2.77
	θ/deg	49.8			47.0	50.0
	ΔV	32.2	32.9	33.3	32.2	32.3
TS_{pseudo}	R/a_0	2.47			2.47	2.47
	θ/deg	71.9			72.0	71.8
	ΔV	33.1	33.7	34.1	35.6	33.2
MSX	R/a_0	2.59			2.59	2.59
	θ/deg	60.0			60.0	60.0
	ΔV	45.4			45.0	45.0
$TS_{isom}^{C_s}$	R_1/a_0	2.31				2.26
	R_2/a_0	2.62				2.70
	θ/deg	109				109
	ΔV	65.0	66.4	67.4		65.1
$TS_{isom}^{C_{2v}}$[d]	R/a_0	2.44			2.43	2.44
	θ/deg	109			106	108
	ΔV	66.1	67.4	68.3	62.7	65.7
$TS_{diss}^{C\infty v}$	R_1/a_0	4.23				4.19
	R_2/a_0	2.09				2.09
	θ/deg	180				180
	ΔV	61.8	63.2	64.2		61.8
$TS_{diss}^{C_{2v}}$	R/a_0	4.23				4.16
	θ/deg	28.9				29.4
	ΔV	65.7	67.3	68.3		65.8
$TS_{diss}^{C_s}$[d]	R_1/a_0					2.12
	R_2/a_0					3.49
	θ/deg					106
	ΔV					69.3
N(^2D)+N_2	ΔV	59.0	60.4	61.4		59.0

[a] Energies are given in kcal mol^{-1} relative to the ground $\tilde{X}^2\Pi_g$ state. [b] From ref 24. [c] At the geometries of column 3. [d] Second-order saddle point.

As usual, the CBS extrapolations will be carried out in split form by treating separately the CASSCF and dynamical correlation components of the energy as obtained with Dunning's AVXZ basis set.[50,51] For the CASSCF energy calculated with $X = T,Q$, the most convenient scheme is perhaps the one due to Karton−Martin[52] (although originally suggested for the Hartree−Fock energy, it has been shown[53] to perform well also for the CAS energy since it does not include any dynamical correlation). Similarly, the dynamical correlation can be reliably extrapolated by using the USTE(T,Q)[53] protocol. Thus, the extrapolated CBS limit of the CAS energy has been calculated by fitting the energies with $E_X^{CAS}(\mathbf{R}) = E_\infty^{CAS}(\mathbf{R}) + B/X^{5.34}$, while the dynamical correlation (E_∞^{dc}) was obtained via a fit to

$$E_X^{dc} = E_\infty^{dc} + \frac{A_3}{(X+\alpha)^3} + \frac{A_5(0) + cA_3^{5/4}}{(X+\alpha)^5} \quad (1)$$

dx.doi.org/10.1021/jp2073396 |J. Phys. Chem. A 2011, 115, 12390–12398

Table 2. Stationary Structures on the Upper Sheet of $N_3(2^2A'')$[a]

		MRCI(Q)			Fitted	
feature	property	AVTZ[b]	AVQZ[c]	CBS[c]	ref 28	DMBE
$^2\Pi_u$	R/a_0	2.41			2.41	2.40
	θ/deg	180			180	180
	ΔV	104	106	107	107	105
$\min_{B_1}$	R/a_0	2.39			2.37	2.38
	θ/deg	120			124	122
	ΔV	72.8	73.5	74.0	70.7	72.9
TS_{B_1}	R/a_0	2.57			2.54	2.55
	θ/deg	86.1			86.4	85.3
	ΔV	109	111	112	104	108
TS_{C_s}	R_1/a_0					3.04
	R_2/a_0					2.17
	θ/deg					119
	ΔV					79.8

[a] Energies are given in kcal mol^{-1} relative to the ground $\tilde{X}^2\Pi_g$ state. [b] From ref 28. [c] At the geometries of column 3.

where $A_5(0) = 0.0037685459E_h$, $c = -1.17847713E_h^{-1/4}$, and $\alpha = -3/8$. The results so obtained for the stationary structures of the ground and excited $^2A''$ states of N_3 are given in Tables 1 and 2. As seen, the barriers for pseudorotation and $N(^2D) + N_2$ reaction do not appreciably change upon CBS extrapolation. The burden of performing even more expensive ab initio calculations looks, therefore, unnecessary.

3. DMBE POTENTIAL ENERGY SURFACE

The upper (u) and lower (l) surfaces of the PES are modeled within double many-body expansion[42−45] theory as

$$V_{u/l}(R_1,R_2,R_3) = V^{(1)} + \sum_{i=1}^{3} V^{(2)}(R_i) + V_{u/l}^{(3)}(R_1,R_2,R_3) \quad (2)$$

where each n-body term is split into an extended Hartree−Fock [$V_{EHF}^{(n)}$] and a dynamical correlation [$V_{dc}^{(n)}$] part. Because the upper and lower surfaces of $^2A''$ symmetry dissociate to ground state N_2 and $N(^2D)$, both states will share common $V^{(1)}$ and $V^{(2)}$ terms. Similarly, the $V_{dc}^{(3)}$ term describing the long-range atom−diatom dispersion and induction energies as an inverse power series of the distance between them, assume a common form for both sheets of the DMBE PES. Following previous work on the quartet state of trinitrogen,[4] the zero energy of the PES at the atom−diatom limit will be fixed by imposing $V^{(1)} = -2D_e$, where D_e is the well depth of N_2. The specific functional forms used to describe $V^{(2)}$ and $V_{dc}^{(3)}$ can be found elsewhere.[4]

3.1. Three-Body Extended Hartree−Fock Energy. All calculated energies have been modeled via a fit to $V_{EHF}^{(3)}$ in eq 2, which is written in symmetry adapted displacement coordinates from a D_{3h} configuration of bond length R_0 as

$$\begin{pmatrix} Q_1 \\ Q_2 \\ Q_3 \end{pmatrix} = \begin{pmatrix} \sqrt{1/3} & \sqrt{1/3} & \sqrt{1/3} \\ 0 & \sqrt{1/2} & -\sqrt{1/2} \\ \sqrt{2/3} & -\sqrt{1/6} & -\sqrt{1/6} \end{pmatrix} \begin{pmatrix} R_1 - R_0 \\ R_2 - R_0 \\ R_3 - R_0 \end{pmatrix} \quad (3)$$

Table 3. Stratified Root-Mean-Square Deviations for the Two Sheets of the N_3 DMBE PES (kcal mol^{-1})

	$1^2A''$		$2^2A''$	
energy[a]	N[b]	rmsd	N[b]	rmsd
10	11	0.158		
20	18	0.424		
30	27	0.566		
40	60	0.722		
50	103	0.784	10	0.382
60	166	0.811	20	0.668
80	359	0.838	69	1.510
100	387	0.844	141	2.009
120	424	0.934	225	2.576
140	428	0.936	257	3.143
160	432	0.933	280	3.587
180	438	0.935	289	3.602

[a] Relative to the ground $\tilde{X}^2\Pi_g$ state. [b] Number of calculated ab initio points up to the indicated energy range.

The potential must then be made symmetrical with respect to permutation of the coordinates, a criterion that can be satisfied by using the integrity basis:[54,55]

$$\begin{aligned} \Gamma_1 &= Q_1 \\ \Gamma_2^2 &= Q_2^2 + Q_3^2 \\ \Gamma_3^3 &= Q_3(Q_3^2 - 3Q_2^2) \end{aligned} \quad (4)$$

Note that the functions Γ_i are totally symmetric in the three-particle permutation group S_3, and hence, any polynomial built as $P_{(m)} = \sum_{i,j,k} c_{ijk}^{(m)} \Gamma_1^i \Gamma_2^{2j} \Gamma_3^{3k}$ will also transform as the totally symmetric representation of S_3.

The nonanalytical part of the potential of H_3 has long been known to occur along the line of D_{3h} symmetry,[56,57] and so was the fact that such nonanalicity can be expressed by an additional polynomial in integer powers of the various monomers multiplied by Γ_2. In this work, we follow the same strategy as successfully applied recently[46] to the triplet state of H_3^+. This allows the fit of the adiabatic surfaces by ensuring their degeneracy along the D_{3h} line. Thus, the upper (u) and lower (l) surfaces are written as

$$\begin{aligned} V_{EHF,u}^{(3)}(\mathbf{R}) &= [P_{1,u} + \Gamma_2 P_{2,u}] \times T(\mathbf{R}) \\ V_{EHF,l}^{(3)}(\mathbf{R}) &= [P_{1,l} - \Gamma_2 P_{2,l}] \times T(\mathbf{R}) \end{aligned} \quad (5)$$

Because both Γ_2 and Γ_3 are zero at D_{3h} configurations, the only condition required to make both adiabatic sheets degenerate along the line of D_{3h} symmetry (i.e., $V_{EHF,l}^{(3)} = V_{EHF,u}^{(3)}$) is that the coefficients of the polynomials P_1, depending only on Γ_1, are kept the same, that is, $c_{i00}^{(1,l)} = c_{i00}^{(1,u)}$ for any value of i. Because eq 5 ensures that the two sheets behave as a linear function of the Jahn−Teller coordinate Γ_2 in the vicinity of the intersection seam (note that higher order terms are negligible there), the only additional constraint to impose that they have the same slope is to fix $c_{000}^{(2,l)} = c_{000}^{(2,u)}$. Finally, one may ensure that the three-body term vanishes at large interatomic distances by multiplying the polynomials in eq 5 by a

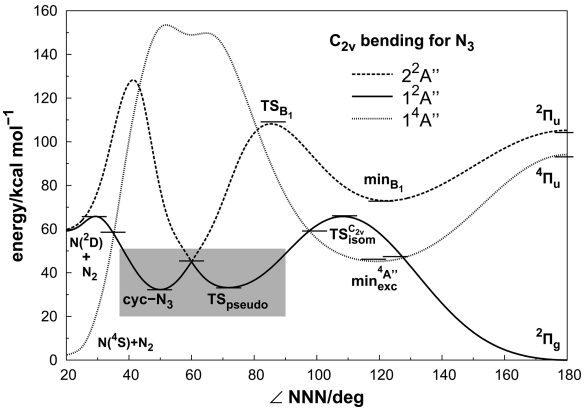

Figure 3. C_{2v} optimized energy profile for the two lowest sheets of the $^2A''$ DMBE PES, jointly with the one of $1^4A''$ (ref 4.). The bars show the MRCI(Q)/AVTZ prediction for the stationary structures and minima of crossing seams (ref 24). Shaded are as in Figure 1.

range-decaying term $T(\mathbf{R})$ defined as

$$T(\mathbf{R}) = \prod_{j=1}^{3} \{1 - \tanh[\gamma(R_j - R_0)]\} \tag{6}$$

The $V^{(3)}_{\mathrm{EHF},u/l}$ functions defined above contain 80 linear parameters $c^{(m)}_{ijk}$ each, which have been calibrated using a total of 507 ab initio points for the lower sheet and 386 for the upper one. For a better description of the stationary structures, a grid of points have been calculated at their vicinities and higher weights given to such points. As it is shown in Table 3, a good overall fit to the ab initio points has been obtained for the whole PES. Note that the ground state shows chemical accuracy over the entire range of fitted energies, while the upper one shows a somewhat larger deviation due to the presence of two other crossings with higher electronic states (see Figures 1 and 2) that were taken as avoided crossings for fitting purposes. The fitted coefficients and other relevant parameters defining both the upper and lower sheets can be found in the Supporting Information.

4. FEATURES OF THE POTENTIAL ENERGY SURFACE

Table 1 shows all known stationary structures of the lower sheet as predicted by MRCI(Q)/AVTZ optimizations[24] together with the values corresponding to the DMBE PES and the fitted form of ref 28. As shown, the DMBE PES reproduces accurately the MRCI(Q) calculations on the lower sheet, including the minima of the crossing seam (MSX) and the barriers for the $N(^2D) + N_2$ reaction. The rather complicated behavior of the upper sheet for both linear and T-shaped configurations (see Figures 1 and 2), which is due to interactions with higher electronic states, is also approximately described as avoided crossings. Note, however, that the regular stationary structures are accurately described, as shown in Table 2.

The C_{2v} bending of N_3 with optimized common bond length is shown in Figure 3 for both $^2A''$ states here studied. Also shown for completeness is the quartet state ($^4A''$) DMBE PES previously[4] reported. To assess the accuracy of the DMBE PESs, the MRCI(Q) optimized values obtained from refs 24 and 28 are shown in this plot with line segments. As shown, all features of both doublet PESs are well described, including the location and energetics of the spin-forbidden crossings. This is so despite the fact that the fit to the quartet state employed different ab initio methods. There are only two doublet/quartet crossings[24] that are not shown in this plot (due to their non-C_{2v} symmetry): one is of C_s symmetry lying close in energy and bond angle to the one shown at 99.3°, the other refers to the linear dissociation of the $^2\Pi_g$ structure, which is also modeled within 1 kcal mol^{-1} by the DMBE PESs. Note that the lowest lying spin-forbidden crossing is the one shown in Figure 3, with an angle of 125° at 47.4 kcal mol^{-1} above the linear minima. Clearly, the stability of both isomers toward spin-forbidden or spin-allowed dissociation is well mimicked by the DMBE fits.

To allow the visualization of all stationary structures of the PES, together with all possible equivalent permutations and the connections between them, a relaxed triangular plot[58] using scaled hyperspherical coordinates, $\beta^\star = \beta/Q$ and $\gamma^\star = \gamma/Q$:

$$\begin{pmatrix} Q \\ \beta \\ \gamma \end{pmatrix} = \begin{pmatrix} 1 & 1 & 1 \\ 0 & \sqrt{3} & \sqrt{3} \\ 2 & -1 & -1 \end{pmatrix} \begin{pmatrix} R_1^2 \\ R_2^2 \\ R_3^2 \end{pmatrix} \tag{7}$$

is employed. Note that the sum of squares of all bond distances in the triatom is relaxed such that the energy is lowest at any shape of the triangle formed by the three atoms. The lower PES is shown in Figure 4, where the stationary structures predicted by MRCI(Q) calculations and the locus of the C_{2v} symmetries are highlighted. The equilateral triangle (D_{3h}) geometry is located at the center of the plot ($\gamma^\star = \beta^\star = 0$), which is surrounded by two sets of three equivalent minima. Closer to the center of the diagram are the minima associated to the cyc-N_3 isomers that result in a direct way from the Jahn−Teller distortion and are connected among themselves via a pseudorotation path around the conical intersection (see also refs 59−61). Note that the transition states for isomerization $TS^{C_{2v}}_{\mathrm{isom}}$ (actually a second-order saddle point as noted above) and $TS^{C_s}_{\mathrm{isom}}$ are correctly modeled in the DMBE PES by showing two imaginary frequencies for the former and a single one for the latter.

All barriers in the $N + N_2$ entrance channel are presented. The two transition state structures have been predicted in previous ab initio calculations:[24] one for formation of the linear minima ($TS^{C}_{\mathrm{diss}\infty v}$), the other for the ring isomer ($TS^{C_{2v}}_{\mathrm{diss}}$). Although not relevant from a chemical point of view, a topological analysis shows that there is also a second-order saddle point connecting these two transition states, hereafter referred to for simplicity as $TS^{C_s}_{\mathrm{diss}}$ and shown in Figure 4 by the symbol ×; for the geometrical and energetic attributes, see Table 1.

The upper sheet of the present N_3 DMBE PES is also presented as a relaxed triangular plot in Figure 5, where the three known structures ($^2\Pi_u$, min_{B_1}, and TS_{B_1}) are highlighted. Starting at min_{B_1} and following the antisymmetric stretching coordinate, one is led to another transition state that (to the best of our knowledge) has not been reported before. This transition state (TS_{C_s}) is also shown in Figure 5, connecting min_{B_1} with the dissociation to $N_2 + N(^2D)$ and has been located by CASSCF/AVTZ optimizations at a geometry of $R_1 = 2.229a_0$, $R_2 = 2.727a_0$, and $\theta = 120.7°$ with a single imaginary frequency of 1558 cm^{-1} corresponding to the antisymmetric stretch. This is predicted by the DMBE fit to lie 6.9 kcal mol^{-1} above min_{B_1}. The stability of min_{B_1} was previously[27] given to be 13.8 kcal mol^{-1} relative to the $N_2 + N(^2P)$ dissociation. If referred to the newly reported TS_{C_s}, its stability is significantly reduced.

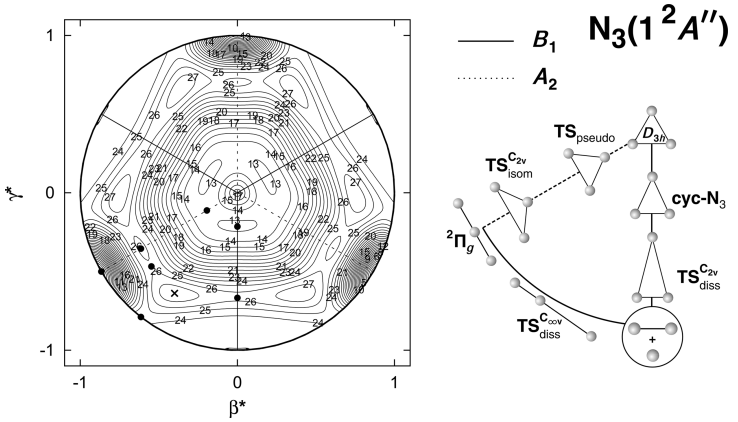

Figure 4. Relaxed triangular plot of the lower sheet of N_3 showing all its stationary structures and atomic permutations. The locus of C_{2v} geometry correlating with the $^2B_1$ electronic state is highlighted with a solid line, whereas the $^2A_2$ one is shown in dashed. Contours start at the linear minima and are spaced by 2.51 kcal mol^{-1}.

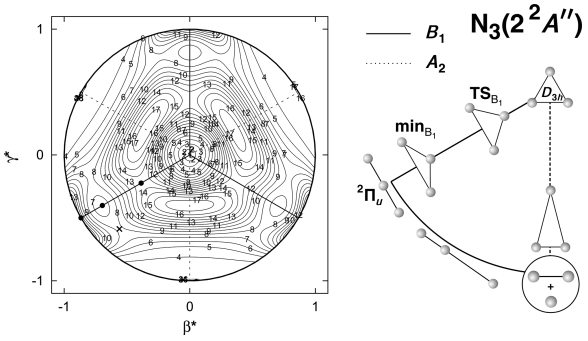

Figure 5. Relaxed triangular plot of the upper sheet of N_3 using the previous notation for the electronic states. Contours start at the minima of the crossing seam and are spaced by 5 kcal mol^{-1}.

As Figure 1 shows, the part of the upper sheet that correlates with the $^2A_2$ electronic state shows only the avoided crossing at the exit channel. Starting at TS_{B_1} (this has the imaginary frequency along the bending motion) and by following the antisymmetric stretching coordinate, it undergoes a pseudorotation that leads to the above-mentioned avoided crossing which shows two imaginary frequencies. A plot showing both surfaces together, provides a better perspective of such features and is given in Figure 6 (a cut has been made to allow visualization of the conical intersection and the well corresponding to the cyclic isomer). As this perspective view seems to suggest, the stability of min_{B_1} may not be large enough to provide a possible photoexcitation pathway for the production of cyclic N_3, as previously advanced.[27] Instead, after being brought to the $^2\Pi_u$ state, the system is likely to bend toward min_{B_1} and dissociate passing through the newly proposed TS_{C_s}, rather than overcoming the large barrier imposed by TS_{B_1}.

The isotropic (V_0) and leading anisotropic (V_2) terms in a Legendre expansion of the N_2−N interaction potential are important quantities for the study of scattering processes,[62,63] where the sign of V_2 indicates the preferred direction of the incoming atom: a negative value favors the collinear approach, while a positive value favors an attack via C_{2v} geometries. Such potentials are shown in

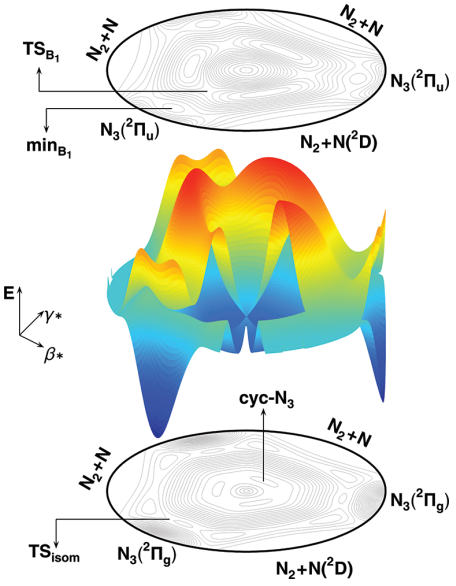

Figure 6. Perspective view of the two sheets of N_3 using a relaxed triangular plot.

Figure 7, where the collinear approach is shown to be preferred on the lower sheet, as expected due to the deeper well. Because the upper sheet is mostly repulsive, especially for T-shaped configurations, both components show a positive value on the short-range region. For distances larger than $7a_0$, that is, at the van der Waals interaction part of the potential, V_0 is the dominant term for both sheets, while V_2 is mostly positive, which reflects the fact that the minima of the van der Waals well lies on a T-shaped geometry, in agreement with ref 64.

5. QUASICLASSICAL STUDY OF N(^2D) + N_2 EXCHANGE REACTION

Due to the large masses of the atoms, quasiclassical trajectories for the N(^4S) + N_2 exchange reaction[5] yielded results that compared

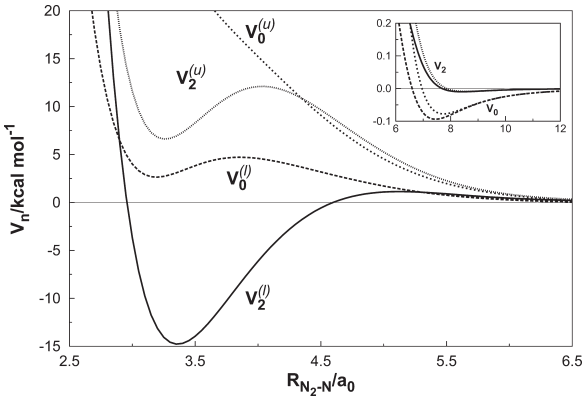

Figure 7. Isotropic (V_0) and leading anisotropic (V_2) components of the N−N_2 interaction potential, with the diatomic fixed at the equilibrium geometry.

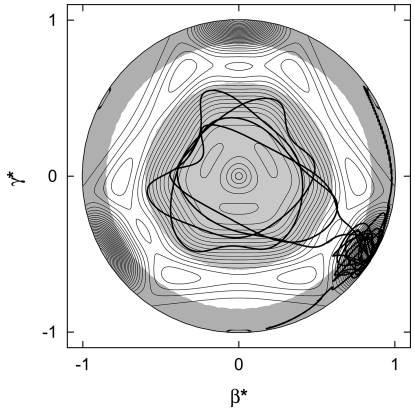

Figure 8. Trajectory path on scaled hyperspherical coordinates of eq 7, with initial translational energy of 5.8 kcal mol^{-1}. The two circles of radius 0.60 and 0.85 used to define the "linear" and "cyclic" isomeric regions are shown in gray.

very well with quantum mechanical calculations,[37,38] and therefore, we use this approach to perform a first study of atom−diatom collisions also on the lowest $^2A''$ state of the system. First we have integrated trajectories[65,66] for N(^2D) + N_2(v,j = 0) collisions for fixed values of the relative translational energy to obtain the excitation function. All calculations used a time step of 0.2 fs with the reactants initially separated by 17a_0, while the maximum value of the impact parameter (b_{max}) has been optimized by trial and error for each translational energy. The cross sections were then obtained as $\sigma = \pi b_{max}{}^2 N_r/N$, and the 68% associated errors by $\Delta\sigma = \sigma((N - N_r)/(NN_r))^{1/2}$, with N being the total number of trajectories run and N_r being the number of reactive ones.

For a study on the formation of N_3 from atom−diatom collisions, one must have present a third body that removes energy from the complex. Rather than attempting this (say by adding a rare gas atom), we have used the present N_3($1^2A''$) PES and analyzed trajectories passing through each isomer before leaving to products by counting their number and setting it as N_r. For this, we have defined two regions on the PES using geometric and energetic criteria with the scaled hyperspherical coordinates

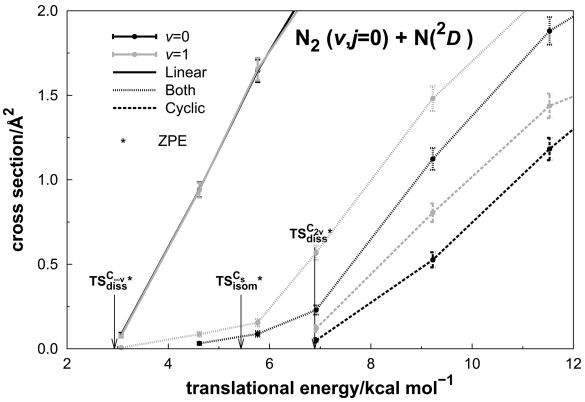

Figure 9. Excitation function for formation of N_3 in N(^2D) and N_2(v,j = 0) collisions, with separated contribution from "linear", "cyclic", and both regions of the PES. The results for v = 0 are shown in black, while those for v = 1 are shown on gray.

of eq 7. A trajectory is counted as proceeding via the cyclic isomer if passing through a region inside a circle of radius 0.6 centered at $\gamma^\star = \beta^\star = 0$ and with potential energy 5 kcal mol^{-1} lower than the dissociation limit (to ensure counting only "bound" complexes). Similarly, the reaction was counted to proceed via the linear minima if it enters a region with radius larger than 0.85 and with a potential energy of 5 kcal mol^{-1} lower than the dissociation limit. The two circles defining such regions are visualized in Figure 8, which also illustrates a trajectory that passes through both isomers before forming products (with exchanged nitrogen atoms).

Figure 9 shows the excitation function for the two lowest vibrational states of N_2, considering trajectories that proceeded exclusively either via the linear isomer or the ring one, or passed instead through both (thus, implying trajectories that suffered isomerization before leaving to products). This graph also indicates the barriers in the PES once corrected for zero-point energy (ZPE), which should provide a threshold for each curve: $TS^{C_{\infty v}}_{diss}$ for the linear minima, $TS^{C_{2v}}_{diss}$ for the cyclic one, and $TS^{C_s}_{isom}$ for covering both minima. Although the excitation functions for the formation of only one of the isomers reasonably obey the mentioned barriers, a considerable number of trajectories with translational energies lower than $TS^{C_s}_{isom}$ were able to proceed through both linear and cyclic regions. This may be explained by ZPE leakage on the classical trajectories, because after the linear isomer is formed, the initial ZPE of N_2(v = 0) that corresponds to 3.3 kcal mol^{-1} can be exchanged to promote the system on overcoming the isomerization barrier.

In a recent experiment on the formation of the azide radical from radiated solid nitrogen,[12] it was argued that the thermal energy available for collisions with N(^2D) would not be sufficient to overcome the barrier and form the linear isomer, although a quantum of vibrational excitation on the N_2 molecule could allow such a reaction. The QCT results reported in Figure 9 show that such a vibrational excitation is also inefficient, as would be expected from an early barrier in the context of the Polanyi rules. Indeed, vibrational to translational energy exchange would be necessary to occur before the interaction region, which is unlikely to happen. We believe that the explanation to form linear N_3 at low temperatures should then be that the nitrogen atom, formed from the decomposition of N_2, did not get thermalized and, hence, has a translational energy content larger than might

Table 4. Thermal Rate Constants ($10^{13}k(T)/\mathrm{cm}^3\ \mathrm{s}^{-1}$) for the $N(^2D) + N_2$ Atom-Exchange Reaction

		contributions		
T/K	total	linear	cyclic	both
500	2.42 ± 0.14	2.23	0.00	0.19
750	8.75 ± 0.30	6.94	0.40	1.41
1000	17.92 ± 0.47	12.51	1.61	3.81

be anticipated from the temperature of the solid. Of course, the dynamics here reported is rather preliminary, because a study involving formation of the linear N_3 isomer would also require consideration of the ground $^2A'$ state (see Figure 1).

Finally, a prediction of thermal rate constants for the above atom-exchange reaction has been carried out using the PES for the $^2A''$ ground-state. For fixed temperatures, we have then sampled the relative atom−diatom translational energy and the ro-vibrational state of the N_2 molecule via cumulative distribution functions according to the QCT method.[5,65,66] The final rate constant assumes the form

$$k(T) = g_e(T)\left(\frac{8k_BT}{\pi\mu}\right)^{1/2}\sigma(T) \qquad (8)$$

where μ is the reduced mass of the reactants and $g_e(T)$ is the electronic degeneracy factor. Although the latter is usually considered to be 1/5 as its high temperature limit, we have instead used its more general form of $g_e(T) = q_{N_3}/q_{N(^2D)}q_{N_2}$, where $q_{N_2} = 1$, $q_{N_3} = 2$, and $q_{N(^2D)} = 6 + 4\exp(-12.53/T)$ is the partition function of $N(^2D)$. Table 4 gives the results of the total exchange rate constant for three temperatures (T = 500, 750, 1000 K), together with the specific contributions due to trajectories that "formed" only a specific isomer or both. Because this excited state of the nitrogen atom plays an important role in the atmosphere[32] (due to its reactions with O_2), and because N_2 molecules are also available in large abundances, this reaction may be relevant for the study of atmospheric chemistry, although the formation of a stable N_3 molecule is very unlikely under such conditions and, even if formed, should be quickly decomposed by reactions with other reactive species.

6. CONCLUDING REMARKS

We have reported a global representation of the two lowest $^2A''$ states of the azide radical using DMBE theory and MRCI(Q)/AVTZ calculations for the calibration procedure. To our knowledge, this is the only available PES suitable for scattering calculations because it describes all dissociation channels. Moreover, it accurately reproduces all stationary structures predicted for the lower and upper adiabatic sheets. A preliminary QCT study on the dynamics of this system on the lowest sheet of the potential energy surface has also been reported, with the contribution of each isomer pathway being investigated during the collisional process.

■ ASSOCIATED CONTENT

Supporting Information. All coefficients necessary to construct the potential energy surfaces reported in this work are available in four tables. This material is available free of charge via the Internet at http://pubs.acs.org.

■ AUTHOR INFORMATION

Corresponding Author
*E-mail: varandas@qtvs1.qui.uc.pt.

■ ACKNOWLEDGMENT

This work has the support of Fundação para a Ciência e Tecnologia, Portugal, under Contracts PTDC/QUI-QUI/099744/2008 and PTDC/AAC-AMB/099737/2008.

■ REFERENCES

(1) Samartzis, P. C.; Wodtke, A. M. *Int. Rev. Phys. Chem.* **2006**, *25*, 572.
(2) Zarko, V. E. *Combust., Explos., Shock Waves* **2010**, *46*, 121.
(3) Bittererová, M.; Östmark, H.; Brinck, T. *J. Chem. Phys.* **2002**, *116*, 9740.
(4) Galvão, B. R. L.; Varandas, A. J. C. *J. Phys. Chem. A* **2009**, *113*, 14424.
(5) Caridade, P. J. S. B.; Galvão, B. R. L.; Varandas, A. J. C. *J. Phys. Chem. A* **2010**, *114*, 6063.
(6) Tian, R.; Facelli, J. C.; Michl, J. *J. Chem. Phys.* **1988**, *92*, 4073.
(7) Tian, R.; Michl, J. *Faraday Discuss., Chem. Soc.* **1988**, *86*, 113.
(8) Hassanzadeh, P.; Andrews, L. *J. Phys. Chem.* **1992**, *96*, 9177.
(9) Khabasheskua, V. N.; Margrave, J. L.; Waters, K.; Schultz, J. A. *J. Appl. Phys.* **1997**, *82*, 1921.
(10) Sankaran, K.; Sundararajan, K.; Viswanathan, K. S. *J. Phys. Chem. A* **2001**, *105*, 3995.
(11) Hudson, R. L.; Moore, M. H. *Astrophys. J.* **2002**, *568*, 1095.
(12) Amicangelo, J. C.; Collier, J. R.; Dine, C. T.; Saxton, N. L.; Schleicher, R. M. *Mol. Phys.* **2007**, *105*, 989.
(13) Jamieson, C. S.; Kaiser, R. I. *Chem. Phys. Lett.* **2007**, *440*, 98.
(14) Brazier, C. R.; Bernath, P. F.; Burkholder, J. B.; Howard, C. J. *J. Chem. Phys.* **1988**, *89*, 1762.
(15) Douglas, A. E.; Jones, W. J. *Can. J. Phys.* **1965**, *43*, 2216.
(16) Thrush, B. A. *Proc. R. Soc., A* **1956**, *235*, 143.
(17) Martin, J. M. L.; François, J. P.; Gijbels, R. *J. Chem. Phys.* **1989**, *90*, 6469.
(18) Hansen, N.; Wodtke, A. M. *J. Phys. Chem. A* **2003**, *107*, 10608.
(19) Samartzis, P. C.; J. J.-M. Lin, T.-T. C.; Chaudhuri, C.; Lee, Y. T.; Lee, S.-H.; Wodtke, A. M. *J. Chem. Phys.* **2005**, *123*, 051101.
(20) Zhang, J.; Zhang, P.; Chen, Y.; Yuan, K.; Harich, S. A.; Wang, X.; Wang, Z.; Yang, X.; Morokuma, K.; Wodtke, A. M. *Phys. Chem. Chem. Phys.* **2006**, *8*, 1690.
(21) Samartzis, P. C.; J. J.-M. Lin, T.-T. C.; Chaudhuri, C.; Lee, S.-H.; Wodtke, A. M. *J. Chem. Phys.* **2007**, *126*, 041101.
(22) Samartzis, P. C.; Wodtke, A. M. *Phys. Chem. Chem. Phys.* **2007**, *9*, 3054.
(23) Larson, C.; Ji, Y.; Samartzis, P. C.; Quinto-Hernandez, A.; Lin, J. J.; Ching, T.-T.; Chaudhuri, C.; Lee, S.-H.; Wodtke, A. M. *J. Phys. Chem. A* **2008**, *112*, 1105.
(24) Zhang, P.; Morokuma, K.; Wodtke, A. M. *J. Chem. Phys.* **2005**, *112*, 014106.
(25) Yu, X.-F.; Jin, L.; Ding, Y.-H. *J. Mol. Struct.: THEOCHEM* **2009**, *911*, 13.
(26) Jin, L.; Yu, X.-F.; Pang, J.-L.; Zhang, S.-W.; Ding, Y.-H. *J. Phys. Chem. A* **2009**, *113*, 8500.
(27) Kerkines, I. S. K.; Wang, Z.; Zhang, P.; Morokuma, K. *Mol. Phys.* **2009**, *107*, 1017.
(28) Wang, Z.; Kerkines, I. S. K.; Morokuma, K.; Zhang, P. *J. Chem. Phys.* **2009**, *130*, 044313.
(29) Murrell, J. N.; Novaro, O.; Castillo, S. *Chem. Phys. Lett.* **1982**, *90*, 421.
(30) Wasilewski, J. *J. Chem. Phys.* **1996**, *105*, 10969.
(31) Continetti, R. E.; Cyr, D. R.; Osborn, D. L.; Leahy, D. J.; Neumark, D. M. *J. Chem. Phys.* **1993**, *99*, 2616.

(32) Tohmatsu, T. *Compendium of Aeronomy*; Kluwer Academy: Norwell, MA, 1990.
(33) Kunsch, P. L.; Dressler, K. *J. Chem. Phys.* **1978**, *68*, 2550.
(34) Kunsch, P. L. *J. Chem. Phys.* **1978**, *68*, 4564.
(35) Oehler, O.; Smith, D. A.; Dressler, K. *J. Chem. Phys.* **1977**, *66*, 2097.
(36) Kajihara, H.; Okada, F.; Koda, S. *Chem. Phys.* **1994**, *186*, 395.
(37) Wang, D.; Stallcop, J. R.; Huo, W. M.; Dateo, C. E.; Schwenke, D. W.; Partridge, H. *J. Chem. Phys.* **2003**, *118*, 2186.
(38) Garcia, E.; Saracibar, A.; Gomez-Carrasco, S.; Laganá, A. *J. Phys. Chem. A* **2008**, *10*, 2552.
(39) Babikov, D.; Zhang, P.; Morokuma, K. *J. Chem. Phys.* **2004**, *121*, 6743.
(40) Babikov, D.; Kendrick, B. K.; Zhang, P.; Morokuma, K. *J. Chem. Phys.* **2005**, *122*, 044315.
(41) Babikov, D.; Kendrick, B. K. *J. Chem. Phys.* **2010**, *133*, 174310.
(42) Varandas, A. J. C. *J. Mol. Struct.: THEOCHEM* **1985**, *21*, 401.
(43) Varandas, A. J. C. *Adv. Chem. Phys.* **1988**, *74*, 255–337.
(44) Varandas, A. J. C. In *Lecture Notes in Chemistry*; Laganá, A., Riganelli, A., Eds.; Springer: Berlin, 2000; Vol. 75, pp 33−56.
(45) Varandas, A. J. C.; *Advanced Series in Physical Chemistry*; World Scientific Publishing: Hackensack, NJ, 2004; Chapter 5, p 91.
(46) Varandas, A. J. C.; Alijah, A.; Cernei, M. *Chem. Phys.* **2005**, *308*, 285–295.
(47) Werner, H. J.; Knowles, P. J. *J. Chem. Phys.* **1988**, *89*, 5803.
(48) Knowles, P. J.; Werner, H. J. *Chem. Phys. Lett.* **1988**, *145*, 514.
(49) Werner, H.-J.; Knowles, P. J.; Lindh, R.; Manby, F. R.; Schütz, M.; Celani, P.; Korona, T.; Mitrushenkov, A.; Rauhut, G.; Adler, T. B.; Amos, R. D.; Bernhardsson, A.; Berning, A.; Cooper, D. L.; Deegan, M. J. O.; Dobbyn, A. J.; Eckert, F.; Goll, E.; Hampel, C.; Hetzer, G.; Hrenar, T.; Knizia, G.; Köppl, C.; Liu, Y.; Lloyd, A. W.; Mata, R. A.; May, A. J.; McNicholas, S. J.; Meyer, W.; Mura, M. E.; Nicklass, A.; Palmieri, P.; Pflüger, K.; Pitzer, R.; Reiher, M.; Schumann, U.; Stoll, H.; Stone, A. J.; Tarroni, R.; Thorsteinsson, T.; Wang, M.; Wolf, A. *Molpro*, version 2008.3, a package of ab initio programs; 2008.
(50) Dunning, T. H., Jr. *J. Chem. Phys.* **1989**, *90*, 1007.
(51) Kendall, R. A.; Dunning, T. H., Jr.; Harrison, R. J. *J. Chem. Phys.* **1992**, *96*, 6796.
(52) Karton, A.; Martin, J. M. L. *Theor. Chem. Acc.* **2006**, *115*, 330–333.
(53) Varandas, A. J. C. *J. Chem. Phys.* **2007**, *126*, 244105.
(54) Weyl, H. *The Classical Theory of Groups*; Princeton University Press: Princeton, NJ, 1946.
(55) Murrell, J. N.; Carter, S.; Farantos, S. C.; Huxley, P.; Varandas, A. J. C. *Molecular Potential Energy Functions*; Wiley: Chichester, 1984.
(56) Varandas, A. J. C.; Murrell, J. N. *Faraday Discuss., Chem. Soc.* **1977**, *62*, 92–109.
(57) Porter, R. N.; Stevens, R. M.; Karplus, M. *J. Chem. Phys.* **1968**, *49*, 5163.
(58) Varandas, A. J. C. *Chem. Phys. Lett.* **1987**, *138*, 455.
(59) Babikov, D.; Mozhayskiy, V. A.; Krylov, A. I. *J. Chem. Phys.* **2006**, *125*, 084306.
(60) Mozhayskiy, V. A.; Babikov, D.; Krylov, A. I. *J. Chem. Phys.* **2006**, *124*, 224309.
(61) Babikov, D. *J. Chem. Phys.* **2011**, *134*, 114305.
(62) Norbeck, J. M.; Certain, P. R.; Tang, K. T. *J. Chem. Phys.* **1975**, *63*, 590.
(63) Varandas, A. J. C. *J. Chem. Phys.* **1979**, *70*, 3786.
(64) Stallcop, J. R.; Partridge, H. *Phys. Rev. A* **2001**, *64*, 042722.
(65) Peslherbe, G. H.; Wang, H.; Hase, W. L. *Adv. Chem. Phys.* **1999**, *105*, 171.
(66) Hase, W. L.; Duchovic, R. J.; Hu, X.; Komornik, A.; Lim, K. F.; Lu, D.-H.; Peslherbe, G. H.; Swamy, K. N.; van de Linde, S. R.; Varandas, A. J. C.; Wang, H.; Wolf, R. J. *QCPE Bull.* **1996**, *16*, 43.

THE JOURNAL OF CHEMICAL PHYSICS **137**, in press (2012)

N(^4S/^2D)+N_2: accurate *ab initio*-based DMBE potential energy surfaces and surface-hopping dynamics

B. R. L. Galvão, P. J. S. B. Caridade, A. J. C. Varandas[1, a)]
Departamento de Química, Universidade de Coimbra
3004-535 Coimbra, Portugal

(Dated: 30 April 2012)

This work gives a full account of the N($^4S/^2D$)+N_2($^1\Sigma_g^+$) interactions via accurate electronic structure calculations and study of the involved exchange reactions. A 2×2 diabatic representation of the potential energy surface is suggested for N_3($^2A'$) which, combined with the two previously reported adiabatic forms for $^2A''$ and another for $^4A''$, completes the set of five global potentials required to study the title collisional processes. The trajectory results provide the first N(^2D)+N_2 rate constants, and allow a comparison with the ones for N(^4S)+N_2. Nonadiabatic effects are estimated by surface hopping, and the geometrical phase effect assessed by following the trajectories that encircle the crossing seam.

I. INTRODUCTION

The azide radical (N_3) is an intriguing chemical species from several points of view. Being the smallest polynitrogen molecule, it shows both a linear and a cyclic structures, each having completely different chemical characteristics. Although the linear one is widely known experimentally[1–5], the ring form has only recently[6–11] been detected but its isolation remains elusive. As a nitrogen allotrope, it has potential applications as a high-energy density material[12,13], and its natural tendency to dissociate to molecular nitrogen would make it a "clean" propellant.

In this work we are interested in the dynamics of N($^4S/^2D$)+N_2($^1\Sigma_g^+$) collisions, which are relevant under several conditions ranging from atmospheric chemistry to the formation and dissociation of the stable N_3 molecule. The fundamental step for such a theoretical study is the construction of the relevant potential energy surfaces (PESs), including the correct asymptotic limits, long range forces as well as an accurate description of the covalent region of the supermolecule. Indeed, the accuracy of any subsequent dynamics calculations will largely depend on the quality of the PES. For collisions involving ground-state atomic nitrogen, the interaction between reactants correlates with a PES of N_3($^4A''$) symmetry, and the atom-exchange reaction can only occur under extreme atmospheric conditions such as during the reentry of spacecrafts in the atmosphere[14]. PESs have been constructed for this purpose by various groups[14–17], and used for calculating rate constants both for reactive and non-reactive collisions[18–22].

The importance of nitrogen atoms in electronically excited states on such extreme conditions has been emphasized in Ref. 23, but has so far been overlooked in the previous theoretical studies[16,18–21]. Indeed, excited nitrogen is abundant in the ionosphere[24] even under ordinary conditions, and its collision with N_2 is believed to be the source of N_3 in solid nitrogen under intense radiation fields[25–32], which is important for astrochemistry[30]. N(^2D)+N_2 collisions should then deserve theoretical attention.

There are five PESs involved in the N(^2D)+N_2 interaction ($1,2,3\,^2A''$ and $1,2\,^2A'$), with global analytical PESs recently proposed by us for the $1,2^2A''$ states[33]. The PES for the state $3^2A''$ may be discarded since it is highly repulsive and does not appear to have low-lying intersection with lower ones. Conversely, the $1\,^2A'$ PES is attractive and its contribution is fundamental for reactive studies. The aim of the present work is therefore to obtain an accurate double-sheeted representation of the two lowest $^2A'$ states, thus allowing the first predictions of rate constants including all relevant states. The importance of nonadiabatic effects is also analyzed.

The paper is organized as follows. Section II contains a survey on the $^4A''$ and $^2A''$ electronic states, while the calculation and modelling of a multi-sheeted $^2A'$ PES is described in section III. A quasiclassical trajectory (QCT) study performed for the N+N_2 exchange reaction is presented in section IV. The conclusions are in section V.

II. THE ^{4}A" AND ^{2}A" STATES

The PESs of the azide radical have been much studied by Morokuma and coworkers[34–36], and previously by other groups[37–41], for geometry optimizations, fundamental frequencies, dipole moments, minima on the seam of crossings (MSX) and vertical excitations. A brief survey of such attributes is given here, while presenting our previous PESs as modelled via double many-body expansion (DMBE[42,44–46]) theory, which will later be used for the dynamics calculations.

The quartet state of N_3 is repulsive and hence its global minimum corresponds to a van der Waals well at large N(^4S)-N_2 separations. The transition state

a)Electronic mail: varandas@qtvs1.qui.uc.pt

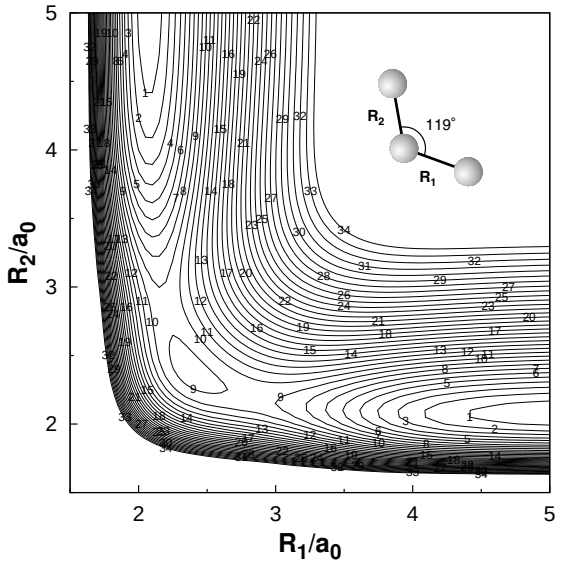

Figure 1. Contour plot for bond stretching of $N_3(^4A'')$ with the bond angle fixed at 119 deg. Contours are equally spaced by 5 kcal mol^{-1} starting at the $N(^4S)$+N_2 limit.

(TS) for the atom-exchange reaction is nonlinear with a bond angle of about 117 deg[14]. It has C_s symmetry, and a permutationally equivalent arrangement occurring on the exit channel (see Fig. 1). A shallow volcanic well lies between these two equivalent TSs, which connect it to the reactant and product channels. Such a well has been shown to be responsible for a rich reactive resonance structure that is observed in quantal studies of the exchange reaction[18,19]. The DMBE PES for $N_3(^4A'')$[17] in Fig. 1 shows the two equivalent TSs for the exchange process to lie 45.9 kcal mol^{-1} above dissociation, with the best theoretical estimate[47] for this attribute reported thus far being predicted to be of (45.6 ± 0.8) kcal mol^{-1}. Not surprisingly therefore, dynamics calculations reported on the DMBE PES have provided rate constants for the atom-exchange reaction[22] that agree better than previous ones[21,48] with the experimental results.[49,50] Our work has also shown that the quasiclassical treatment of the nitrogen atom-exchange reaction gives rate constants in perfect agreement with the quantum mechanical ones, as one would expect due to the large mass of the nitrogen atom.

The doublet state correlates to $N(^2D)$+N_2 and is so attractive that the linear $N_3(^2\Pi_g)$ isomer lies slightly below the $N(^4S)$+N_2 limit [note that the $N(^4S)/N(^2D)$ energy separation is 55 kcal mol^{-1}]. The cyc-N_3 isomer, on the other hand, lies about 30 kcal mol^{-1} above this spin-forbidden limit and shows large barrier to isomerization or dissociation[34], which makes it a good candidate as a high energy density material[12,13]. For this reason it has received considerable attention, and has been already detected experimentally,[6–9] but not isolated yet.

We have also reported[33] a global double-sheeted PES for the $^2A''$ state of N_3 which is so far the only PES suitable for scattering calculations, since it also accurately describes the asymptotic limits and long-range forces. This state holds both the linear $N_3(^2\Pi_g)$ and cyc-N_3 isomers, and we have already reported atom-exchange rate constants where the contributions of trajectories that passed through each minimum are discriminated. By plotting together the $N_3(^2A'')$ and $N_3(^4A'')$ PESs we have shown that even the spin-forbidden crossings match very closely the ones reported by Zhang *et al.*[34]

The $N_3(1^2A'')$ PES shows several features, including a TS for dissociation of each isomer, and a TS for isomerization between them. For visualizing all stationary structures together, including their permutationally equivalent ones, Fig. 2 shows a relaxed-triangular contour plot[51] in hyperspherical coordinates, which are related to the interatomic distances by[52]:

$$\begin{pmatrix} Q \\ \beta \\ \gamma \end{pmatrix} = \begin{pmatrix} 1 & 1 & 1 \\ 0 & \sqrt{3} & -\sqrt{3} \\ 2 & -1 & -1 \end{pmatrix} \begin{pmatrix} R_1^2 \\ R_2^2 \\ R_3^2 \end{pmatrix} \qquad (1)$$

By relaxing the "size" Q such as to give the lowest energy for each "shape" (β and γ) of the triangle formed by the three atoms, the relaxed plot is obtained using the scaled coordinates[51]

$$\begin{aligned} \beta^\star &= \beta/Q \\ \gamma^\star &= \gamma/Q. \end{aligned} \qquad (2)$$

Note that linear geometries lie at the border of the circumscribing circle, while the equilateral triangle (D_{3h}) geometry is located at the center of the plot ($\gamma^\star = \beta^\star = 0$), where a Jahn-Teller conical intersection (CI) occurs and distorts to the three equivalent minima related to cyc-N_3. They are connected amongst themselves via a pseudo-rotation path around the CI (see also Refs. 53–55).

The ground $^2A'$ state is Renner-Teller degenerate with the $^2A''$ one for linear configurations, and hence is also necessary for the study of the atom-diatom collisions. Since there is no PES suitable for scattering calculations for this state, we report the relevant double-sheeted DMBE form in the present work.

III. DOUBLE-SHEETED POTENTIAL ENERGY SURFACE FOR $N_3(^2A')$

Modelling of adiabatic PESs is often complicated by the presence of conical intersections, where the adiabatic energies change in a discontinuous way. This makes a diabatic representation often necessary for a correct description of both electronic sheets. If the

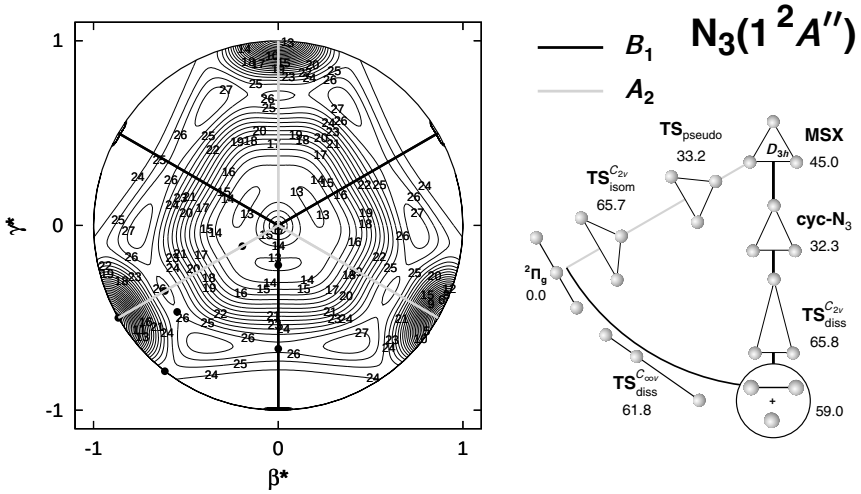

Figure 2. Relaxed triangular plot of the $N_3(1^2A'')$ PES in the hyperspherical coordinates of Eq. (2). The geometrical representation of the stationary structures are also displayed jointly with their relative energies (in kcal mol^{-1}). The locus of C_{2v} geometries correlating with the $^2B_1$ or $^2A_2$ electronic state is highlighted. Contours start at the energy of the linear minimum and are equally spaced by 2.51 kcal mol^{-1}.

adiabatic energies V_X and V_B are provided as the solutions of the electronic Schrödinger equation, the diabatic potential matrix is obtained from an unitary transformation as

$$\begin{pmatrix} V_{11} & V_{12} \\ V_{12} & V_{22} \end{pmatrix} = \begin{pmatrix} \cos\alpha & \sin\alpha \\ -\sin\alpha & \cos\alpha \end{pmatrix} \begin{pmatrix} V_X & 0 \\ 0 & V_B \end{pmatrix} \begin{pmatrix} \cos\alpha & -\sin\alpha \\ \sin\alpha & \cos\alpha \end{pmatrix} \tag{3}$$

where α is the mixing angle and all the above terms are functions of the internuclear coordinates. Solving for the diabatic elements, gives:

$$\begin{aligned} V_{11} &= V_X \cos^2\alpha + V_B \sin^2\alpha \\ V_{22} &= V_X \sin^2\alpha + V_B \cos^2\alpha \\ V_{12} &= (V_B - V_X)\cos\alpha \sin\alpha \end{aligned} \tag{4}$$

The only unknown in the above diabatization of the *ab initio* energies is the mixing angle α, and there has been several approaches to this problem[56–66]. In this work, we use the global diabatization angle (GDA[64]) method developed in our group, which has the advantage of giving the expected value of the angle where it is known from symmetry (or other requirements) while avoiding the calculation of molecular properties[57] (other than the energy) that often fail to provide the correct mixing angle at dissociation.

Once a suitable function can be devised for the angle, the diabatic points can be obtained and fitted to polynomial forms of the many-body expansion (MBE[59,67,68]) or double many-body expansion (DMBE[42–46]) families. The adiabatic representation is recovered as the eigenvalues of the diabatic matrix, giving

$$V_{B/X} = \frac{1}{2}(V_{11} + V_{22}) \pm \frac{1}{2}[(V_{22} - V_{11})^2 + 4V_{12}^2]^{1/2} \tag{5}$$

A. Ab initio calculations and potential energy features

All calculations have been done with the MOLPRO package[69] and the AVTZ[70,71] basis set. State-averaged CASSCF (complete active space self-consistent field) calculations were first performed with 15 correlated electrons in 12 active orbitals (thus leaving the N 1s orbitals closed), followed by multi-reference configuration interaction ones including the Davidson correction, MRCI(Q)[72,73].

Although the covalent features of this system have been well discussed by Morokuma and co-workers[34–36], the asymptotic limits may have found less attention. Their major characteristics at the CASSCF level of theory are illustrated in Fig. 3 which provides a general overview of the linear dissociation path with relaxed bond length. As seen, for linear configurations, the $1^2A'$ state (lowest solid black line) is degenerate with the $1^2A''$ (gray points) showing the $^2\Pi_g$ minimum and a small barrier (above the asymptote) for the $N(^2D)$+N_2 dissociation. The excited states are seen to be mainly repulsive and showing several intersections between them. Besides the $^2\Pi_u$ structure (which is degenerate on both $2^2A'$ and $2^2A''$), the $2^2A'$ state also holds the $^2\Sigma_g^+$ minimum which is well known experimentally[1–5,74]. Both excited minima lie on a $D_{\infty h}$ path, with a $2^2A'/3^2A'$ conical intersection between them. Because the present representation is based on a 2×2

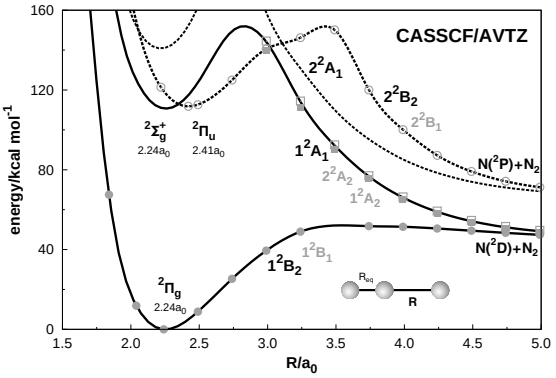

Figure 3. Linear dissociation obtained via CASSCF/AVTZ optimizations at a grid of values of one bond length, with the other relaxed. The electronic states correlating to $^2A'$ are shown in black and connected by splines, while those correlating to $^2A''$ are indicated by the gray symbols.

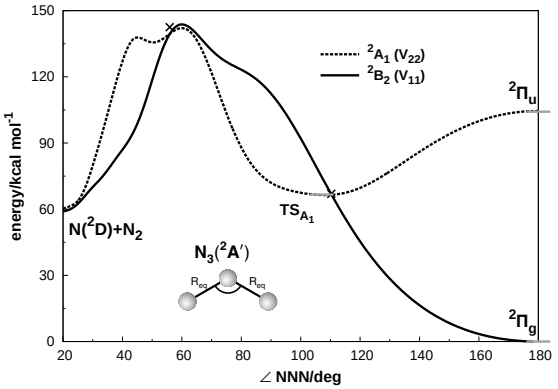

Figure 4. C_{2v} optimized energy profile for the final DMBE diabatic sheets of $N_3(^2A')$. The line segments show the MRCI(Q)/AVTZ prediction for the stationary structures and the points show the minima of the crossing seam from Ref. 36.

potential matrix, the $2^2A'/3^2A'$ crossings can only be described as maxima (avoided crossings) in the PES, with both ground and excited states dissociating to $N(^2D)$+N_2.

For a T-shaped approach of $N(^2D)$, the behavior of the $1^2A'$ sheet is mostly repulsive as it does not hold the cyc-N_3 isomer. This is seen in Fig. 4, which gives a general overview of the symmetric C_{2v} geometries with relaxed bond length (note that the dissociation limit is obtained for acute bond angles). Bending the $^2\Pi_g$ structure leads to a crossing between the $^2B_2$ and $^2A_1$ states with the MSX lying only 8 kcal mol^{-1} above the dissociation limit[35]. This suggests that this conical intersection may play a role in $N(^2D)$+N_2 collisions and therefore it is carefully analyzed in the present work. If the bond angle is decreased slightly from the CI point, a stationary structure is seen in the $^2A_1$ PES which, although looking like a minimum in the C_{2v} plot of Fig. 4, has one imaginary frequency on the antisymmetric stretching mode that leads to dissociation, and hence is here denoted TS_{A_1}.

Note that there are crossings with higher excited states[35] that are indicated by maxima in Fig. 4. The two lowest sheets cross again near D_{3h} configurations, but not without interference with such excited states (specially the 2^2B_2). In fact, even more than one crossing may be present. Since such a crossing lies high in energy (84 kcal mol^{-1} above dissociation[35]), it should be less important. In fact, it seems from our CASSCF exploratory calculations that above 55 kcal mol^{-1} from the $N(^2D)$+N_2 limit the number of crossings between excited doublet sheets (and even quartet ones) for C_{2v} geometries is so large that dynamical studies cannot be performed accurately in this regime, unless 8 doublet and at least 4 quartet PESs are involved. Thus, special attention is here given to the first crossing, while providing a reasonably accurate description of the D_{3h} one.

B. The global diabatization angle

From Eq. (4) it is clear that when the mixing angle α is zero, we have $V_{11} = V_X$ and $V_{22} = V_B$, and the opposite when $\alpha = \pi/2$. Within the GDA approach[64,75,76], α is written in a suitable analytical form, such as to warrant that at symmetric configurations it will vary from 0 to $\pi/2$. It was first[64] chosen, for a given ABC triatomic, to be a product of three functions, one per channel:

$$\alpha(\mathbf{R}) = \frac{\pi}{2}\alpha_{\mathrm{A-BC}}(\mathbf{R})\alpha_{\mathrm{B-AC}}(\mathbf{R})\alpha_{\mathrm{C-AB}}(\mathbf{R}) \qquad (6)$$

where for the channel A-BC it reads

$$\alpha_{\mathrm{A-BC}}(\mathbf{R}) = \frac{1}{2}\Big(1 - \tanh(\zeta[x - x_0(\mathbf{R})])\Big) \qquad (7)$$

with x being the atom-diatom Jacobi separation. Note that for symmetrical geometries, $x_0(\mathbf{R})$ should be a function that describes the locus of the conical intersection, while smoothly evolving for non-symmetrical ones. Although this functional form was chosen by convenience, it has been demonstrated[66] that Eq. (7) falls into a group of functions that would give rise to a non-adiabatic coupling term (F_{12}) with correct properties: peaking at the crossing and decaying exponentially away from it.

Irrespective of the triatomic, the scaled hyperspherical coordinates of Eq. (2), offer a great advantage in that the location of the linear and T-shaped geometries are clearly defined. We suggest here the use of the GDA approach in polar coordinates

$$\begin{aligned} r^2 &= \beta^{\star 2} + \gamma^{\star 2} \\ \theta &= \arctan2(\gamma^\star, \beta^\star) \end{aligned} \qquad (8)$$

where arctan2 is a function that gives the angle in the correct quadrant. As graphically shown in Fig 2, the C_{2v} geometries are given by $\theta = (2n+1)\pi/6$, and the linear ones by $r = 1$. Therefore, instead of writing the GDA approach as the product over channels in Jacobi coordinates (Eq. 6), the mixing angle is written as

$$\alpha(\mathbf{R}) = \alpha(r, \theta, Q) \tag{9}$$

Note that this is only possible because the (r, θ, Q) set of coordinates is unique, unlike Jacobi or valence coordinates. The three dissociation channels can also be easily identified with $\theta = \pi/6, 5\pi/6$, and $3\pi/2$.

The first step in the GDA approach consists of identifying where the mixing angle α should be 0 or $\pi/2$. For the title system, the two crossings between the ground and first excited states of $N_3(^2A')$ occur at T-shaped configurations (Fig. 4). Since the $^2B_2$ state lies lowest for all linear arrangements including dissociation and the $^2\Pi_g$ minimum, and remains so for bent structures up to 110 deg, it can be associated to the diabatic V_{11} term while $^2A_1$ is associated with V_{22}. The diabatization angle must then be $\pi/2$ when $^2A_1$ lies lowest, (from Fig. 4 it can be seen that this happens between the two intersections) and zero for other T-shaped geometries and all linear arrangements (where $^2B_2$ is the lowest), varying smoothly for non-symmetrical configurations.

The lower $^2A'$ sheet is shown in a relaxed plot of $\beta^\star$ and $\gamma^\star$ in Fig. 5, where it is highlighted what parts should correlate to $^2B_2$ and $^2A_1$. Note that one crossing is taken to be at D_{3h} configurations ($r=0$) and the other to occur with C_{2v} symmetry with $r=0.72$. The appropriate value of the mixing angle α can be written with a sinusoidal function in θ, which assumes either a value of zero or $\pi/2$ for C_{2v} arrangements. This can be suitably modelled by the following formula:

$$\alpha = \frac{\pi}{4}\left[1 + \sin(3\theta - \pi)\right] \frac{1}{2}\Big\{1 - \tanh\left[\zeta(Q)(r - r_0(Q))\right]\Big\} \tag{10}$$

Note that this differs substantially from the product over channels in Eq. (6), because all three dissociation channels are handled collectively by the polar angle θ.

Fixing the crossing locus to happen at $r_0 = 0.72$ for any "size" Q corresponds to a line at a fixed bond angle of 110.3 deg for any bond length, and this simple scalar gives a good description of the three equivalent loci of conical intersection and could largely simplify the equations. Although this exemplifies the power of these coordinates in modelling PESs, we decided to describe the slight variation of the crossing point for different bond lengths. This is done by performing $1D$ cuts for different Q and obtaining the point of crossing r_0 for each, followed by modelling the locus via:

$$r_0(Q) = r_a + r_b \exp[-r_c(Q - r_d)] \tag{11}$$

The work by Varandas[66] on the C_2 molecule has provided the method for determining the parameter ζ of the hyperbolic tangent in Eq. (10) from the sigmoidal shape of the dynamical correlation split between ground and excited state. This is incorporated here for the $3D$ case by calculating ζ for the above mentioned $1D$ cuts and modelling its variation with $\zeta = \zeta(\mathbf{R})$. The exponential form is used again, giving:

$$\zeta(Q) = \zeta_a + \zeta_b \exp[-\zeta_c(Q - \zeta_d)] \tag{12}$$

The other crossing around D_{3h} geometries is already modelled by Eq. (10) without a hyperbolic tangent, but with the mixing angle α showing a discontinuous variation. This turns out to be a good approximation, because this region involves three or more electronic states and according to Ref. 65, the sigmoidal shape of the dynamical correlation split is lost in such cases, as clearly verified here: thus, there is no point in attributing a value of ζ to it.

C. Fitting the diagonal diabatic terms V_{11} and V_{22}

After the *ab initio* energies are diabatized via Eq. (4), the V_{11} and V_{22} points can be modelled to analytical functions. Within DMBE theory[42,44–46], each diagonal diabatic term is expanded as

$$V_{11/22}(\mathbf{R}) = V^{(1)} + \sum_{i=1}^{3}\Big[V^{(2)}_{\rm EHF}(R_i) + V^{(2)}_{\rm dc}(R_i)\Big] + \Big[V^{(3)}_{\rm dc}(\mathbf{R}) + V^{(3)}_{\rm EHF,[11/22]}(\mathbf{R})\Big] \tag{13}$$

Because the upper and lower surfaces of $^2A'$ symmetry dissociate to ground state N_2 and $N(^2D)$, the only term in the above equation that is specific to V_{11} or V_{22} is the three-body extended Hartree-Fock ($V^{(3)}_{\rm EHF,[11/22]}$) term.

The $V^{(3)}_{\rm dc}$ term describes the long range atom-diatom dispersion and induction energies as an inverse power series of the distance between them, and is common for the A' and A'' DMBE PESs[17,33]. The zero of energy of the PES is fixed at the atom-diatom limit by imposing $V^{(1)} = -2D_e$, where D_e is the well depth of N_2. The specific functional forms used to describe $V^{(2)}$ and $V^{(3)}_{\rm dc}$ can be found elsewhere[17].

The coefficients to be fitted to the diabatic energies are then those of $V^{(3)}_{\rm EHF,[11/22]}$ and to define its functional form we make use of the integrity basis[59,77]:

$$\begin{aligned} \Gamma_1 &= Q_1 \\ \Gamma_2^2 &= Q_2^2 + Q_3^2 \\ \Gamma_3^3 &= Q_3(Q_3^2 - 3Q_2^2) \end{aligned} \tag{14}$$

where Q_i are symmetry-adapted displacement coordinates from a D_{3h} configuration of bond length R_0[59,68]. Note that the functions Γ_i are totally symmetric in

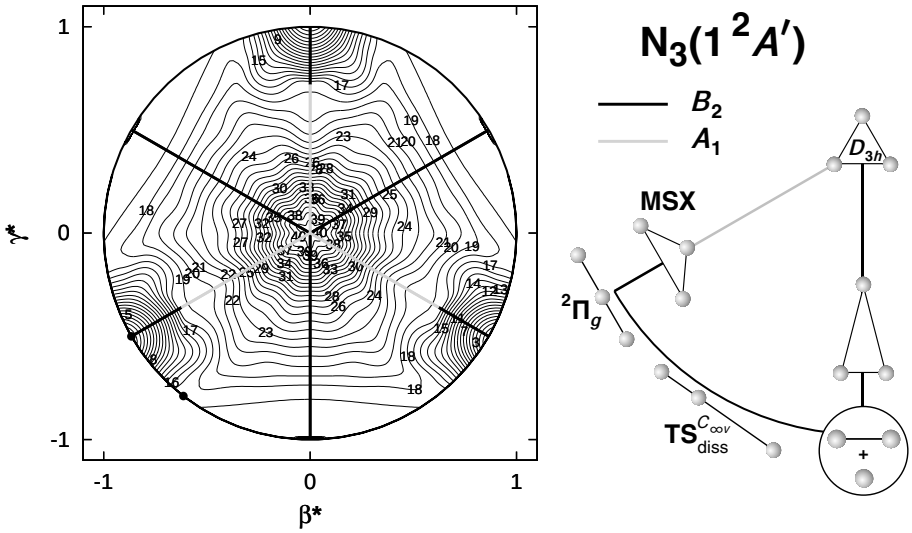

Figure 5. Relaxed triangular plot in the hyperspherical coordinates of Eq. (2) for the lower sheet of $N_3(^2A')$. The locus of geometries correlating with the $^2B_2$ electronic state is highlighted with a solid black line, while the $^2A_1$ one is in gray. Contours start at the linear minimum and are equally spaced by 3.5 kcal mol^{-1}.

the three-particle permutation group S_3, and hence any polynomial built as $P^{[m]} = \sum_{i,j,k} c_{ijk}^{[m]} \Gamma_1^i \Gamma_2^{2j} \Gamma_3^{3k}$ will also transform as the totally symmetric representation of S_3. The final form reads

$$V^{(3)}_{\mathrm{EHF},[11/22]}(\mathbf{R}) = \left[\sum_{i,j,k} c_{ijk}^{[11/22]} \Gamma_1^i \Gamma_2^{2j} \Gamma_3^{3k} \right] T(\mathbf{R}) \quad (15)$$

where $T(\mathbf{R})$ is a range determining factor that ensures that the three-body term vanishes at large interatomic distances. As in Ref. 78, it is convenient to damp the three-body term also for extremely short bond lengths to avoid possible instabilities, yielding:

$$T(\mathbf{R}) = \prod_{j=1}^{3} \left\{ 1 - \tanh\left[\gamma_1 \left(R_j - R_0 \right) \right] \right\} T'_j(R_j) \quad (16)$$

with the short-range part given by $T'_j(R_j) = \tanh\left(\gamma_2 R_j\right)$.

The above functions contain 77 linear parameters $c_{ijk}^{(m)}$ for V_{11} and 68 for V_{22}, which have been calibrated from a total of 429 *ab initio* energies via a linear least-squares fit. For an improved description of the stationary structures, a grid of points has been calculated at their vicinities and large weights given.

D. Nondiagonal diabatic term V_{12} and final nonlinear fit

The next step for obtaining the final PES is to fit the nondiagonal term of the diabatic potential matrix (V_{12}). It is seen from Eq. (5) that, if the adiabatic PESs are degenerate at some point ($V_X = V_B$), V_{12} must vanish there. Following Murrell *et al.*[58], this term is written as a three-body polynomial, such as in Eq. (15), and multiplied by a function that makes it vanish at symmetrical configurations and at the asymptotic limit. The use of the polar coordinates of Eq. (8) makes this straightforward, and we have chosen the form:

$$V^{(3)}_{12}(\mathbf{R}) = \left[\sum_{i,j,k} c_{ijk}^{[12]} \Gamma_1^i \Gamma_2^{2j} \Gamma_3^{3k} \right] \times \frac{1}{2} \Big[1 - \cos(6\theta - \pi) \Big] \Big(- r^2 + r \Big) \Big[1 - \tanh(\gamma(Q - Q_0)) \Big] \quad (17)$$

Even without the polynomial part, this functional form gives a qualitatively correct shape, and thus few coefficients are enough for V_{12}. A linear least-squares fit is again used with the fitted points obtained through diabatization. After all diabatic elements are obtained, the adiabatic potentials are recovered in analytical form by Eq. (5).

The adiabatic PESs obtained are then fine tuned through a final nonlinear least-squares fit to the original *ab initio* energies, where all the c_{ijk} coefficients of V_{11}, V_{22} and V_{12} are optimized together. The coefficients previously obtained when fitting the diabatic terms are used as a first guess, and the good general behavior of the nonlinear fit will depend on them. The weights for the stationary structures are kept and a somewhat larger weight generally assigned to the points belonging to the lower sheet. Special care was exercised to ensure that the diabatic sheets did not show any spurious crossings near the atom-diatom limit, as they closely approach each other.

The diabatic and adiabatic representations ob-

Table I. Stratified root-mean-square deviations for the two sheets of the $N_3(^2A')$ DMBE PES in kcal mol^{-1}.

	$1^2A'$		$2^2A'$	
Energy[a]	N[b]	rmsd	N[b]	rmsd
10	10	0.11		
20	20	0.38		
30	29	0.45		
40	38	0.57		
50	51	0.68		
60	78	0.64	8	1.42
80	208	0.59	96	1.85
100	264	0.79	173	2.49
120	336	0.83	277	2.87
140	348	0.84	313	3.12
160	359	1.01	337	3.55
180	377	1.00	362	3.66
200	379	1.07	368	3.74
220	400	1.05	381	3.87
240	405	1.05	389	3.92

[a] Relative to the ground $\tilde{X}^2\Pi_g$ state.
[b] Number of calculated *ab initio* points up to the indicated energy range.

tained after the final non-linear fit are shown in Fig. 6 for one-dimensional cuts using Eq. (8) and the size variable Q relaxed for the V_{11} sheet. The evolution from C_{2v} to non-symmetrical configurations is seen to be smooth, which is in fact one of the major advantages of using the GDA approach.

As it is shown in Table I, a good overall fit to the *ab initio* points has been obtained for the whole PES. Note that the ground state shows chemical accuracy over the entire range of fitted energies, while the upper one shows a somewhat larger deviation due to the presence of five crossings with higher electronic states (see Figs. 3 and 4). The fitted coefficients are given as supplementary material[79].

E. Features of the double-sheeted potential energy surface

The lower adiabatic sheet of $^2A'$ symmetry holds most of the important features, while the upper one shows mostly linear excited structures. Table II gives a comparison between the stationary structures of the DMBE PES and the ones obtained in Ref. 36, where the present fit is shown to accurately mimic the *ab initio* data, even for the position and energy of the minimum on the crossing seam. As seen in Table II, there is one stationary structure (TS_{up}) found in this work for the upper sheet that, to the best of our knowledge, has not been reported before (perhaps due to its asymmetric C_s nature). This transition state connects the upper cone (MSX) with the dissociation limit and its imaginary frequency corresponding to the antisymmetric stretch was obtained at the CASSCF/AVTZ level to be 345 cm^{-1}. The correct general behavior over the whole configurational space is best seen from the relaxed plots of Figs. 5 and 7 for the lower and upper adiabatic sheets, respectively.

Table II. Stationary structures for the $^2A'$ adiabatic PESs of N_3[a].

			fitted	
structure	property	MRCI(Q)[b]	Ref. 36	DMBE
$^2\Pi_g$ ($1^2A'$)	R/a_0	2.24	2.24	2.24
	Θ/deg	180	180	180
	ΔV	0.0	-0.94	0.0
	ω/cm^{-1}			1756, 1328, 433(2)
$TS^{C_{\infty v}}_{diss}$ ($1^2A'$)	R_1/a_0	4.23		4.18
	R_2/a_0	2.09		2.09
	Θ/deg	180		180
	ΔV	61.8		61.8
	ω/cm^{-1}			273i, 2310, 106(2)
TS_{A_1} ($1^2A'$)	R/a_0	2.38	2.38	2.37
	Θ/deg	107	109	108
	ΔV	66.6	66.1	66.4
	ω/cm^{-1}			1472, 507, 316i
MSX	R/a_0	2.38	2.37	2.37
	Θ/deg	110	111	110
	ΔV	66.9	66.7	66.5
TS_{up} ($2^2A'$)	R_1/a_0			2.16
	R_2/a_0			3.09
	Θ/deg			107
	ΔV			89.7
	ω/cm^{-1}			1982, 805i, 567
$^2\Pi_u$ ($2^2A'$)	R/a_0	2.41	2.41	2.42
	Θ/deg	180	180	180
	ΔV	104	104	104
	ω/cm^{-1}			1264, 906, 471i (2)
N(^2D)+N_2	ΔV	59.0		59.0

[a] Energies are given in kcal mol^{-1} relative to the ground $\tilde{X}^2\Pi_g$ state, with geometries in valence coordinates.
[b] From Refs. 34,36.

The final form of the diabatic DMBE PES is shown in the plot of Fig. 4, where it can be seen that the minimum on the crossing seam is accurately modelled. The maximum seen in the left side of this graph comes from the $2^2A'$ *ab initio* energies calculated in this region and stem from the presence of other electronic states. It is also seen that a correct description of both $^2\Pi_g$ and $^2\Pi_u$ structures is given, although as mentioned earlier, the presence of a $2^2A'/3^2A'$ crossing for shorter bond lengths makes the description of the $^2\Sigma^+_u$ not possible on the 2×2 representation of this work. However, this should not be important for atom-diatom collisions, due to the high energies involved.

All five adiabatic sheets necessary for N($^4S/^2D$)+N_2 collisions are shown together for C_{2v} configurations with relaxed bond lengths in Fig. 8. The $^2A''$ sheets from our previous work[33] is given in gray and the $^4A''$ in dotted gray[17]. Note that the cusp from the conical intersection for the

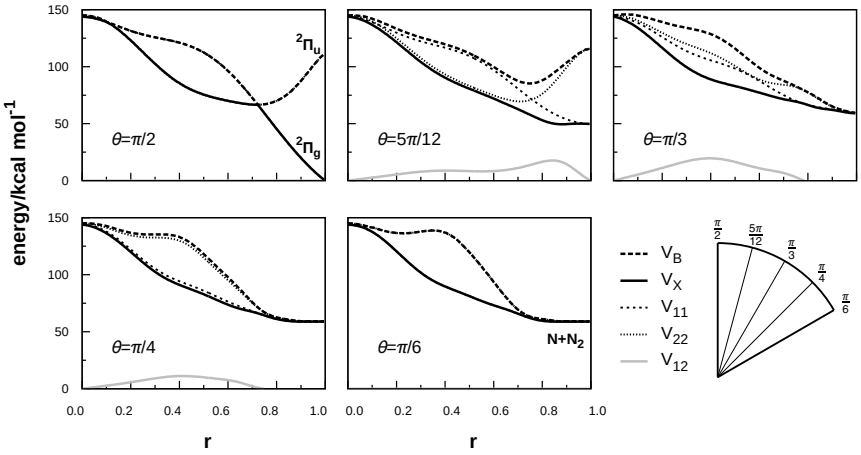

Figure 6. One-dimensional cuts for fixed values of the polar angle showing the evolution of the diabatic and adiabatic representations for non-symmetrical configurations; for the coordinates, see Eq. (8).

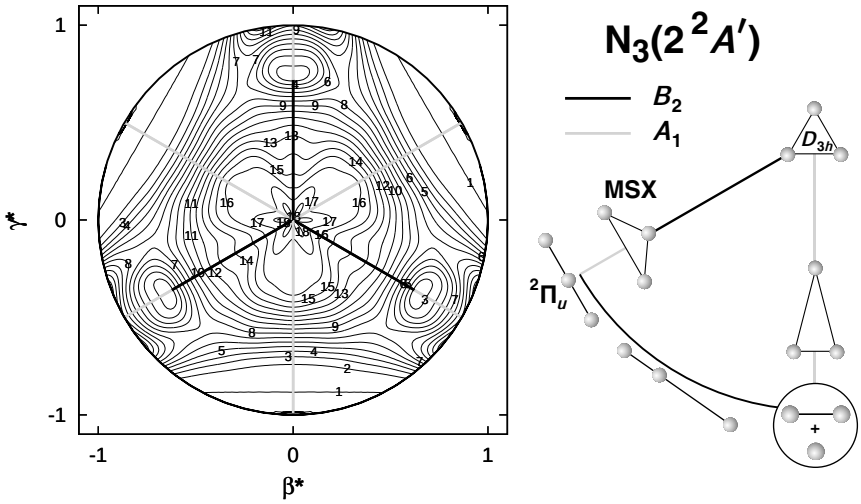

Figure 7. Relaxed plot in the coordinates of Eq. (2) for the upper sheet of $N_3(^2A')$. Contours start at the dissociation limit and are spaced by 5 kcal mol^{-1}.

$^2A'$ sheets is accurately given, as imposed by the formalism. This plot also shows the location and energy of the crossings (conical intersections, CIs) involving states of the same spin-spatial symmetry, $^2A'/^2A''$, and others with involving different spin ($^4A''/^2A''$) calculated in Refs. 34–36. As can be seen, the three crossings of different spin agree well with the *ab initio* calculated values. The plot additionally shows that there are several other spin forbidden crossings, and although most of them involve an excited doublet state, we want to call attention to the one between the $1^2A'/1^4A''$ sheets (with a bond angle around 120 deg) which appears to be the lowest in energy and not previously discussed. The $^2A'/^2A''$ crossings reported in Refs. 35,36 are also satisfactorily described.

IV. QUASICLASSICAL STUDY OF N+N$_2$ ATOM-EXCHANGE REACTION

In this section we report the first predictions of $N(^2D)$+N_2 atom-exchange rate constants, including all necessary contributions, while also comparing them with the ones involving ground-state atomic nitrogen. Although quantum calculations are important for picking reactive resonances in the $N(^4S)$+N_2 exchange reaction[18,19], we have shown[22] that quasiclassical trajectories is all that is required for predicting more averaged quantities such as rate constants, in this case mostly due to the large atomic masses involved. Thus, the same approach will be followed here. On the other hand, nonadiabatic effects cannot be discarded *a priori* since there are low-lying conical intersections, which makes the current dynamics

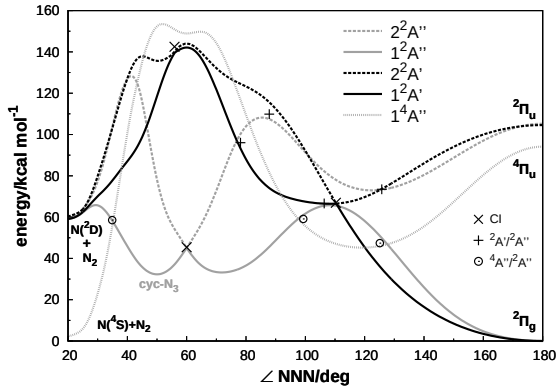

Figure 8. Optimized energy profile in C_{2v} symmetry for the five adiabatic DMBE PESs[17,33]. The MRCI(Q)/AVTZ prediction[34,36] for the minima on the seam of different types of crossings is indicated with the symbols.

problem a formidable one even when using trajectory surface hopping (TSH) methods. Furthermore, the unique characteristics of the $^2A''$ PES makes it largely prone to the appearance of geometric phase effects, as has been demonstrated by spectroscopic[55,80,81] calculations, and here we explore its eventual importance on scattering problems via trajectory calculations.

A. Method

In a first part, trajectories were integrated for the ground adiabatic $^2A'$ and $^2A''$ PESs separately without considering the upper sheets, denoted here as QCT-A (with A standing for adiabatic). Rate constants for the atom-exchange reaction have been obtained for fixed temperatures by sampling the relative atom-diatom translational energy, the ro-vibrational state of the N_2 molecule and the impact parameter according to the QCT method[22,82,83]. The calculations used a time step of 0.2 fs with the reactants initially separated by 17 a_0, while the maximum value of the impact parameter (b_{max}) has been optimized by trial and error for each temperature and each PES.

The total rate constant for the $N(^2D)$+N_2 atom-exchange reaction is given as the sum of the contribution of the two PESs ($k(T) = k_{^2A'}(T) + k_{^2A''}(T)$) while each term is given by:

$$k_x(T) = g_e(T) \left(\frac{8k_BT}{\pi\mu}\right)^{1/2} \pi b_{max}^2 \frac{N_r}{N} \qquad (18)$$

In the above equation, N ($= 5 \times 10^4$) is the total number of trajectories and N_r the number of reactive ones, while μ is the reduced mass of the reactants and $g_e(T)$ is the electronic degeneracy factor. Although the latter is usually considered to be 1/5 as its high temperature limit, we have instead used the more rigorous form of $g_e(T) = q_{N_3}/q_{N(^2D)}q_{N_2}$, where $q_{N_2} = 1$, $q_{N_3} = 2$, and $q_{N(^2D)} = 6 + 4\exp(-12.53\,K/T)$ is the partition function of $N(^2D)$. Finally, the 68 % associated errors bars are given by $\Delta k = k\left(\frac{N-N_r}{NN_r}\right)^{1/2}$.

Besides the atom-exchange reactivity, we also recorded collisional properties (irrespective of the trajectory outcome), such as the amount of time each trajectory spent with potential energy less than 1 kcal mol^{-1}, in order to estimate the average time that the system spend as an unstable azide complex (N_3^*) and how many trajectories are able to enter the potential wells. Furthermore, in the case of the $^2A''$ PES, which shows a CI at D_{3h} configurations with very little barriers for pseudo-rotation, we have also followed the trajectories checking for loops around the crossing point to consider the probabilities of geometric phase (GP) effects. An algorithm to count the number of loops was obtained using the polar coordinates of Eq. (8), and used for subsequent analysis of the results.

In oder to estimate the effect of electronic transitions, we repeated the above calculations but implementing the trajectory surface hopping (QCT-TSH) method of Tully and Preston[84–86] as implemented in Ref. 87. Although this method has limitations, and more sophisticated algorithms have been proposed[88–91] (and references therein), a simple estimate of the hopping probability over a large number of trajectories is here enough for drawing the conclusions needed in the next section. In our implementation, after the initial conditions were selected the trajectory starts on the ground adiabatic potential energy surface (V_X) and is monitored at each integration step. If the energy difference between the two adiabatic sheets ($\Delta V = V_B - V_X$) reaches a minimum, the probability of a nonadiabatic transition is calculated using the Landau-Zener formula:

$$P_{LZ} = \exp\left(-2\pi A^2/\hbar B u\right) \qquad (19)$$

where u is the velocity, and A and B are the parameters that define the splitting between V_X and V_B at the instant t, given by

$$\Delta V = [B^2u^2(t-\tau)^2 + 4A^2]^{1/2} \qquad (20)$$

where τ is the time corresponding to the minimum of ΔV. These parameters are determined using the three previous integration steps. After calculating the Landau-Zener probability a random number ξ is generated and, if $P_{LZ} < \xi$, the trajectory continues on the same PES. If, on the other hand $P_{LZ} > \xi$ the trajectory hops to the other potential energy surface and the momentum is adjusted according to the procedure suggested by Tully and Preston[84] while the coordinates are kept unchanged. This approximation enforces conservation of both energy and momenta.

Another detail that must be taken into account is that the title system is degenerate in the asymptotic

limit, and since the method may allow hops to occur at any point, the trajectory is likely to stay hopping back and forth in this region for a long time. As noted in Ref. 92, this asymptotic hopping is an unwanted feature of the original Tully's method, and does not occur in other algorithms such as the Blais-Truhlar one[88]. We follow previous work[92,93] and do not allow hops to occur for large atom-diatom separations. To set the maximum value, we have plotted the hopping probability as a function of the atom-diatom Jacobi coordinate, and observed that such a probability peaks around the CI but quickly dies-off on both sides. Only for high temperatures does a raise occur at large separations which, although of minor effect, has been eliminated by setting at $4a_0$ the maximum distance where hopping can occur.

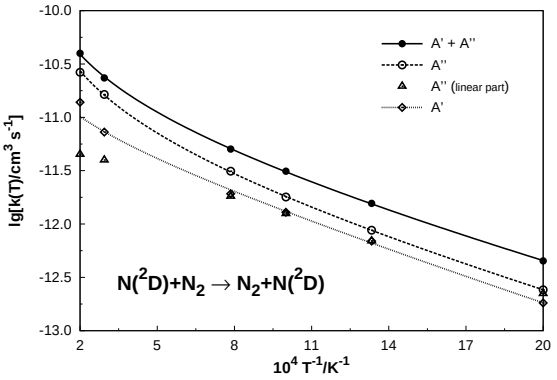

Figure 9. Logarithm of the exchange rate constants obtained in this work (QCT-A), showing the total rate and its contributions.

B. Results and discussion

The results obtained in the present calculations for the $N(^2D)$+N_2 atom-exchange rate constants are given in Table III, along with the $N(^4S)$+N_2 ones[22] to allow a comparison (at least qualitative) between the reactivity of the two states of atomic nitrogen. The lower reactivity of the ground state atom is clearly expected, since the classical barrier height for this process is 45.9 kcal mol^{-1}, sixteen times larger than for the excited state. Although we do not have information about how much $N(^2D)$ is formed under the extreme atmospheric conditions achieved in spacecraft re-entry, we hope that the rate constants given in Table III may serve as a guide to assess whether or not this reaction will be relevant for heat-shield designing or for studies of nitrogen containing plasmas.

It is interesting to note that, although both $^2A'$ and $^2A''$ sheets have exactly the same barrier height of 2.8 kcal mol^{-1} for the linear reaction (as they are degenerate for $C_{\infty v}$ arrangements), the $^2A''$ state shows a bigger reactivity specially for higher temperatures, as graphically shown in Fig. 9. This happens because the $^2A'$ state is repulsive for a T-shaped attack, while $^2A''$ has a barrier (of 6.8 kcal mol^{-1}) that leads to the well corresponding to the cyc-N_3 species. In fact, the cyc-N_3 region can be reached for even lower energies via isomerization after a trajectory enters the linear well, lying the barrier in this case 6.1 kcal mol^{-1} above dissociation. The contribution of each of these regions to the exchange rate constant was singled out in our previous paper[33], while we give now in Table IV the probability for a trajectory to enter one of the potential wells, either linear ($P_{\rm lin}$) or cyclic ($P_{\rm cyc}$), as calculated in the QCT-A treatment and without separating reactive from non-reactive events. For those trajectories that have entered the wells, we also give the average time spent there as an unstable N_3^* complex, hoping that this information may give some insight on the possibility of its detection in gas phase. However, the actual average lifetimes are obtained by multiplying the tabulated probabilities and times for forming each complex. From this, it is observed that the linear complex is predominant by about a factor of two at all temperatures here considered.

The $^2A'$ rate constant should be more fairly compared with the part of the $^2A''$ rate constant calculated without the trajectories that passed through the cyclic well, since in this case the barrier is exactly the same. In fact, for temperatures under 1273K the two contributions are very similar to each other as shown in Fig. 9, since the internal energy is rarely enough to allow isomerization on the $^2A''$ sheet, a situation that changes for higher temperatures as the cyclic pathway becomes important and trajectories that suffer isomerization no longer contribute to "linear" $^2A''$. There is a small difference between them for 500 K, although lying inside the error bar of our predictions. Because the trajectories have very low translational energy at this temperature, the rate constants become very sensitive to the PES, and such effect is explained by the differences among the two potentials for slightly nonlinear attacks, where the degeneracy is lost. The barrier height of the $^2A'$ state reaches (at most) 0.28 kcal mol^{-1} above $^2A''$ one for such configurations, but this small separation may still explain the difference in the calculated rate constant.

We now address the TSH results which are shown in Table III, jointly with the differences relative to the QCT-A ones. As it is apparent, the observed differences from this Table look unsystematic and comparable to the calculated 68 % statistical errors. In turn, Table IV shows that the hopping probabilities are small except at high temperatures. The main observation is therefore that nonadiabatic transitions should be of little relevance for the rate constants here reported. This may be rationalized from the fact that hopping can only occur after the entrance barrier is overcome, which is achieved for a very reduced percentage of the total number of trajectories. Once en-

Table III. Thermal rate constants for the $N(^4S/^2D)+N_2$ atom-exchange reaction in $cm^3\,s^{-1}$.

	$^2A'+{}^2A''$	$^2A'$		$^2A''$		$^4A''$
T/K	$10^{13}k(T)$[a]	$10^{13}k(T)$[a]	Δ[b]	$10^{13}k(T)$[a]	Δ[b]	$k(T)$[c]
500	3.99±0.25	1.83±0.12	0.01	2.16±0.13	−0.26	
750	14.89±0.55	6.73±0.26	−0.19	8.16±0.29	−0.59	
1000	31.12±0.87	12.71±0.39	−0.18	18.41±0.48	0.49	
1273	49.88±1.21	19.49±0.53	0.28	30.39±0.68	−0.86	0.54×10^{-18}
3400	241.03±3.27	77.98±1.37	3.97	163.05±1.90	−0.77	1.33×10^{-13}
5000	407.22±4.69	138.00±2.01	−1.48	269.22±2.68	4.50	1.69×10^{-12}

[a] Calculated with TSH.
[b] Difference between TSH and QCT-A.
[c] From Ref. 22.

Table IV. Statistical properties of the $N(^2D)+N_2$ collisions.[a]

	$^2A'$				$^2A''$				
T/K	T_{vib}[b]	$P_{\rm hop}$[c]	$P_{\rm lin}$[d]	τ_{lin}[e]	T_{vib}[b]	$P_{\rm hop}$[c]	$P_{\rm GP}$[f]	$P_{\rm lin}/P_{\rm cyc}$[d]	τ_{lin}/τ_{cyc}[ce]
500	680	0.00	1.25	951	710	0.05	0.05	1.26/0.10	1162/15454
750	885	0.02	3.47	799	1015	0.23	0.25	3.53/0.51	949/6118
1000	1103	0.08	6.40	751	1124	0.53	0.58	6.10/1.25	765/2676
1273	1404	0.15	9.14	569	1469	0.84	1.09	8.64/2.41	606/1241
3400	4122	1.71	26.34	176	3904	2.64	4.73	23.1/12.6	205/240
5000	6630	3.10	31.65	96	6151	3.22	5.89	28.0/18.4	92/163

[a] Probabilities in % and properties calculated by QCT-A, except for $P_{\rm hop}$.
[b] Fitted vibrational temperature of the exchanged products.
[c] Probability for a trajectory to perform an electronic transition.
[d] Probability for a trajectory to enter the potential well.
[e] Average time in fs spent as N_3^* complex for trajectories that entered the well.
[f] Probability for a trajectory to perform an odd number of loops around the conical intersection.

tered the covalent region, the trajectory may hop near the crossing point (see Table IV for such probabilities), but for making a difference in the calculated rate constants the hops should largely favor the formation of products over the reactants (or the opposite), which seems to be not the case.

Because the $^2A'$ and $^2A''$ states are markedly different from each other (see Fig. 8), they must be analyzed separately. Regarding $^2A'$, the minimum of the crossing seam lies 7.5 kcal mol^{-1} above reactants and it is not reachable for most trajectories under normal temperatures (see Table IV). Further analysis has shown that the probability for a hop to occur is reduced for small rotational quantum numbers of the reactant diatomic, which is possibly due to the bent nature of the crossing, while the minimum energy path is linear. On the other hand, the $^2A''$ state shows a Jahn-Teller CI that lies under the reactants limit, with hops being likely to occur whenever the trajectory enters the cyclic well (the barrier to access this region is 6.1 kcal mol^{-1} above reactants). However, the upper cone lies high in energy (see Fig. 8) and hence, unless the trajectory can accommodate 49 kcal mol^{-1} of internal energy, it will be trapped there and will not yield products. This means that it will most certainly hop back to the ground state from where it can enter the products' valley.

For a fixed temperature of $T=1000$ K, Fig. 10 gives a complete description of the percentage of trajectories that enter the various potential wells, whether atom-exchange occurs or the trajectory goes back to reactants, as well as the probability for hops to occur in each state symmetry. Note that this representation is schematic (straight lines do not represent real paths), with trajectories that enter both minima (irrespective of the order) being separated as an item per se. This makes it clear that even if all hops led to reaction, which is not the case, they would still not make a large difference in the final rate constant, since the total probability is still quite low. Specifically for the $^2A''$ PES, hops are quite probable to occur after the cyclic well is reached, but the latter event is in turn quite improbable. Thus, in this case too, the prediction is that the state-to-state reaction rate constants cannot dramatically change. In fact, the probability distribution of the products both for the QCT-A and TSH results shows that there is a warming in the products vibrational distribution at the expenses of the translational one, *i.e.*, due to translational to vibrational energy transfer. This is seen in Table IV and Fig. 11, and may be attributed to the translational energy lost in overcoming the entrance barrier[33], which

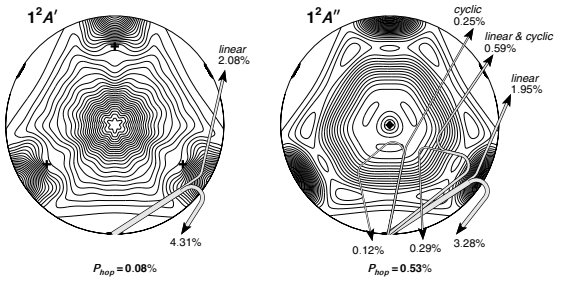

Figure 10. Schematic representation of the probabilities for reactive and nonreactive (recrossing) events after entering the potential wells from QCT-A calculations at $T = 1000$K. For simplicity, the percentage is shown at one part of the PES but it includes contributions from the other permutationally equivalent one. The hopping probability comes from the TSH calculations.

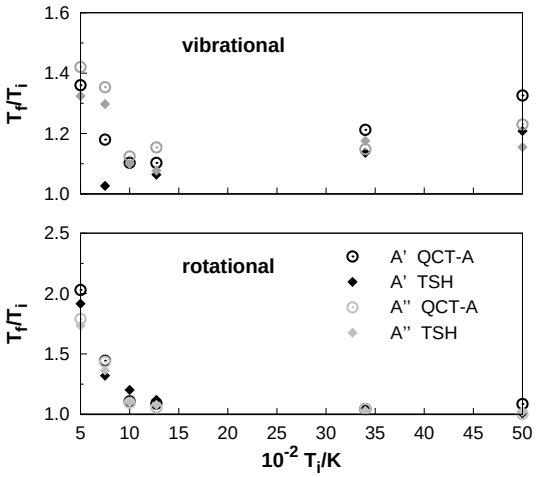

Figure 11. Ratio of vibrational and rotational temperatures (products/reactants) for the title reaction.

gets randomized in the potential well. Conversely, the rotational distribution is little affected except for low temperatures.

Apart from electronic transitions, geometric phase effects may play a role in the $^2A''$ PES since pseudorotation around the D_{3h} conical intersection is almost barrier-free, and a typical trajectory inside this well may encircle the CI even more than once before leaving to the products. Although much has been achieved in understanding how the geometrical-phase effect can influence bound states[94,95], and a study of the GP effect has been specifically performed for the title system[55,80,81], it is less studied in scattering problems[96,97] (see also Ref. 98). Such effects are likely to cancel out in the final properties (as in the H+H_2 case[96]), but it would be interesting to assess how probable they can be in the $N_3(^2A'')$ PES, given its unique characteristics. By counting the number of complete

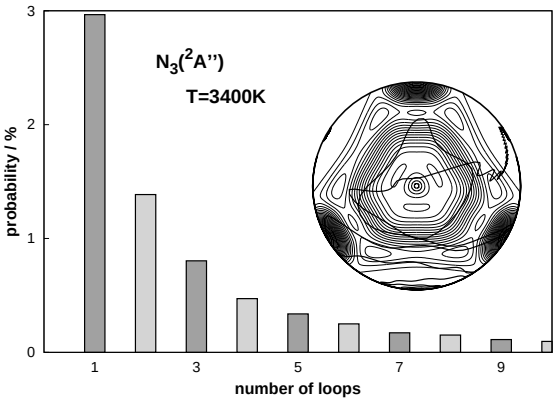

Figure 12. Probability for a trajectory (for the $T = 3400$K batch) to perform a given number of closed paths around the conical intersection. The insert shows a sample trajectory in the coordinates of Eq. (2) performing one loop around the CI.

loops around the line of D_{3h} symmetry, we have calculated the probability for a trajectory to loop around the seam an odd number of full cycles. The results are shown in Table IV for the batches of trajectories run for fixed temperatures. Note that an even number of closed loops annihilates the GP effect. It is seen that the probability of showing GP effect is small but non-negligible, and comparable in magnitude with the surface hopping probability. Interestingly, the number of trajectories showing an odd number of loops decreases nearly exponentially with the looping order, as shown from Fig. 12. Certainly, only a full quantum dynamics[52,99,100] study can provide quantitative results on the GP effect, but the probabilities calculated in this work can give an idea of how much GP can affect the rate constant.

V. CONCLUDING REMARKS

We have given a full account of $N(^4S/^2D)+N_2(^1\Sigma_g^+)$, with accurate and global potential energy surfaces presented for all the five relevant states. Starting with a survey of the $^4A''$ and $^2A''$ sheets, we modelled a 2×2 diabatic representation of the electronic Hamiltonian for $N_3(^2A')$. Based on accurate *ab initio* energies and using the DMBE theory for the fit, this is the first set of PESs suitable for scattering calculations for $N(^2D)+N_2$ collisions, while also giving an accurate representation of stationary structures.

A complete study of the $N(^2D)+N_2$ atom-exchange reaction was performed for the first time, using quasiclassical trajectories and including the relevant contributions ($^2A'$ and $^2A''$). The results are compared with the analogous $N(^4S)+N_2$ collision, and the relevance of the processes for atmospheric conditions is

discussed. Although non adiabatic transitions may occur in such collisions, the effects on the final exchange rate constant are shown to be negligible. The probability of encircling a conical intersection is given for a first idea on the possibility of geometric phase effects in scattering.

ACKNOWLEDGMENTS

This work is financed by FEDER through "Programa Operacional Factores de Competitividade - COMPETE" and national funds under the auspices of Fundação para a Ciência e a Tecnologia, Portugal (projects PTDC/QUI-QUI/099744/2008, PTDC/AAC-AMB/099737/2008, and SFRH/BD/61229/2009).

REFERENCES

[1]B. A. Thrush, Proc. R. Soc. Lond. A. **235**, 143 (1956).
[2]A. E. Douglas and W. J. Jones, Can. J. Phys. **43**, 2216 (1965).
[3]R. A. Beaman, T. Nelson, D. S. Richards, and D. W. Setser, J. Phys. Chem. **91**, 6090 (1987).
[4]C. R. Brazier, P. F. Bernath, J. B. Burkholder, and C. J. Howard, J. Chem. Phys. **89**, 1762 (1988).
[5]R. E. Continetti, D. R. Cyr, D. L. Osborn, D. J. Leahy, and D. M. Neumark, J. Chem. Phys. **99**, 2616 (1993).
[6]N. Hansen and A. M. Wodtke, J. Phys. Chem. A **107**, 10608 (2003).
[7]P. C. Samartzis, J. J.-M. Lin, T.-T. Ching, C. Chaudhuri, Y. T. Lee, S.-H. Lee, and A. M. Wodtke, J. Chem. Phys. **123**, 051101 (2005).
[8]J. Zhang, P. Zhang, Y. Chen, K. Yuan, S. A. Harich, X. Wang, Z. Wang, X. Yang, K. Morokuma, and A. M. Wodtke, Phys. Chem. Chem. Phys. **8**, 1690 (2006).
[9]P. C. Samartzis, J. J.-M. Lin, T.-T. Ching, C. Chaudhuri, S.-H. Lee, and A. M. Wodtke, J. Chem. Phys. **126**, 041101 (2007).
[10]P. C. Samartzis and A. M. Wodtke, Phys. Chem. Chem. Phys. **9**, 3054 (2007).
[11]C. Larson, Y. Ji, P. C. Samartzis, A. Quinto-Hernandez, J. J. Lin, T.-T. Ching, C. Chaudhuri, S.-H. Lee, and A. M. Wodtke, J. Phys. Chem. A **112**, 1105 (2008).
[12]P. C. Samartzis and A. M. Wodtke, Int. Rev. Phys. Chem. **25**, 572 (2006).
[13]V. E. Zarko, Combustion, Explosion, and Shock Waves **46**, 121 (2010).
[14]D. Wang, J. R. Stallcop, W. M. Huo, C. E. Dateo, D. W. Schwenke, and H. Partridge, J. Chem. Phys. **118**, 2186 (2003).
[15]A. Laganà, E. Garcia, and L. Ciccarelli, J. Phys. Chem. **91**, 312 (1987).
[16]E. Garcia, A. Saracibar, S. Gomez-Carrasco, and A. Laganá, J. Phys. Chem. A **10**, 2552 (2008).
[17]B. R. L. Galvão and A. J. C. Varandas, J. Phys. Chem. A **113**, 14424 (2009).
[18]W. Wang, W. M. Huo, C. E. Dateo, D. W. Schwenke, and J. R. Stallcop, J. Phys. Chem. A **120**, 132 (2003).
[19]D. Wang, W. M. Huo, C. E. Dateo, D. W. Schwenke, and J. R. Stallcop, J. Chem. Phys. **120**, 6041 (2004).
[20]F. Esposito, I. Armenise, and M. Capitelli, Chem. Phys. **331**, 1 (2006).
[21]S. Rampino, D. Skouteris, A. Laganà, E. Garcia, and A. Saracibar, Phys. Chem. Chem. Phys. **11**, 1752 (2009).
[22]P. J. S. B. Caridade, B. R. L. Galvão, and A. J. C. Varandas, J. Phys. Chem. A **114**, 6063 (2010).
[23]A. Laricchiuta, F. Pirani, G. Colonna, D. Bruno, C. Gorse, R. Celiberto, and M. Capitelli, J. Phys. Chem. A **113**, 15250 (2009).
[24]T. Tohmatsu, *Compendium of Aeronomy* (Kluwer Academy, Norwell, Mass., 1990).
[25]R. Tian, J. C. Facelli, and J. Michl, J. Chem. Phys. **92**, 4073 (1988).
[26]R. Tian and J. Michl, Faraday Discuss. Chem. Soc. **86**, 113 (1988).
[27]P. Hassanzadeh and L. Andrews, J. Phys. Chem. **96**, 9177 (1992).
[28]V. N. Khabasheskua, J. L. Margrave, K. Waters, and J. A. Schultz, J. Appl. Phys. **82**, 1921 (1997).
[29]K. Sankaran, K. Sundararajan, and K. S. Viswanathan, J. Phys. Chem. A **105**, 3995 (2001).
[30]R. L. Hudson and M. H. Moore, Astrophys. J. **568**, 1095 (2002).
[31]J. C. Amicangelo, J. R. Collier, C. T. Dine, N. L. Saxton, and R. M. Schleicher, Mol. Phys. **105**, 989 (2007).
[32]C. S. Jamieson and R. I. Kaiser, Chem. Phys. Lett. **440**, 98 (2007).
[33]B. R. L. Galvão and A. J. C. Varandas, J. Phys. Chem. A **115**, 12390 (2011).
[34]P. Zhang, K. Morokuma, and A. M. Wodtke, J. Chem. Phys. **112**, 014106 (2005).
[35]I. S. K. Kerkines, Z. Wang, P. Zhang, and K. Morokuma, Mol. Phys. **107**, 1017 (2009).
[36]Z. Wang, I. S. K. Kerkines, K. Morokuma, and P. Zhang, J. Chem. Phys. **130**, 044313 (2009).
[37]J. N. Murrell, O. Novaro, and S. Castillo, Chem. Phys. Lett. **90**, 421 (1982).
[38]M. Bittererová, H. Östmark, and T. Brinck, J. Chem. Phys. **116**, 9740 (2002).
[39]J. Wasilewski, J. Chem. Phys. **105**, 10969 (1996).
[40]J. M. L. Martin, J. P. François, and R. Gijbels, J. Chem. Phys. **90**, 6469 (1989).
[41]C. Petrongolo, J. Mol. Struct. **175**, 215 (1988).
[42]A. J. C. Varandas, J. Mol. Struct. Theochem. **21**, 401 (1985).
[43]A. J. C. Varandas and A. I. Voronin, Mol. Phys. **85**, 497 (1995).
[44]A. J. C. Varandas, Adv. Chem. Phys. **74**, 255 (1988).
[45]A. J. C. Varandas, in *Lecture Notes in Chemistry*, edited by A. Laganá and A. Riganelli (Springer, Berlin, 2000), vol. 75, pp. 33–56.
[46]A. J. C. Varandas, *Conical Intersections: Electronic Structure, Spectroscopy and Dynamics* (World Scientific Publishing, 2004), chap. 5, p. 91, Advanced Series in Physical Chemistry.
[47]A. J. C. Varandas, J. Chem. Phys. **133**, 064104 (2010).
[48]F. Esposito and M. Capitelli, Chem. Phys. Lett. **302**, 49 (1999).
[49]A. Bar-Nun and A. Lifshitz, J. Chem. Phys. **47**, 2878 (1967).
[50]R. K. Lyon, Can. J. Chem. **50**, 1437 (1972).
[51]A. J. C. Varandas, Chem. Phys. Lett. **138**, 455 (1987).
[52]C. A. Mead and D. G. Truhlar, J. Chem. Phys. **70**, 2284 (1979).
[53]D. Babikov, V. A. Mozhayskiy, and A. I. Krylov, J. Chem. Phys. **125**, 084306 (2006).
[54]V. A. Mozhayskiy, D. Babikov, and A. I. Krylov, J. Chem. Phys. **124**, 224309 (2006).
[55]D. Babikov, J. Chem. Phys. **134**, 114305 (2011).
[56]M. Baer, Chem. Phys. Lett. **35**, 112 (1975).
[57]H. J. Werner and W. Meyer, J. Chem. Phys. **74**, 5802 (1981).
[58]J. N. Murrell, S. Carter, I. M. Mills, and M. F. Guest, Mol. Phys. **42**, 605 (1981).
[59]J. N. Murrell, S. Carter, S. C. Farantos, P. Huxley, and

A. J. C. Varandas, *Molecular Potential Energy Functions* (Wiley, Chichester, 1984).
[60]T. Pacher, L. S. Cederbaum, and H. Köppel, Adv. Chem. Phys. **84**, 293 (1993).
[61]W. Domcke, C. Woywod, and M. Stengle, Chem. Phys. Lett. **226**, 257 (1994).
[62]G. J. Atchity and K. Ruedenberg, Theor. Chem. Acc. **97**, 47 (1997).
[63]A. J. Dobbyn and P. J. Knowles, Mol. Phys. **91**, 1107 (1997).
[64]V. C. Mota and A. J. C. Varandas, J. Phys. Chem. A **112**, 3768 (2008).
[65]A. J. C. Varandas, J. Chem. Phys. **129**, 234103 (2008).
[66]A. J. C. Varandas, Chem. Phys. Lett. **471**, 315 (2009).
[67]K. S. Sorbie and J. N. Murrell, Mol. Phys. **29**, 1387 (1975).
[68]A. J. C. Varandas and J. N. Murrell, Faraday Discuss. Chem. Soc. **62**, 92 (1977).
[69]H.-J. Werner, P. J. Knowles, R. Lindh, F. R. Manby, M. Schütz, P. Celani, T. Korona, A. Mitrushenkov, G. Rauhut, T. B. Adler, R. D. Amos, A. Bernhardsson, A. Berning, D. L. Cooper, M. J. O. Deegan, A. J. Dobbyn, F. Eckert, E. Goll, C. Hampel, G. Hetzer, T. Hrenar, G. Knizia, C. Köppl, Y. Liu, A. W. Lloyd, R. A. Mata, A. J. May, S. J. McNicholas, W. Meyer, M. E. Mura, A. Nicklass, P. Palmieri, K. Pflüger, R. Pitzer, M. Reiher, U. Schumann, H. Stoll, A. J. Stone, R. Tarroni, T. Thorsteinsson, M. Wang, and A. Wolf, MOLPRO, version 2008.3, a package of ab initio programs (2008), see http://www.molpro.net.
[70]T. H. Dunning Jr., J. Chem. Phys. **90**, 1007 (1989).
[71]R. A. Kendall, T. H. Dunning Jr., and R. J. Harrison, J. Chem. Phys. **96**, 6796 (1992).
[72]H. J. Werner and P. J. Knowles, J. Chem. Phys. **89**, 5803 (1988).
[73]P. J. Knowles and H. J. Werner, Chem. Phys. Lett. **145**, 514 (1988).
[74]R. . E. Continetti, D. R. Cyr, R. B. Metz, and D. M. Neumark, Chem. Phys. Lett. **182**, 406 (1991).
[75]V. C. Mota, P. J. S. B. Caridade, and A. J. C. Varandas, J. Theor. Comp. Chem. **8**, 849 (2009).
[76]V. C. Mota, P. J. S. B. Caridade, and A. J. C. Varandas, Int. J. Quantum Chem. **111**, 3776 (2011).
[77]H. Weyl, *The Classical Theory of Groups* (Princeton University Press, 1946).
[78]L. P. Viegas, A. Alijah, and A. J. C. Varandas, J. Chem. Phys. **126**, 074309 (2007).
[79]See Supplementary Material Document No. for the numerical data to define the potential energy surface. For information on Supplementary Material, see http://www.aip.org/pubservs/epaps.html.
[80]D. Babikov, P. Zhang, and K. Morokuma, J. Chem. Phys. **121**, 6743 (2004).
[81]D. Babikov, B. K. Kendrick, P. Zhang, and K. Morokuma, J. Chem. Phys. **122**, 044315 (2005).
[82]G. H. Peslherbe, H. Wang, and W. L. Hase, Adv. Chem. Phys. **105**, 171 (1999).
[83]W. L. Hase, R. J. Duchovic, X. Hu, A. Komornicki, K. F. Lim, D. Lu, G. H. Peslherbe, K. N. Swamy, S. R. V. Linde, A. J. C. Varandas, H. Wang, and R. J. Wolf, QCPE Bull. **16**, 43 (1996).
[84]J. C. Tully and R. K. Preston, J. Chem. Phys. **55**, 562 (1971).
[85]R. K. Preston and J. C. Tully, J. Chem. Phys. **54**, 4297 (1971).
[86]J. C. Tully, in *Modern Theoretical Chemistry, Dynamics of Molecular Collisions, PartB*, edited by W. Miller (Plenum Press, New York, 1977), p. 217.
[87]A. I. Voronin, J. M. C. Marques, and A. J. C. Varandas, J. Phys. Chem. A **102**, 6057 (1998).
[88]N. C. Blais and D. G. Truhlar, J. Chem. Phys. **79**, 1334 (1983).
[89]J. C. Tully, J. Chem. Phys. **93**, 1061 (1990).
[90]M. S. Topaler, T. C. Allison, D. W. Schwenke, and D. G. Truhlar, J. Chem. Phys. **109**, 3321 (1998).
[91]C. Fermanian-Kammerer and C. Lasse, J. Math. Chem. **50**, 620 (2012).
[92]G. C. Schatz, L. A. Pederson, and P. J. Kuntz, Faraday Discuss. **108**, 357 (1997).
[93]F. J. Aoiz, L. Bañares, M. Brouard, J. F. Castillo, and V. J. Herrero, J. Chem. Phys. **113**, 5339 (2000).
[94]A. J. C. Varandas and Z. R. Xu, in *Adv. Chem. Phys.*, edited by M. Baer and G. D. Billing (Wiley, New York, 2002), pp. 659–741.
[95]W. Domcke, D. R. Yarkony, and H. Köppel, editors, *Conical Intersections: Electronic Structure, Spectroscopy and Dynamics*, Advanced Series in Physical Chemistry (World Scientific Publishing, Singapore, 2004).
[96]J. C. Juanes-Marcos, S. C. Althorpe, and E. Wrede, J. Chem. Phys. **126**, 044317 (2007).
[97]J. C. Juanes-Marcos, A. J. C. Varandas, and S. C. Althorpe, J. Chem. Phys. **128**, 211101 (2008).
[98]A. J. C. Varandas and L. P. Viegas, Chem. Phys. Lett. **367**, 625 (2003).
[99]B. Lepetit and A. Kuppermann, Chem. Phys. Lett. **166**, 581 (1990).
[100]S. Mahapatra, H. Köppel, and L. S. Cederbaum, J. Phys. Chem. A **105**, 2321 (2001).

Fundamental Issues in the Aerothermodynamics of Planetary Atmosphere Re-Entry

ESA Contract 21790/08/NL/HE

Mario Capitelli[a,b], Olga De Pascale[b], Domenico Bruno[b], Roberto Celiberto[b,c], Fabrizio Esposito[b], Annarita Laricchiuta[b], Savino Longo[a,b]

[a] Dipartimento di Chimica, Università di Bari (Italy)

[b] CNR IMIP (Istituto di Metodologie Inorganiche e Plasmi) Bari (Italy)

[c] Dipartimento di Ingegneria delle Acque e Chimica, Politecnico di Bari (Italy)

Antonio Laganà and Dimitrios Skouteris

Dipartimento di Matematica e Informatica, Università di Perugia (Italy)

Dipartimento di Chimica, Università di Perugia (Italy)

B.R.L. Galvão, V.C. Mota, P.J.S.B. Caridade and Antonio J. C. Varandas

Departamento de Química, Universidade de Coimbra (Portugal)

Jonathan Tennyson

Department of Physics & Astronomy, University College London (UK)

Carlo Petrongolo

Dipartimento di Chimica, Università degli Studi di Siena (Italy)

Per Jensen

Department of Chemistry, Bergische Universität Wuppertal (Germany)

Brian T. Sutcliffe

Laboratoire de Chimie Quantique et Photophysique, Université Libre De Bruxelles (Belgium)

Mario Lino da Silva

Instituto de Plasmas e Fusão Nuclear, Instituto Superior Técnico, Lisboa (Portugal)

Ioan F. Schneider

Laboratoire Ondes & Milieux Complexes (LOMC) CNRS, Université du Havre (France)

Yuriy E. Gorbachev

St. Petersburg State Polytechnic University, St. Petersburg (Russia)

8 Accurate electronic manifolds and their use in dynamics

(Antonio J.C. Varandas *et al* WP 1.2.3)

8.1 $N + N_2$: the adiabatic picture

Extreme thermal environmental conditions arise when an object enters the Earth atmosphere. Such conditions can promote chemical reactions ranging from simple excitations to dissociation and recombination of atoms and molecules. Due to their critical implications, such processes can be of key importance when designing heat shields for space vehicles where temperatures may reach up to 20000 K [1]. They can also play a key role when simulating objects' entries in other planets. One of the most relevant species found in such kinetic modeling studies is molecular nitrogen, since it is the major constituent of Earth's atmosphere as well as of the atmosphere of other planets and satellites. Under such atmospheric conditions, a great quantity of atomic nitrogen can also be found, enhanced by the interaction of molecular nitrogen with radiation. Thus, $N + N_2$ collisions can be of key importance for understanding such atmospheric regimes. To our knowledge, experimental studies of such collisions have been reported [2, 3, 4] only at two temperatures, namely 1273 and 3400 K, both affected by large uncertainties of the measurements. As a result, extrapolation of such data to higher temperatures lacks reliability.

A major goal of the Coimbra T&CC group has been to perform an accurate study of the PES for the $^4A''$ state of N_3 under the adiabatic framework, and model it using DMBE [5, 6, 7, 8] theory. Using such a global PES, a detailed study of the $N + N_2$ exchange reaction and vibrational relaxation processes has also been carried [9] by the QCT method [10].

8.1.1 Potential energy surface

Motivated by recent progress [11, 12] in obtaining energies at the CBS (complete basis set) limit via scaling and extrapolation of low cost *ab initio* ones, the Coimbra T&CC group has reported [13] a DMBE PES for the $^4A''$ ground electronic state of N_3 by fitting an extensive set of *ab initio* energies extrapolated to the CBS limit. Using both CCSD(T) [14] and MRCI(Q) [15, 16] methods with AVXZ basis sets of the Dunning [17, 18] type (with cardinal numbers $X = T : 3$ and $Q : 4$), such

CBS extrapolated energies predict a barrier height lying $192\,\mathrm{kJ\,mol^{-1}}$ above the reactants channel, with a potential well (of the Eyring-lake type) located $180\,\mathrm{kJ\,mol^{-1}}$ above the same reference. All topographical details are accurately mimicked by the modeled DMBE function.

Figure 8.1 shows a representation of the DMBE PES using optimized hyperspherical coordinades [19]. Clearly visible are the three equivalent metastable potential wells of C_{2v} symmetry that are separated from the N(^4S)+N_2 asymptotes by energy barriers as predicted from the fitted *ab initio* data. The potential well and barrier height predicted by the DMBE form [13] lie about $6\,\mathrm{kJ\,mol^{-1}}$ lower than previous theoretical estimates. The *ab initio* calculations also predict a $^4B_1/^4A_2$ conical intersection and reveal a new minimum with D_{3h} symmetry which lies $613\,\mathrm{kJ\,mol^{-1}}$ above the atom-diatom asymptote and might be relevant when studying the nitrogen dissociation process, since it lies under the limit of three separated atoms. We emphasize that all major topographical features of the PES, including the weakly bound van der Waals minima at large atom-diatom separations, are accurately mimicked by the DMBE function.

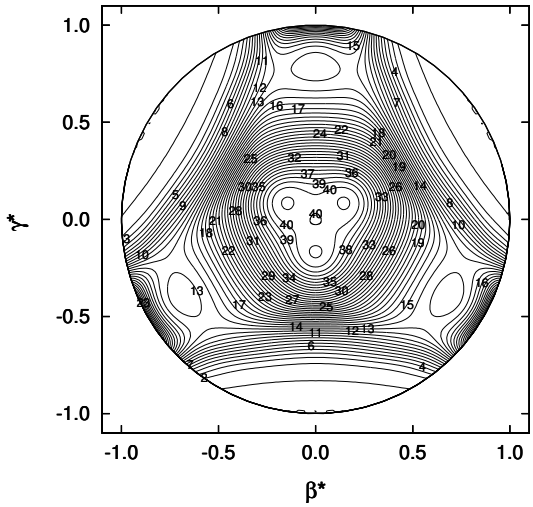

Figure 8.1: Relaxed triangular plot [19] of the $N_3(^4A'')$ DMBE PES [13]. Contours are equally spaced by 6 mE_h, starting at 0 E_h.

8.1.2 The $N + N_2$ reaction

The $N + N_2$ exchange reaction has been studied by several groups with different PESs and dynamical approaches. Wang *et al.* [1] used the time-dependent wave packet method to perform a $3D$ calculation on the WSHDSP PES while Rampino *et al.* [20] employed the L4 and L4w functions to perform time-independent quantal studies. Both groups performed the calculations for zero total angular momentum, $J = 0$. We have run trajectories on the DMBE PES (as well as previous PESs) to compare its predictions for the $N + N_2(v, j = 0)$ reaction at $J = 0$, having considered three initial vibrational states for N_2: $v = 0$, 1 and 2.

Panel (a) of figure 8.2 shows the vibrational state-specific reaction probability as a function of the total energy. The QCT results with $J = 0$ on the DMBE PES are shown to differ appreciably from the ones reported by Rampino *et al* [20], although such a behavior is to be expected since the barrier for reaction

predicted by the DMBE potential energy surface is $6.3\,\mathrm{kJ\,mol^{-1}}$ smaller than L4. When comparing the dynamical energy threshold, the differences between both PESs show even larger differences, reaching $20\,\mathrm{kJ\,mol^{-1}}$ or so for $v = 0$. In comparison with the results of Wang *et al* , [21] the present calculations show a threshold value larger by more than $40\,\mathrm{kJ\,mol^{-1}}$.

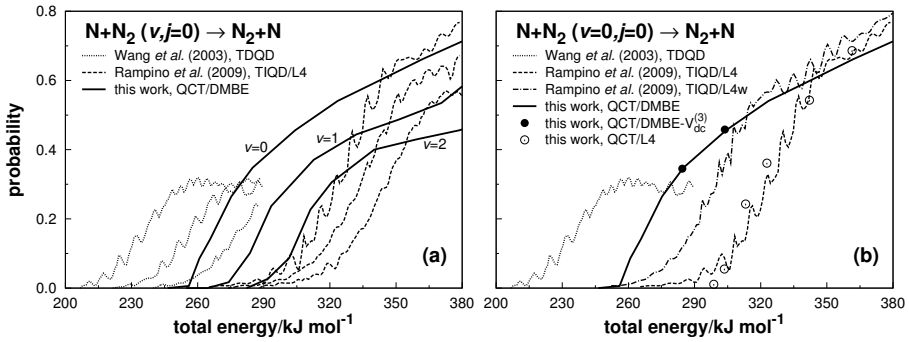

Figure 8.2: State-specific probabilities for J = 0 for different PESs. Panel (a): reactants with vibrational levels v = 0, 1, 2 (from left to right). Panel (b) comparison between methodologies for v = 0

The above differences could partly be attributed to the classical nature of the dynamical approach employed in the present work. To test this, additional calculations have been carried out on the L4 surface for $v = 0$, and compared with the TIQD results on the same PES. The agreement between the QCT and TIQD results is clearly visible from panel (b) of figure 8.2, while no attempt has been made to describe the region near threshold due lack of statistics near such a critical value. Away from such critical regions, the comparison between the QCT and TIQD results shows a fairly good agreement.

Rampino *et al* [20], interpreted the difference from the work of Wang *et al.*, [21] as due to long-range forces. Starting from the L4 surface, they have then added an ad-hoc long-range term (the new function has been denoted L4w), and the dynamics calculations repeated. Their new results are shown in panel (b) of figure 8.2. In an attempt to rationalize the role of long-range forces in the $\mathrm{N} + \mathrm{N_2}$ exchange reaction, the long-range terms in DMBE have been removed and test calculations performed for $v = 0$. Since the DMBE PES has built-in a realistic description of the dispersion interaction between $\mathrm{N}(^4S)$ and $\mathrm{N_2}(X\,^1\Sigma_g^+)$, one might think that the role of long-range forces could be judged by setting them on/off. As observed from the panel (b) of figure 8.2 (cf, points vs solid line), the two sets of results are indistinguishable, suggesting that such reaction cannot be strongly influenced by long-range forces. This result could somehow be anticipated from the energetics of the reaction as its dynamics is largely dictated by the large energy barrier that needs to be overcome for reaction to occur.

The lack of statistics and the existence of rare events are major difficulties encountered in the calculation of thermal rate coefficients for reactions with large barriers under thermal conditions. In the present study, the probability of finding a trajectory above the classical threshold ($E_{tr} \geq 192\mathrm{kJ\,mol^{-1}}$) for $T = 1273\,\mathrm{K}$ is $\sim 2 \times 10^{-7}$, *i.e.*, 2 in 10^7 trajectories have sufficient translational energy to overpass the barrier. A simple scheme that speeds up the process is the quantum mechanical threshold [22] method: all trajectories with total energy below $192\,\mathrm{kJ\,mol^{-1}}$ are considered a priori as non-reactive, and hence not run. Importance sampling methods can also be used to accelerate the convergence, and we have utilized also this approach. Suffice it to say that we have sectioned [9] the Boltzmann distribution into bits, with a different number of trajectories integrated for each sector according to the desired statistics.

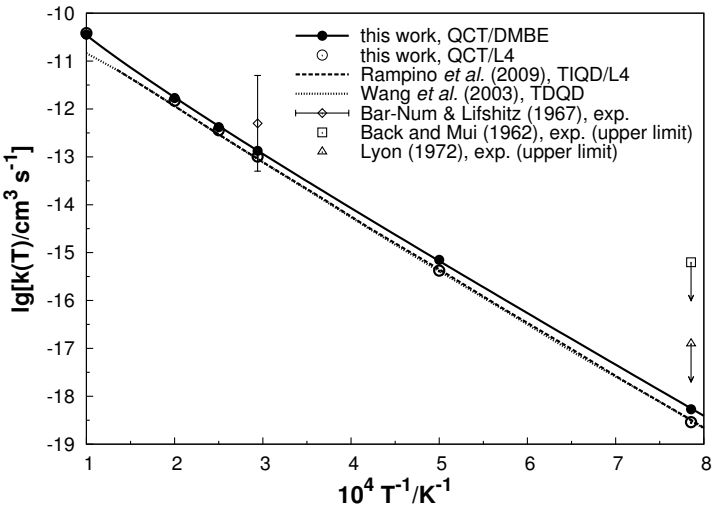

Figure 8.3: Comparison of the rate constants on the DMBE PES with other data available in literature

Figure 8.3 shows a comparison with the available theoretical and experimental results. As shown, the present calculations predict a rate constant somewhat larger than previously reported calculations [1, 20], especially at low temperature regimes. This could have been anticipated from the lower barrier height of the DMBE form. For high temperatures, all calculations point to the same limit, although the QCT ones predict a slightly larger value. This behavior can have important implications on the extrapolated rate constants for extreme temperatures, where the QCT/DMBE results predict a rate constant about 2 to 3 times larger than the quantum mechanical ones. The temperature dependence of the rate constant can be modeled via a modified Arrhenius equation as $k(T) = AT^m \exp\left(-BT^{-1}\right)$, with the fit to the results on the DMBE yielding $A = 5.8287 \times 10^{-14}\,\mathrm{K^{-m}\,cm^3\,s^{-1}}$, $m = 0.9467$, and $B = 23327.67\,\mathrm{K}$.

Vibrational energy transfer including the exchange reaction, $\mathrm{N}+\mathrm{N}_2(v) \rightarrow \mathrm{N}_2(v')+\mathrm{N}$, has been studied using the MGB method [23], with the rate constants and ratios reported in Ref. [9]. Suffice it to say here that a salient feature from such results is the contribution of multi-quanta transitions to vibrational relaxation, which clearly dominates over excitation. The most probable transition involves the ground vibrational state as final outcome irrespective of the initial state. For example, for initial vibrational state $v = 5$, the transition to $v = 0$ represents 36% while one quantum transitions amount to only 13%. The behavior here reported suggests a statistical-type reaction, where all vibrational states have equal probability of occurrence. This can partly be attributed to the "Lake Eyring", which may allow some randomization of the internal energy of N_3. As for excitation, the dominant process corresponds to one quantum transitions.

8.1.3 Summary

An accurate PES has been obtained for the ground quartet state of tri-nitrogen based on a fit to CBS extrapolated CCSD(T) and MRCI(Q) energies and DMBE modeling. It represents a significant improvement over previous surfaces, calling also attention for the conical intersection involving the $^4B_1$ and $^4A_2$ states at geometries with C_{2v} symmetry and predicting a lower barrier for the exchange

reaction. Quasiclassical trajectories run on this PES show that such a lower energy barrier has significant impact on the dynamics, in particular on the reaction threshold and rate constants. The analysis of vibrational energy transfer has also shown to enhance the population of low vibrational states.

8.2 NO_2

The study of non-adiabatic processes that occur on PESs showing conical intersections has long been a highly challenging field in molecular theory. For triatomic molecules, conical intersections correspond to two-fold one-dimensional degeneracies, but can assume a higher-dimensionality for larger polyatomic species [24]. We focus here on the simplest case of a triatomic system, not necessarily possessing any permutation symmetry.

The construction [7, 8, 25] of a multi-sheeted PES capable of describing such conical intersections and hence non-adiabatic effects, plays a key role in any accurate study of non-adiabatic processes within the Born-Oppenheimer-Huang [26, 27] framework, and can still be considered an open field of research even for triatomic molecules due to the intricacy of the details that are involved. Approaches based on diabatization techniques [28, 29, 30] are perhaps the most promising route for facing such a challenge [31]. In a previous paper [31], we have surveyed most diabatization schemes that are available in the literature for double-sheeted PESs, and analyzed them according to their suitability to construct forms of MBE [25] type, in particular DMBE [5, 6, 7, 8, 32] ones. As a major outcome, we have shown the necessity for a new general approach to the problem, so-called GDA approach [31], and successfully used to construct a double-sheeted DMBE PES for the first two $^2A'$ states of HN_2.

The first steps towards a generalization of such a methodology [31] will be presented in the remainder of this report. The specificity of a diabatization process [33] favors the use of different schemes for different problems, with the approach here described being designed to provide a diabatic matrix for manifolds with three or more dimensions within the DMBE framework. The aim is to construct a diabatic matrix such as

$$\begin{pmatrix} \Phi_3 \\ \Phi_2 \\ \Phi_1 \end{pmatrix} = \begin{pmatrix} r_{33} & r_{32} & r_{31} \\ r_{23} & r_{22} & r_{21} \\ r_{13} & r_{12} & r_{11} \end{pmatrix} \begin{pmatrix} \psi_3 \\ \psi_2 \\ \psi_1 \end{pmatrix} \tag{8.1}$$

where r_{ij} are elements of a general rotation matrix $\mathcal{R}$ that represents a diabatic potential matrix that merges into the adiabats at the atom-diatom dissociation limit while correctly describing the topology of crossing seams and avoided crossings [31]. It is also hoped to devise rules that may help on considering further excited states in future applications. Although the literature on diabatization schemes is relatively scarce for electronic manifolds with three or more sheets [7, 8, 25, 34, 35, 36, 37, 38, 39, 40, 41, 42, 43, 44, 45, 24], diabatization methods to model PESs from the resulting diabats are even less common, especially if aiming at global representations.

The system chosen here for the illustration is NO_2, reinforcing the interest of our group on the manifolds of this molecule [40, 46]. Central for this choice are the many non-adiabatic couplings occurring on this triatom [40, 46, 47, 48, 49, 50, 51, 52, 53, 54, 55, 56], which makes it an excellent candidate for testing new diabatization schemes. Perhaps more important is the fact that NO_2 combines intricacy

with a wide practical interest in atmospheric chemistry and combustion processes [40, 54].

Several electronic manifolds [47, 48, 49] are of general interest in NO_2. Of particular interest in atmospheric chemistry and combustion are the $^2A'$ and $^2A''$ manifolds as shown from various theoretical studies [49, 50, 51]. Of them, the $^2A'$ manifold has been the most extensively studied [40, 49, 50, 51, 52, 53, 55]. Restricting to global approaches, the DMBE-based 8×8 matrix reported of Varandas[40] is perhaps the most accurate multisheeted PES thus far reported for the $NO_2(^2A')$ manifold. Based on the dressed DIM [7] formalism (referred to in the original paper as multivalued DMBE), it represents a significant improvement over earlier work [35, 52, 57]. It is semiempirical in nature as its calibration employs both CASSCF/AV*T*Z [58, 59] and CASPT2/AV*T*Z [60] calculations and the energy switching [61] scheme to confer spectroscopic accuracy to the ground-state PES. This PES has been employed by Varandas and co-workers [46, 62] to study both the $N + O_2$ and $O + NO$ reactions by running trajectories. More recently, Schinke and co-workers reported a series of studies [54, 55, 56] on the $^2A'$ and $^2A''$ manifolds. In turn, Ivanov and Schinke [54] have improved the ground state of the double-sheeted MRCI [15, 16] PES of Kurkal [53] *et al.* for the first two $^2A'$ of NO_2 for studying the exchange and recombination reactions in $O(^3P) + NO(^2\Pi)$ collisions. For this, additional [63] MRCI(Q)/V*Q*Z calculations have been performed to correct the long range regions of the earlier PES [53] by using cubic splines [54] for the interpolation. Two-state calculations have also been performed for the $^2A''$ manifold, of which the lowest $1^2A''$ state has been used in their QCT studies. Subsequently, Schinke [55] *et al.* constructed a PES for the third $^2A'$ adiabatic state at the same level of theory [54] aiming to study photodissociation dynamics in the second absorption band. The first five $^2A'$ states have then been mapped, with some cuts for the first five $^2A''$ states being also reported. Additionally, Schinke[56] performed calculations for both $^2A'$ and $^2A''$ manifolds with the MRCI(Q)/AV*Q*Z method to study the $\tilde{D} \rightarrow \tilde{C}$ emission spectrum of NO_2. This encompassed up to five states of the $^2A'$ manifold and three $^2A''$ states which have been subsequently diabatized by eye [64] and fitted using cubic splines. In summary, both the near-spectroscopic accuracy of the realistic DMBE multi-sheeted PES reported by Varandas and the detailed series of calculations by Schinke and co-workers [54, 55, 56] are certainly a reference on the mapping of the $^2A'$ and $^2A''$ manifolds of NO_2.

The studies on the $^2A''$ manifold are scarcer. Besides the work of Schinke and co-workers [54, 55, 56], only a few papers have been devoted to the investigation of its non-adiabatic aspects. The investigation of the mechanism of formation of vibrationally excited NO in the upper atmosphere through the reactions

$$N(^2D) + O_2(X^3\Sigma_g^-) \rightarrow NO(X^2\Pi) + O(^1D) \tag{8.2}$$

and

$$N(^2D) + O_2(X^3\Sigma_g^-) \rightarrow NO(X^2\Pi) + O(^3P) \tag{8.3}$$

led Braunstain and Duff [49] to an extensive *ab initio* investigation of the manifolds involved. They calculated 1000 CASPT2 points with the Pople-type 6311G(d) basis set [65] to map the first six $^2A'$ and $^2A''$ states. They have also built single-sheeted MBE PESs for the $2^2A'$, $3^2A'$, $1^2A''$ and $2^2A''$ states, which have been subsequently used for QCT calculations. A similar investigation was carried out by González *et al.*[51], who have utilized a larger basis set (V*T*Z) at the same level of theory (CASPT2) to study the reactions (8.2) and (8.3). Transition state theory as well as variational transition state theory have then been applied to investigate the rate of the reactions involved. Although showing significant differences in barrier heights when compared with the PES of Ref. [49], similar conclusions have been drawn relative to the predominance of reaction (8.2) over reaction (8.3). In a subsequent publication, González *et al.* [50] utilized the *ab initio* points [51] to build a MBE PES for the first

$NO_2(^2A'')$ state, with special attention being paid to the stationary states of $NO_2(^2A'')$ and conical intersections that arise near the minimum energy path for the insertion reaction.

A global multi-sheeted PES for the first $^2A''$ states showing a realistic description of the crossing seams is therefore not yet available. This makes the $^2A''$ manifold a suitable target for the analysis [66] presented in the remaining sections of the present report.

8.2.1 *Ab initio* calculations and topological features

Given the exploratory nature of this work, all calculations are of CASSCF/VDZ quality, having been performed with the Molpro [67] package for electronic structure calculations. Up to 3500 points have been computed for $1.68 \leq r_1/\mathrm{a_0} \leq 3.2$, $0 \leq \theta/\mathrm{deg} \leq 90$ and $1.0 \leq R_1/\mathrm{a_0} \leq 6.0$ for the $\mathrm{N}-\mathrm{O_2}$ channel, and up to 9000 geometries for $1.7 \leq r_2/\mathrm{a_0} \leq 3.4$, $0 \leq \theta/\mathrm{deg} \leq 180$ and $1.0 \leq R_2 \leq 6.0$ for $\mathrm{O}-\mathrm{NO}$; r, θ and R are Jacobi coordinates (from now on indicated with the sub-indexes 1 and 2, respectively for the $\mathrm{N}-\mathrm{O_2}$ and $\mathrm{O}-\mathrm{NO}$ channels).

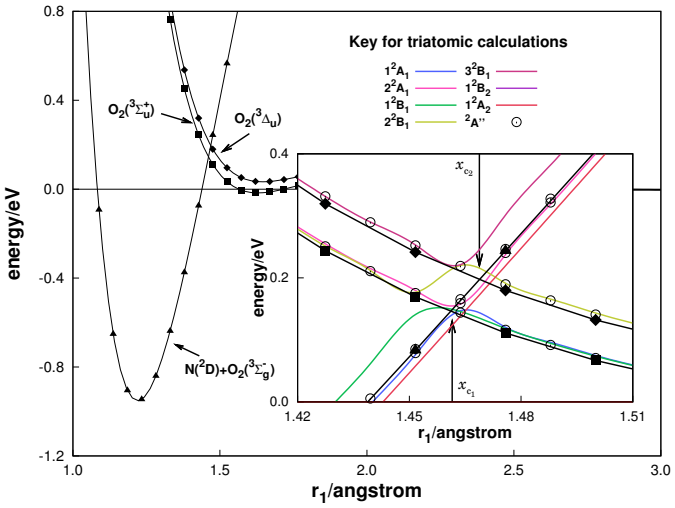

Figure 8.4: Diatomic states and asymptotic triatomic curves. Black lines were interpolated from diatomic calculations to guide the eye, and color lines represents interpolated triatomic $\mathbf{C_{2v}}$ calculations. Key for $\mathrm{O_2}$ diatomic states in main graphic: (■), $^3\Sigma_u^+$; (♦), $^3\Delta_u$; (▲), $\mathrm{N}(^2D)+\mathrm{O_2}(^3\Sigma_g^-)$.

Figure 8.4 shows calculations for the $\mathrm{N}-\mathrm{O_2}$ asymptote jointly with calculations on the relevant states of $\mathrm{O_2}$. Shown are the first four $^2A''$ triatomic states as well as the corresponding states in C_{2v} symmetry.

The outcome is the following dissociation scheme:

$$
\mathrm{NO_2} \Rightarrow \begin{cases}
\begin{array}{lcll} 1^2A'', 2^2A'' & & \mathrm{O_2}(^3\Sigma_g^+) + \mathrm{N}(^2D) & \\ 3^2A'' & \Rightarrow & \mathrm{O_2}(^3\Delta_u) & \text{for} \quad r_1 < x_{c1} \\ 4^2A'' & & \mathrm{O_2}(^3\Sigma_u^+) & \end{array} \\
\begin{array}{lcll} 1^2A'' & & \mathrm{O_2}(^3\Delta_u) & \\ 2^2A'', 3^2A'' & \Rightarrow & \mathrm{O_2}(^3\Sigma_g^+) + \mathrm{N}(^2D) & \text{for} \quad x_{c1} < r_1 < x_{c2} \\ 4^2A'' & & \mathrm{O_2}(^3\Sigma_u^+) & \end{array} \\
\begin{array}{lcll} 1^2A'' & & \mathrm{O_2}(^3\Delta_u) & \\ 2^2A'' & \Rightarrow & \mathrm{O_2}(^3\Sigma_u^+) & \text{for} \quad r_1 > x_{c2} \\ 3^2A'', 4^2A'' & & \mathrm{O_2}(^3\Sigma_g^+) + \mathrm{N}(^2D) & \end{array}
\end{cases}
\tag{8.4}
$$

where x_{c1} and x_{c2} are the points where indicated states cross (see insert of figure 8.4). For the $\mathrm{O} - \mathrm{NO}$ channel, all the first four $^2A''$ states share a common dissociation into $\mathrm{O}(^3P) + \mathrm{NO}(^2\Pi)$ fragments.

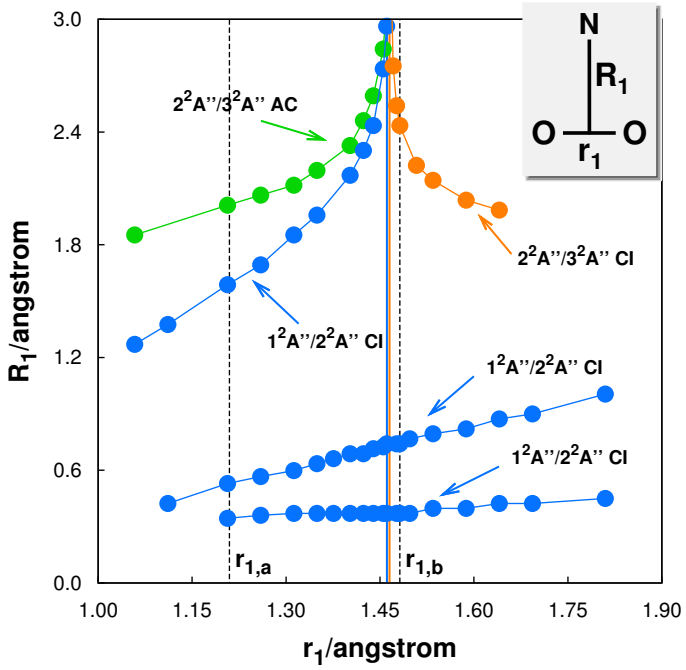

Figure 8.5: T-shaped non-adiabatic structures. The vertical blue line cuts the x-axis in $\mathbf{x_{c1}}$ and the vertical pink line in $\mathbf{x_{c2}}$. AC and CI stands respectivelly for avoided crossings and conical intersections.

The crossing points x_{c_1} and x_{c_2} shown in figure 8.4 correspond to the asymptotic limits of the evolving T-shaped crossing seams as indicated in figure 8.5. This result stems from a detailed analysis of C_s and C_{2v} calculations up to the dissociation limit. The calculations have also revealed other non-adiabatic features indicated in figure 8.5: avoided intersection seam, and crossing seam between the $2^2A''$ and $3^2A''$, both fully mapped. Additional T-shaped $1^2A''/2^2A''$ crossing seams are also shown, for which no evolution until the asymptotes has been found. An illustration of a crossing point along cuts (dotted lines in figure 8.5) is shown in figure 8.6.

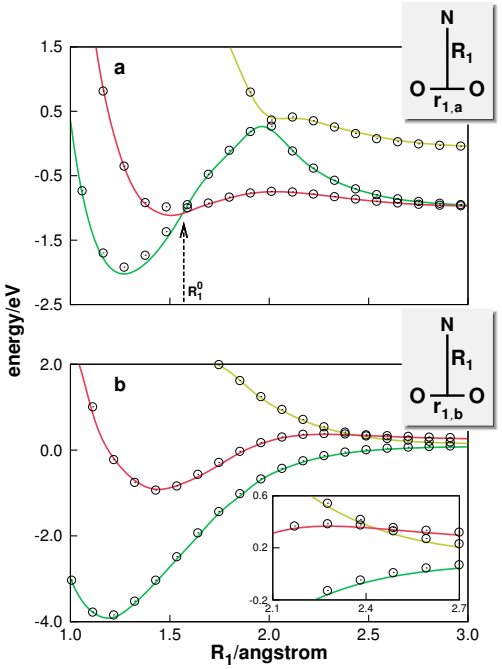

Figure 8.6: Profiles of C_s and C_{2v} states of the triatom. Key for simbols as in figure 8.4

The crossing seams at linearity are shown in figure 8.7. A first observation concerns the proximity of the $1^2A''/2^2A''$ and $2^2A''/3^2A''$ seams. Yet, only by accident can the two seams cross each other as established by the non-crossing rule [68]. In fact, despite referring to only slightly displaced loci, they have different symmetries. Such a closeness is already present in the crossings for O_2 shown in figure 8.4. The second aspect to be observed is that for a given NO distance (r_2) the $1^2A''/2^2A''$ crossing seam occurs for slightly smaller values of the r_2' or r_1 coordinate (thus, also of R_2) than the $2^2A''/3^2A''$ seam. It occurs therefore more internally in the linear plots referred above. Note that a similar result is also observed for the T-shaped structures, with the $1^2A''/2^2A''$ non-adiabatic seam occurring for shorter values of the R_1 coordinate at any r_1 value. Finally, it should be remarked that, unlike T-shaped arrangements, the linear crossings do not extend to the asymptotes.

8.2.2 Diabatization scheme

8.2.3 The O – NO channel

A first step in the diabatization procedure consists of treating separately the two distinct channels, following the successful experience with [31] $HN_2(^2A')$. It is then observed that the linear seams (which are better accessed via the $O - NO$ channel) have a crucial common feature with the linear HN_2 ones, namely the fact of not extending to the asymptote.

Consider first a consecutive pair of states (*e.g.*, $1^2A''/2^2A''$ and $2^2A''/3^2A''$) for the $O - NO$ channel by exploring the topology of the avoided crossings. Proceeding as described for [31] $HN_2(^2A')$, the

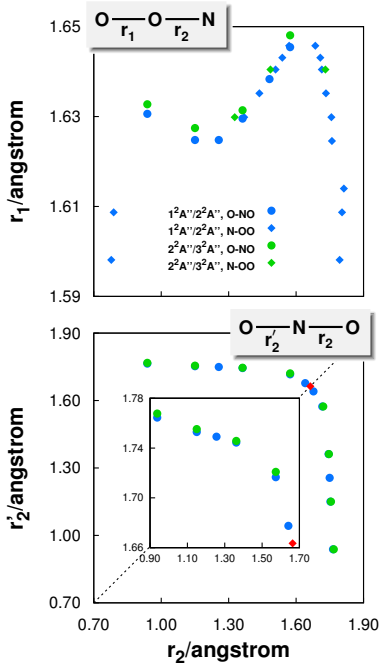

Figure 8.7: Linear crossing seams. Upper and lower panels shows respectively NOO **and** ONO **arrangements. In the lower panel the notation r_2' is used to differenciate between the two independent** NO **stretchings for** ONO **linear arrangements. The red ($\Diamond$) symbol therein indicates the $D_{\infty h}$ conical intersection.**

coordinate R_2^0 where the adiabatic curves show their minimum energy approach is stored for each pair (r_2, θ_2) of Jacobi coordinates. Note that the calculated grid of *ab initio* points is dense enough to obtain an equally dense grid of (avoided) crossing points. From this, an avoided intersection surface can be generated for each pair of states ($1^2A''/2^2A''$ and $2^2A''/3^2A''$) in a fashion similar to the $HN_2(^2A')$ case, with the only difference being that such a function has now a more rugged topography. Following such a strategy, rather than attempting to model analytically as in the $HN_2(^2A')$ case, interpolation schemes (of cubic-spline type) are now employed. Thus, the correct behavior at the boundaries NOO and ONO will be insured by interpolation, although a judiciously chosen extrapolation is necessary to warrant proper behavior at the $r_2 \to 0$ and $r_2 \to \infty$ limits. Figure 8.8 illustrates the avoided intersection surfaces $R_2^{0,12}(\theta_2, r_2)$ and $R_2^{0,23}(\theta_2, r_2)$ so obtained.

With the avoided intersection surfaces $R_2^{0,12}(\theta_2, r_2)$ and $R_2^{0,23}(\theta_2, r_2)$, the procedure follows with the modeling of each of the diabatization angles associated to the pairs of consecutive states $1^2A''/2^2A''$ and $2^2A''/3^2A''$. The absence of any asymptotic evolution suggests to adopt the HN_2 procedure [31] by using the function

$$\alpha_2^p(\mathbf{R}) = \frac{\pi}{4}\left\{1 - \tanh\left\{\gamma_2^p\left[R_2 - R_2^{0,p}(\theta_2, r_2)\right]\right\}\right\} \tag{8.5}$$

which warrants a well defined behavior at the $R_2 \to 0$ and $R_2 \to \infty$ limits, being finite in the first case and evolving as $\alpha_2^p \to 0$ in the second. To test Eq. (8.5), two steps have been followed. First, each of the consecutive state pairs is independently diabatized. For the $1^2A''/2^2A''$ pair, this has been done by

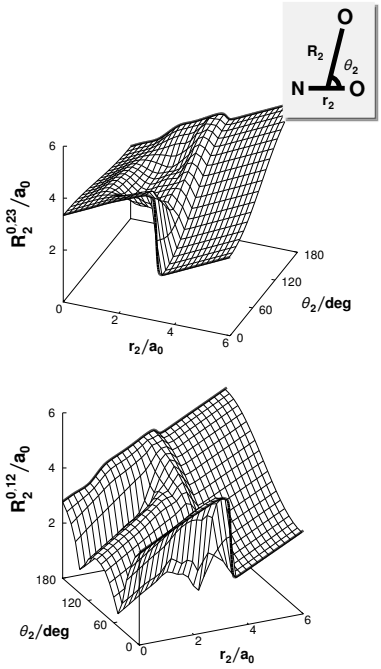

Figure 8.8: Avoided intersection surfaces for the $O-NO$ channel. The sub-index 2 indicates this channel in the correspondent jacobi coordinates.

using the rotation matrix

$$\mathcal{R}_2^{12}(\mathbf{R}) = \begin{pmatrix} 1 & 0 & 0 \\ 0 & \cos\left[\alpha_2^{12}(\mathbf{R})\right] & \sin\left[\alpha_2^{12}(\mathbf{R})\right] \\ 0 & -\sin\left[\alpha_2^{12}(\mathbf{R})\right] & \cos\left[\alpha_2^{12}(\mathbf{R})\right] \end{pmatrix} \tag{8.6}$$

which brings us to a diabatic form where one of the diabatic states coincides with the third adiabatic one. For the $2^2A''/3^2A''$ pair, the corresponding rotation matrix is

$$\mathcal{R}_2^{23}(\mathbf{R}) = \begin{pmatrix} \cos\left[\alpha_2^{23}(\mathbf{R})\right] & \sin\left[\alpha_2^{23}(\mathbf{R})\right] & 0 \\ -\sin\left[\alpha_2^{23}(\mathbf{R})\right] & \cos\left[\alpha_2^{23}(\mathbf{R})\right] & 0 \\ 0 & 0 & 1 \end{pmatrix} \tag{8.7}$$

thus leading to a diabatic form where one of the diabatic states is the first adiabatic state. No undesirable features have been met during such a two-step diabatization procedure, with the diabatic states evolving properly between the two crossing seams at the NOO and ONO linear arrangements, and merging with the adiabatic states at the asymptotes.

For the three-state diabatization on this channel, we have explored our finding in section 8.2.1 that the $1^2A''/2^2A''$ and $2^2A''/3^2A''$ crossing seams are ordered, with the former lying "more internally" than the latter (see figure 8.7). The total rotation matrix for the $O-NO$ channel reads

$$\mathcal{R}_2(\mathbf{R}) = \mathcal{R}_2^{23}(\mathbf{R})\,\mathcal{R}_2^{12}(\mathbf{R}) \tag{8.8}$$

with $\mathcal{R}_2^{12}(\mathbf{R})$ and $\mathcal{R}_2^{23}(\mathbf{R})$ defined in Eqs. (8.6) and (8.7). With $\mathcal{R}_2(\mathbf{R})$ matrix, the problem will first be transformed from the adiabatic space into a space where the first two states are decoupled, and via

$\mathcal{R}_2^{23}(\mathbf{R})$ from such a space to three decoupled diabatic states. It should be noted that all three diabatic states smoothly evolve between the ONO and NOO linear boundaries, crossing always at the minimum adiabatic energy gap. The correct merging of the diabatic into the adiabatic states at the atom-diatom limit should also be highlighted.

8.2.4 The $N-O_2$ channel

The $N-O_2$ channel presents novel challenges for the GDA method due to the crossing seams that extend to the asymptotes (see figure 8.5). The representation of the avoided intersection surfaces with the same functional dependence as for HN_2, *i.e.*, $R_1^{0,p} = f(\theta_1, r_1)$ would imply a divergent form for $R_1^{0,p}$ at both $r_1 \to x_{c1}$ for $p = 12$, and $r_1 \to x_{c2}$ for $p = 23$. Moreover, for the $1^2A''/2^2A''$ crossing it would not be defined for $r_1 \in [x_{c1}, \infty[$. Similarly, the corresponding surface of avoided intersections for the $2^2A''/3^2A''$ states would not be defined for $r_1 \in [0, x_{c2}]$. A more convenient form for the latter is

$$r_1^{0,p} = f(\theta_1, R_1) \tag{8.9}$$

where the diatomic separation along the crossing seams and avoided intersection points $r_1^{0,p}$ is a function of θ_1 and R_1. The avoided intersection surfaces built as described above are shown in figure 8.9. Note that numerical interpolation has been employed as well.

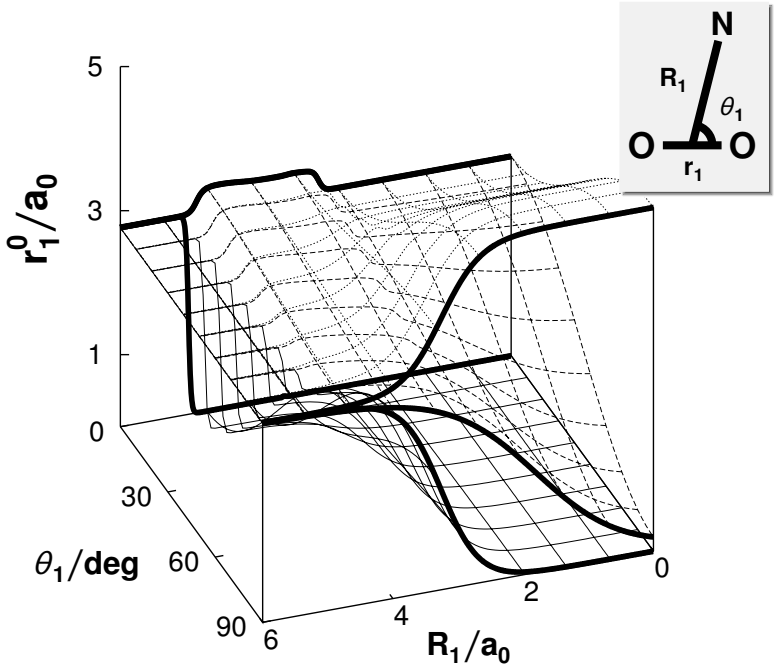

Figure 8.9: Avoided intersection surfaces for the $N-O_2$ channel. The sub-index 1 indicates this channel in the correspondent jacobi coordinates. Key: full lines for $r_1^{0,23,2}(\theta_1, R_1)$, dashed lines for $r_1^{0,12}(\theta_1, R_1)$ and dotted lines for $r_1^{0,23}(\theta_1, R_1)$; Thick lines for θ_1 equal to 0 and 90 degrees represents the interpolated results for the crossing seams in this channel.

With the representations chosen to model the locus of avoided intersections, $r_1^{0,12}(\theta_1, R_1)$ and

$r_1^{0,23}(\theta_1, R_1)$, the next step consists of testing a form for the diabatization angle in this channel, namely

$$\alpha_1^p(\mathbf{R}) = \frac{\pi}{4}\left\{1 - \tanh\left\{\gamma_1^p\left[r_1 - r_1^{0,p}(\theta_1, R_1)\right]\right\}\right\} \tag{8.10}$$

An inspection of Eq. (8.10) shows that, similarly to Eq. (8.5), it ensures a unique and well defined behavior at $r_1 \to 0$ and $r_1 \to \infty$, being finite in the first case and vanishing in the second. Following the procedure utilized for the $O - NO$ channel, the states $1^2A''/2^2A''$ and $2^2A''/3^2A''$ are first diabatized independently to insure that each of the forms in Eq. 8.10 with $p = 12$ and $p = 23$ gives an adequate description of the resulting diabats. Similar rotation matrices as for the $O - NO$ channel have been employed, namely $\mathcal{R}_1^{23}(\mathbf{R})$ and $\mathcal{R}_1^{12}(\mathbf{R})$. No undesirable features have been found in such diabatizations, with the diabats evolving correctly between the two crossing seams at the linear OON and T-shaped arrangements and merging properly with the adiabatic states at the asymptotes.

For the three-state diabatization, a procedure similar to the $O - NO$ case has been followed by exploring the fact that the $1^2A''/2^2A''$ and $2^2A''/3^2A''$ T-shaped and linear crossing seams are ordered (the former lies more internally than the latter; figures 8.7 and 8.8, and section 8.2.2). The total rotation matrix for the $N - O_2$ channel now reads

$$\mathcal{R}_1(\mathbf{R}) = \mathcal{R}_1^{23}(\mathbf{R})\,\mathcal{R}_1^{12}(\mathbf{R}) \tag{8.11}$$

with the matrix $\mathcal{R}_1^{12}(\mathbf{R})$ transforming yielding two decoupled states. A fully diabatized matrix is then obtained via $\mathcal{R}_1^{23}(\mathbf{R})$. As for the $O - NO$ channel, all three diabatic states smoothly evolve between the linear NOO and T-shaped boundaries, crossing at the minimal adiabatic energy gap point as so desired. A perfect merging between adiabatic and diabatic states is also observed at the asymptotes.

8.2.5 Global diabatization

The global diabatization stems from the fact that the $1^2A''/2^2A''$ crossing seams lie, for both the $O - NO$ and $N - O_2$ channels, more internally than the $2^2A''/3^2A''$ ones. A similar argumentation as used in Eqs. (8.8) and (8.11) suggests now a global matrix of the form

$$\mathcal{R}(\mathbf{R}) = \mathcal{R}^{23}(\mathbf{R})\,\mathcal{R}^{12}(\mathbf{R}) \tag{8.12}$$

where $\mathcal{R}^{12}(\mathbf{R})$ and $\mathcal{R}^{23}(\mathbf{R})$ are defined in a similar fashion as in Eqs 8.6 and 8.7. Note that the $\mathcal{R}(\mathbf{R})$ matrix (via $\mathcal{R}^{12}(\mathbf{R})$) transforms the adiabatic problem into a diabatic one where one of the states coincides with the third $^2A''$ state, and then (via $\mathcal{R}^{23}(\mathbf{R})$) into the final diabatic form. Finally, to account simultaneously for both channels, the global diabatization angles α^p are defined by the symmetrized product

$$\alpha^p(\mathbf{R}) = \alpha_1^p(\mathbf{R})\,\alpha_2^p(\mathbf{R}) \tag{8.13}$$

following the recent application to the $HN_2(^2A')$ manifold.

Figure 8.10 shows adiabatic and diabatic profiles, the latter obtained after the application of the rotation matrix in Eq. (8.12), for cuts involving linear NOO, linear ONO and T-shaped arrangements as well as neighbor geometries. As seen, the diabatic states exhibit all the features that one would expect. In particular, the merging with adiabatic states at the atom-diatom limits is warranted, with the avoided intersections smoothly evolving into conical intersections at the boundaries.

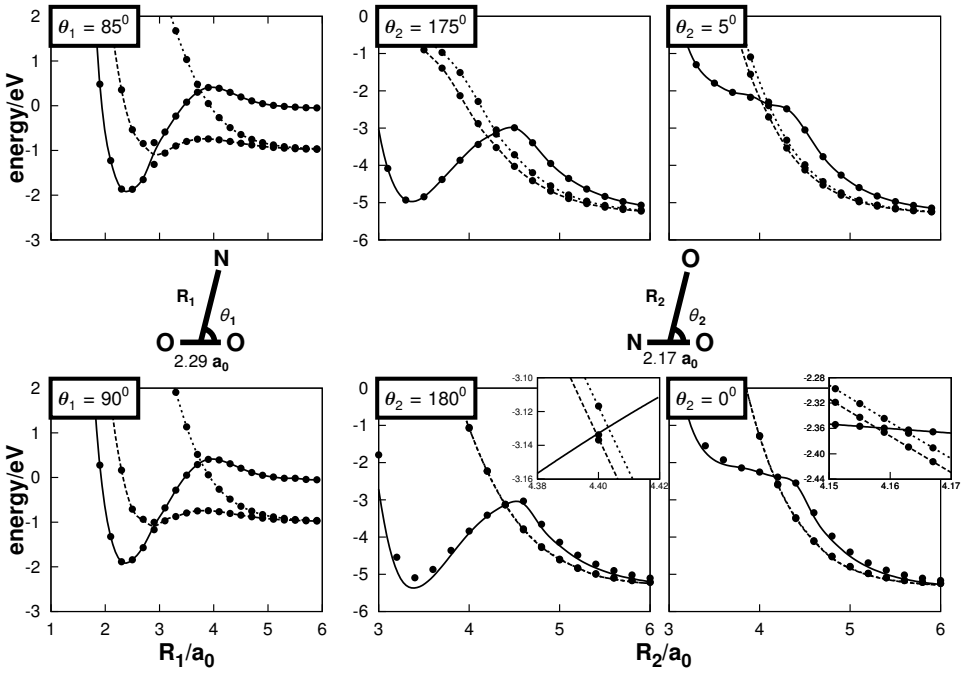

Figure 8.10: Evolution of the diabats in the vicinity of the several conical intersection. Points denote the adiabats, while the lines denotes the diabats.

8.3 Summary

Exploratory FVCAS calculations mapping the crossing seams and dissociation channels of the lower $^2A''$ states of NO_2 have been presented, revealing strong couplings between such states. They suggest that a correct description of the lower $NO_2(^2A'')$ states demands modeling a manifold of at least three sheets. With a view to later use, we have successfully sketched a diabatization procedure which, as shown, may lead us to a successful modeling of the $NO_2(^2A'')$ manifold via DMBE theory.

The diabatization performed provides an extension of the GDA [31] method to the 3-state case. Following earlier work, the problem has been split into two parts, each involving a separate atom-diatom channel, in such a way that the diabatization/ angles so constructed ensured a correct behavior at the corresponding asymptote. A proper description of the crossing seams and avoided crossings as viewed from each of those channels separately has also been warranted. For this, we have first treated each of the consecutive pairs of states separately, using two sequential rotations to diabatize each of the channels. To diabatize simultaneously both channels, we have explored the internal ordering of the crossing seams, leading to a global angle for each state-pair. This has also led to the introduction of a third global angle to better describe in the future a seam of $2^2A''/3^2A''$ avoided intersection. In fact, this may be key for describing the $N - O_2$ channel. Although promising results have been obtained from such a procedure, previous experience with [31] HN_2 suggest that a complete assessment of its capabilities stems from the ability of modeling a 3×3 DMBE diabatic matrix. Such a work is currently in progress.

8.4 Outlook

The working tasks of the CU group project have been completed according to the proposed schedule. First, an accurate DMBE PES for $N_3(^4A'')$ has been reported [13], and dynamics studies of the $N + N_2$ reaction concluded [9]. The calculated rate constants for this system are possibly the best theoretical ones thus far reported, and are believed to be sufficiently realistic for inclusion in databases for simulation purposes. Second, work towards a realistic 3×3 DMBE PES for the $NO_2(^2A'')$ electronic manifold is under completion, pursued using a generalization of the scheme utilized [31] for the 2×2 DMBE PES of HN_2. The work has so far been completed at an exploratory level of *ab initio* theory, and will be pursued using electronic structure calculations at a higher level. The goal is to make available realistic multi-sheeted DMBE potential energy surfaces both for the [8, 31] $^2A'$ and $^2A''$ manifolds of NO_2. It is hoped that the electronic manifold recently published [69] for the H_3^+ system can also be utilized for further accurate nonadiabatic dynamics studies such as those reported in Ref. [70]. Finally, for practical matters related to use by other members of the Group, a global single-sheeted form for $NO_2(^2A'')$ has been calculated using accurate MRCI calculations and modelled with the DMBE methodology. Moreover, other issues that are of generic use have benefited from the ESA funding. These include the development of a variant of second-order Møller-Plesset theory (so-called variable-oposed-spin MP2 [71]), and a novel generalized Born-Oppenheimer theory for Jahn-Teller systems with electronic manifolds of arbitrary degeneracy [72].

References

[1] Wang, D., Stallcop, J. R., Huo, W. M., Dateo, C. E., Schwenke, D. W., and Partridge, H., "Quantal study of the exchange reaction for N+N_2 using an *ab initio* potential energy surface," *Journal of Chemical Physics*, Vol. 118, 2003, pp. 2186.

[2] Back, R. A. and Mui, J. Y. P., "The reactions of active nitrogen with NO and N_2," *Journal of Physical Chemistry*, Vol. 66, 1962, pp. 1362.

[3] Bar-Nun, A. and Lifshitz, A., "Kinects of the homogeneous exchange reaction $^{14-14}N_2$+$^{15-15}N_2$ $\rightarrow$ $2^{14-15}N_2$," *Journal of Chemical Physics*, Vol. 47, 1967, pp. 2878.

[4] Lyon, R. K., "Search for the N-N, Exchange Reaction," *Canadian Journal of Chemistry*, Vol. 50, 1972, pp. 1437.

[5] Varandas, A. J. C., "A general approach to the potential energy function of small polyatomic systems: molecules and van der Waals molecules," *Journal of Molecular Structure THEOCHEM*, Vol. 120, 1985, pp. 401.

[6] Varandas, A. J. C., "Intermolecular and intramolecular potentials: topographical aspects, calculation, and functional representation via a DMBE expansion method," *Advances in Chemical Physics*, Vol. 74, 1988, pp. 255–337.

[7] Varandas, A. J. C., "Multivalued potential energy surfaces for dynamics calculations," *"Lecture Notes in Chemistry", edited by A. Laganá & A. Riganelli (Springer, Berlin)*, Vol. 72, 2000, pp. 33–56.

[8] Varandas, A. J. C., "Conical Intersections: Electronic Structure, Spectroscopy and Dynamics," *"Advanced Series in Physical Chemistry", World Scientific Publishing (chapter 5)*, 2004, pp. 91.

[9] Caridade, P. J. S. B., Galvão, B. R. L., and Varandas, A. J. C., "Quasiclassical trajectory study of atom-exchange and vibrational relaxation processes in collisions of atomic and molecular nitrogen," *Journal of Physical Chemistry A*, Vol. 114, 2010, pp. 6063.

[10] Hase, W. L., Duchovic, R. J., Hu, X., Komornicki, A., Lim, K. F., Lu, D., Peslherbe, G. H., Swamy, K. N., Linde, S. R. V., Varandas, A. J. C., Wang, H., and Wolf, R. J., "VENUS96: A General Chemical Dynamics Computer Program," *QCPE Bull.*, Vol. 16, 1996, pp. 43.

[11] Varandas, A. J. C., "Extrapolating to the one-electron basis-set limit in electronic structure calculations," *Journal of Chemical Physics*, Vol. 126, 2007, pp. 244105.

[12] Varandas, A. J. C., "Accurate global ab initio potentials at low-cost by correlation scaling and extrapolation to the one-electron basis set limit," *Chemical Physics Letters*, Vol. 443, 2007, pp. 398.

[13] Galvão, B. R. L. and Varandas, A. J. C., "Accurate double many-body expansion potential energy surface for $N_3(^4A'')$ from correlation scaled ab initio energies with extrapolation to the complete basis set limit," *Journal of Physical Chemistry A*, Vol. 113, 2009, pp. 14424.

[14] Watts, J. D., Gauss, J., and Bartlett, R. J., "Coupled-cluster methods with noniterative triple excitations for restricted open-shell HartreeFock and other general single determinant reference functions. Energies and analytical gradients," *Journal of Chemical Physics*, Vol. 98, 1993, pp. 8718.

[15] Werner, H. J. and Knowles, P. J., "An efficient internally contracted multiconfigurationreference configuration interaction method," *Journal of Chemical Physics*, Vol. 89, 1988, pp. 5803.

[16] Knowles, P. J. and Werner, H. J., "An efficient method for the evaluation of coupling coefficients in configuration interaction calculations," *Chemical Physics Letters*, Vol. 145, 1988, pp. 514.

[17] Dunning Jr., T. H., "Gaussian basis sets for use in correlated molecular calculations. I. The atoms boron through neon and hydrogen," *Journal of Chemical Physics*, Vol. 90, 1989, pp. 1007.

[18] Kendall, R. A., Dunning Jr., T. H., and Harrison, R. J., "Electron affinities of the first-row atoms revisited. Systematic basis sets and wave functions," *Journal of Chemical Physics*, Vol. 96, 1992, pp. 6796.

[19] Varandas, A. J. C., "A useful triangular plot of triatomic potential energy surfaces," *Chemical Physics Letters*, Vol. 138, 1987, pp. 455.

[20] Rampino, S., Skouteris, D., Laganà, A., Garcia, E., and Saracibar, A., "A comparison of the quantum state-specific efficiency of $N+N_2$ reaction computed on different potential energy surfaces," *Physical Chemistry Chemical Physics*, Vol. 11, 2009, pp. 1752.

[21] Wang, D., Huo, W. M., Dateo, C. E., Schwenke, D. W., and Stallcop, J. R., "Quantum study of the $N+N_2$ exchange reaction: State-to-state reaction probabilities, initial state selected probabilities, Feshbach resonances, and product distributions," *Journal of Chemical Physics*, Vol. 120, 2004, pp. 6041.

[22] Truhlar, D. G., "Accuracy of trajectory calculations and transition state theory for thermal rate constants of atom transfer reactions," *Journal of Physical Chemistry*, Vol. 83, 1979, pp. 188.

[23] Varandas, A. J. C., "Trajectory binning scheme and non-active treatment of zero-point energy leakage in quasi-classical dynamics," *Chemical Physics Letters*, Vol. 439, 2007, pp. 386.

[24] Varandas, A. J. C., "Geometrical phase effect in Jahn-Teller systems: Twofold electronic degeneracies and beyond," *Chemical Physics Letters*, Vol. 487, 2010, pp. 139–146.

[25] Murrell, J. N., Carter, S., Farantos, S. C., Huxley, P., and Varandas, A. J. C., *"Molecular Potential Energy Functions" (Wiley, Chichester)*, 1984.

[26] Born, M. and Oppenheimer, J. R., "Zür Quantentheorie der moleken," *Annalen der Physik*, Vol. 84, 1927, pp. 457.

[27] Born, M. and Huang, K., *"Dynamical Theory of Crystal Lattices" (Clarendon Press, Oxford)*, 1954.

[28] Lichten, W., "Molecular wave functions and inelastic atomic collisions," *Physical Review*, Vol. 164, 1967, pp. 131.

[29] Smith, F. T., "Diabatic and adiabatic representations for atomic collision problems," *Physical Review*, Vol. 179, 1969, pp. 111.

[30] O'Malley, T. F., "Diabatic states of molecules-quasistationary electronic states," *"Advances in Atomic and Molecular Physics", edited by Bates D.R. and Esterman I. (Academic, New York)*, Vol. 7, 1971, pp. 223–249.

[31] Mota, V. C. and Varandas, A. J. C., "$HN_2(^2A')$ electronic manifold. II. Ab initio based double-sheeted DMBE potential energy surface via a global diabatization angle," *Journal of Physical Chemistry A*, Vol. 112, 2008, pp. 3768–3786.

[32] Varandas, A. J. C., "A new formulation of three-body dynamical correlation energy for explicit potential functions," *Chemical Physics Letters*, Vol. 194, 1992, pp. 333.

[33] Mead, C. A. and Truhlar, D. G., "Conditions for the definition of a strictly diabatic electronic basis for molecular systems," *Journal of Chemical Physics*, Vol. 77, 1982, pp. 6090.

[34] Ellison, F. O., "A method of Diatomics in Molecules. I. General theory and application to H_2O," *Journal of American Chemical Society*, Vol. 85, 1963, pp. 3540.

[35] Varandas, A. J. C. and Voronin, A. I., "Towards a double many-body expansion method for multivalued potential energy surfaces. The H_3, FH_2 and NO_2 systems," *Molecular Physics*, Vol. 85, 1995, pp. 497.

[36] Kendrick, B. K. and Pack, R. T., "Potential energy surfaces for the low-lying $^2A''$ and $^2A'$ states of HO_2: use of the diatomics in molecules model to fit ab initio data," *Journal of Chemical Physics*, Vol. 102, 1995, pp. 1994.

[37] Varandas, A. J. C. and Voronin, A. I., "Potential-energy surfaces for the low-lying $^2A''$ states of HO_2 via a multivalued double many-body expansion. Modeling basic attributes," *Journal of Physical Chemistry*, Vol. 99, 1995, pp. 15846.

[38] Varandas, A. J. C., Voronin, A. I., and Caridade, P. J. S. B., "Energy switching approach to potential surfaces. III. Three-valued function for the water molecule," *Journal of Chemical Physics*, Vol. 108, 1998, pp. 7623.

[39] Varandas, A. J. C., "On the geometric phase effect in Jahn-Teller systems," *in "Fundamental World of Quantum Chemistry: A Tribute Volume to the Memory of Per-Olov Löwdin", edited by E. J. Brändas and E. S. Kryachko (Kluwer, Dordrecht) (chapter 2)*, Vol. 2, 2003, pp. 33–92.

[40] Varandas, A. J. C., "A realistic multi-sheeted potential energy surface for $NO_2(^2A')$ from the double many-body expansion method and a novel multiple energy-switching scheme," *Journal of Chemical Physics*, Vol. 119, 2003, pp. 2596.

[41] Mebel, A. M., Halász, G. J., Vibók, Á., Alijah, A., and Baer, M., "Quantization of the 3×3 nonadiabatic coupling matrix for three coupled states of the C_2H molecule," *Journal of Chemical Physics*, Vol. 117, 2002, pp. 991.

[42] Vértese, T., Bene, E., Vibók, Á., Halász, G. J., and Baer, M., "N-state adiabatic-to-diabatic transformation angle: theory and application," *Journal of Physical Chemistry A*, Vol. 109, 2005, pp. 3476.

[43] Halász, G. J., Vibók, Á., Baer, R., and Baer, M., "D matrix analysis of the Renner-Teller effect: an accurate three-state diabatization for NH_2," *Journal of Chemical Physics*, Vol. 125, 2006, pp. 094102.

[44] Sarkar, B. and Adhikari, S., "Extended Born-Oppenheimer equation for a three-state system," *Journal of Chemical Physics*, Vol. 87, 2006, pp. 074101.

[45] Vibók, Á., Halász, G. J., Suhai, S., Hoffman, D. K., Kouri, D. J., and Baer, M., "Two-state versus three-state quantization: an ab initio study of the three lower states of the $\{N,H_2|A'\}$ system," *Journal of Chemical Physics*, Vol. 124, 2006, pp. 024312.

[46] Caridade, P. J. S. B., Mota, V. C., Mohallem, J. R., and Varandas, A. J. C., "A theoretical study of rate coefficients for the O+NO vibrational relaxation," *Journal of Chemical Physics*, Vol. 112, 2008, pp. 960–965.

[47] Gillespie, G. D., Khan, A. U., Wahl, A. C., Hosteny, R. P., and Krauss, M., "The electronic structure of nitrogen dioxide. I. Multiconfiguration self-consistent-field calculation of the low-lying electronic states," *Journal of Chemical Physics*, Vol. 63, 1975, pp. 3425.

[48] Jackels, C. F. and Davidson, E. R., "An ab initio potential-energy surface study of several electronic states of NO_2," *Journal of Chemical Physics*, Vol. 65, 1976, pp. 2941.

[49] Braunstein, M. and Duff, J. W., "Theoretical study of the N(^2D)+O_2($X^3\Sigma_g^-$)→O+NO reaction," *Journal of Chemical Physics*, Vol. 113, 2000, pp. 7406.

[50] Gonzáles, M., Miquel, I., and Sayós, R., "Ab initio, VTST, and QCT study of the $1\,^2A''$ potential energy surface of the N(^2D)+O_2($X^3\Sigma_g^-$)→ O(^3P)+NO($X^2\Pi$) reaction," *Journal of Chemical Physics*, Vol. 115, 2001, pp. 8838.

[51] Gonzáles, M., Miquel, I., and Sayós, R., "VTST kinetics study of the N(^2D)+O_2($X^3\Sigma_g^-$) → NO($X^2\Pi$)+O(^3P,^1D) reactions based on CASSCF and CASPT2 ab initio calculations including excited potential energy surfaces," *Chemical Physics Letters*, Vol. 335, 2001, pp. 339.

[52] Mahapatra, S., Köppel, H., Cederbaum, L. S., Stampfuβ, P., and Wenzel, W., "Nonadiabatic wave packet dynamics on the coupled $\tilde{X}\,^2A_1/\tilde{A}\,^2B_2$ electronic states of NO_2 based on a new ab initio potential energy surfaces," *Chemical Physics*, Vol. 259, 2000, pp. 211.

[53] Kurkal, V., Fleurat-Lessard, P., and Schinke, R., "NO_2: Global potential energy surfaces of the ground ($1\,^2A_1$) and the first excited ($1\,^2B_2$) electronic states," *Journal of Chemical Physics*, Vol. 119, 2003, pp. 1489–1501.

[54] Ivanov, M. V., Zhu, H., and Schinke, R., "Theoretical investigation of exchange and recombination reactions in O(^3P)+NO($^2\Pi$) collisions," *Journal of Chemical Physics*, Vol. 126, 2007, pp. 054304.

[55] Schinke, R., Grebenshchikov, S. Y., and Zhu, H., "The photodissociation of NO_2 in the second absorption band: ab initio and quantum dynamics calculations," *Chemical Physics*, Vol. 346, 2008, pp. 99.

[56] Schinke, R., "Theoretical study of the $\tilde{D} \rightarrow \tilde{C}$ emission spectrum of NO_2," *Journal of Chemical Physics*, Vol. 129, 2008, pp. 124303.

[57] Reignier, D., Stoecklin, T., Voronin, A., and Rayez, J. C., "Analytical global potential energy surfaces of the two lowest $^2A'$ states of NO_2," *Physical Chemistry Chemical Physics*, Vol. 3, 2001, pp. 2726.

[58] Roos, B. O., Taylor, P. R., and Siegbahn, P. E. M., "A complete active space SCF method (CASSCF) using a density matrix formulated super-CI approach," *Chemical Physics*, Vol. 48, 1980, pp. 157.

[59] Roos, B. O., *"Ab Initio Methods in Quantum Chemistry", edited by K. Lawley (Wiley, New York)*, 1987, pp. 399.

[60] Andersson, K., "Different forms of the zeroth-order Hamiltonian in second-order perturbation theory with a complete active space self-consistent field reference function," *Theoretica Chimica Acta*, Vol. 91, 1995, pp. 31.

[61] Varandas, A. J. C., "Energy switching approach to potential energy surfaces: an accurate single-valued function for the water molecule," *Journal of Chemical Physics*, Vol. 105, 1996, pp. 3524.

[62] Caridade, P. J. S. B. and Varandas, A. J. C., "Dynamics study of the N(^4S)+O_2 reaction and its reverse," *Journal of Physical Chemistry A*, Vol. 108, 2004, pp. 3556.

[63] Langhoff, S. R. and Davidson, E. R., "Configuration interaction calculations on the nitrogen molecule," *International Journal of Quantum Chemistry*, Vol. 8, 1974, pp. 61–72.

[64] Hay, P. G., Pack, R., Walker, R. B., and Heller, E. J., "Photodissociation of ozone in the Hartley band. Exploratory potential energy surfaces and molecular dynamics," *Journal of Physical Chemistry*, Vol. 86, 1982, pp. 862.

[65] Krishnan, R., Binkley, J. S., Seeger, R., and Pople, J. A., "Self-consistent molecular orbital methods. XX. A basis set for correlated wave functions," *Journal of Chemical Physics*, Vol. 72, 1980, pp. 650.

[66] Mota, V. C., Caridade, P. J. S. B., and Varandas, A. J. C., "Toward the modeling of the NO_2 ($^2A''$) manifold," *International Journal of Quantum Chemistry*, 2010, pp. DOI:10.1002/qua.22907.

[67] Werner, H.-J., Knowles, P. J., Lindh, R., Manby, F. R., Schütz, M., et al., "MOLPRO, version 2008.3, a package of ab initio programs," 2008.

[68] Teller, E., "The crossing of potential surfaces," *Journal of Physical Chemistry*, Vol. 41, 1937, pp. 109.

[69] Viegas, L., Alijah, A., C., A. J., and Varandas, "Accurate ab initio based multisheeted double many-body expansion potential energy surface for the three lowest electronic singlet states of H_3^+," *Journal of Chemical Physics*, Vol. 126, 2007, pp. 074309.

[70] Chu, T. S., Varandas, A. J. C., and Han, K., "Nonadiabatic effects in D^++H_2 and H^++D_2," *Chemical Physics Letters*, Vol. 471, 2009, pp. 222–228.

[71] Varandas, A. J. C., "Spin-component-scaling second-order Møller-Plesset theory and its variants for economical correlation energies: Unified theoretical interpretation and use for quartet N_3," *Journal of Chemical Physics*, Vol. 133, 2010, pp. 064104.

[72] Varandas, A. J. C. and Sarkar, B., "Generalized Born-Oppenheimer treatment of Jahn-Teller systems in Hilbert spaces of arbitrary dimension. Theory and application to a three-state model potential," *Physical Chemistry Chemical Physics (in press)*, 2011.

Part III

Conclusions

Conclusions

The present thesis provides an extensive report on the work done during the doctoral program pursued by the candidate. It was divided into two parts: a theoretical background that surveys the theory behind the methodology utilized, and a second part that presents the results obtained by our research as manuscripts published in peer-reviewed journals. A summary of the work done and the major results obtained are given below.

High level electronic structure calculations were performed for the H_2O system and extrapolated to the complete basis set limit in order to improve a previous global (PES). The new PES was then merged (using the energy-switching method) to a highly accurate local polynomial form fitted using extensive calculations around the deep well, which includes small physical effects such as core-valence, relativistic, quantum electrodynamics and diagonal Born-Oppenheimer correction. The resulting surface was then used to calculate the ro-vibrational levels of water up to 20000cm^{-1}, where the global deviation from the experimentally measured levels was around 1cm^{-1}. The PES thus obtained may be employed to predict higher energy levels up to the dissociation limit, where the former local polynomial could not be used, and even dynamical calculations may be performed on such spectroscopic accurate PES.

Turning the focus to collisions between atomic and molecular nitrogen, we have performed electronic structure calculations for the $N_3(^4A'')$ system at the MRCI(Q) and CCSD(T) levels, followed by extrapolation to the complete basis set limit and modeling of an accurate PES for the system using the double many-body expansion (DMBE) method. In this work, we have predicted a new barrier height for the exchange reaction of 45.9 kcal mol^{-1}, which is $\sim$ 1.5 kcal mol^{-1} lower than previous theoretical estimates.

Also, new features of the $^4A''$ electronic state were found, arising from a crossing between $^4A_2/^4B_1$ states under C_{2v} symmetry but lying higher in energy. These new features are also modeled by our potential and, as an asset of the DMBE theory, the long range attractive forces are accurately described.

The PES described above was then used on a quasiclassical trajectory (QCT) study of collisions between atomic and molecular nitrogen for the atom exchange reaction and also for vibrational energy transfer from non-reactive scattering. In this study we have shown that, due to the large masses of the nitrogen atoms, quantum mechanical effects are negligible and the results obtained by classical means for the averaged thermal rate constants are essentially the same. Previous theoretical calculations have suggested that the long range attractive forces should be important for the exchange reaction, a result that comes as a surprise, since one would anticipate that this is more likely to happen for barrierless reactions, but certainly not for a large barrier such as the present case. We have investigated this assumption and showed that, as would be theoretically expected, the rate constant depends solely on the height and position of the barrier, and not on the long range potential. A detailed analysis on the vibrational energy transfer was also performed, showing that for non-reactive collisions one-quantum transitions are the most probable event, while for the reactive ones the vibrational relaxation to ground state products is the most favorable. As a major outcome however, we have predicted the exchange rate constant to be higher than previous theoretical estimates (due to a lower reaction barrier) and found improved agreement with experiments. Furthermore, it is shown that if the barrier is reduced such as to reproduce the experimental value at 3400 K, it yields a PES that fails to obey the experimental upper limit of the rate constant at 1273 K. These predictions are perhaps the most reliable ones available in the literature, as corroborated by a recent study on the the $N(^4S)+N_2$ transition state.

The recent findings regarding the new cyclic structure for the azide radical (N_3) and also the presence of excited nitrogen atoms in the atmosphere prompted us to extend the work to the doublet sheets of trinitrogen, which allowed for the first time the study of dynamical properties of $N(^2D)+N_2$ collisions and the formation of both isomers through this fundamental step.

The $^2A''$ state, which holds both linear and cyclic isomers, shows a Jahn Teller conical intersection at D_{3h} configurations that distorts to form cyclic N_3. Given that this conical intersection lies low in energy and that it is relevant for spectroscopy studies, we have included it in the model by fitting together the two adiabatic sheets with the DMBE theory. After calculating a large set of state-averaged MRCI(Q) energies, the two lowest states of $^2A''$ symmetry were obtained for the first time in a global form that describes dissociation, showing new stationary structures that were unknown to previous works. The $^2A'$ state is also necessary for dynamics studies, given that it is degenerate with the $^2A''$ one for linear configurations (where the minimum energy path lies) but does not show the cyclic structure. It's most important conical intersection is located on a C_{2v} configuration and was modeled through the eigenvalues of a 2×2 diabatic matrix.

With this collection of PESs in hand, we were able to predict the rate constants for the nitrogen exchange reaction in $N(^2D)$+N_2 collisions for the first time. The role played by nonadiabatic transitions to the upper sheets was investigated with the trajectory surface hopping method of Tully and Preston as implemented by Voronin *et al.*, where it was found that the adiabatic dynamics is reliable and such transitions do not play a major role in the exchange reaction.

Finally, regarding the study of the fundamental vibrational excitation of the nitric oxide (NO) from collisions with atomic oxygen, we have performed a thorough QCT study in order to obtain new insights on this subject that has fundamental relevance to the modeling of the thermosphere. Using two adiabatic potential energy surfaces of different symmetry ($^2A'$ and $^2A''$ of NO_2), trajectories have been integrated for temperatures of 500, 750, 1000K and two different methods for the quantization of the product rovibrational levels were used for analysis. The rate constants so obtained for the vibrational excitation were compared to available experimental data.

Among the discussed issues are the use of the detailed balance formula for this reaction from both theoretical and experimental perspectives and also the role that the features of the PES may present in the final results. The major result obtained was that, as suggested by previous work, the rotational envelopes of the 5.3 μm emission can be described by a Maxwell-Boltzmann distribution with the local temperature. This con-

tradicts the findings by Sharma *et al.* who suggested that this could only be true for lower temperatures where further collisions of nascent NO with other molecules may cause thermalization, and the consequences on the modeling of the temperature of the thermosphere as a function of altitude were analyzed.